



AN ANALYTICAL AND EXPERIMENTAL STUDY OF SHIPPING WATER
EVOLUTION AND RELATED VERTICAL LOADING

Jassiel Vladimir Hernández Fontes

Tese de Doutorado apresentada ao Programa de Pós-graduação em Engenharia Oceânica, COPPE, da Universidade Federal do Rio de Janeiro, como parte dos requisitos necessários à obtenção do título de Doutor em Engenharia Oceânica.

Orientadores: Sergio Hamilton Sphaier
Marcelo de Araujo Vitola

Rio de Janeiro
Maio de 2018

AN ANALYTICAL AND EXPERIMENTAL STUDY OF SHIPPING WATER
EVOLUTION AND RELATED VERTICAL LOADING

Jassiel Vladimir Hernández Fontes

TESE SUBMETIDA AO CORPO DOCENTE DO INSTITUTO ALBERTO LUIZ
COIMBRA DE PÓS-GRADUAÇÃO E PESQUISA DE ENGENHARIA (COPPE)
DA UNIVERSIDADE FEDERAL DO RIO DE JANEIRO COMO PARTE DOS
REQUISITOS NECESSÁRIOS PARA A OBTENÇÃO DO GRAU DE DOUTOR
EM CIÊNCIAS EM ENGENHARIA OCEÂNICA.

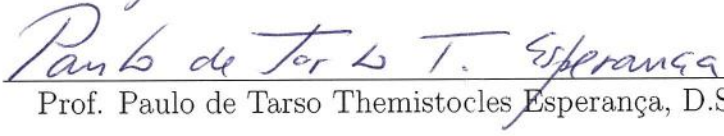
Examinada por:



Prof. Sergio Hamilton Sphaier, Dr.-Ing.



Dr. Marcelo de Araujo Vitola, D.Sc.



Prof. Paulo de Tarso Themistocles Esperança, D.Sc.



Prof. Claudio Alexis Rodríguez Castillo, D.Sc.



Prof. Su Jian, D.Sc.



Prof. Alexandre Nicolaos Simos, D.Sc.

RIO DE JANEIRO, RJ – BRASIL
MAIO DE 2018

Hernández Fontes, Jassiel Vladimir

An analytical and experimental study of shipping water evolution and related vertical loading/Jassiel Vladimir Hernández Fontes. – Rio de Janeiro: UFRJ/COPPE, 2018.

XVIII, 159 p.: il.; 29, 7cm.

Orientadores: Sergio Hamilton Sphaier

Marcelo de Araujo Vitola

Tese (doutorado) – UFRJ/COPPE/Programa de Engenharia Oceânica, 2018.

Bibliografia: p. 117 – 122.

1. Analytical convolution model. 2. Shipping water loading. 3. Wet dam-break experiments. I. Sphaier, Sergio Hamilton *et al.* II. Universidade Federal do Rio de Janeiro, COPPE, Programa de Engenharia Oceânica. III. Título.

To my wife and family

Acknowledgement

I would like to thank to the next institutions that, partially or totally, supported expenses of my graduate studies in Brazil and the development of the research project, including the high costs of the experimental research (e.g., construction of installations, sensors acquisition, operation and technical assistance), travel tickets (Mex-Bra, Bra-Mex), health insurance, medical assistance of major expenses, travel insurance, accommodation, maintenance, assistance to congresses, training courses, bibliography acquisition, manuscript revisions, journal publications, as well as production of the thesis:

To ANP (National Agency of Petroleum, Natural Gas and Biofuels) and to LABOCEANO (Ocean Technology Laboratory, COPPE/UFRJ) of Brazil.

To CONACYT (National Council of Science and Technology), the Veracruz state government and SENER (Secretary of Energy) of Mexico (CONACYT-Veracruz/SENER/Hidrocarburos).

To OUTREACH for Engineers Program of the ASME (American Society of Mechanical Engineers), USA.

Moreover, I would like to thank to the next people that contributed to my professional development during my graduate studies abroad:

To my supervisors Prof. Sergio H. Sphaier and Dr. Marcelo A. Vitola, and to professors and researchers from the Ocean Engineering program at COPPE/UFRJ: Drs. Paulo de Tarso T. Esperança, Murilo A. Vaz, Antonio C. Fernandes (Tatalo), Marcelo A. S. Neves, Claudio A. Rodríguez, Juan B. Wanderley, Julio C. R. Cyrinho, Carlos E. Parente and Monica Campos, for their guidance and teaching.

To Dr. Alberto O. Vázquez-Hernández from IMP (Mexican Petroleum Institute) for his constant help and to Dr. Fernando S. Flores-Ávila from PEMEX (Petroleum of Mexico) for his recommendations.

To Drs. Aldo Cruces, Federico Barranco, Oscar Godoy and Oscar Valle from IMP (Mexican Petroleum Institute) for their help to begin my studies in Rio.

To my family: wife Karla Lopes de Almeida, parents Costantina Fontes and David Hernández, brothers Irving and Towssaint Hernández-Fontes, and to the brazilian/portuguese family Lopes de Almeida Sueira, for their love and emotional support.

Resumo da Tese apresentada à COPPE/UFRJ como parte dos requisitos necessários para a obtenção do grau de Doutor em Ciências (D.Sc.)

UM ESTUDO ANALÍTICO E EXPERIMENTAL DA EVOLUÇÃO DO
EMBARQUE DE ÁGUA E DO CARREGAMENTO VERTICAL
RELACIONADO

Jassiel Vladimir Hernández Fontes

Maio/2018

Orientadores: Sergio Hamilton Sphaier
Marcelo de Araujo Vitola

Programa: Engenharia Oceânica

Estruturas costeiras, navais e offshore estão expostas ao problema de embarque de água no convés. Métodos analíticos ajudam na pesquisa do embarque de água devido à praticidade na implementação e ao baixo custo computacional comparados com métodos numéricos. Entretanto, métodos analíticos clássicos tendem a superestimar as amplitudes da água embarcada e as cargas verticais derivadas, não considerando a tendência real do fenômeno. A presente tese visa investigar o problema de embarque de água por métodos analíticos e experimentais alternativos que permitam um melhor entendimento da sua evolução e do carregamento vertical gerado. O problema de embarque de água foi modelado pela equação de advecção-difusão. Um modelo de convolução, solução dessa equação, foi proposto para estimar a evolução da água embarcada e as cargas verticais derivadas no convés de uma estrutura fixa retangular, considerando efeitos de atrito do fundo de uma maneira prática. Uma pesquisa experimental alternativa foi realizada para validar o método analítico. Esta consiste na geração de eventos de embarque de água isolados de uma maneira sistemática usando o método de *wet dam-break*. Os resultados analíticos obtidos para as elevações de água e as cargas verticais apresentaram boa concordância com os experimentos, aproximando as tendências e os valores máximos das séries temporais experimentais, melhorando os resultados obtidos com o método tradicional de *dam-break*.

Abstract of Thesis presented to COPPE/UFRJ as a partial fulfillment of the requirements for the degree of Doctor of Science (D.Sc.)

AN ANALYTICAL AND EXPERIMENTAL STUDY OF SHIPPING WATER
EVOLUTION AND RELATED VERTICAL LOADING

Jassiel Vladimir Hernández Fontes

May/2018

Advisors: Sergio Hamilton Sphaier
Marcelo de Araujo Vitola

Department: Ocean Engineering

Coastal, naval and offshore structures are exposed to the problem of shipping of water on their decks. Analytical approaches are useful for the shipping water research because of their practical implementation and low computational cost compared with numerical approaches. However, classical analytical methods tend to overestimate the shipping water amplitudes and derived vertical loading, disregarding the real tendency of the phenomenon. The present thesis aims to investigate the shipping water problem by alternative analytical and experimental methods that allow a better understanding of its evolution and generated vertical loading. The shipping water problem was modelled by the advection-diffusion equation. A convolution model, solution of this equation, was proposed to estimate shipping water evolution and derived vertical loads on deck of a rectangular fixed structure, considering frictional effects of the bottom in a practical way. An alternative experimental investigation was performed to validate the analytical approach. It consisted in generating isolated shipping water events in a systematic way using the wet dam-break approach. Obtained analytical results for water elevations and vertical loads presented good agreement with experiments, approximating the trends and maximum values of experimental time series, improving the results obtained with the traditional dam-break method.

Contents

List of Figures	xii
List of Tables	xviii
1 Introduction	1
1.1 The shipping water problem	1
1.1.1 Framework and scope of the study	4
1.1.2 Literature review of historical developments	5
1.2 The present study	10
1.2.1 Thesis structure	12
1.2.2 Summary of main findings and results	13
2 Analytical Methods	14
2.1 Proposed model	14
2.1.1 Model assumptions	14
2.1.2 Model development	15
2.2 The dam-break model	22
2.3 Vertical loading estimation	23
3 Experimental Methods	25
3.1 The wet dam-break approach	25
3.2 Experimental setup	28
3.2.1 General arrangement	28
3.2.2 Dimensions and sensors arrangement	29
3.2.3 Test matrix	31
3.3 Water evolution measurements	33
3.3.1 Water elevation: conventional wave probes	33
3.3.2 Water elevation: virtual wave probes	34
3.3.3 Water on deck kinematics: visual inspection	35
3.4 Load measurements	36
3.4.1 Vertical load measurements	36
3.4.2 Dynamic effects during the experiment	39

4	Experimental Results	41
4.1	Incoming wave	41
4.1.1	Wave generation	42
4.1.2	Wave propagation	49
4.2	Shipping water	62
4.2.1	Shipping water events	63
4.2.2	Shipping water evolution	67
4.2.3	Shipping water kinematics	76
4.3	Shipping water vertical loading	78
4.3.1	Vertical loading	79
4.3.2	Dynamic effects during the experiment	86
5	Analytical Results	91
5.1	Analytical model preliminaries and calibration	91
5.1.1	Input function selection	92
5.1.2	Kernel function time step analysis	93
5.1.3	Sensitivity analysis for model calibration	94
5.2	Application 1: Shipping water evolution	100
5.2.1	Comparison with DB model	104
5.3	Application 2: Loading on deck estimation	106
6	Conclusions	113
	Bibliography	117
A	Model development	123
A.1	Assumptions	123
A.2	From Navier-Stokes equations to 2D shallow water equations (z-direction integration)	124
A.2.1	Depth-averaged integration of the continuity equation	124
A.2.2	Depth-averaged integration of the momentum equation	127
A.3	From 2D to 1D shallow water equations (y-direction integration)	133
A.3.1	1D shallow water equations: Integration of the continuity equation	134
A.3.2	1D shallow water equations: Integration of the momentum equation	136
A.4	Dimensional analysis to simplify terms	140
A.5	The constant shear stress assumption	141
A.6	The advection-diffusion model	142
B	Complementary experimental setup illustrations	145

C	A tentative for wave characterization	149
D	Examples of shipping water events obtained with $h_0/h_1 = 0.6, 0.5, 0.4$	152
E	Related publications	156

List of Figures

1.1	Experimental observations of shipping water events on a fixed structure obtained with broken (left) unbroken (right) incoming waves.	2
1.2	A resemblance of types of shipping water that may be obtained with single unbroken waves interacting with a barge-shaped fixed structure. (a) Dam-Break type (DB). (b) Plunging-Dam-Break type (PDB). (c) Hammer-Fist type (HF)	3
2.1	Division of the shipping water problem in different regions.	14
2.2	Region of interest in the present study.	15
2.3	Euler system defining the layer of fluid bounded by bottom and free surface.	16
2.4	Fluid layer considered for the y- direction integration of the shallow water equations.	17
2.5	Semi-infinite domain considered for the present one-dimensional problem.	21
2.6	Dam-break model and its relation to shipping water prediction. (a) Application to a surface. (b) Application to a rectangular structure.	24
2.7	(a) Surface of interest discretization. (b) Assumed acting force on a region.	24
3.1	Wet-dam break. (a) Initial conditions. (b) Main stages after dam-break. Adapted from the Stoker's method.	26
3.2	Graphical solution for the wet dam-break problem with the Stoker method.	27
3.3	General arrangement of the experimental setup.	29
3.4	(a) Gate. (b) Weight.	30
3.5	Tank side details.	30
3.6	Main tank dimensions and sensors arrangement for the experiment with structure.	31
3.7	Main tank dimensions and sensors arrangement for the experiment without structure.	32

3.8	Scene field of view (FOV) of CAM1 for the experiment with the internal fixed structure. Virtual wave probes positions for the incoming wave and shipping water propagation domains.	35
3.9	Wavefront displacement measurements. (a) Wavefront edge close to the bow edge of the structure. (b) Wavefront well developed close to the end of the structure.	36
3.10	Force balance to measure vertical loading. (a) General view. (b) Accelerometer installed under the sensing element.	37
3.11	Views and dimensions of the force balance.	38
3.12	Different views of the force balance embedded to the deck of the internal fixed structure. (a) Top view. (b) Front view. (c) Back view.	40
4.1	Gate edge vertical displacement (z_{gate}) vs time (mean and standard deviation values) for all cases of the experiment without structure. (a) Case 1 (C1w). (b) Case 2 (C2w). (c) Case 3 (C3w). (d) Case 4 (C4w). (e) Case 5 (C5w).	43
4.2	Linear regression for gate edge mean vertical displacement (z_{gate}) vs time (t) for the experiment without structure. (a) Case 1 (C1w). (b) Case 2 (C5w).	44
4.3	Gate edge vertical velocity (w_{gate}) vs time (t) for the experiment without structure (Case 2).	45
4.4	Stages of wave generation for the experiment without structure (Case 1, C1w).	46
4.5	Stages of wave generation for the experiment without structure (Case 5, C5w).	47
4.6	Comparison between spatial distributions of wave elevations (η vs x) at different points in time for Case 1w (experiment without structure). Dash-dot lines correspond to the theoretical Stoker model. (a) $t_1 = 0.35$ s and $t_2 = 0.40$ s. (b) $t_1 = 0.35$ s and $t_2 = 0.45$ s. (c) $t_1 = 0.35$ s and $t_2 = 0.50$ s. (d) $t_1 = 0.35$ s and $t_2 = 0.55$ s. (e) $t_1 = 0.35$ s and $t_2 = 0.60$ s. (f) $t_1 = 0.35$ s and $t_2 = 0.75$ s.	49
4.7	Comparison of time series of water elevations (η) between the probe WP3 and its respective VWP located at the same position for the experiment with structure. (a) Case 3. (b) Case 5.	51
4.8	Two-dimensional reconstruction of the incoming wave evolution for the experiment with internal structure. The bow edge of the structure was considered as the origin. (a) Case 1. (b) Case 5.	52
4.9	Incoming wave evolution for Cases 1 and 5. (a) Case 1: η vs x . (b) Case 1: t vs x . (c) Case 5: η vs x . (d) Case 5: t vs x	53

4.10 Influence of the structure on the incoming wave evolution for Case 1 at several VWPs. (a) η vs t : case with structure. (b) η vs t : case without structure. (c) t vs x : case with structure. (d) t vs x : case without structure.	55
4.11 Influence of the structure on the incoming wave water elevation time series in experiments with and without the fixed structure for Case 1. The bow edge of the structure is considered as the origin. (a) $x=-0.1$ m. (b) $x=-0.2$ m. (c) $x=-0.3$ m. (d) $x=-0.4$ m.	57
4.12 Influence of the structure on the incoming wave water elevation time series in experiments with and without the fixed structure for Case 5. The bow edge of the structure is considered as the origin. (a) $x=-0.1$ m. (b) $x=-0.2$ m. (c) $x=-0.3$ m. (d) $x=-0.4$ m.	59
4.13 Maximum water elevations of the incoming wave (η , mean and standard deviation) at different positions (x) for the five cases considered. (a) Experiment without the fixed structure. (b) Experiment with the structure.	60
4.14 Comparison of the incoming wave crest horizontal velocity (U_{ED}) for the experimental setup without structure and the Stoker's approach (U_0).	61
4.15 Incoming wave crest horizontal velocities for the experimental setup with the internal structure, for regions defined by points A-D. Results obtained with the Stoker's approach for U_0 are shown for comparisons.	62
4.16 Representative snapshots of shipping water for Case 1.	64
4.17 Representative snapshots of shipping water for Case 3.	65
4.18 Representative snapshots of shipping water for Case 5.	66
4.19 Initial stages of shipping water at bow of the structure. (a,b) Case 1. (c,d) Case 3. (e,f) Case 5.	67
4.20 Comparison of time series of water elevations (η , mean and standard deviation values) between WP1, WP2 and VWPd0. (a) Case 3. (b) Case 5.	68
4.21 2D reconstruction of the shipping water evolution on deck (η vs x and t). (a) Case 1. (b) Case 4.	70
4.22 Shipping water evolution (t vs x). (a) Case 1. (b) Case 2. (c) Case 4. (d) Case 5.	71
4.23 Freeboard exceedance time series comparisons by VWPs measured before ($VWPw0 - D$, $x = -0.005$ m) and after ($VWPD0$, $x = 0.005$ m) the bow edge of the deck . (a) Case 1. (b) Case 2. (c) Case 4. (d) Case 5.	73

4.24	Time series of shipping water elevations (η) at different positions onto the deck (33 VWP's, $[0.01 \leq x \leq 0.33$ m, VWPd01 to VWPd33]). (a) Case 1. (b) Case 2. (c) Case 4. (d) Case 5.	75
4.25	Analysis of wavefront propagation onto the deck. (a) Case 1: x_{deck} vs t . (b) Case 3: x_{deck} vs t . (c) Case 1: U_{front} vs t . (d) Case 3: U_{front} vs t	77
4.26	Linear regressions performed to mean wavefront edge displacements (x_{deck}) values to estimate the wavefront velocity U_{front} at different regions over the deck. (a) Case 2: x_{deck} vs t for $0 < x < 0.02$ m. (b) Case 2: x_{deck} vs t for $0.1 < x < 0.35$ m. (c) Case 4: x_{deck} vs t for $0 < x < 0.02$ m. (d) Case 4: x_{deck} vs t for $0.1 < x < 0.35$ m.	78
4.27	Mean and standard deviation values of time series of vertical loads given by the four load cells in the Case 3. (a) Load cell 1 (LC1). (b) Load cell 2 (LC2). (c) Load cell 3 (LC3). (d) Load cell 4 (LC4).	80
4.28	Effects of initial stages of shipping water on the individual load cells performance.	82
4.29	Time series of total vertical loads for the five repetitions performed in the Case 3.	82
4.30	Snapshots of representative shipping water propagation stages for vertical loading analysis for the Case 3.	83
4.31	Calculated points of application of vertical loads over the sensing element of the balance. (a) Case 3. (b) Case 5.	84
4.32	Mean and standard deviation values of the total vertical load time series. Images under the graphs represent the stage at which the maximum loading on the balance occurred in each case. (a) Case 1. (b) Case 2. (c) Case 3. (d) Case 4.	86
4.33	Data from the accelerometer attached to the balance (Acc_{bal}). (a) Case 1, acceleration in X. (b) Case 5, acceleration in X. (c) Case 1, acceleration in Y. (d) Case 5, acceleration in Y. (e) Case 5, acceleration in Y. (e) Case 1, acceleration in Z. (f) Case 5, acceleration in Z.	87
4.34	Data from accelerometer attached to the tank vertical wall (Acc_{wall}): Cases 1 and 5, transversal direction (X).	89
4.35	Data from accelerometer attached to the tank vertical wall (Acc_{wall}): Cases 1 and 5, vertical direction (Y).	89
4.36	Data from accelerometer attached to the tank vertical wall (Acc_{wall}): Case 1 and 5, longitudinal direction (Z).	90

5.1	Input series selection for Case 4 (a) Mean and standard deviation values of time series measured at $x = -0.005$ m (VWPw0-D) and $x = 0.005$ m (VWPd0). (b) Input series and maximum freeboard exceedance definition (η_0) considered for model implementation. . . .	93
5.2	Kernel function time step analysis for the Case 1. (a) Kernel function at $x = 0.01$ m. (b) Kernel function at $x = 0.03$ m	95
5.3	Model outputs from the sensitivity analysis to identify the S_f parameter that better attains the maximum elevations of experiments, $x = 0.19$ m, Case 3. (a) $S_f = 0.1$. (b) $S_f = 0.2$	96
5.4	Sensitivity analysis of \bar{u} and S_f for Case 1. (a) Constant $S_f = 0.2$, \bar{u} varies, $x = 0.010$ m. (b) Constant $\bar{u} = 0.3$ m/s, S_f varies, $x = 0.010$ m. (c) Constant $S_f = 0.2$, \bar{u} varies, $x = 0.11$ m. (d) Constant $\bar{u} = 0.3$ m/s, S_f varies, $x = 0.11$ m. (e) Constant $S_f = 0.2$, \bar{u} varies, $x = 0.19$ m. (f) Constant $\bar{u} = 0.3$ m/s, S_f varies, $x = 0.19$ m	98
5.5	Sensitivity analysis of \bar{u} and S_f for Case 5. (a) Constant $S_f = 0.2$, \bar{u} varies, $x = 0.010$ m. (b) Constant $\bar{u} = 0.3$ m/s, S_f varies, $x = 0.010$ m. (c) Constant $S_f = 0.2$, \bar{u} varies, $x = 0.11$ m. (d) Constant $\bar{u} = 0.3$ m/s, S_f varies, $x = 0.11$ m. (e) Constant $S_f = 0.2$, \bar{u} varies, $x = 0.19$ m. (f) Constant $\bar{u} = 0.3$ m/s, S_f varies, $x = 0.19$ m	99
5.6	Model validation Case 1. Time step = $5E - 5$ s, $S_f = 0.2$, $\bar{u} = 0.3$ m/s.	101
5.7	Model validation Case 3. Time step = $5E - 5$ s, $S_f = 0.2$, $\bar{u} = 0.3$ m/s.	102
5.8	Model validation Case 5. Time step = $5E - 5$ s, $S_f = 0.2$, $\bar{u} = 0.3$ m/s.	103
5.9	Proposed model and experimental results comparison with the DB approach for Case 2. Time step = $5E - 5$ s, $S_f = 0.2$, $\bar{u} = 0.3$ m/s, $\eta_0 = 0.054$ m.	105
5.10	Proposed model and experimental results comparison with the DB approach for Case 4. Time step = $5E - 5$ s, $S_f = 0.2$, $\bar{u} = 0.3$ m/s, $\eta_0 = 0.063$ m.	106
5.11	Areas under the water elevation time series for $0 < t < 2$ s. (a) Proposed model and experiments. (b) Dam-break approach and experiments.	107
5.12	Discretization of the sensing area of the balance to estimate time series of water elevations for the vertical loading analysis. (a) Discretization. (b) Mean values of water elevation time series obtained experimentally for Case 2 (illustrative purposes). (c) Mean values of water elevation time series obtained experimentally for Case 4 (illustrative purposes).	108

5.13	Time series of water elevation from experiments used as input series for the vertical loading estimation. (a) Case 1. (b) Case 2. (c) Case 3. (d) Case 4. (e) Case 5.	109
5.14	Total vertical loading on the force balance for the Case 1: Comparison of experiments and results obtained with the proposed model (above) and the dam-break approach (below).	110
5.15	Total vertical loading on the force balance for the Case 3: Comparison of experiments and results obtained with the proposed model (above) and the dam-break approach (below).	111
5.16	Total vertical loading on the force balance for the Case 5: Comparison of experiments and results obtained with the proposed model (above) and the dam-break approach (below).	111
5.17	Areas under the total vertical loading curves for the experimental and analytical results at each study case.	112
A.1	Region of interest in the present study.	123
A.2	Euler system defining the layer of fluid bounded by bottom and free surface.	125
A.3	Fluid layer for the y- direction integration of the shallow water equations.	133
B.1	General view of the complete experimental setup, considering the experiment with the rectangular fixed structure inside the tank. . . .	145
B.2	Typical views of initial conditions for the experiments without (above) and with (below) the internal fixed structure.	146
B.3	Some important stages during sensors preliminary tests: conventional wave probes calibration (above), static-load pre-tests of the balance before each test (below-left) and camera calibration following the image-based methodology described in the Experimental Methods section (below-right).	147
B.4	Force balance top view (above left) and back view (above right). Detailed view of the force balance embedded to the internal fixed structure (below).	148
C.1	Incoming wave (bore) steepness characterization.	150
C.2	Spatial distributions of water elevations considered for $t = 0.85$ s to characterize the steepness of the resulting bores for the experiment without structure. (a) C1w. (b) C2w. (c) C3w. (d) C4w. (e) C5w. . . .	151
D.1	Snapshots of a shipping water event generated with $h_0/h_1 = 0.6$, $h_0 = 0.108$ m and $FB = 0.042$ m (unbroken wave).	153

D.2	Snapshots of a shipping water event generated with $h_0/h_1 = 0.5$,	
	$h_0 = 0.108$ m and $FB = 0.042$ m (unbroken wave). 154
D.3	Snapshots of a shipping water event generated with $h_0/h_1 = 0.4$,	
	$h_0 = 0.108$ m and $FB = 0.042$ m (unbroken wave). 155

List of Tables

3.1	Testing matrix with expected parameters for the experiments with and without the fixed structure.	32
4.1	Reference and obtained gate aperture times (t_r) for the five cases of study without the internal fixed structure (C1w-C5w).	45
4.2	Statistics of incoming wave crest horizontal velocities in different regions for the experiments with and without the structure, and theoretical values from Stoker's approach.	63
4.3	Mean wavefront velocities (U_{front}) estimated from linear regression analysis at different regions over the deck.	79
4.4	Maximum measured vertical loads for all the study cases.	85
5.1	Main information of maximum freeboard exceedance (η_0) for all cases.	92
C.1	Values of the incoming wave (bore) characterization of steepness and their relationship with regular waves.	150

Chapter 1

Introduction

1.1 The shipping water problem

Naval and offshore structures are subjected to the problem of shipping of water on their decks. This problem occurs when incoming waves interact with the structure in different manners, which causes the stages of bow run-up, freeboard exceedance and subsequent shipping of a resultant volume of water that propagates onto the deck. Such phenomena can occur from the bow, stern or sides of fixed, moored, free-floating or advancing structures, depending on the environmental and operation conditions.

The shipping water problem is often related to a series of problems that affect the operations, being possible to highlight the following:

- The shipping of water can affect the safety of the crew that operates on deck or in superstructures. The effects of the water propagating on deck or impacting in installations or crew checkpoints can be severe enough to cause serious human injuries.

- Often, expensive or delicate equipment is installed over the deck, then, it may be susceptible to damages due to unexpected and violent interactions with water. This can also occur for delicate structural arrangements exposed to the shipping water flow.

- The overloading caused by the water-on-deck has an effect in the six motions of floating, moored or advancing bodies. This may produce alterations in the ship dynamics and manoeuvrability for which they were designed to operate. The shipping water loading may contribute highly to the vertical motions; however, it has been verified recently that it may also contribute significantly to the parametric roll in ships (GRECO *et al.* [1]). On the other hand, for fixed structures such as fixed platforms, the shipping water loading can cause dynamic effects, yielding ringing and fatigue of substructures.

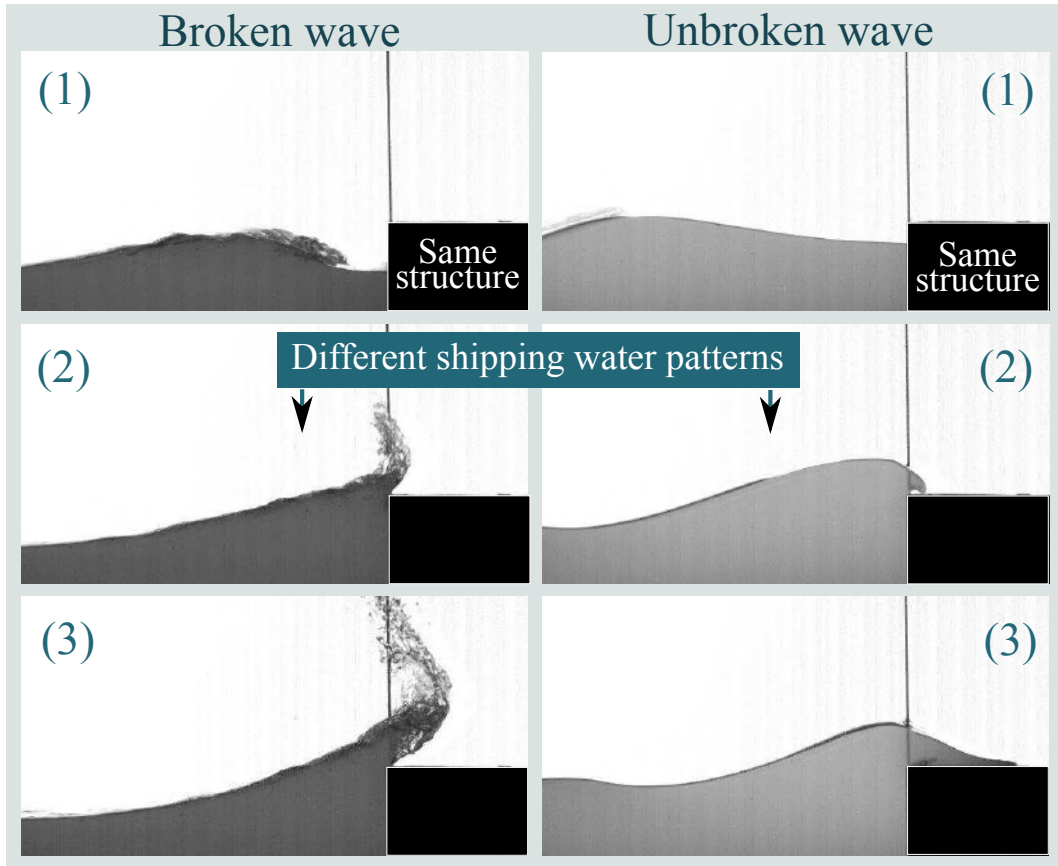


Figure 1.1: Experimental observations of shipping water events on a fixed structure obtained with broken (left) unbroken (right) incoming waves.

The shipping water may be presented in different scenarios (GRECO *et al.* [2, 3]), depending on the characteristics of the incoming wave (e.g., steepness, velocity), as well as the geometry of the structure (e.g., rectangular, curved, plane, inclined, etc.) and its operational conditions (e.g., fixed, moored, controlled, free motion). Combination of these factors may originate different types of wave-structure interactions, yielding different types of shipping water events. By way of example, Figure 1.1 presents some figures of two different types of shipping water on a barge-shaped fixed structure, which were obtained from experimental observations. In both cases, the structure has the same geometry (rectangular) and operation conditions (fixed); however, the incoming waves are different for each case. Images to the left of Fig. 1.1 consider a broken incident wave, whereas the ones to the right consider an unbroken wave. In both cases, an initial bow run-up stage due to the wave interaction with the vertical wall and a subsequent shipping of water onto the deck occurred. However, both cases presented different shipping water patterns. It can be observed that the case with the unbroken wave presented a compact and uniform mass of water shipping on the deck, forming a small plunging at the bow edge, whereas the case with the broken wave presented shipping of water in the form of a water splash

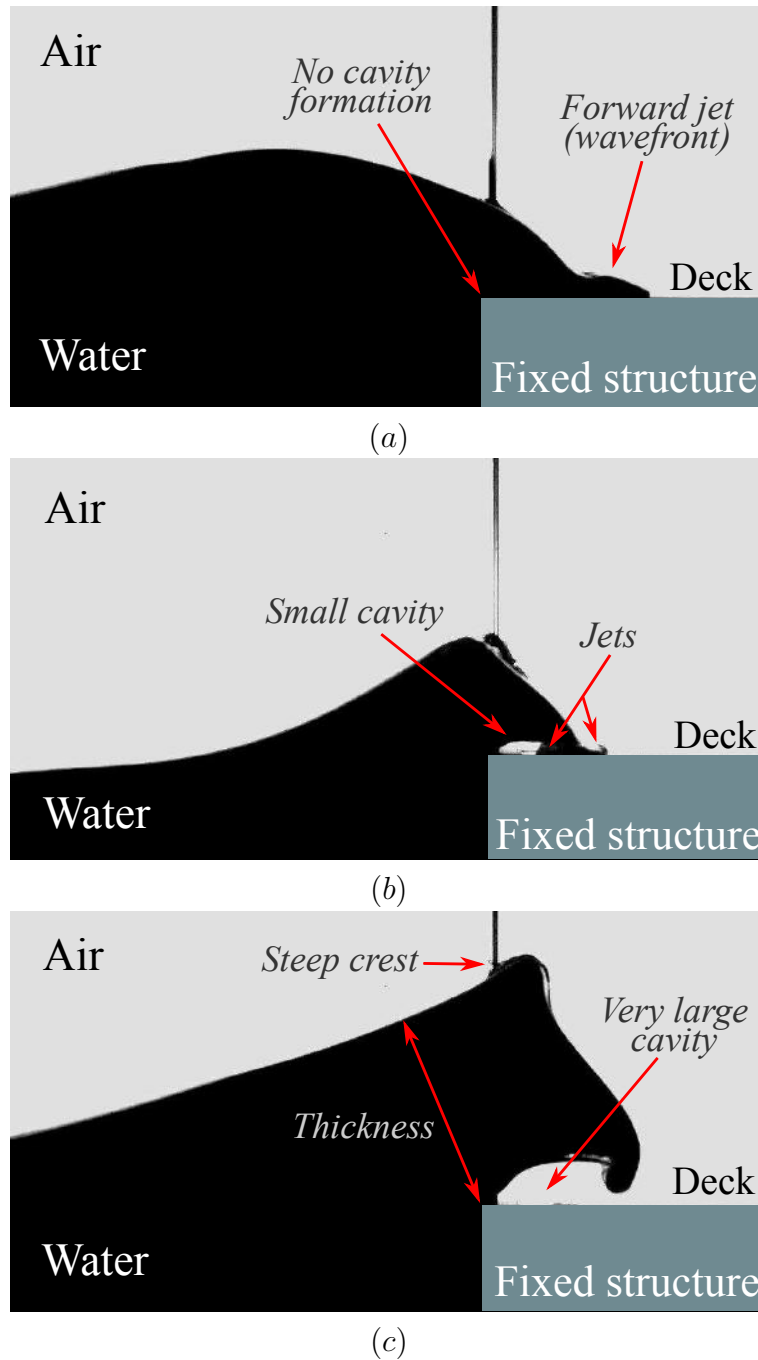


Figure 1.2: A resemblance of types of shipping water that may be obtained with single unbroken waves interacting with a barge-shaped fixed structure. (a) Dam-Break type (DB). (b) Plunging-Dam-Break type (PDB). (c) Hammer-Fist type (HF)

that subsequently ships onto the deck in the form of a fluid arm.

Although differences in the shipping water phenomena between model and prototype scales are always presented, the events shown in the Fig.1.1 may help to describe the shipping water events that can be expected in real cases for ships and offshore structures, namely, *white water* and *green water*. The former, receives its name because a flip-through phenomena may cause significant loading to the front of the structure due to direct impact (GRECO *et al.* [3]), yielding to a rapid upward

flow of water that commonly originates a spray. The latter can be defined as a compact mass of water (i.e., resembling an uniform volume of water) invading the deck. This phenomenon received its name because in the prototype scale, if it is seen from an specific point of view, it may present a green color aspect. The green water problem (hereafter referred just as shipping water) is the one that may cause serious problems to operations because of the large volume of water involved, so, it has been a topic of interest for naval and ocean researchers nowadays.

Some types of green water events, obtained by the interaction of unbroken waves with barge-shaped fixed structures, have been identified experimentally in the literature, considering regular wave trains (GRECO *et al.* [3]) and single waves (bores) (HERNÁNDEZ-FONTES *et al.* [4, 5]). Based on the descriptions of these works, the possible types of events are defined as dam-break (DB), plunging-dam-break (PDB) and hammer-fist (HF), as resembled in Fig.1.2.

The DB-type (Fig.1.2a) can be briefly described as a wavefront (small water jet downstream) followed by a body of water. It received such a name because its similarity with the dry-dam-break flow. Conversely, in the PDB (Fig.1.2b), there is the formation of a plunging wave at bow edge that forms a small cavity. Then, two small water jets are formed as the water floods the deck. At longer distances from the edge, the cavity is trapped by the flow, and the event resembles the DB type. In the HF (Fig.1.2c), it can be observed the formation of a fluid arm suspended at the bow edge that forms a very large cavity over the deck. At the initial stages of this event, the crest of the flow over the bow edge is very sharp. Also, it can be observed that the thickness of the fluid arm remains almost constant during some stages of shipping. More details about the descriptions of these events can be found in GRECO *et al.* [2, 3], HERNÁNDEZ-FONTES *et al.* [4, 5].

1.1.1 Framework and scope of the study

As described above, the shipping water problem is an important topic in coastal, naval and offshore engineering. Among the main goals of research, prediction of the evolution of the shipping water flow on deck of structures has been crucial, because allows the estimation of important parameters, such as loads on deck. However, considering the complexity of green water events, to attain realistic estimation of water evolution on deck is a notable challenge. For its study, experimental, numerical and analytical procedures are required. Nevertheless, when the objective is concerned with preliminary design or initial risk assessment, computational and construction costs limit the availability of numerical and experimental approaches, respectively. Then, analytical models that allow resembling the evolution of shipping water events, at least in an approximated way, play a remarkable role. However,

the development of reliable analytical methodologies require, preferably, systematic experimental studies for their validation.

Whereas analytical solutions to predict the shipping water elevations on deck and related loading are available in literature, there is a lack of alternatives that allow representing the shipping water evolution and its generated vertical loading in a realistic way. Furthermore, to validate these methodologies, systematic and detailed experimental studies, which allow the acquisition of repeatable and high-resolution data, are also required. These studies are possible to be obtained in simplified controlled environments, from which details of the flow evolution can be obtained through high-speed visualization.

In this way, the development of an alternative and realistic analytical method for shipping water evolution and loading estimation, as well as the systematic, controlled and detailed experimentation for its validation are the main topics of the present study. For such purposes, two-dimensional shipping water events on a fixed structure, generated with unbroken incoming waves, have been considered for the thesis. Moreover, the study is concerned with shipping water events of the *green water*-class, where events of the dam-break (DB) and plunging-dam-break (PDB)-types are considered.

1.1.2 Literature review of historical developments

Analytical approaches for shipping water vertical loading

In the naval/offshore field, the vertical loading on deck of a structure due to shipping water events can be described as an initial slamming (impact) force followed by slow-varying force (BEA *et al.* [6]). The former occurs during a short time because accounts for a sudden transfer of momentum from the incoming wave to the structure, whereas the latter occurs during a longer time because is caused during the wave inundation stage. The analytical estimation of shipping water loads, say vertical loads in the concern of present work, has relevance for time-domain applications, including ship-motion and control simulations.

A common method to estimate time series of vertical loading due to shipping water events considers the variation of momentum of the volume of water over the deck. When the structure is in motion, the contributions of the vertical accelerations may be considered (BUCHNER [7]). On the other hand, when the structure is fixed the static water head can be used for the estimation of loading, concerning the shallow water simplifications. In both cases, the knowledge of the shipping water evolution, or time series of water elevations over the deck at several positions, is required.

A classical approach to estimate shipping water evolution on deck has been to

relate the green water flow to the resulting flow from 'breaking of a dam' from hydraulics (i.e., dry dam-break or dam-break for short). The dry dam-break approach consists in assuming a hypothetical vertical wall (dam), retaining an infinite amount of water with initial depth. After the dam is removed ('breaks') instantaneously, a sudden release of water occurs, propagating downstream onto a horizontal surface. The most common analytical models of this kind found in literature are the Ritter's and Stoker's models. Both dry dam-break models present similar solutions for the estimation of water elevations. However, in the Stoker's model, the dam-break approach was extended considering wet-bed conditions on the downstream (i.e., wet dam-break problem, STOKER [8]). This approach, which allowed the analysis of the generation of bores or hydraulic jumps downstream (STOKER [8], NAKAGAWA *et al.* [9]), is a classical topic in the research of fluid mechanics (KLEMP *et al.* [10], STANSBY *et al.* [11], CRESPO *et al.* [12]). The dry and wet dam-break solutions are based on the assumptions of infinite water volume, hydrostatic pressure, uniform vertical profile of velocities and disregarded frictional terms (MOHAPATRA *et al.* [13]).

The Ritter's and Stoker's dry dam-break models have been used by several researchers to study the green water problem, as for instance BUCHNER [7], GODA e MIYAMOTO [14], BUCHNER [15], GRECO [16], RYU *et al.* [17].

One of the former applications, regarding the dry dam-break model relationship with shipping water, was attributed to GODA e MIYAMOTO [14]. They performed experimental tests in a two-dimensional transversal section of a ship considering heave motion. Shipping water events were obtained through incident regular waves. They applied the dry dam-break model of STOKER [8] to make a preliminary analysis of the similitude and difference between analytical results and experiments.

Later on, BUCHNER [15], also discussed the applicability of the dry dam-break approach to resemble the shipping water events obtained experimentally on the deck of a moored FPSO model under regular waves incidence. In that paper, he discussed the importance of relative motions in the resultant freeboard exceedance, and presented a method for estimating loading on deck from knowledge of the shipping water evolution over the deck. Such a research was further extended and detailed in BUCHNER [7], where a more extensive experimental analysis concerning loads on deck of different types of structures was carried out. In BUCHNER [7], the application of the momentum method to estimate loads from water elevations was presented in detail and related to experimental results of some pressure sensors located over the decks of the vessels analyzed. Although the vertical loading was estimated from pressure signals obtained at some locations over the deck, the proposed analytical approach seemed to be a potential approach for practical estimations. In fact, it has been used in some research related to ship dynamics as

a tool to estimate vertical loading to be included in the simulations: OGAWA *et al.* [18], HERNÁNDEZ-FONTES [19], RAJENDRAN *et al.* [20].

GRECO [16] carried out a numerical and experimental analysis of shipping water events in a two-dimensional experimental setup. A barge-shaped fixed structure was installed in a wave flume, where shipping water events using trains of regular waves were generated. Their approach, despite of simplified, allowed the understanding of several physical aspects of such phenomena. Although one of the goals of GRECO [16] was to perform a numerical analysis (boundary element method) to reproduce the physics of shipping water, in her work it was also discussed the applicability that the dry dam-break approach have in the shipping water analyses.

RYU *et al.* [17] performed experiments of shipping water on a fixed structure using the focusing wave method to generate an incident broken wave interacting with the structure. Even though they focused the attention in the kinematics of the events using an image-based technique, they considered the dry dam-break approach to relate the shipping water events obtained, discussing the influence of the structure deck on the kinematics observed.

Although the dry dam-break models are common approaches to relate the shipping water evolution, they tend to over-predict the shipped amount of water (HU *et al.* [21]) and have limitation to assess the decay trends of water propagating on deck. The necessity of more realistic representations of shipping water evolution on deck of structures has motivated researchers to extend the application of the classical dry dam-break approach. Recently, HU *et al.* [21] proposed an engineering approach by means of a modification of the Ritter's dam-break solution to get a decay effect of the resultant time series of water elevations. In their combined wave-dam-break approach, the initial condition of the Ritter's formulation was varied artificially, obtaining outputs that resembled the trends of water elevations at some positions over the deck. The model was compared with numerical results obtained with rogue waves shipping on a fixed structure, capturing water elevations in a close way in some cases.

From another point of view, some alternatives to classical dam-break approaches to represent the shipping water evolution over the deck are the convolution models. These approaches have been idealized from relating open-channel flow (also found in literature as flooding waves) concepts to the shipping water problem. In hydrological applications, a well known model to represent the evolution of water in rivers and channels is the Hayami convolution model (HCM, HAYAMI [22]), obtained from neglecting the acceleration terms in the Saint-Venant equations, which are commonly used to describe open-channel flows (CHANSON [23]). To the best of the author knowledge, the primary reference that applied a *flood-wave* convolution model to the shipping water evolution problem was OGAWA *et al.* [24]. They adapted the

Hayami convolution model to relate the shipping water events on a ship with forward speed to the flow in a river/channel. They used some empirical assumptions to relate such an approach in the estimation of shipping water elevation time series on the deck. Basically, they added an approximate three-dimensional effect multiplying the Hayami model by a ratio of the breadth of the incoming water volume and ship breadth. It seemed that the main assumption made was to consider the channel/river mean propagation velocity as the ship velocity. Thereby, the coefficients required to apply the HCM were both related to the ship velocity. Comparisons were made with experimental results for the water elevations at some positions over the deck. Results seemed to reproduce the tendency of the events; however, details of implementation were lacking. Then, the model was used to estimate loading on deck. Such method was further applied for estimating general loading in ships with forward speed by OGAWA *et al.* [18] and OGAWA *et al.* [25].

More recently, HERNÁNDEZ-FONTES [19] and HERNÁNDEZ-FONTES *et al.* [26] extended the approach of OGAWA *et al.* [24] to be applied to a shipping water event on deck of a Floating Production Storage and Offloading Unit (FPSO) under a regular wave incidence. Results obtained were compared with experimental data from BUCHNER [27] and numerical results from NIELSEN [28]. In this application, it was not possible to consider the ship velocity as the input parameter of the model, as done in OGAWA *et al.* [24], then, a practical engineering approach was proposed to estimate the shipping flow velocity from the regular wave particle velocities. In HERNÁNDEZ-FONTES [19], HERNÁNDEZ-FONTES *et al.* [26] the obtained results were only compared at two positions over the bow deck, being demonstrated the potential of convolution models to represent shipping water elevations after improving the estimation of input parameters. Moreover, it was verified the necessity of verifying the applicability of the model at more positions over a deck.

In the studies described above, regarding the use of convolution to assess the shipping water evolution, more detailed explanations about their development and usage were necessary. For example, it was not clearly defined the approach followed to consider the convection and diffusion terms in the formulation. Moreover, preliminary time step analysis for implementation of the convolution was not reported, which is of concern to capture complete water elevations at upstream positions. In summary, there was a lack of details that would allow applying the convolution models to generic applications, such as fixed structures considering frictional effects. All these topics are of concern in the present study.

Experimental approaches for shipping water vertical loading

The shipping water on structures has been studied experimentally, considering models with forward speed by OGAWA *et al.* [24], OGAWA [29], GRECO *et al.* [30],

GRECO e LUGNI [31], GRECO *et al.* [32], and without forward speed by COX e ORTEGA [33], BUCHNER [34], SULISZ *et al.* [35], RYU *et al.* [36], RYU *et al.* [17], FASHANU-UDOFE [37], LEE *et al.* [38], SONG *et al.* [39], SILVA [40], SILVA *et al.* [41], among others. All these works have been, totally or partially, concerned with the behavior of shipping water evolution and shipping water loads.

Experimental investigations of the loads originated from shipping water on structures are of importance in projects concerned with their design or improvement. Main use of data extracted from experiments regards the validation of analytical or numerical methodologies, then, it is of importance to account with systematic and reliable procedures for their acquisition.

The experimental investigation of shipping water loads on decks of structures has been performed in several research areas, such as coastal, ocean and offshore engineering. A well-known practice has been the use of pressure sensors installed over the deck, as for example GRECO *et al.* [32], LEE *et al.* [38], PHAM e VARYANI [42], SERINALDI e CUOMO [43].

In the naval/offshore applications, LEE *et al.* [38] performed studies of shipping water pressure on deck of an offshore structure by using several pressure sensors distributed over it. They considered three different bow shapes of a fixed barge-type model under the incidence of regular waves. From their tests, temporal and spatial distributions were analyzed, proposing a data-base for numerical model validations. Using a similar approach to measure the vertical loads on deck of a ship with forward speed, GRECO *et al.* [32] performed experimental tests with pressure sensors arranged on the deck to verify the water-on-deck loads. For the case of coastal applications, it has been of concern to study the wave loads in coastal bridges. In this field, SERINALDI e CUOMO [43] also employed pressure sensors to measure impulsive wave-in-deck loads, remarking the importance to know the loading generated in extreme events, such as severe storms, where the wave-on-deck can be large enough to cause overloading.

As the shipping water vertical loads may be separated in impulsive and slow-varying components, the use of pressure sensors may be convenient in applications that demand to measure the impulsive loads at specific locations; however, to attain this, adequate procedures need to be implemented for their installation, maintenance and usage (KIM *et al.* [44]). This is because there are some issues related to the correct use of pressure sensors, which should be overcome if they are employed. Among them, it is possible to mention high costs, installation difficulties to face them with the surface of interest, small working area (SPENCER *et al.* [45]), and signal effects due to the thermal shocks (VAN NUFFEL *et al.* [46]). A complete review of problems found in the use of these sensors applicable to water-structure interactions can be found in VAN NUFFEL *et al.* [46].

Alternative methods to measure vertical loading have been carried out in experiments performed with coastal structures. In these cases, load cells have been employed to measure vertical wave loads in bridge-type models. For instance, BRADNER [47] performed series of experiments to study wave loads on a highway bridge superstructure. The model was free to move along the wave propagation direction to simulate the dynamic response of the structure. They supported the model by a load-cell arrangement, from which vertical loads were measured. One of the objectives was to study impulsive and sustained wave loads. More recently, PARK *et al.* [48] also used load cells to support a generic model of a coastal structure to account with an extensive data sheet of the wave-induced loads in the horizontal and vertical directions. Using a different arrangement, MCPHERSON [49] performed experimental testes in a bridge; however, in that case, vertical wave forces were measured by a multi-directional load cell attached to the top of the model.

In a more generic application, concerning the slamming problem, HUERA-HUARTE *et al.* [50] also addressed some issues of the use of pressure sensors to measure hydrodynamic loading. In their experimental investigation to measure slamming loads, they designed and improved a force panel, formed by high-frequency response load-cell arrangement, acting as a free-fall structure to measure the slamming loads at different angles of entry on a reservoir of water. They demonstrated that it is possible to obtain reliable measurements of hydrodynamic loading by using such type of technique, as an alternative to the use of pressure sensors.

The alternative approach of HUERA-HUARTE *et al.* [50] can be extended to measure vertical loading in shipping water applications, as for example, barge-type fixed structures. Depending on the dynamic response of the load cells employed, the panels developed might account for the slamming (high-response) of slow-varying (low-response) loads.

It is clear that systematic experimental studies, regarding shipping water hydrodynamic loading, are still necessary to validate analytical and numerical approaches. Moreover, in the experimental scale the shipping water events are rapid ($\lesssim 1$ s), then, there is still a lack of information in literature presenting synchronization of shipping flow visualization with loading data, for which use of high-speed video and adequate sampling rates in sensors are required. It would allow a better understanding of the loading process. This is one of the topics of the present study.

1.2 The present study

This study is concerned with the development of an alternative analytical approach to represent the shipping water evolution and the derived vertical loading on deck of a fixed structure. In addition, a systematic experimental method, to acquire

details of water evolution and vertical loading from isolated shipping water events in a barge-shaped fixed structure, is proposed for model validation.

In the analytical investigation, the advection-diffusion equation, commonly used in Hydrology to flood routing, was directly applied to model the shipping water problem. A solution of this equation yielded a convolution model that has been used to account for the water evolution (i.e., time series of water elevations) on deck of a fixed structure. The model corresponds to a solution obtained in a semi-infinite domain with the Green function method, considering Dirichlet-type boundary conditions. It allowed considering a time series of freeboard exceedance as input. Also, frictional effects of bottom can be included practically by means of resistance coefficients. These characteristics of the model allowed a more realistic representation of shipping water elevations on time than classical approaches, attaining peak values and decay trends of time series. Furthermore, the model can be extended to estimate the slow-varying vertical loading on deck under the shallow waters assumptions (i.e., hydrostatic loading). The capabilities of the proposed model to attain both, water elevations and vertical loads, were validated against data obtained from the experimental investigation, which was specially designed for such a purpose.

The experimental work centered on the generation of isolated shipping water events onto a two-dimensional fixed structure representing the deck of a barge-shaped facility. This structure was installed inside of a dam-break type installation, where, single incoming waves (bore-type) were produced by means of the wet dam-break approach as their mechanism of generation. This approach, which was initially presented in HERNÁNDEZ-FONTES *et al.* [4, 5], allowed to control the experiment in order to attain reproducibility of the generated events of shipping water, and to use sensors and video at high sampling rates due to the small time intervals required for the experiments. In the experimental investigation, the stages of incoming wave generation and propagation as well as shipping of water on deck of a fixed structure were analyzed in detail by means of an image-based methodology, already presented in HERNÁNDEZ *et al.* [51], which was validated against conventional wave probe measurements. High-speed video allowed the identification of details of the shipping water events. Furthermore, an experimental technique was improved to measure the vertical loading on the deck and dynamic ringing effects during the testing cases. Regarding this, a force panel formed by four axial load cells (force balance hereafter) was built and installed as a part of the deck of the structure to account for the slow-varying shipping water vertical loads.

1.2.1 Thesis structure

The analytical methods used in the thesis are presented in the Chapter 2. These include the main information of the proposed model, and a brief description of the classical dam-break approach proposed by STOKER [8]. Moreover, the simplified approach to estimate vertical loading from water elevation measurements is described.

Chapter 3 contains the experimental methods employed in the thesis. These include a description of the experimental setup as well as the experimental techniques used for the water evolution and vertical loading measurements. For the water evolution measurements, both conventional and virtual wave probes measurement procedures are briefly described. For the load measurements, details of construction, installation and verification of the proposed technique prior to each test are presented, including a method to analyze dynamic effects transmitted to the structure during the wet dam-break tests.

Next, Chapter 4 presents the experimental results obtained during the investigation. First, the evolution of the incoming wave, including its generation and propagation, is analyzed mainly by means of visualization involving water elevations, longitudinal domain and time (named in this work as two-dimensional reconstruction) from virtual wave probes. In a similar way, the evolution and kinematics of the shipping water events generated are evaluated. Then, the results obtained for the vertical loading and the dynamic effects on the structure are presented. These include performance of the balance and individual load cells, and acceleration measurements to analyze dynamic effects.

Chapter 5 shows the analytical results obtained with the proposed model. First, preliminary steps for model implementation are presented. These include the input function selection, kernel time step definition and a parametric analysis to select the adequate kernel constants (model calibration). Subsequently, application of the model to attain the shipping water evolution in five study cases was performed and validated against experimental data from virtual wave probes. Finally, application of the proposed model to estimate vertical loading on deck was obtained and validated with experiments. For the applications presented in this section (i.e. water elevations and vertical loading), the results obtained with the proposed model were compared against results of a classical dry dam-break approach of Stoker.

The main conclusions, findings and future research are summarized in Chapter 6 and a list of accepted publications derived from the present thesis is shown in the Appendix E.

1.2.2 Summary of main findings and results

- The proposed experimental approach allowed systematic and detailed studies of isolated shipping water events. The incoming wave generation and propagation as well as the shipping water evolution on-deck were two-dimensionally reconstructed with the image-based methodology used in the present work. It allowed to identify trends followed by flow before and after wave-structure interaction. It was found a reflected wave that occurred during the wave run-up stage, before the shipping of water. This may be the cause of the change in the shipping water patterns when consecutive events are analyzed using wave trains. Additionally, the reconstruction allowed detailed information (i.e. virtual wave probes data at several positions over the deck) to validate the proposed analytical methodology.

On the other hand, loading measurements allowed a better understanding of the trends of slow-varying global vertical loads due to shipping water on barge-shaped fixed structures. Synchronization of video snapshots with loading data yield a detailed analysis of the loading process.

- The proposed analytical approach captured well the trends of experiments, attaining peak values and decay trends of time series in approximated manners. Despite of the simplifications made on its development, it allowed capturing realistic trends of data. The extension of the model to estimate vertical loading on deck also presented good agreement with experiments, which confirms the potential of the proposed approach to be improved and extended to other applications. Additionally, the capabilities of the proposed approach over the traditional dam-break model were demonstrated for both, water elevations and vertical loading estimations. The proposed model captured the decay trends of results and yielded approximated information of their maximum values.

Chapter 2

Analytical Methods

2.1 Proposed model

2.1.1 Model assumptions

The shipping water problem under study can be divided into four distinct regions, as shown in Fig.2.1: the inflow region or the region where the incoming wave is generated (1), the region at which the structure (obstacle) is located (2), the region immediately downstream, which corresponds to the deck of the structure (3) and the region where occurs the backwater effects once the on-deck flow interacts with a rigid vertical wall. In each region, it is possible to define characteristic horizontal velocity "u" and layer height "h", where the subscripts denote each region.

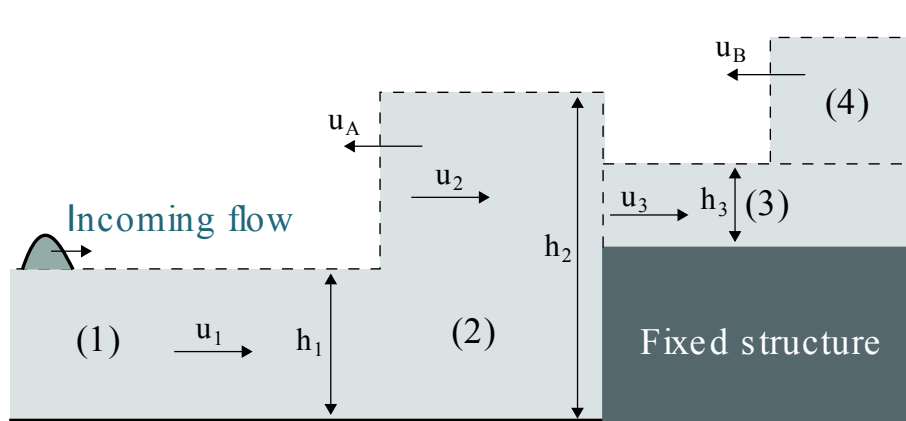


Figure 2.1: Division of the shipping water problem in different regions.

In the present study, let us consider the shipping water problem in the structure deck region (3) shown in Fig.2.2. The x-direction axis corresponds to the streamwise coordinate, whereas the z-direction axis denotes the vertical coordinate. The layer height is denoted by $\eta(x, t)$. $\bar{u}(x, t)$ represents the mean horizontal flow velocity on deck of the structure, whereas \bar{u}_0 the horizontal mean flow velocity at which the

shipping water crosses the deck edge. These velocities are always slower than the wavefront velocity U_{front} . $\eta(0, t)$ represents the freeboard exceedance and η_0 the maximum freeboard exceedance during each shipping water event. D and L_0 are the height and length of the structure, respectively.

In the defined region, the cross-stream variation is neglected and it is considered a layer of fluid of constant density, which flows over a rigid no-slip horizontal surface. The approximations of irrotational with a boundary layer condition at bottom (deck) are followed. In the boundary layer region viscous effects are present in the form of shear stresses.

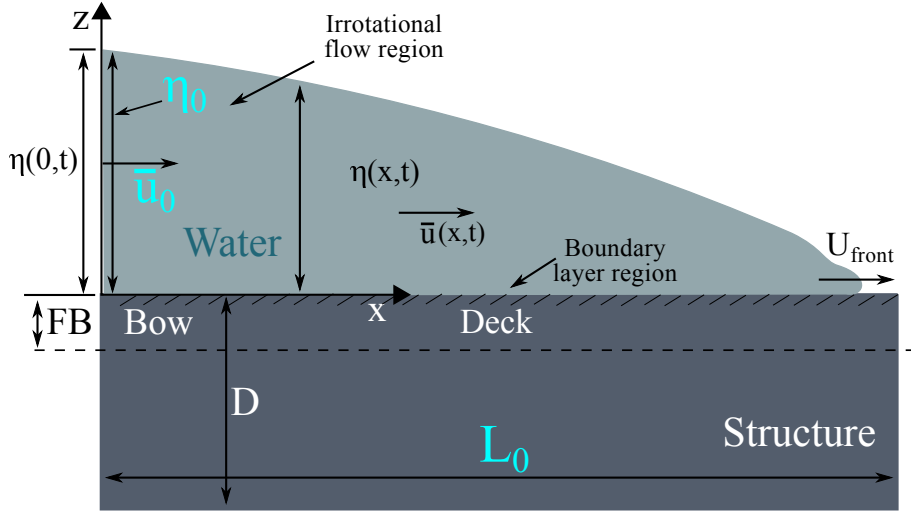


Figure 2.2: Region of interest in the present study.

It is assumed that the horizontal length-scale is greater than the vertical one ($L_x \gg L_z$). Thus, it is possible to formulate the problem under the shallow water assumption, that is, disregarding the vertical accelerations and considering an hydrostatic pressure distribution, as described in next section.

2.1.2 Model development

The Navier Stokes equations can describe the motion of the fluid over the deck shown in Fig. 2.2. If we assume that the horizontal length scale is larger than the vertical one ($L_x \gg L_z$), the z -direction integration of the Navier Stokes equations yields the shallow water system of equations. These allow the description of a layer of fluid in hydrostatic balance, bounded by a free surface and a bottom topography, as shown in the Fig. 2.3, from which it can be observed a layer of fluid bounded by a bottom topography and a free surface. The total depth H is considered as the sum of the undisturbed water depth h and the water elevation η . A detailed development of the model is shown in Appendix A.

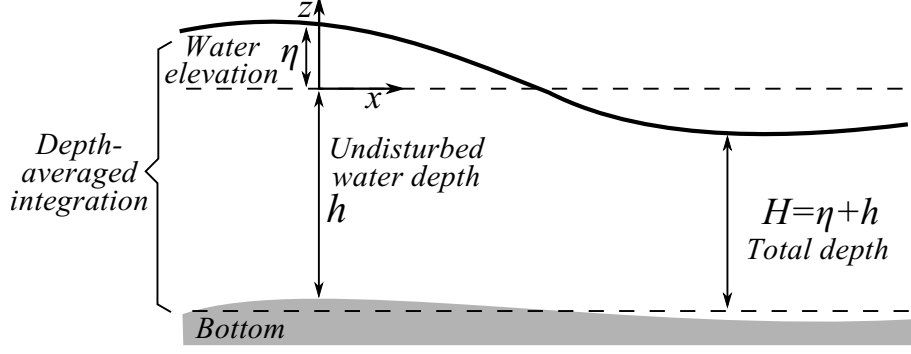


Figure 2.3: Euler system defining the layer of fluid bounded by bottom and free surface.

Considering the assumptions defined above, applying corresponding kinematic and dynamic boundary conditions at the bottom and the free surface, and making the assumption of hydrostatic pressure, it is possible to obtain the Z-direction integrated Navier Stokes equations, also known as the two-dimensional (2D) shallow water system of equations. The depth-integrated continuity equation is written as follows

$$\frac{\partial \bar{u}H}{\partial x} + \frac{\partial \eta}{\partial t} + \frac{\partial h}{\partial t} + \frac{\partial \bar{v}H}{\partial y} = 0 \quad (2.1)$$

where H is the total water depth ($H = \eta + h$), t is time, and \bar{u} and \bar{v} correspond to the depth-averaged flow velocities in the x - and y - directions, respectively:

$$\bar{u} = \frac{1}{H} \int_{-h}^{\eta} u dz, \quad (2.2)$$

$$\bar{v} = \frac{1}{H} \int_{-h}^{\eta} v dz, \quad (2.3)$$

Then, the equation (2.1) can be rewritten as:

$$\frac{\partial H}{\partial t} + \frac{\partial \bar{u}H}{\partial x} + \frac{\partial \bar{v}H}{\partial y} = 0 \quad (2.4)$$

The z -integrated momentum equation in the x -direction is expressed as (LIN [52]):

$$\begin{aligned} & \frac{\partial(\bar{u}H)}{\partial t} + \frac{\partial(\bar{u}^2H)}{\partial x} + \frac{\partial(\bar{u}\bar{v}H)}{\partial y} + \frac{d}{dx} \int_{-h}^{\eta} \tilde{u}\tilde{u}dz + \frac{d}{dy} \int_{-h}^{\eta} \tilde{u}\tilde{v}dz = \\ & -\frac{H}{\rho} \frac{\partial P_a}{\partial x} - gH \frac{\partial \eta}{\partial x} - \frac{g\eta H}{\rho} \frac{\partial \rho}{\partial x} + \frac{1}{\rho} \frac{\partial}{\partial x} \int_{-h}^{\eta} \tau_{xx} dz + \frac{1}{\rho} \frac{\partial}{\partial y} \int_{-h}^{\eta} \tau_{xy} dz \\ & + \frac{1}{\rho} \tau_{xz,\eta} - \frac{1}{\rho} \tau_{xz,-h} \end{aligned} \quad (2.5)$$

where $\tau_{xz,\eta}$ and $\tau_{xz,-h}$ are the free surface and bottom shear stresses. The former is

considered as stress due to wind and the last as the stress due to bottom friction. ρ is water density and P_a is the atmospheric pressure. In our case, let us consider uniform velocity and uniform stresses in the vertical direction. With these assumptions, we can neglect the terms due to velocity fluctuations ($\tilde{u}\tilde{u}$, $\tilde{u}\tilde{v}$).

Let us also assume the terms $\frac{\partial \tau_{xx}}{\partial x}$ and $\frac{\partial \tau_{xy}}{\partial y}$ constant in the z -direction, due to the independence of τ_{xx} and τ_{xy} from z . This allows to integrate the 4th and 5th terms of the right-hand side of (2.5) in the vertical direction. Thus, the equation (2.5) can be simplified as:

$$\begin{aligned} \frac{\partial(\bar{u}H)}{\partial t} + \frac{\partial(\bar{u}^2H)}{\partial x} + \frac{\partial(\bar{u}\bar{v}H)}{\partial y} = & -\frac{H}{\rho} \frac{\partial P_a}{\partial x} - gH \frac{\partial \eta}{\partial x} - \frac{g\eta H}{\rho} \frac{\partial \rho}{\partial x} + \\ & \frac{H}{\rho} \frac{\partial \tau_{xx}}{\partial x} + \frac{H}{\rho} \frac{\partial \tau_{xy}}{\partial y} + \frac{1}{\rho} [\tau_{xz,\eta} - \tau_{xz,-h}] \end{aligned} \quad (2.6)$$

From similar assumptions, the y -direction simplified shallow water moment equation is written as follows:

$$\begin{aligned} \frac{\partial(\bar{v}H)}{\partial t} + \frac{\partial(\bar{u}\bar{v}H)}{\partial x} + \frac{\partial(\bar{v}^2H)}{\partial y} = & -\frac{H}{\rho} \frac{\partial P_a}{\partial y} - gH \frac{\partial \eta}{\partial y} - \frac{g\eta H}{\rho} \frac{\partial \rho}{\partial y} + \\ & \frac{H}{\rho} \frac{\partial \tau_{yx}}{\partial x} + \frac{H}{\rho} \frac{\partial \tau_{yy}}{\partial y} + \frac{1}{\rho} [\tau_{yz,\eta} - \tau_{yz,-h}] \end{aligned} \quad (2.7)$$

Next, the 2D (z -integrated Navier Stokes equations) shallow water system of equations (2.1), (2.6) and (2.7), are integrated along the y -direction (from $-B/2$ to $B/2$) of a layer of unitary width B , as shown in Fig. 2.4. The flow follows the x -direction. The main stresses are due to the wind and bottom, which are opposed to the flow direction. At the sides, no shear stresses are considered.

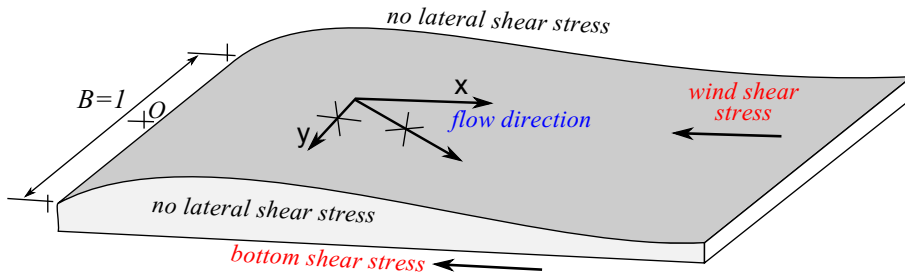


Figure 2.4: Fluid layer considered for the y -direction integration of the shallow water equations.

Considering $B = 1$, the continuity equation is simplified to:

$$\frac{\partial(H)}{\partial t} + \frac{\partial(\bar{u}H)}{\partial x} = 0 \quad (2.8)$$

where H is now the water height per unit breadth, given in m/m . Furthermore, the

x-direction momentum equation is expressed as:

$$\begin{aligned} \frac{\partial(\bar{u}H)}{\partial t} + \frac{\partial(\bar{u}^2H)}{\partial x} = & -gH\frac{\partial H}{\partial x} + gH\frac{\partial h}{\partial x} + 1\frac{H}{\rho}\frac{\partial\tau_{xx}}{\partial x} \\ & + \frac{B}{\rho}\tau_{xz,\eta} - \frac{1}{\rho}\tau_{xz,-h} \end{aligned} \quad (2.9)$$

Neglecting the normal stress (τ_{xx}) due to the assumption of no viscous effects, which are present only in the shear stress components in the boundaries, yields:

$$\frac{\partial(\bar{u}H)}{\partial t} + \frac{\partial(\bar{u}^2H)}{\partial x} = -gH\frac{\partial H}{\partial x} + gH\frac{\partial h}{\partial x} + \frac{1}{\rho}\tau_{xz,\eta} - \frac{1}{\rho}\tau_{xz,-h} \quad (2.10)$$

It is considered an horizontal bottom and the mean level located at the bottom surface. Then equality $H = \eta + h$ with $h = 0$ becomes $H = \eta$. With this, $dh/dx = 0$ and the above equation can be rewritten as:

$$\frac{\partial(\bar{u}\eta)}{\partial t} + \frac{\partial(\bar{u}^2\eta)}{\partial x} = -g\eta\frac{\partial\eta}{\partial x} + \frac{1}{\rho}\tau_{xz,\eta} - \frac{1}{\rho}\tau_{xz,-h} \quad (2.11)$$

Assuming that the shear stress caused by the air is smaller than the one caused by the bottom boundary ($\tau_{xz,-h} \gg \tau_{xz,\eta}$), last equation can be simplified to:

$$\frac{\partial(\bar{u}\eta)}{\partial t} + \frac{\partial(\bar{u}^2\eta)}{\partial x} = -g\eta\frac{\partial\eta}{\partial x} - \frac{1}{\rho}\tau_{xz,-h} \quad (2.12)$$

which represents the momentum equation of the one-dimensional (1D) shallow water system of equations.

Momentum equation simplification

The momentum equation of the 1D shallow water system (2.12) is non-linear, restricting the development of analytical approximate solutions for the considered problem. Thus, simplifications of terms have been performed by means of a non-dimensional analysis. This has been done considering non-dimensional elevation (η^*), mean horizontal velocity (\bar{u}^*), time (t^*) and distance over the deck (x^*), based on the reference parameters (η_0 , \bar{u}_0 and L_0) showed in Fig.2.2. Then, the dimensionless parameters are defined as:

$$\eta^* = \frac{\eta}{\eta_0}, \bar{u}^* = \frac{\bar{u}}{\bar{u}_0}, t^* = \frac{\bar{u}_0 t}{L_0}, x^* = \frac{x}{L_0} \quad (2.13)$$

where \bar{u}_0 is the mean shipping flow velocity, t is time, x is the horizontal distance over the deck and η is the water elevation. Substituting the dimensionless terms in the continuity equation (2.8), it can be rewritten as:

$$\frac{\bar{u}_0 \eta_0}{L_0} \left(\frac{\partial \eta^*}{\partial t^*} + \frac{\partial \eta^* \bar{u}^*}{\partial x^*} \right) = 0 \quad (2.14)$$

which yields,

$$\left(\frac{\partial \eta^*}{\partial t^*} + \frac{\partial \eta^* \bar{u}^*}{\partial x^*} \right) = 0 \quad (2.15)$$

Following a similar procedure, the momentum equation (2.12) can be expressed as:

$$\frac{\bar{u}_0^2 \eta_0}{L_0} \frac{\partial (\bar{u}^* \eta^*)}{\partial t^*} + \frac{\bar{u}_0^2 \eta_0}{L_0} \frac{\partial (\bar{u}^{2*} \eta^*)}{\partial x^*} = -\frac{g \eta_0^2}{L_0} \frac{\partial \eta^*}{\partial x^*} \eta^* - \frac{\tau_{xz,-h}}{\rho} \quad (2.16)$$

multiplying by $\frac{L_0}{g \eta_0^2}$ we have:

$$F_n^2 \left(\frac{\partial (\bar{u}^* \eta^*)}{\partial t^*} + \frac{\partial (\bar{u}^{2*} \eta^*)}{\partial x^*} \right) = -\frac{\partial \eta^*}{\partial x^*} \eta^* - \frac{L_0}{g \eta_0^2} \frac{\tau_{xz,-h}}{\rho} \quad (2.17)$$

where F_n represents the Froude number, which in the present work is defined as:

$$F_n = \frac{\bar{u}_0}{\sqrt{g \eta_0}} \quad (2.18)$$

Let us neglect the inertial terms (left-side) by assuming subcritical flow ($F_n < 1$). Analyzing the order of the terms we observe that for such assumption, the momentum equation can be simplified as follows:

$$\frac{\partial \eta}{\partial x} = -\frac{\tau_{xz,-h}}{g \rho \eta} \quad (2.19)$$

The constant shear stress assumption

The τ_{xz} component of the shear stress tensor noted in (2.19) is commonly expressed in fluid mechanics as a vector component that accounts for the shear stress at spatial and temporal coordinates (x and t). However, the present approach aims a practical consideration, thus, it is assumed that the roughness of the surface is constant and that $\tau_{xz,-h}$ can be considered as a constant value. The shear stresses can be accounted for as resistance coefficients. The friction resistance coefficients can be defined as (LIN [52]):

$$S_f = \frac{\tau_b}{\rho g \eta} \quad (2.20)$$

where τ_b is the bottom shear stress or constant $\tau_{xz,-h}$ for the present work. Empirical assumptions to relate constant bottom shear stresses (τ_b) to constant resistance coefficients (S_f) are preferred in many cases in terms of practicability. These type of

assumptions are widely used, for instance, in hydrological applications, where the use of Chezy or Manning formulations are alternatives to be considered (GOTTARDI e VENUTELLI [53]).

In the present study, the friction coefficient has been considered constant, form based on the Manning approach (GOTTARDI e VENUTELLI [53]):

$$S_f = \left(\frac{u}{kH^m} \right) \quad (2.21)$$

where $k = 1/n$, with n as the Manning roughness coefficient (dimension $L^{1/3}T$) and $m = 2/3$.

The advection diffusion model

Let us consider the 1D continuity equation (Eq.(2.8)) in its non-conservative form:

$$\frac{\partial \eta}{\partial t} + \eta \frac{\partial \bar{u}}{\partial x} + \bar{u} \frac{\partial \eta}{\partial x} = 0 \quad (2.22)$$

Then, defining the bottom resistance coefficient as defined in (2.20) and (2.21), the 1D momentum equation (2.19) can be rewritten as:

$$\frac{\partial \eta}{\partial x} = - \left(\frac{\bar{u}}{k\eta^m} \right)^2 \quad (2.23)$$

Deriving with respect to x:

$$\frac{\partial \bar{u}}{\partial x} = - \frac{k^2 \eta^{2m}}{2\bar{u}} \frac{\partial^2 \eta}{\partial x^2} + \frac{\bar{u}m}{\eta} \frac{\partial \eta}{\partial x} \quad (2.24)$$

Substituting (2.24) in the continuity equation (2.22):

$$\frac{\partial \eta}{\partial t} + \bar{u}(m+1) \frac{\partial \eta}{\partial x} = \frac{k^2 \eta^{2m} \eta}{2\bar{u}} \frac{\partial^2 \eta}{\partial x^2} \quad (2.25)$$

which after some algebra yields,

$$\frac{\partial \eta}{\partial t} + \bar{u}(m+1) \frac{\partial \eta}{\partial x} = \frac{\bar{u}\eta}{2S_f} \frac{\partial^2 \eta}{\partial x^2} \quad (2.26)$$

It has been obtained a single partial differential equation, known as advection-diffusion equation, with η as the dependent variable. From this equation, let us define the advection A and diffusion B coefficients as:

$$A = \bar{u}(m+1) \quad (2.27)$$

$$B = \frac{\bar{u}\eta}{2S_f} \quad (2.28)$$

To allow an analytical solution of (2.26), the A and B coefficients have been assumed constant. There are some well-documented procedures in literature to solve such an equation analytically, such as Laplace transform or the Green function method. In the present thesis, the Green function method has been chosen to solve the advection-diffusion equation to obtain solutions in the form of convolution integrals, as described below.

Analytical solution

In the present study, the solution of the advection diffusion equation (2.26) has been obtained through the Green function method. From a mathematical perspective, it has been assumed that the fundamental solution of the equation (i.e. its corresponding Green function) stands for, say, the subsequent water mass distribution incurred by an instantaneous unit water mass pulse (dirac) at the location x and at the moment t . With such a consideration, the present problem has been defined as a boundary value problem of the Dirichlet type in semi-infinite domain (Fig. 2.5). The mass fraction of water (η per unit width) is defined as the solved variable $\eta = \eta(x, t)$. To obtain the solution, it is required to establish an initial condition $\eta(x, 0) = g(x)$, which for the present study case $\eta(x, 0) = 0$, and a boundary condition at the upstream $\eta(0, t)$, which is considered as the freeboard exceedance time series $F(t)$.

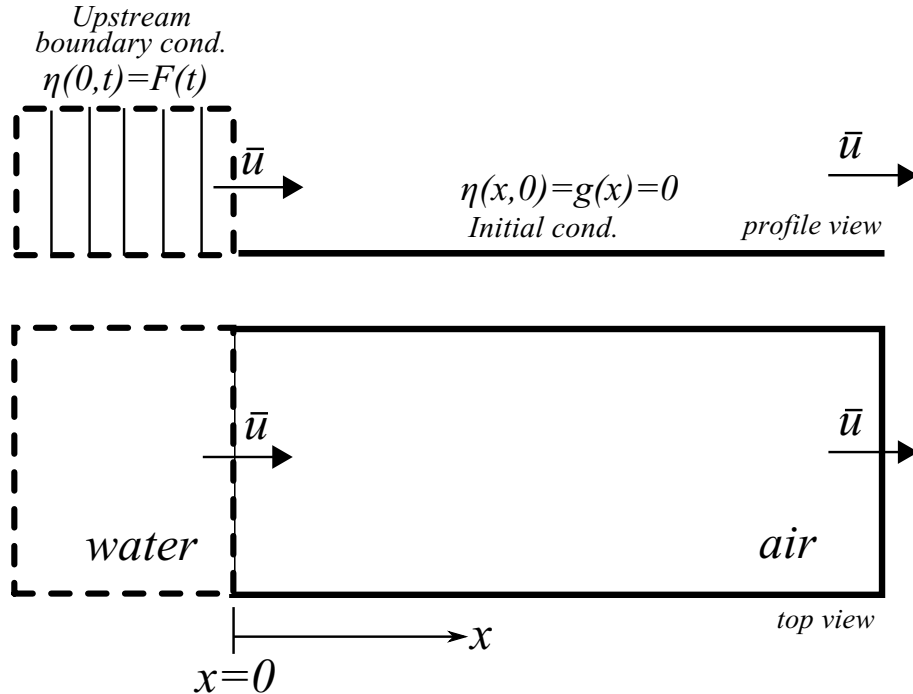


Figure 2.5: Semi-infinite domain considered for the present one-dimensional problem.

Well-known procedures to obtain solutions for specific problems regarding the advection-diffusion equation (2.26), considering constant A and B parameters, can

be found in literature: XU *et al.* [54], STAKGOLD [55]. For the present problem, the complete solution procedure of the equation with the initial and boundary conditions described, can be found in XU *et al.* [54], from which the next solution applies:

$$\eta(x, t) = \int_0^t \frac{F(\tau)}{\sqrt{16\pi B(t-\tau)^3}} [M + N] d\tau \quad (2.29)$$

with

$$M = [x - A(t - \tau)] \exp \left[-\frac{[x - A(t - \tau)]^2}{4B(t - \tau)} \right] \quad (2.30)$$

$$N = [x + A(t - \tau)] \exp \left[\frac{Ax}{B} - \frac{[x + A(t - \tau)]^2}{4B(t - \tau)} \right] \quad (2.31)$$

where F is the input function and $[M + N]$ represent the kernel function of the convolution.

2.2 The dam-break model

This section briefly describes the analytical dam-break model proposed by STOKER [8] to attain water elevations. Disregarding frictional effects and considering a horizontal bed, the simplified shallow water equations for the x-direction are expressed as,

$$\frac{\partial \bar{u}}{\partial t} + \bar{u} \frac{\partial \bar{u}}{\partial x} + g \frac{\partial \eta}{\partial x} = 0 \quad (2.32)$$

$$\frac{\partial \bar{u} \eta}{\partial x} + \frac{\partial \eta}{\partial t} = 0 \quad (2.33)$$

where \bar{u} is the horizontal velocity, η is water elevation and g is the gravity acceleration, as already defined in this work. By means of the method of characteristics, STOKER [8] obtained a solution for the dam-break problem.

The dam-break model of Stoker consists in supposing an infinite amount of water retained by a fixed vertical wall (dam). Assuming that the vertical wall is removed instantaneously (breaking of the dam), the retained flow releases and propagates along a horizontal surface. This flow is known as dam-break type flow and has been widely applied to relate the flow propagation in shipping water events. The analytical dam-break Stoker's solution for the water elevation η on a horizontal surface can be expressed as:

$$\eta(x, t) = \frac{1}{9g} \left(-\frac{x}{t} + 2\sqrt{g\eta_{dam}} \right)^2 \quad (2.34)$$

where η_{dam} is the initial water depth level of the reservoir of water before breaking of the dam and x represents the positions along the horizontal surface with the dam position as the origin. Assuming that the vertical wall that retains the dam is removed at $t = 0$, water flows instantaneously from η_{dam} . At the origin ($x = 0$, $t \approx 0$), an instantaneous water depth (η_I) is observed (Fig. 2.6a). The Stoker's development suggest that this η_I corresponds to:

$$\eta_I = \frac{4}{9}\eta_{dam} \quad (2.35)$$

For applying the dam-break model to the shipping water case, the η_I and maximum freeboard exceedance of the shipping water event described before (η_0) must be related as shown in Fig. 2.6b. To accomplish with (2.34), it is necessary to find the η_{dam} value from knowledge of the η_0 value at the beginning of the deck. Then, η_{dam} is found as follows:

$$\eta_{dam} = \frac{9}{4}\eta_0 \quad (2.36)$$

2.3 Vertical loading estimation

Regarding the shallow water assumptions, the vertical loading was considered as the static water head estimated from the water elevation time series $\eta_i(x_i, t)$ at several positions x_i over the deck (Fig. 2.7). To do this, the local pressure P_i at each x_i over the surface of interest was estimated from the water elevations at such a position as:

$$P_i(x_i, t) = \rho g \eta_i(x_i, t), i = 1, 2, \dots, n \quad (2.37)$$

where n is the number of regions at which the surface of interest has been discretized, as illustrated in Fig. 2.7a. In this figure, the surface of interest is subdivided in several regions ($A_1 - A_n$) in which the water elevation time series $\eta_i(x_i, t)$ are obtained and the local pressures $P_i(x_i, t)$ are calculated. The latter are assumed constant over their respective regions $A_i(x_i)$ (Fig. 2.7b).

A local vertical force $F_i(x_i, t)$ is estimated acting on the centre of each region (Fig. 2.7b) as:

$$F_i(x_i, t) = P_i(x_i, t)A_i(x_i) = \rho g \eta_i(x_i, t)A_i(x_i) \quad (2.38)$$

Then, the time series of total force over the surface of interest $F_t(t)$ corresponds to the sum of the local forces $F_i(x_i, t)$:

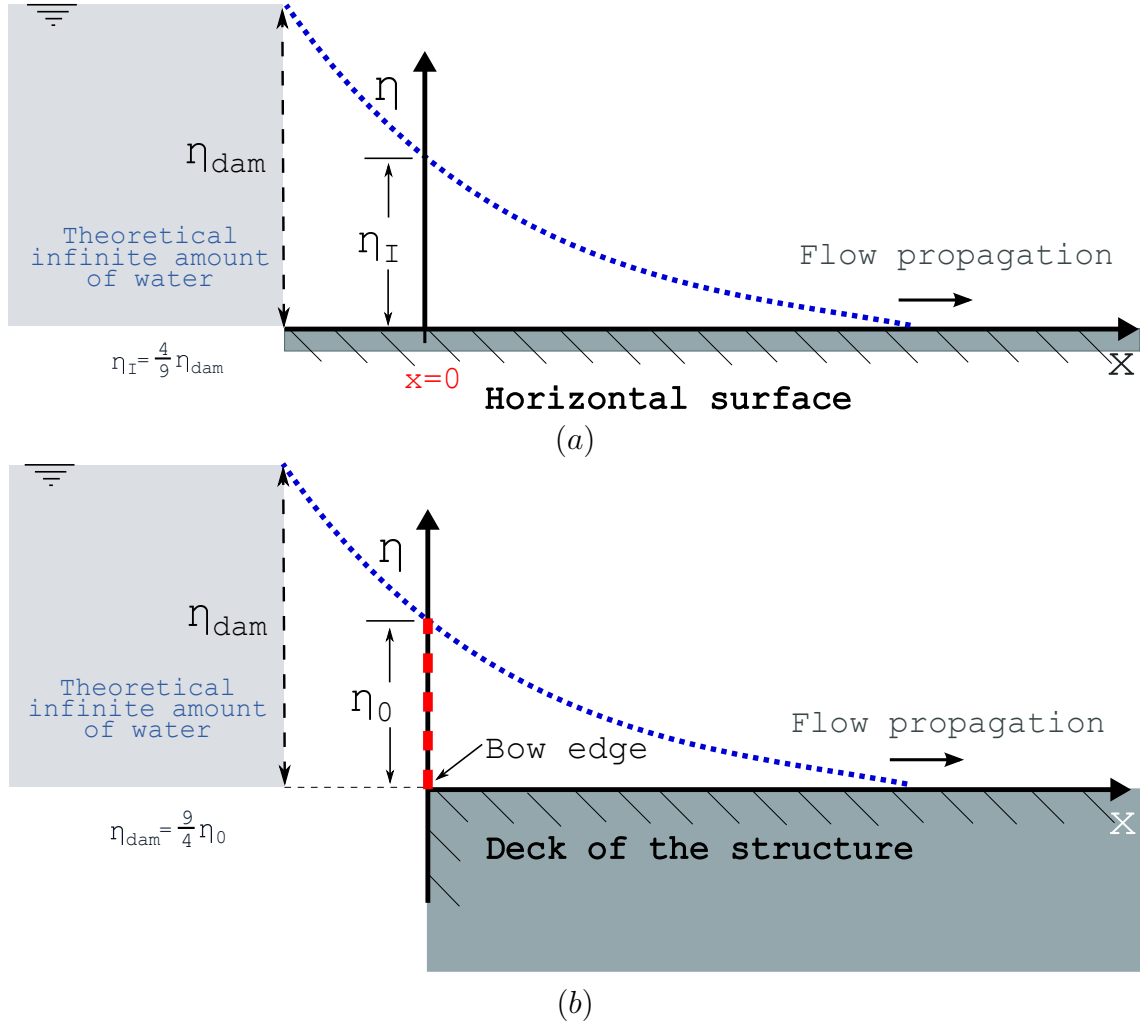


Figure 2.6: Dam-break model and its relation to shipping water prediction. (a) Application to a surface. (b) Application to a rectangular structure.

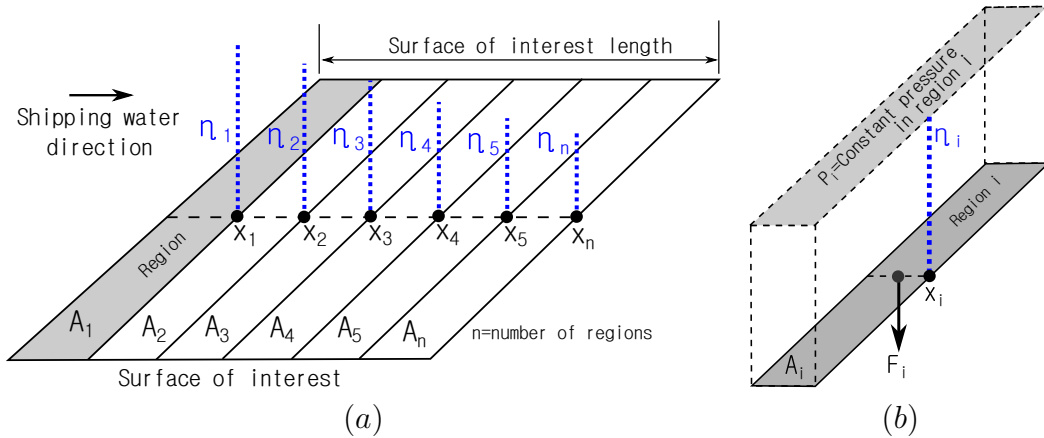


Figure 2.7: (a) Surface of interest discretization. (b) Assumed acting force on a region.

$$F_t(t) = \sum_{i=1}^n F_i(x_i, t) = \sum_{i=1}^n P_i(x_i, t) A_i(x_i) = \sum_{i=1}^n \rho g \eta_i(x_i, t) A_i(x_i) \quad (2.39)$$

Chapter 3

Experimental Methods

In this chapter, the experimental methods employed in the thesis are presented. To start with, a brief explanation about the wet dam-break approach used for the incoming wave generation is described in order to define the incoming wave parameters used in the analyses. Subsequently, the experimental setup is described, showing details of the experimental procedure followed and the sensors arrangement. Next, the methods used for water evolution measurements are described. This part includes a description of the conventional wave probe sensors and of the image-based technique employed for virtual wave probe measurements. Finally, the experimental methods used for measuring vertical loads and dynamic effects during experiments are described.

3.1 The wet dam-break approach

In the present investigation, the isolated shipping water events on deck of a fixed structure have been reproduced using the wet dam-break method as the mechanism to generate a single bore approaching the structure (incoming wave hereafter). A well-known analytical study of the wet dam-break problem has been proposed by STOKER [8]. This approach can be described by following the illustration of Fig. 3.1 as follows (STOKER [8]):

A dam (gate) separates two sides of a horizontal tank of constant cross section at $x = 0$. Upstream and downstream the dam, there are two volumes of water with initial water depths h_1 and h_0 , respectively (Fig. 3.1a). It is assumed that the tank extends to infinite in the upstream and downstream directions, and that h_1 is always higher than h_0 .

At the initial condition, the water at both sides of the dam is assumed undisturbed (i.e. at rest position). It is considered that, as in the dam-break problem with no initial water depth at the downstream (see for instance STOKER [8], Section 2.2), the dam is suddenly removed at $t = 0$. After this stage, it is expected

the sudden formation of a *shock wave* (named in this way by STOKER [8]) on the downstream region propagating with front velocity U_0 over the lower layer of water (Fig. 3.1b). This wave formation is due to the interaction of the upstream volume on the downstream one by the action of gravity, which acts like a piston pushing water downstream. Afterwards, an instantaneous velocity is obtained by water at $x = 0$, yielding the direct formation of a resulting wave (i.e. bore or hydraulic jump, STOKER [8]), on the downstream side.

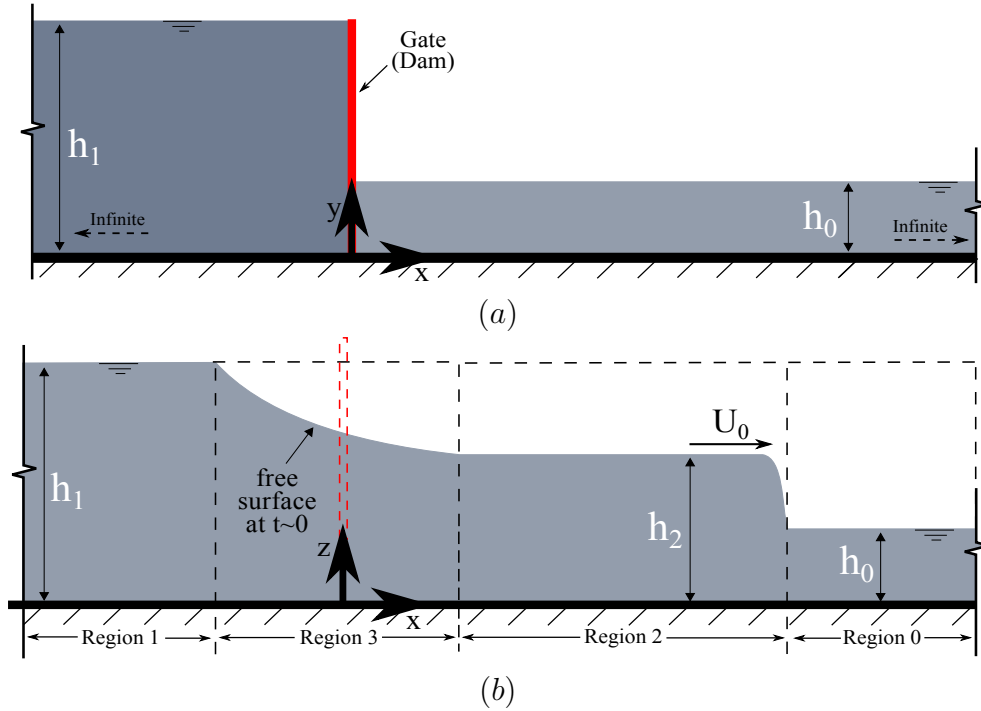


Figure 3.1: Wet-dam break. (a) Initial conditions. (b) Main stages after dam-break. Adapted from the Stoker's method.

If we consider the stage for $t \approx 0$, immediately after the gate has been removed, as shown in Fig. 3.1b, four different regions can be considered: the calm water downstream zone (region 0), which starts at the end of the generated wave; a zone of undisturbed water at the upstream (region 1); a zone of steady state where the shock wave acts downstream (region 2) and a simple wave that connects the shock wave constant state and the region 1 (i.e., region 3). In the figure, h_0 , h_1 and h_2 represent the elevations at regions 0, 1 and 2, respectively.

Using the method of characteristics, Stoker proposed relations between the variables shown in Fig. 3.1. The shock conditions for the passage from the regions 0 to 2 (Fig. 3.1) are written as follows (STOKER [8]):

$$-U_0(u_2 - U_0) = \frac{1}{2}(c_0^2 + c_2^2) \quad (3.1)$$

$$c_2^2(u_2 - U_0) = -c_0^2 U_0 \quad (3.2)$$

where u_2 is the flow velocity after the wavefront and c_i is the wave propagation speed, expressed as,

$$c_i^2 = gh_i \quad (3.3)$$

where the index i indicates an specific region of Fig. 3.1. From equations (3.1) and (3.2), a set of equations relating the kinematics of the resultant bore was proposed by STOKER [8]:

$$\frac{u_2}{c_0} = \frac{U_0}{c_0} - \frac{c_0}{4U_0} \left(1 + \sqrt{1 + 8 \left(\frac{U_0}{c_0} \right)^2} \right) \quad (3.4)$$

$$\frac{c_2}{c_0} = \left[\frac{1}{2} \left(\sqrt{1 + 8 \left(\frac{U_0}{c_0} \right)^2} - 1 \right) \right]^{1/2} \quad (3.5)$$

$$\frac{u_2}{c_0} + \frac{2c_2}{c_0} = \frac{2c_1}{c_0} \quad (3.6)$$

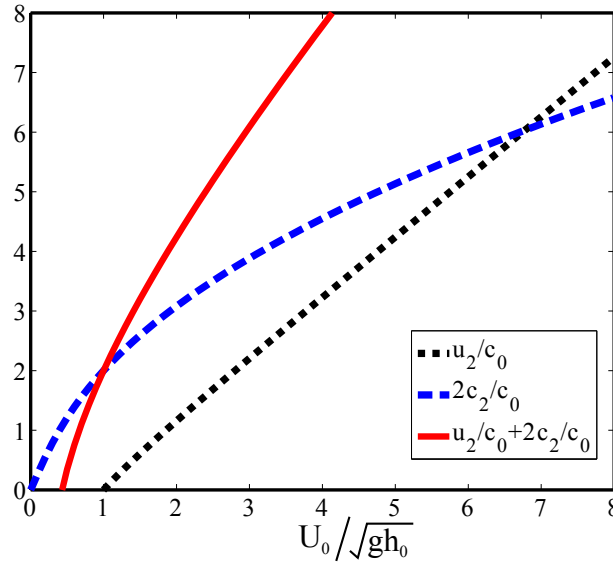


Figure 3.2: Graphical solution for the wet dam-break problem with the Stoker method.

To obtain information about the assumed constant state of region 2, that is, the non-dimensional front velocity of the bore (U_0/c_0 or $U_0/\sqrt{gh_0}$) as well as the constant water depth of the zone 2 (h_2), the graphical solution of Eqs. (3.4) to (3.6) has been considered, as shown in Fig. 3.2 (see also the graphical solution in STOKER [8], Section 10.8). In this way, with knowledge of the initial conditions (h_1/h_0) and use of (3.3), it is possible to establish the next relations to use the graphical solution shown above:

$$\frac{c_1^2}{c_0^2} = \frac{h_0}{h_1} \quad (3.7)$$

Then, h_2 can be estimated from the c_2/c_0 relation (3.5) as:

$$\frac{c_2^2}{c_0^2} = \frac{h_2}{h_0} \quad (3.8)$$

The wet dam-break approach allows to reproduce isolated shipping water events of different types in a systematic and detailed way, as demonstrated experimentally in some papers submitted previously as preliminary results of this thesis: HERNÁNDEZ-FONTES *et al.* [4, 5].

3.2 Experimental setup

3.2.1 General arrangement

The experiments were carried at the Ocean Technology Laboratory (LabOceano) facilities of the Federal University of Rio de Janeiro (COPPE/UFRJ), Brazil.

The general arrangement of the experiment can be observed in Fig. 3.3. A prismatic tank, made of polymethyl methacrylate (PMMA) plates 25 mm thick to reduce hydroelastic effects, was mounted on an structural arrangement. This tank has a fixed structure installed inside on its right side to represent the deck of a coastal, naval or offshore structure. At the left side of the tank, a vertical gate that separates two volumes of water can be observed. The gate was made of a PMMA plate 15 mm thick (Fig. 3.4a). The gate was pulled upwards during the dam-break action by a release mechanism mounted in a vertical structure separated from the one supporting the tank. The release mechanism was formed by a 16 kg weight which was hold at the beginning of the experiments by an electromagnet (Fig. 3.4b). When the trigger was activated, the weight fell down and opened the gate by means of a pulley arrangement with a 3 mm thick stainless steel cable. An optimal cable length has been selected in order to elevate the gate sufficiently to allow the retained water to flow and to damp the falling weight by means of a sand reservoir. The same level of sand was verified prior each test to maximize the repeatability of the experiments. Water was pumped into the tank by means of a hydraulic pump located at ~ 2 m from the left side of the tank. A system of valves was arranged to allow a practical procedure to fill and empty the tank for each experiment.

The initial water levels upstream and downstream the gate (i.e., initial conditions for the wet dam-break method) were monitored by visual inspection before the trigger was activated. To set these initial water levels, two stainless steel rules installed at both sides of the gate, inside the tank, were used. Watertightness of the gate was improved as much as possible by installing a foam tape around it.

Figure 3.5 shows the side view of the tank from which more details of the exper-

imental arrangement can be observed. Note that an impact absorber was installed to the top of the structure to retain the gate (in case necessary). Moreover, it can be observed the rear of the structure, where it was installed an accelerometer to measure the dynamic effects on the tank. Note that there is a hole in the wall, from which the balance cables and a drain hose are introduced. This drain allowed to remove the water filtered under the deck after each experiment, reducing the filtered water level to 2-3 mm for each test. In the figure, it can also be observed a panel LED of $\approx 1.5 \text{ mH} \times 0.4 \text{ mV}$ installed behind the tank to improve illumination. The panel was energized by two power sources installed below the tank. More information regarding the details of the experiment are further described in the present chapter. Complementary illustrations, regarding the experimental methods, are presented in the Appendix [B](#) for illustrative purposes.

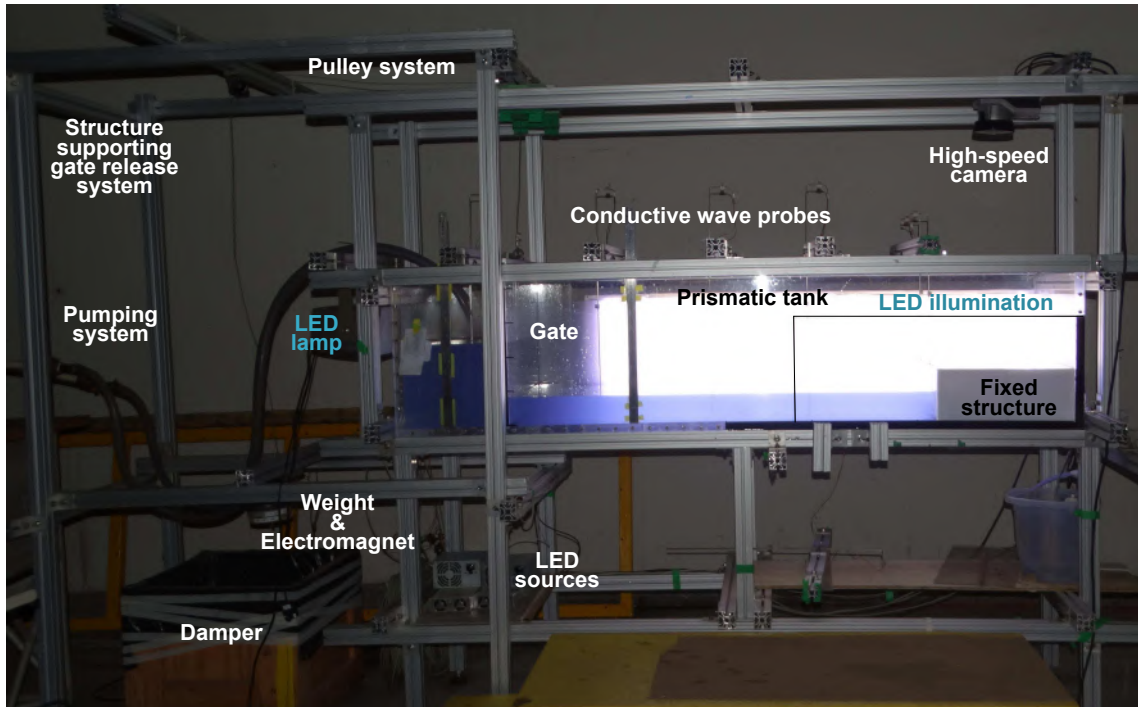


Figure 3.3: General arrangement of the experimental setup.

3.2.2 Dimensions and sensors arrangement

In the present investigation, two types of experiments were carried out, considering the dam-break installation (tank) with and without the fixed structure. The main dimensions of the tank arrangement as well as the sensors positions for both experiments are shown in Figs. [3.6](#) and [3.7](#).

For the experiment with the internal fixed structure (Fig. [3.6](#)), it can be observed that four conductive wave probes ($WP1$ to $WP4$) were used to measure water elevations and an accelerometer (ACC_{wall}) was installed in the vertical wall to account

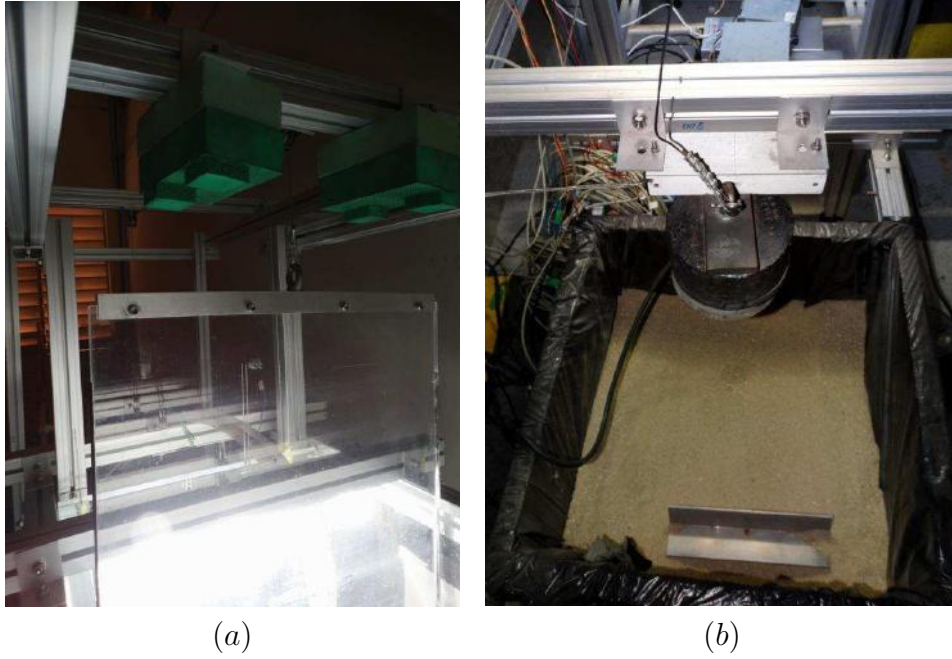


Figure 3.4: (a) Gate. (b) Weight.

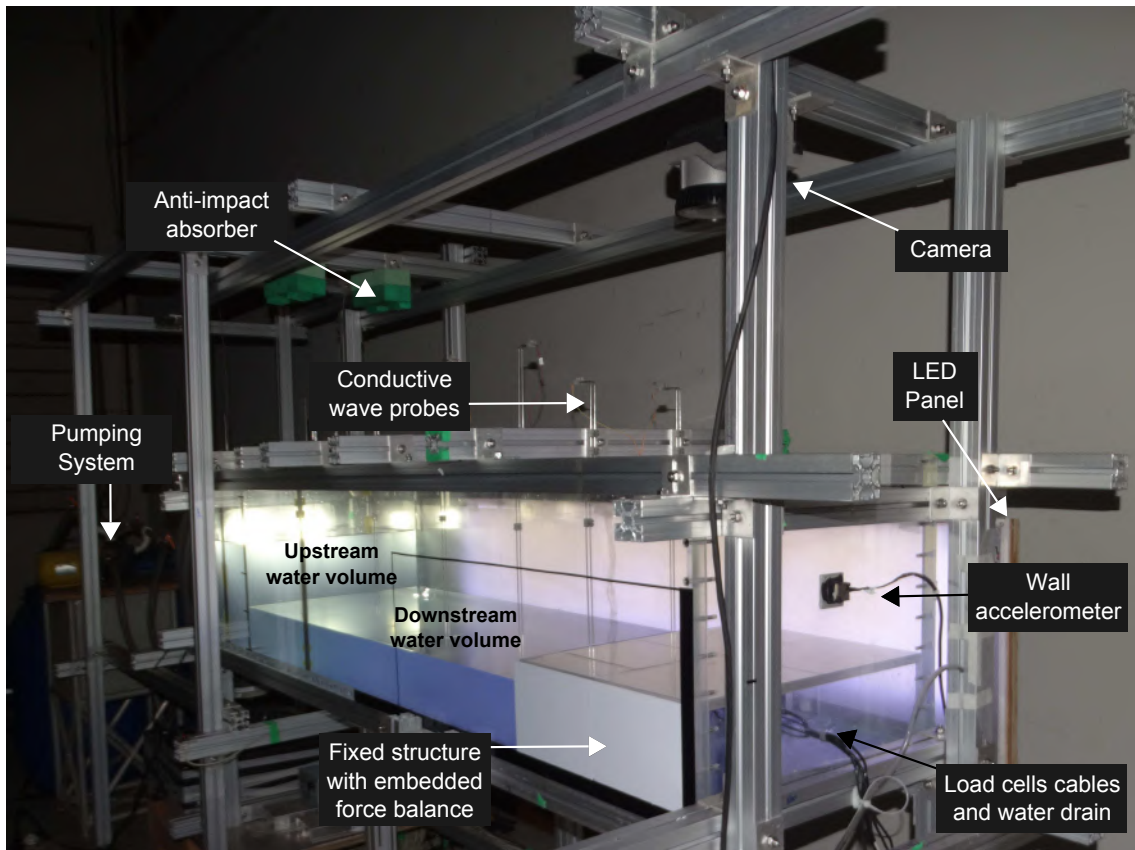


Figure 3.5: Tank side details.

for dynamic effects during the experiments. Furthermore, two cameras (*CAM1*, *CAM2*) were installed parallel to the side and top of the structure to monitor water evolution and wavefront displacement on the structure, respectively.

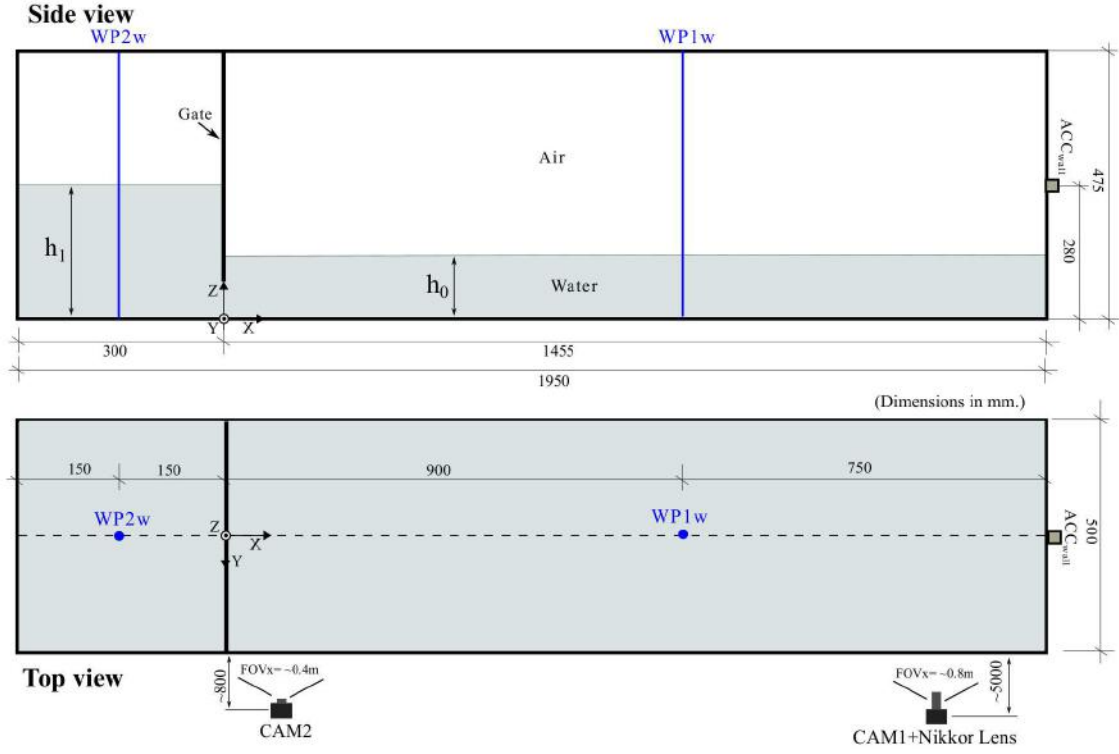


Figure 3.7: Main tank dimensions and sensors arrangement for the experiment without structure.

both, the experiment with (C1-C5) and without (C1w-C5w) the structure.

Table 3.1: Testing matrix with expected parameters for the experiments with and without the fixed structure.

WITH ST.	Case	h_0 (mm)	h_1 (mm)	h_0/h_1	FB (mm)
	C1	108	180	0.6	42
	C2	120	200	0.6	30
	C3	126	210	0.6	24
	C4	132	220	0.6	18
	C5	144	240	0.6	6
WITHOUT ST.	Case	h_0 (mm)	h_1 (mm)	h_0/h_1	FB (mm)
	C1w	108	180	0.6	-
	C2w	120	200	0.6	-
	C3w	126	210	0.6	-
	C4w	132	220	0.6	-
	C5w	144	240	0.6	-

It is important to mention that the shipping water events to be obtained with the unbroken waves were considered in the present study because they resemble more the type of flow on deck considered for the development of the analytical model (i.e., DB and PDB types).

However, it is important to say that with the proposed wet dam-break method, different types of incoming waves (i.e., broken, unbroken) can be generated with the use of different wet dam-break ratios, allowing the study of more types of shipping water events. The study of the events generated with these ratios is out of the scope of the present thesis; however, a summary of snapshots of events verified during the experimental investigation, which can be reproduced considering a single freeboard ($FB = 42$ mm) and wet dam-break ratios $h_0/h_1 = 0.5, 0.4$, are presented in Appendix [D](#) for illustrative purposes.

3.3 Water evolution measurements

Water elevations of the incoming wave as well as the shipping water on deck were measured using conventional and virtual wave probes. For the former, conductive wave probes were considered. For the latter, a binary image-based methodology developed by HERNÁNDEZ *et al.* [\[51\]](#) was adapted and used with the high-speed videos obtained from the cameras. Both methods to measure water elevations are briefly described below.

3.3.1 Water elevation: conventional wave probes

In the experiment with the internal fixed structure, water levels were measured by four conductive wave probes (WP1 to WP4), as shown in [Fig. 3.6](#). WP1 and WP2, which were separated by a distance of 200 mm in the y-direction, were installed close to the structure edge (at 2 mm from the edge, $x = 2$ mm) to measure the freeboard exceedance. Moreover, WP3 ($X = 900$ mm) and WP4 ($X = -150$ mm) monitored the water levels downstream and upstream the gate, respectively.

On the other hand, in the experiment without structure, WP1 and WP2 were not considered. Instead, WP1w ($X = 900$ mm) and WP2w ($X = -150$ mm) were used to monitor water levels downstream and upstream the gate, respectively ([Fig. 3.7](#)).

The wave probes were made of Stainless Steel 2.4 mm diameter rods placed 9 mm apart. A model DHI 102E wave probe amplifier was used. Signal conditioning was performed using a NI SCXI 1520 module. A 100 Hz analog low-pass filter was applied to the signals, which were acquired at 500 Hz. The conversion, synchronization and acquisition of the signals were performed with a NI PXI-6289 data acquisition (DAQ) board and a NI PXI-8109 embedded controller. NI-DAQ and LABVIEW were used as the application software for data acquisition.

Calibration of wave probes was performed following the recommended procedures of the International Towing Tank Conference ITTC [\[56\]](#). From these procedures, an uncertainty in calibration of ± 2 mm was verified for each wave probe.

3.3.2 Water elevation: virtual wave probes

To capture the evolution of water, a high-speed digital camera (CAM1) model QUALISYS Oqus 310 was employed. This camera was used with additional lens AF DC-NIKKOR 105 mm f/2 D. The camera was set to 500 fps, with a resolution of 1284 x 1024 pixels. The camera was located to capture the side view of the tank, with center of view aligned to the bow edge of the structure, as shown in Fig. 3.6, for the experiment with the internal structure. For the experiment without structure (Fig. 3.7), CAM1 was used at the same place.

A second camera (CAM2), model QUALISYS Oqus 110 was used in the experiments with and without the structure to record the wavefront displacement of shipping water and the wave generation during the gate aperture, respectively. For both cases, it was set at 200 fps, with a resolution of 640 x 480 pixels.

For the two cameras used in each experiment the software QUALISYS QTM was employed for video acquisition, visualization and analysis.

The virtual wave probes measurements were obtained from video acquired by the cameras located parallel to the side view of the tank, that is, the CAM1 for the two experiments and the CAM2 for the experiment without structure. To do this, the binary image-based methodology proposed by HERNÁNDEZ *et al.* [51] was employed in the present work. The methodology includes the three main stages of an artificial vision system: image acquisition, processing and analysis. These stages were implemented using the ImageJ open-source software. Overall, gray-scale images are obtained from video, then they are processed by intensity modulation and pseudo-color segmentation to obtain binarized images. Finally, through basic morphological operations, image analysis was carried out to obtain water elevations at different regions of interest (ROIs) over the scene. See the work of HERNÁNDEZ *et al.* [51] for details regarding the procedures for image calibration, processing and analysis to obtain the water elevation measurements. For more information, see the provided guidelines, data and software for the use of the methodology, which are available in the Mendeley data repository DOI: 10.17632/9vwdgv2g5z.1.

Virtual wave probes positions

For the experiment with the internal fixed structure, virtual wave probes (VWPs) have been located at specified ROIs along the incident wave and shipping water propagation domains defined, regarding the allowable field of view (FOV) of the recorded videos, as shown in Fig. 3.8. In the figure, it can be observed that the FOV in the x- and z- directions corresponds to ~ 0.83 and ~ 0.3 m, respectively. A reference system of coordinates has been located at the beginning of the structure.

Since the conventional wave probes (WP1 and WP2) are placed at 2 mm from

the origin (i.e., bow edge), these interfered with the image analysis to measure the freeboard exceedance, that is, the water elevations at the bow edge of the structure ($x = 0$). Thus, two VWP's have been considered to measure the freeboard exceedance. These VWP's, denoted as VWPw0 and VWPd0, were located at $x = -0.005$ m and $x = 0.005$ m from the origin, respectively. Moreover, to monitor the water elevations onto the deck, 33 VWP's separated by a distance of 0.01 m, starting from $x = 0.01$ m (VWPd01) to $x = 0.33$ m (VWPd33), were considered.

To monitor the water elevations in the domain for the incident wave propagation, 42 VWP's separated by a distance of 0.01 m were considered. These were numerated as VWPw01 ($x = -0.01$ m) to VWPw42 ($x = -0.42$ m).

For the experiment without the internal structure, measurements at the same positions for VWPd01-VWPd33 and VWPw01-VWPw42 were also obtained.

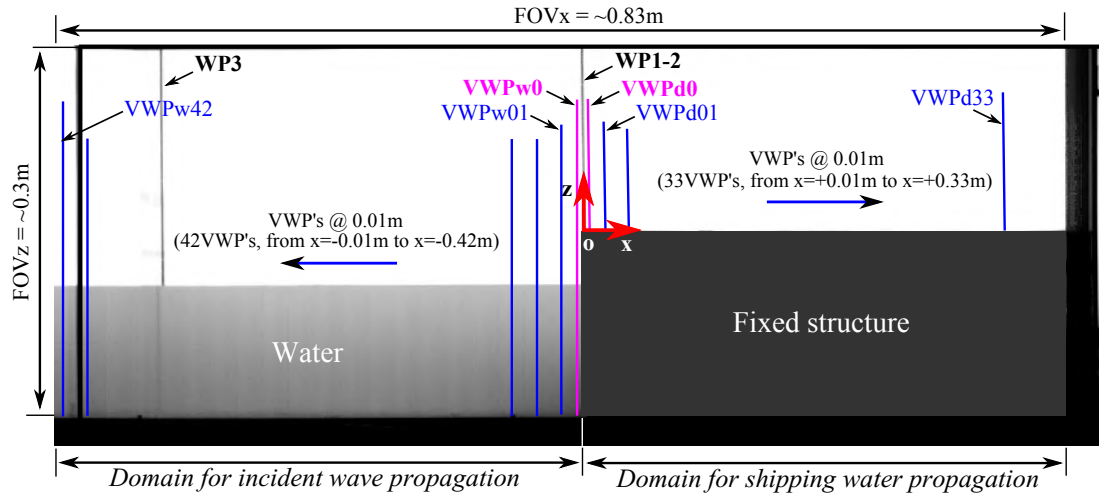


Figure 3.8: Scene field of view (FOV) of CAM1 for the experiment with the internal fixed structure. Virtual wave probes positions for the incoming wave and shipping water propagation domains.

3.3.3 Water on deck kinematics: visual inspection

As stated before, the CAM2 was installed parallel to the deck in the experiment with structure to capture the shipping water wavefront displacement (Fig. 3.6). From the calibrated videos, the velocity of the wavefront (U_{front}) was measured manually using the available tools in the ImageJ software. The position of the wavefront at different times was measured as water propagated over the deck.

Figures 3.9a and b show two typical frames captured by CAM2 for the Case 5 ($t = 1.155$ s and $t = 1.555$ s, respectively) in order to illustrate the method followed. To obtain the data, the intersection of the wavefront edge and the centre line of the deck was monitored at every 0.01 s. A total of 50 points was obtained for each video, starting from the instant at which the edge was firstly visible close to the structure

edge. From the spatial and temporal information captured, the wavefront velocities (U_{front}) were estimated considering the five repetitions of each case. Then, mean and standard deviation values were considered for the analyses.

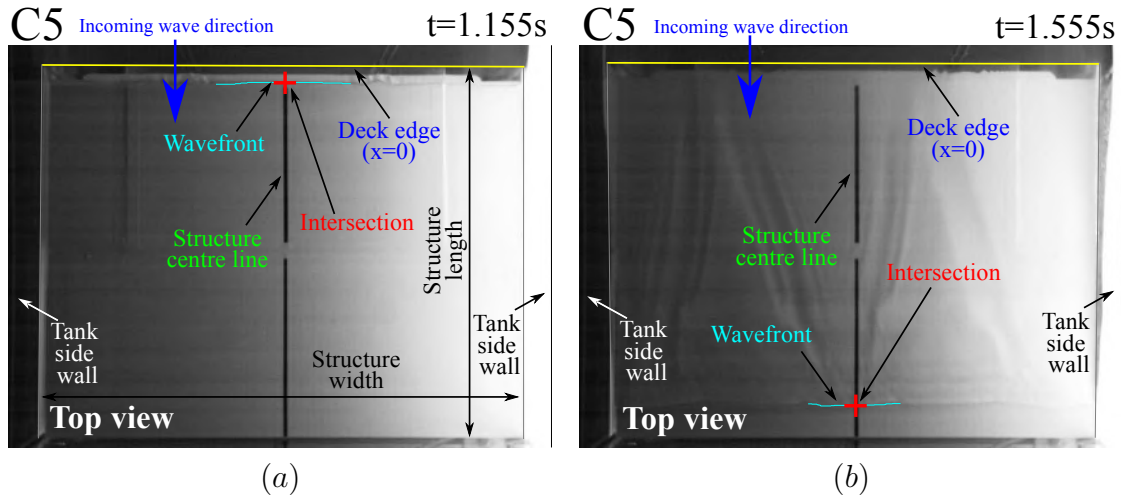


Figure 3.9: Wavefront displacement measurements. (a) Wavefront edge close to the bow edge of the structure. (b) Wavefront well developed close to the end of the structure.

3.4 Load measurements

This section describes the experimental methods used to measure the vertical loading on deck derived from the shipping water events and to analyze the dynamic effects transmitted to the tank during each experiment.

3.4.1 Vertical load measurements

To measure the vertical loading due to the shipping of water onto the deck, a force panel made with 4-axial load cells (named force balance) was considered for the application. It was installed as a part of the deck (embedded to the fixed structure), as observed in the sketch of Fig. 3.6.

The aspect of the force balance is shown in Fig. 3.10a. It was made with a four S-type axial load cells arrangement mounted over a horizontal rigid surface. A rigid horizontal plate was installed on the top of the load cells in order to perform like the sensing element. A triaxial accelerometer was installed at the center position below the sensing element (Fig. 3.10b) to verify possible dynamic effects (e.g., ringing) on the balance during the experiments. To minimize effects of horizontal wave loading in load cell measurements, a rigid vertical wall was installed at the side of the balance where the incoming wave interaction occurred. All plates were made of acrylic plexiglass 150 mm thick. It was assumed their rigidity disregarding hydroelastic effects.

Connections between the different elements of the balance are made by SS-M5 bolts. All the elements of the force balance were mounted on a precision granite surface plate using a digital inclinometer to ensure the horizontal surface alignment.

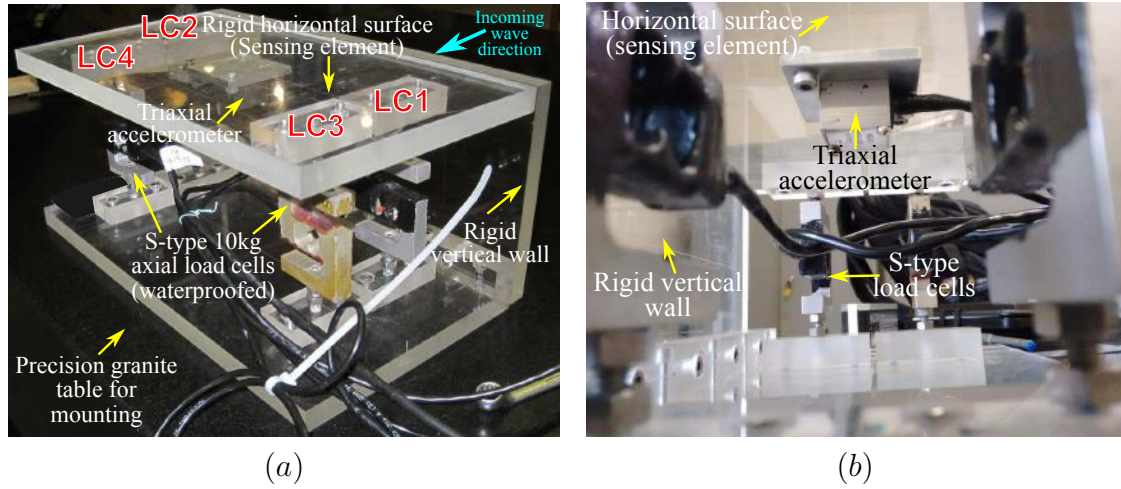


Figure 3.10: Force balance to measure vertical loading. (a) General view. (b) Accelerometer installed under the sensing element.

The overall dimensions of the balance are 334 mm width, 150 mm height and 195 mm length. The sensing element has dimensions of 334 mm width, ~ 180 mm length and 15 mm thick. There is a separation of approximately 0.5 mm between the vertical wall of the balance and the sensing element. The front, lateral and top views, including the main dimensions of the device, are shown in the sketch of Fig. 3.11. It is observed that the accelerometer (ACC_{bal}) is located at the center of the sensing plate with the x_b and y_b directions corresponding to the longitudinal and transversal tank directions, respectively. Likewise, the load cells ($LC1 - LC4$) are equally spaced from each other by 63.5 mm and 220 mm in the longitudinal and transversal direction, respectively, considering the center of the accelerometer as the origin.

Force balance instrumentation

Load cells. Four S-type aluminum load cells manufactured by Alfa instruments (Brazil) with nominal capacity of 5 to 10 kg were used. Their sensibility is of 2 mV/V $\pm 10\%$. They have overall dimensions of 64 mm height, 50 mm width and 12 mm thick.

The measured force on the sensing element equals the summation of the four arms reactions. The total forces measured by the sensing element do not depend of the application point (BALBINOT e BRUSAMARELLO [57]), being possible to measure the vertical loading in all the sensing area. Before mounting the platform, the load cells were calibrated under compression loads from 0 to 9 kg. For each load

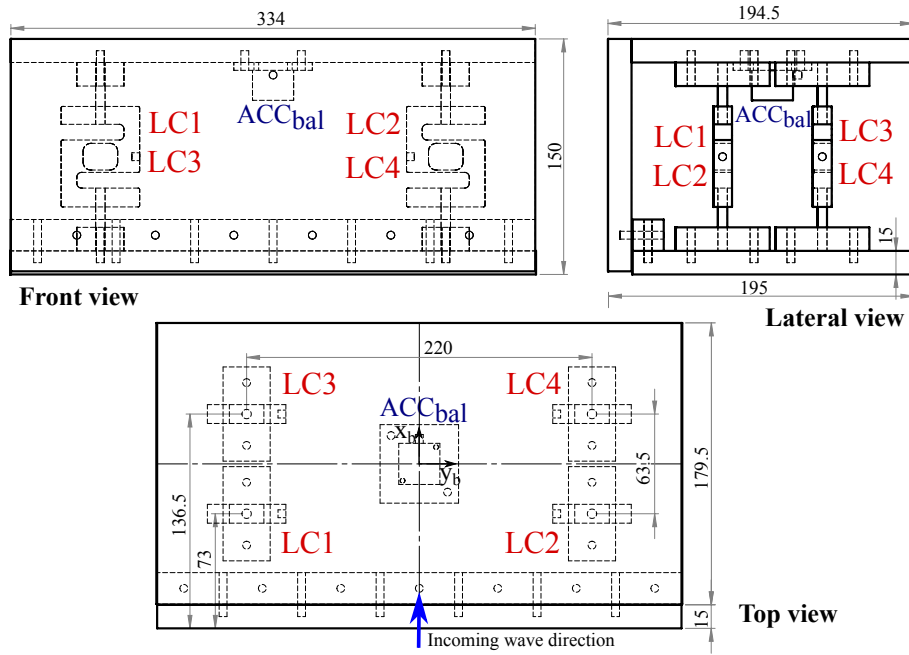


Figure 3.11: Views and dimensions of the force balance.

cell, an uncertainty in calibration in the range ± 10 gr was estimated (ITTC [56]).

Accelerometer. To have an idea of the dynamic effects of the dam-break experiments transmitted to the tank (e.g., ringing), a triaxial accelerometer MEAS 4803A-0002 (Model 4803 with range up to 2g) was used. The accelerometer weight without connection cable is 0.06 kg. It was assumed that its weight did not cause effects in the sensing element. Its cover is made of stainless steel. The dimensions of the accelerometer are 21.34 mm length, 21.34 mm width and 19.1 mm height. Most important dynamic parameters include: Sensitivity of 1000 mV/g, frequency response of 0-200 Hz, and damping ratio of 0.7. The X, Y and Z directions of the accelerometer correspond to the longitudinal, transversal and vertical ones in relation to the tank, respectively.

The sensors that compose the force balance were all calibrated by following the ITTC recommended procedures [56]. The data acquisition devices are the same described for the wave probes sensors (Section 3.3.1).

Force balance installation and measuring procedure

The force balance was embedded to the fixed structure installed inside the tank, as observed in Fig. 3.12. In this figure, it is possible to observe the top, front and back views of the embedded force balance. The top view (Fig. 3.12a) allows to see the deck surface. Notice that the balance surface was covered by a layer of white adhesive tape to facilitate the flow visualization.

Before each test, the deck was completely dried with help of pressurized air to

remove water remaining in the joints of the sensing element with the internal fixed structure. Also, these joints were covered by adhesive tape to prevent water entry during the tests. Regarding this procedure, the performance of the balance was verified prior each test by means of static load verification. That is, a weight of 0.2 kg was put and static measurements were taken in order to ensure that the water inside the gaps was completely removed, and that the tape covering the joints did not have significant effect on the overall measurements. This procedure was strictly followed before each test in order to keep the repeatability of the testing matrix.

Additionally, it is important to mention that there were small gaps (< 1 mm) between the joints of the fixed structure deck and the tank walls. These were kept to have an exit for possible air compressed under the sensing element. It was verified that in a close region for measurements, this air may cause effects in the measurements. Thus, it was ensured to keep the joints water-free before each test using air compressed, minimizing in this way the possible effects in the force balance performance to measure the positive axial loads ($+ \downarrow$).

In the front view (Fig. 3.12b), details of the balance and the deck extension can be observed. In all the joints shown in the front view, silicone was used for fixation. Pretests were carried out to prevent water leakage in all the joints of the vertical wall, which always were in contact with water.

Finally, Fig. 3.12c presents the back view of the structure (tank side). Note that there was a hole in the vertical wall of the tank, which allowed the entrance of the load cells cables. Moreover, this hole was also useful to have an exit of the air entrapped beneath the deck of the fixed structure. After each shipping water event, water leaked by the slots (joints) between the deck and the tank. Then, in order to keep repeatability for each test, an small hose was introduced through the hole to drain the remain water. This action was repeated carefully before each test until remaining a water level of approximately 2 – 3 mm on the tank bottom. Once water was drained, it was ensured to remove the hose to allow the air to escape.

3.4.2 Dynamic effects during the experiment

Since the dam-break is a sudden motion that presents a rapid release of the gate, some dynamic effects (e.g., ringing) might have been transmitted to the tank. To analyze these effects, an accelerometer was attached to the tank wall as a mean of monitoring. A triaxial accelerometer, similar to the one used in the force balance (Section 3.4.1), was installed on the vertical wall of the structure at a distance of 0.28 m in relation to the tank bottom (see Figs. 3.5, 3.6 and 3.7: ACC_{wall}). Details of the installation arrangement of this accelerometer can be verified in Fig. 3.12c. For this accelerometer, the X, Y and Z directions correspond to the transversal,

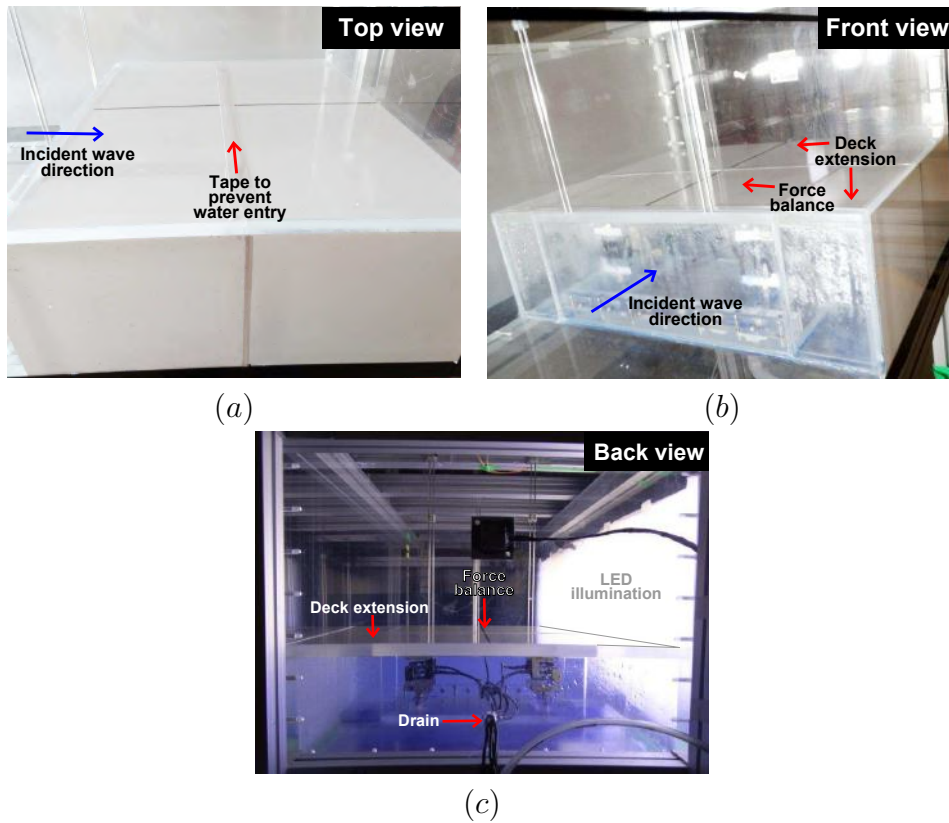


Figure 3.12: Different views of the force balance embedded to the deck of the internal fixed structure. (a) Top view. (b) Front view. (c) Back view.

vertical and longitudinal ones in relation to the tank orientation, respectively. The characteristics of the accelerometer as well as the data acquisition requirements and calibration are the same as described in the previous sections (Sections [3.3.1](#) and [3.4.1](#)).

Chapter 4

Experimental Results

This chapter presents the experimental results of the thesis. The first part of the chapter treats the evolution of the incoming wave, from its generation to the stage before shipping water occurs on the fixed structure. On this subject, both experiments with and without the fixed structure are considered to extract and examine data, concerning the evolution of water elevations and the kinematics of the incoming wave crest.

The next part of the chapter is related to the study of the evolution of the shipping water on the fixed structure. This includes the analysis of the wave elevation variation in time and space as well as the study of the wavefront velocities.

Finally, the last part of the chapter includes the analysis of vertical loading on deck of the structure, caused by the shipping water events, and of the dynamic ringing effects caused during the experiments of wet dam-break.

4.1 Incoming wave

The experimental results corresponding to the incoming wave include the water elevation variation and kinematics, considering the experiments with and without the structure. Relevant information for these parameters was obtained by means of image-based procedures, previously described in Chapter 3.

First, information referent to the gate aperture and its repeatability for all cases is presented. Secondly, the generation of the incident wave at the region close to the gate is analyzed in order to know the initial stages of the wave formation and its development downstream the gate until it attains an stable form.

Subsequently, the evolution of the fully-developed incident wave at a downstream region (near the fixed structure) is investigated by means of a detailed flow evolution visualization, named hereafter as *two-dimensional reconstruction* only for description purposes, which allowed visualization of the temporal and spatial evolution of

the incident wave, and verification of the influence of the structure on the incident flow.

Finally, kinematics of the incoming wave and shipping water are examined from the available data. Horizontal crest velocities of the incoming waves at different regions over the domain considered are estimated from experimental approaches and compared with theory of STOKER [8]. Also, a practical procedure to relate wet dam-break waves to regular waves is presented.

4.1.1 Wave generation

Gate opening

Experimentally, the gate aperture time (t_r) should be as short as possible in order to consider a sudden release of the gate. However, this is complex to attain in real cases, so, recommendations found in literature to set an adequate t_r for all cases were considered for the present study. Concerning this, to attain a gate aperture time that approximates the theoretical approach for a sudden gate release, the condition proposed by HAGER e LAUBER [58] apud LAUBER e HAGER [59] for a dry dam-break experiment was considered. Their condition, despite of being obtained through experiments of dry dam-break by relating the gate release motion with that from free-fall rigid body theory, was adapted to the present study, disregarding the effects originated on the gate by the downstream volume of water. Thus, the next condition was attained to consider the present tests as dam-break:

$$t_r < \frac{\sqrt{2}}{\sqrt{g/h_1}} \quad (4.1)$$

where t_r is time for gate release, g is acceleration due to gravity, and h_1 is the initial water depth in the volume of water upstream the gate.

Before performing the matrix of tests, several pretests were carried out to find optimal t_r for each case. It was verified that a weight of ≈ 16 kg allowed attaining the condition of Eq. (4.1) for all cases.

From video obtained with CAM2 in the experiment without structure (Table 3.1, C1w-C5w), the gate release was monitored using ImageJ tools for tracking points in order to obtain the velocity of aperture. To do this, deck edge displacement (z_{gate}) was followed at every 0.005 s until it reached a height of approximately 0.3 m.

Figures 4.1a-e shows the vertical position of the gate (z_{gate}) against time (t) for the five cases C1w-C5w, respectively. The figures show the mean and standard deviation values obtained with five repetitions. As can be seen, the trend followed by the curves is very similar for all the cases. In spite of an small change in the linear trend of results at $z_{gate} \approx 0.15$ m, all cases seem to keep a quase-linear trend.

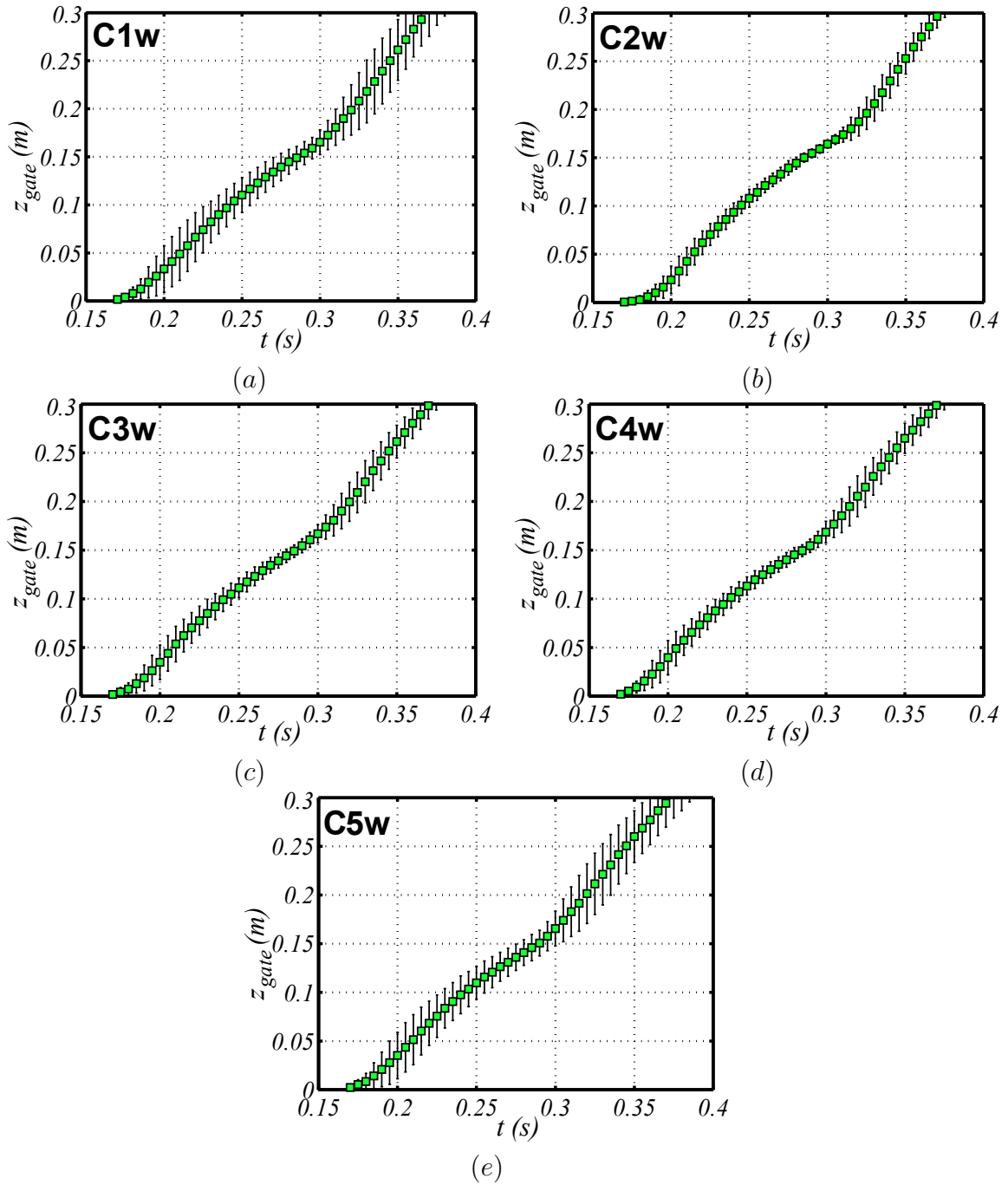


Figure 4.1: Gate edge vertical displacement (z_{gate}) vs time (mean and standard deviation values) for all cases of the experiment without structure. (a) Case 1 (C1w). (b) Case 2 (C2w). (c) Case 3 (C3w). (d) Case 4 (C4w). (e) Case 5 (C5w).

To verify the tendency followed by results, a linear regression analysis was performed to the mean values observed in Fig. 4.1. Regarding this, Figure 4.2 shows the curves fitted to the experimental data for Cases C1w (Fig. 4.2a) and C5w (Fig. 4.2b), which were chosen as representative of the other cases. In both cases, good adjustment was obtained with experimental data ($R^2 \approx 0.99$, where R^2 is the coefficient of determination of the linear regression). Moreover, the equations obtained for the fitted curves were very similar, representing a constant velocity (see slope of the fitted curve) of 1.5 m/s for both cases. Such a value of velocity was also observed for the other cases.

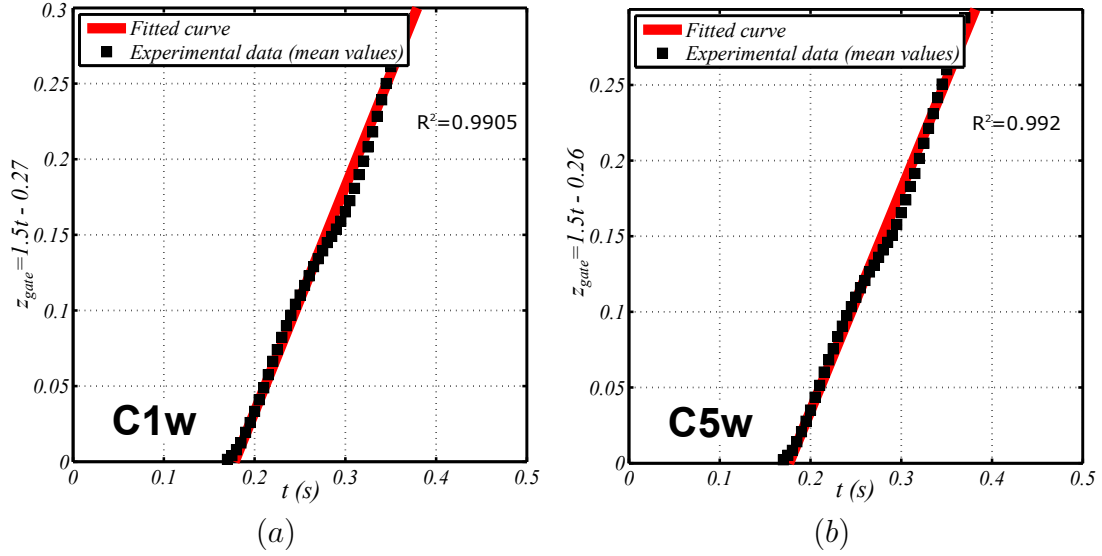


Figure 4.2: Linear regression for gate edge mean vertical displacement (z_{gate}) vs time (t) for the experiment without structure. (a) Case 1 (C1w). (b) Case 2 (C5w).

On the other hand, Figure 4.3 shows the gate edge vertical velocity (w_{gate}) against time for C2w, which was taken as representative of the other cases. Following the trend represented by the mean values, it is observed that there is an almost constant acceleration until $t \approx 0.22$ s, then, the gate decelerates until $t \approx 0.3$ s, to finally present a second acceleration after this time. The decrease of acceleration observed may be attributed to a small interaction of the gate with the tank walls during the gate release. However, its effect was disregarded in the analysis, considering the mean gate velocity from $z_{gate} = 0$ m to $z_{gate} = 0.3$ m.

The mean gate opening velocities assumed from the linear regression shown in Fig. 4.2 (i.e., 1.5 m/s for all cases), can be considered to demonstrate the assessing of the gate aperture condition of Eq. (4.1) for each wet dam-break ratio considered.

Table 4.1 presents the gate aperture times (t_r) for the five cases analyzed with the experiment without structure. In the table, the t_r values considered as reference are shown, which were calculated with the Eq. (4.1), using the respective h_1 value for each case. Furthermore, the t_r values obtained from the experiments are also

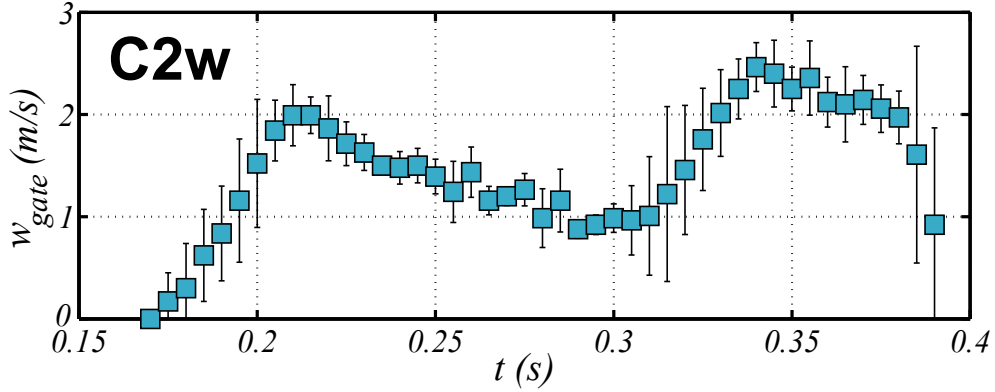


Figure 4.3: Gate edge vertical velocity (w_{gate}) vs time (t) for the experiment without structure (Case 2).

shown. These values were calculated with the constant velocity obtained from the linear regression analysis presented above (i.e. 1.5 m/s). As expected, the shorter aperture times were those for which h_1 presented the lower values. That is, for Cases C1w and C5w, the differences between the obtained and reference t_r values were 0.0716 s and 0.0618 s, respectively. Then, it can be verified that in all cases, the opening times are into the range defined by the condition presented in Eq. 4.1.

Table 4.1: Reference and obtained gate aperture times (t_r) for the five cases of study without the internal fixed structure (C1w-C5w).

Case	h_1	t_r (reference)	t_r (obtained)
C1w	.18 m	0.1916 s	0.1200 s
C2w	.20 m	0.2019 s	0.1333 s
C3w	.21 m	0.2069 s	0.1400 s
C4w	.22 m	0.2118 s	0.1467 s
C5w	.24 m	0.2218 s	0.1600 s

Wave formation initial stages

In the present approach, when the gate opens, it is formed a resulting bore (incoming wave hereafter) that propagates downstream. To the best of the author knowledge, there is lack of detailed visualization in literature that allows observing the transition of the wave formed from the gate location ($X = 0$, Fig. 3.7) to some stages downstream. In the present study, the CAM2 allowed visualization at 200 fps of these stages for the experiment without the structure. This might give important and detailed information regarding the wave formation process.

Figure 4.4 presents snapshots of different points in time of the wave formation stages for the Case 1w. The first point in time ($t = 0.175$ s) shows the initial

condition of the experiment just before the gate started moving upwards. Between $t = 0.3$ s and $t = 0.375$ s, the gate opened completely for the initial water level considered and a depression wave started forming. From $t = 0.45$ s to $t = 0.75$ s, it can be observed that the wave developed and propagated downstream, attaining an undular shape, which was considered as a well developed wave (see figure at $t = 0.75$ s).

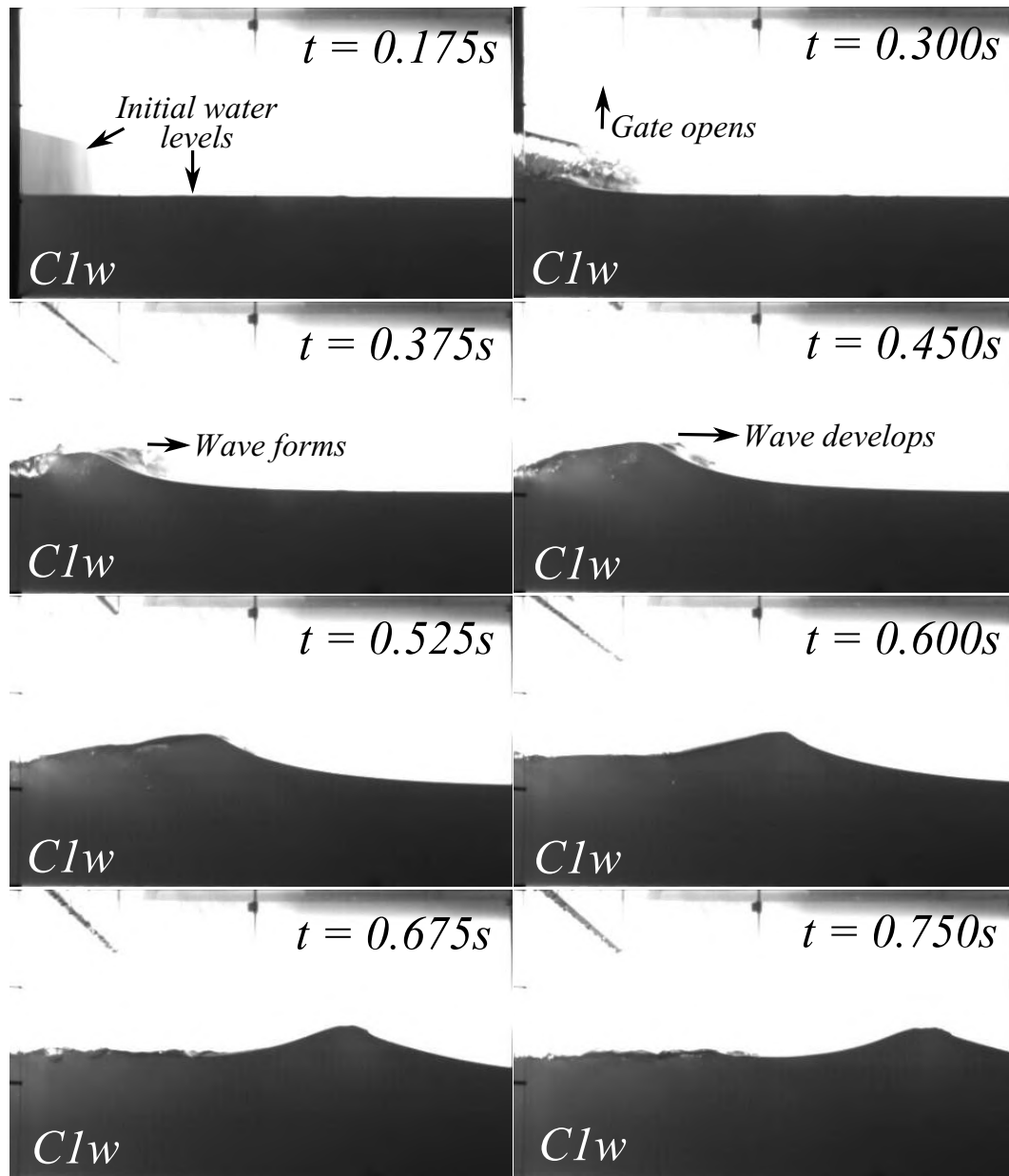


Figure 4.4: Stages of wave generation for the experiment without structure (Case 1, C1w).

In a similar manner, Figure 4.5 shows the wave formation stages for the Case 5w, considering the same points in time as in Fig. 4.4. According to the repeatability analysis performed for the gate aperture, the gate started opening at the same time ($t = 0.175$ s). Then, it can be observed how the wave started forming and

developing as its crest moved downstream (see images from $t = 0.3$ s to $t = 0.675$ s), until reaching an almost symmetric crest at $t \approx 0.75$ s (i.e., well developed wave). Differently to Case 1w, this case presented a larger amount of water propagating downstream. In all cases examined, the same behavior was verified, obtaining the well developed incoming waves propagating downstream the gate.

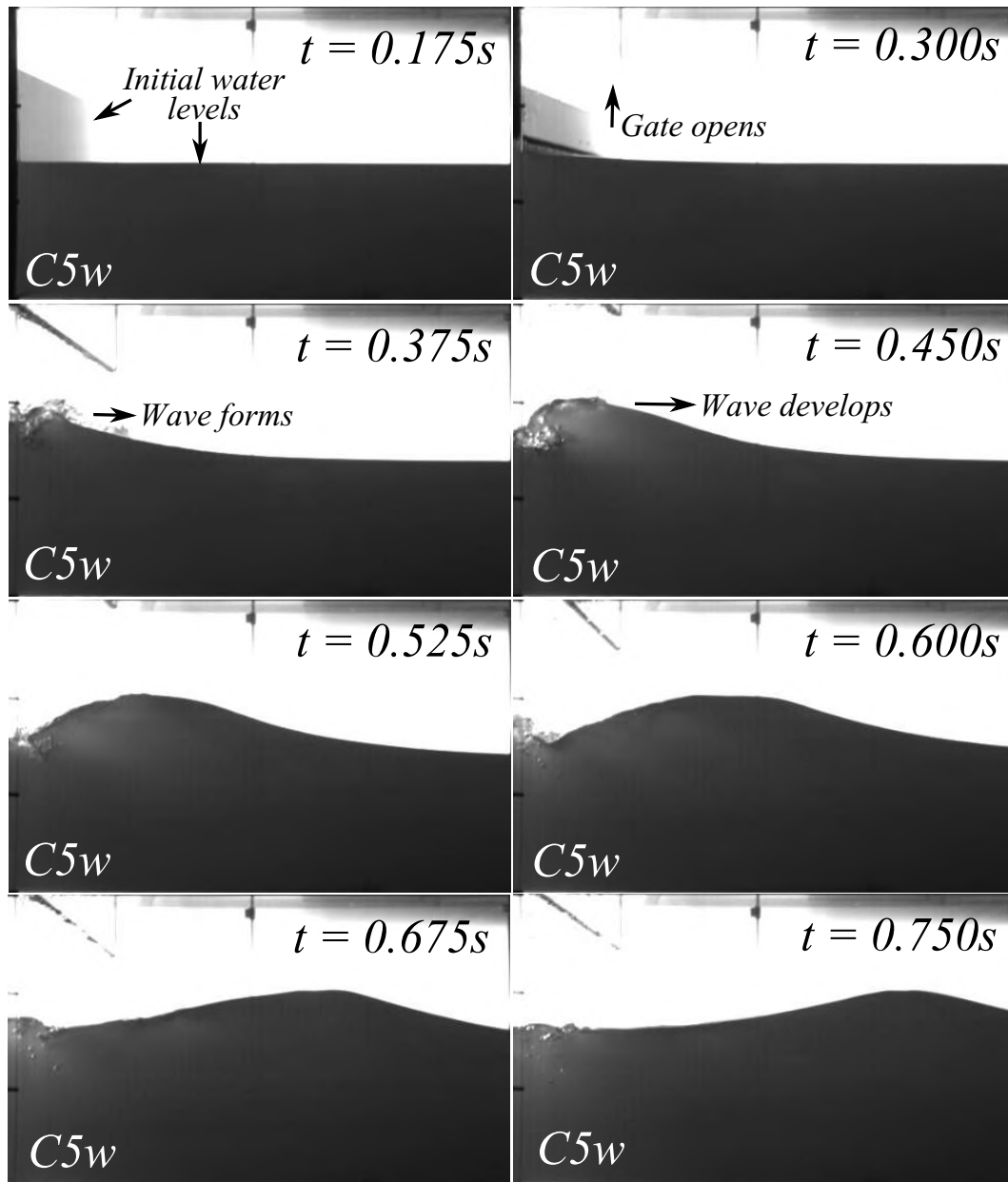


Figure 4.5: Stages of wave generation for the experiment without structure (Case 5, C5w).

From the very beginning of the wave formation, close to the gate position, to the stages at which the bore developed and maintained a regular (quasi-symmetric) shape, there was a change in the shape and in the maximum elevations that can not be well observed in the Figs. [4.4](#) and [4.5](#). In order to better examine the transition of

the wave development, from the region near the gate to some distance downstream, some spatial distributions of water elevations obtained from virtual wave probes were analyzed.

Figure 4.6 presents a comparison of wave profiles (i.e., water elevations, η , against the longitudinal positions from the gate, x) taken at several points in time for the Case 1w. Moreover, the theoretical value h_2 estimated with the approach of Stoker (see Section 3.1) has been added to the plots to make comparisons with the obtained results. The comparisons were made to verify the range of applicability of the theoretical values in the experimental results obtained.

As can be observed in Fig. 4.6, two points in time are considered in each graph and their corresponding profile images from the experiment are presented at the upper-left region of each figure. In all the comparisons, the stage corresponding to $t_1 = 0.35$ s has been considered as a reference. This point in time corresponds to approximately 0.175 s after the gate started opening, and the wave started forming, presenting the shape of a steep front of water, as described in STOKER [8]. It can be observed in Figs. 4.6a-f how this wave profile resembles a steep hydraulic jump with amplitudes close to the theoretical ones from the Stoker model. Conversely, for latter stages the shape of the profiles observed (t_2) changes, modifying the aspect from steep front to an undular bore.

In Figs. 4.6a-c, the wave profiles for $t_2 = 0.4, 0.45$ and 0.5 s, respectively, are shown in the comparisons against t_1 . It can be seen that for these results, the form of the wave changed as the wave crest became better defined, and propagated downstream. Next, when the maximum value of the wave crest appeared near $X = 0.2$ m, downstream the gate (Fig. 4.6d), the wave started developing an small cave and a following second crest of smaller amplitude (Fig. 4.6e). These cave and the second crest were better defined when the wave crest reached a quasi-symmetric shape, as observed in Fig. 4.6f. Similar behaviors were observed for the other cases, presenting larger amplitudes from Cases 1w to 5w. The present analysis for Case 1w was chosen as representative to demonstrate that there is a difference between the experimental wave maximum value of the fully-developed wave (bore) and the theoretical value obtained for the region 2 shown in the sketch of Fig. 3.1 for the Stoker approach. However, these theoretical values are closer to the amplitude of the steep jump observed at the early stage after the gate release ($x \lesssim 0.1$ m). The well developed bore is further characterized at the end of this section in order to make approximate analogies with linear wave theory.

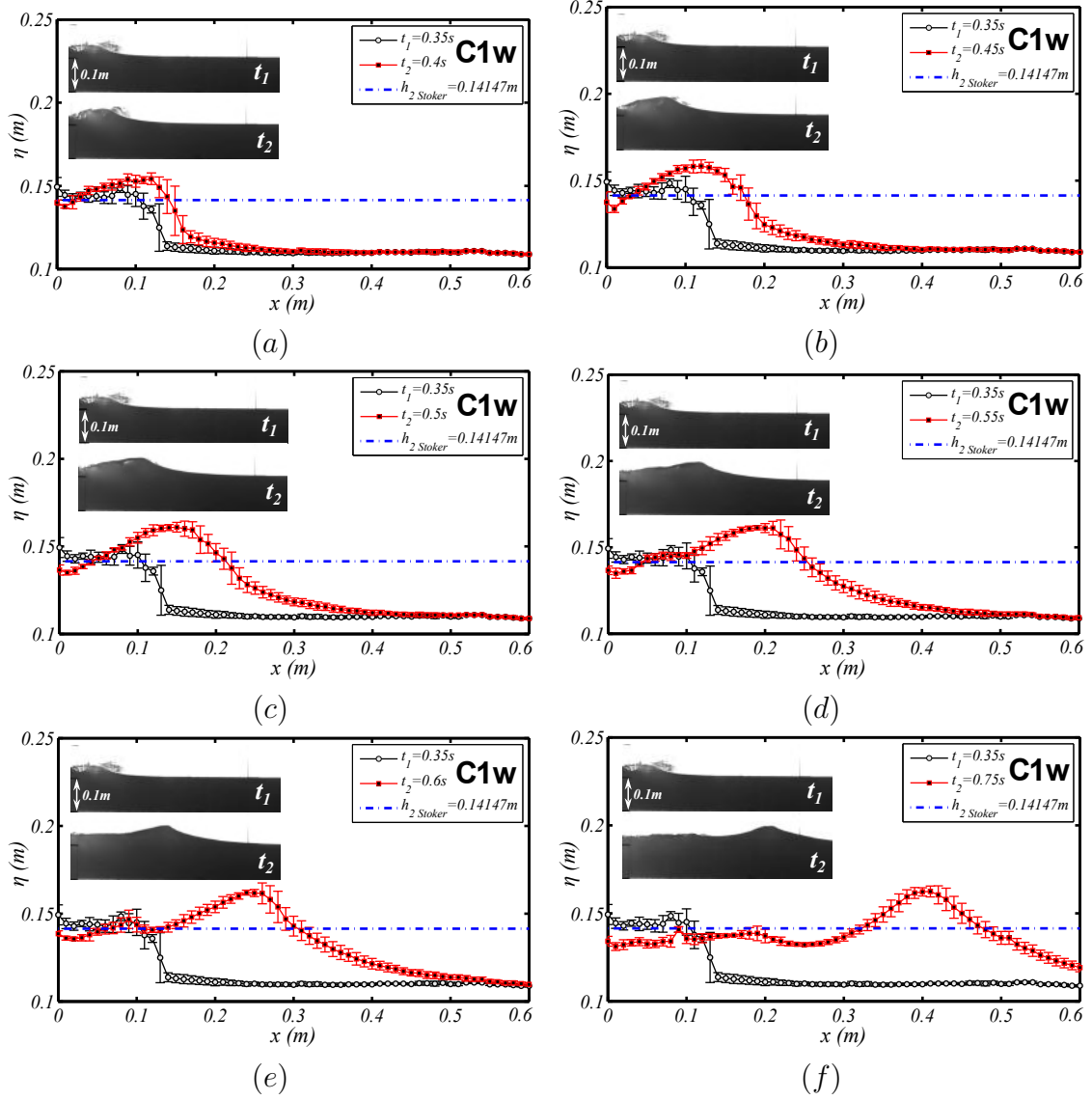


Figure 4.6: Comparison between spatial distributions of wave elevations (η vs x) at different points in time for Case 1w (experiment without structure). Dash-dot lines correspond to the theoretical Stoker model. (a) $t_1 = 0.35$ s and $t_2 = 0.40$ s. (b) $t_1 = 0.35$ s and $t_2 = 0.45$ s. (c) $t_1 = 0.35$ s and $t_2 = 0.50$ s. (d) $t_1 = 0.35$ s and $t_2 = 0.55$ s. (e) $t_1 = 0.35$ s and $t_2 = 0.60$ s. (f) $t_1 = 0.35$ s and $t_2 = 0.75$ s.

4.1.2 Wave propagation

In this section, the incoming wave propagation parameters (i.e. wave elevations and crest horizontal velocities) are extracted and analyzed from experimental data. First, the validity of the binary-image-based technique employed to capture water elevations is tested against conventional wave probe measurements. Then, two-dimensional reconstruction of the water surface is carried out at different positions (VWPs separated at 0.01 m from each other) along the travel distance of the incoming wave to better visualize its trend. Next, the effects of the presence of the structure on the incoming wave elevations are presented by comparing water eleva-

tions time series at different positions from the structure edge. Subsequently, wave kinematic parameters are calculated and compared with the theoretical approach of Stoker. Finally, the incoming wave characterization is presented.

Virtual wave probes validation

Figure 4.7 shows the comparison of water elevation (η) time series (including mean and standard deviation) between the WP3 and the VWP located at the same position for the experiment with structure. Figure 4.7a shows the results for the Case 3, whereas Fig. 4.7b shows the data for Case 5. It can be observed that in both cases there is a close agreement between the values and trends followed by the water elevations. Differences between the mean initial values correspond to ≈ 2 mm and ≈ 0.5 mm respectively for Cases 1 and 5 (C1 and C5), whereas differences between maximum values correspond to ≈ 4 mm (temporal shift ≈ 0.02 s) for both cases. These differences are assumed as acceptable, considering the range presented by the standard deviation for each case. Additionally, it has to be considered the range of uncertainty in calibration obtained for the conventional wave probes (WPs) and the one associated to the image-based technique (see HERNÁNDEZ *et al.* [51] for reference). Regarding this, the applicability of the image-based methodology observed for the VWPs presented in Fig. 4.7, indicates that is possible to use it with confidence to monitor water elevations at desired positions over the entire domain of interest.

Incoming wave elevations

Once the image-based method used to obtain the virtual wave probes has been verified, water elevations time series were obtained at the positions defined in Fig. 3.8 ($VWPw01 - VWPw42$) for the incident wave propagation region (from $x = -0.010$ m to $x = -0.420$ m, separation: 0.010 m between each VWP, considering the origin at the bow edge of the structure). This allowed to obtain a two-dimensional reconstruction of the incoming waves, as shown in Figs. 4.8a and b for the Cases 1 and 5, respectively. In these figures, it is possible to identify water elevations and the main stages of the incoming wave on time and space. For both cases, it can be noted that the wave propagates with almost a constant elevation (see constant color region of the incoming wave) until it felt the influence of the structure (see peak values region of the incoming wave), increasing the elevations. These maximum elevations are presented just before the shipping of water on the structure. Moreover, it can be observed the generation of reflected waves by the structure just after the incoming wave has reached its peak value during the runup stage on the bow of the structure. The resultant backflow had also considerable amplitudes, but it did not have a

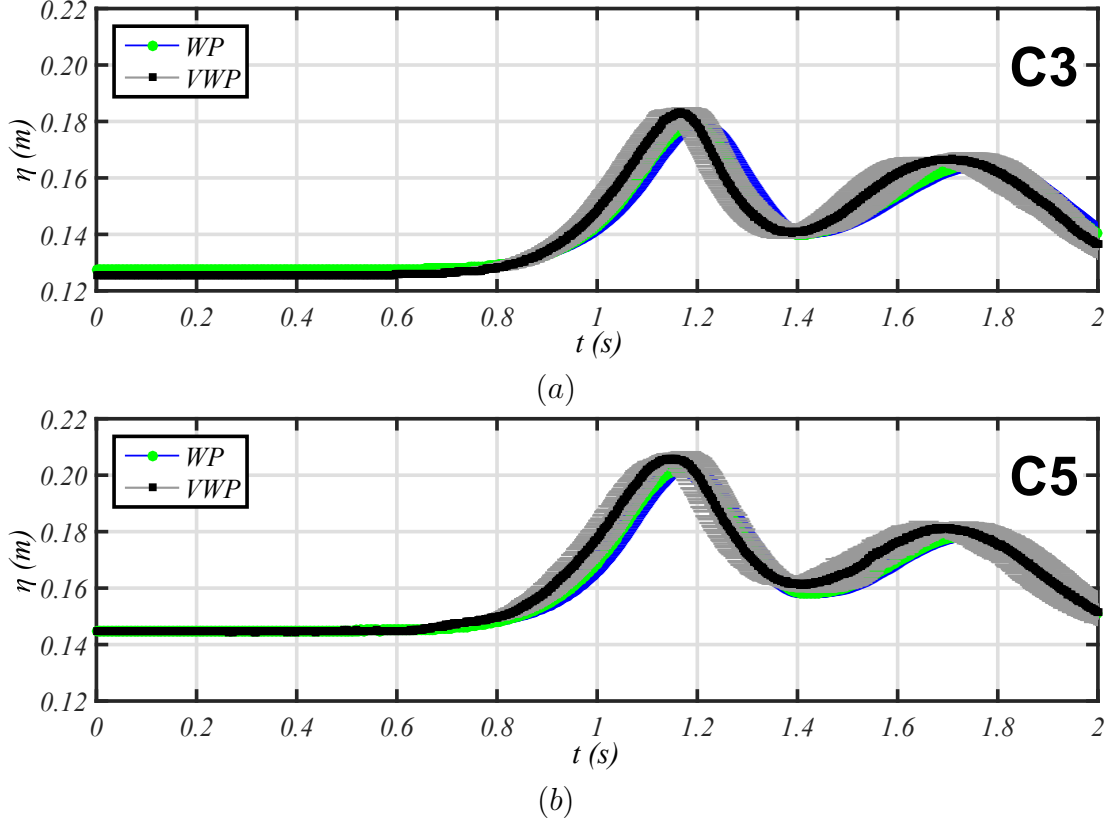


Figure 4.7: Comparison of time series of water elevations (η) between the probe WP3 and its respective VWP located at the same position for the experiment with structure. (a) Case 3. (b) Case 5.

direct effect on the shipping water on deck. Nevertheless, the backflow generated after bow run-up may present significant effects on after-coming waves, in situations where incoming wave trains are considered to study the shipping water problem or in real situations. Thus, in these cases, the resultant events of shipping water on deck may be also dependent of the possible effects caused by the backflow observed.

To visualize more information related to the incoming wave propagation, η vs x and t vs x views are shown in Fig. 4.9. This figure clearly illustrates the variation in water elevations maxima while the incoming wave propagates from the beginning of the field of view ($x = -0.420$ m) to the vertical wall of the structure ($x = 0$). Figures 4.9a and c show the maximum water elevations along different positions (x) for Cases 1 and 5, respectively. In these figures, it can be verified the effect of the presence of the structure on the maximum elevation of the incoming wave. For the Case 1, this elevation is almost constant until $x \approx -0.160$ m, whereas for the Case 5, it seems to start changing at $x \approx -0.280$ m. This indicates that for the cases with lower freeboards (e.g. Case 5), there is a variation of the constant maximum elevation of the incoming wave, which occurred at a longer distance from the structure than for the other cases.

On the other hand, Figures 4.9b and d show water elevations in a t vs x view

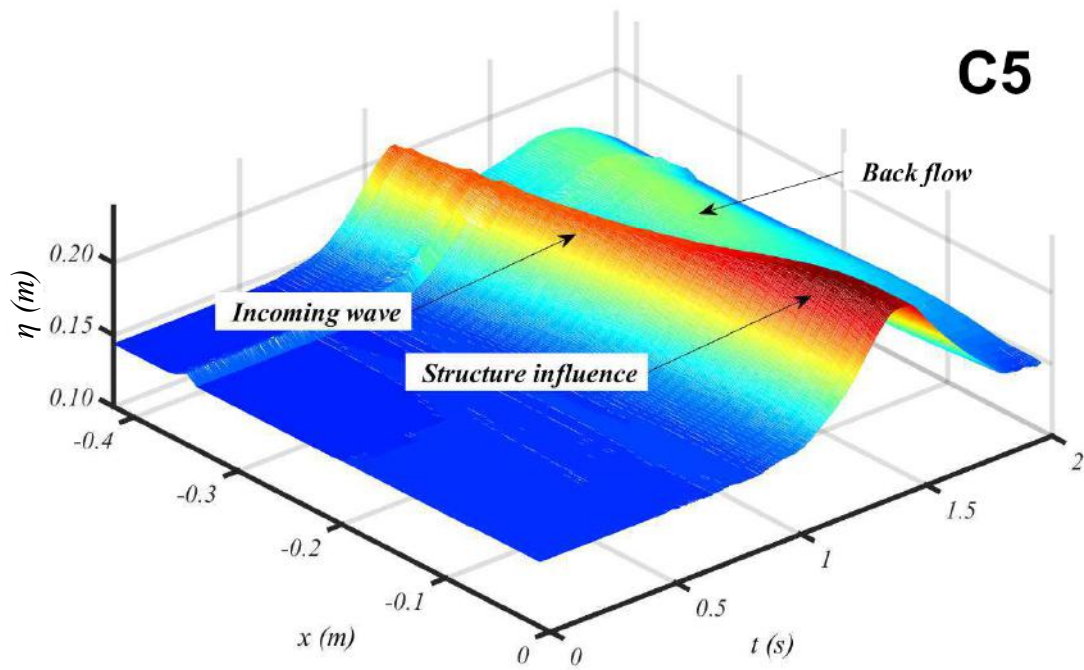
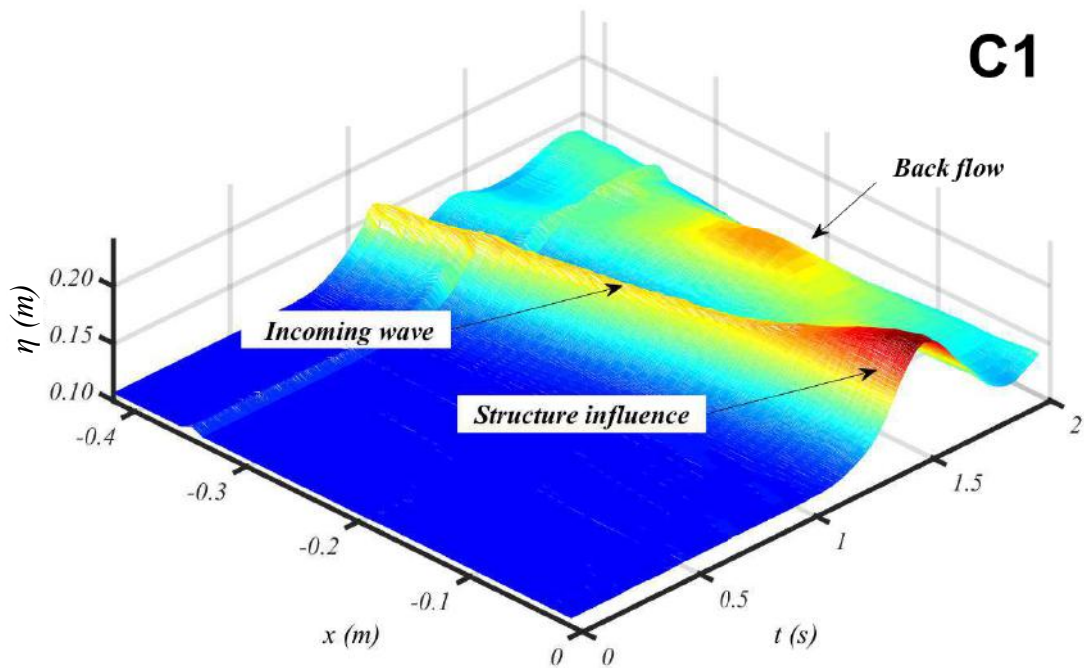


Figure 4.8: Two-dimensional reconstruction of the incoming wave evolution for the experiment with internal structure. The bow edge of the structure was considered as the origin. (a) Case 1. (b) Case 5.

for the Cases 1 and 5, respectively. The color regions from these figures help to understand how the incoming wave propagated with almost a constant elevation and velocity (inferred from the slope defined by the constant color region, $x < 0$) until it interacted with the structure, where the maxima values (darkest regions, near $x = 0$) are observed. It can be noted that maxima values of approximately 0.170 m and 0.220 m are presented for Cases 1 and 5, respectively. These values define the range of maximum freeboard exceedances expected for all the cases, as further described in Section [4.2.2](#)

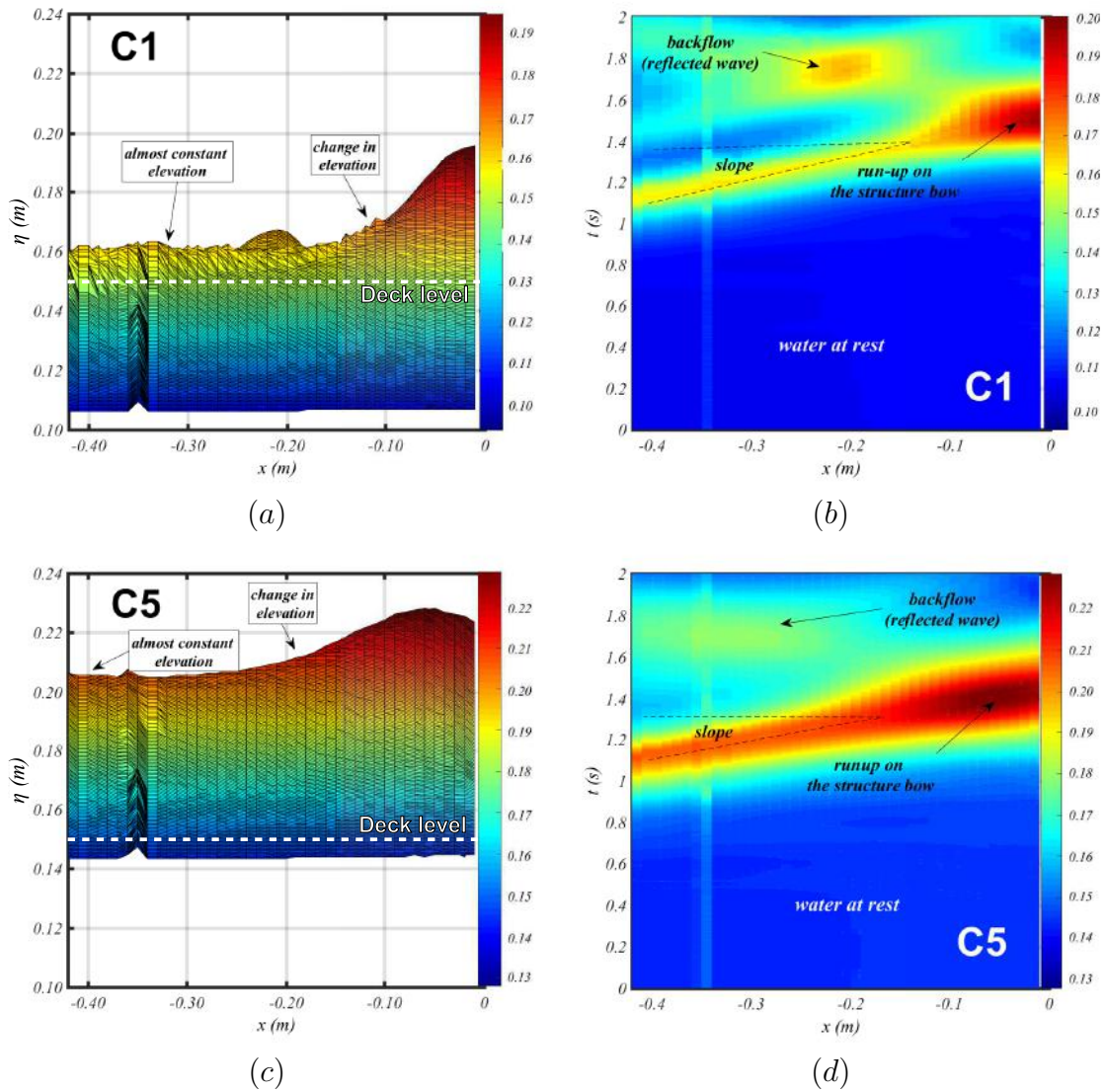


Figure 4.9: Incoming wave evolution for Cases 1 and 5. (a) Case 1: η vs x . (b) Case 1: t vs x . (c) Case 5: η vs x . (d) Case 5: t vs x .

Influence of the structure on wave propagation

From the visualization of the incoming wave evolution presented before, it is evident that the structure has an effect on the wave elevations approaching the structure for

each case. Such an effect can be verified by comparing time series of the experiments carried out with and without the structure. Regarding this, Figure 4.10 shows water elevation time series at several positions ($VW Pw01 - VW Pw42$) for the Case 1, obtained from the experiments with (Fig. 4.10a) and without the structure (Fig. 4.10b).

Note that the case with structure (Fig. 4.10a) clearly presents the increase in water elevations at probes located closer to the fixed structure. Conversely, in the case without structure (Fig. 4.10b), it is evident how the wave propagates with almost an almost unchanged maximum elevation until backflow is observed due to the reflexion caused by the tank wall.

The influence of the structure on the increase of the amplitudes and backflow effects are better illustrated in Figs. 4.10c and d, which show the evolution of the maximum values of the incoming wave (t vs x plot) for the cases with and without structure, respectively. From these graphs, notice that for the case with structure (Fig. 4.10c), the increment in the wave elevations started from $x \approx -0.1$ m at $t \approx 1.4$ s. Then, there is observed a considerable region of maximum values due to backflow caused during bow run-up by the structure (i.e., reflected wave) for $t \gtrsim 1.6$ s at $x \approx -0.2$ m. By contrast, for the case without structure (Fig. 4.10d), the regions of maximum elevations verified in Fig. 4.10c for the incoming wave and backflow are not observed. Instead, continuous color regions for the incident (forward-advancing wave) and the backflow are observed, which suggests that the incident wave propagates with almost constant elevation and velocity. Parallel to the colored region representing the incident wave, it is possible to visualize the backflow region, which is formed due to the reflection of the tank wall. It can be confirmed that the peak values observed in Fig. 4.10c are not observed. Then, it is confirmed the formation of a reflected wave of significant amplitude in the case considering the structure, due to the bow run-up stage of shipping water.

The influence of the structure in the water elevations time series can be verified with more details in the comparisons shown in Figs. 4.11 and 4.12. These figures present the water elevations (mean and standard deviation from repetitions) obtained from virtual wave probes located at $x = -0.1, -0.2, -0.3$ and -0.4 m (considering the bow edge of the structure as the origin) for the Cases 1 and 5, respectively. Data from the experiments with and without the internal structure have been compared.

For the Case 1, corresponding to the case with the highest freeboard ($FB = 0.042$ m, Fig. 4.11), it can be observed in Fig. 4.11a that the case without structure presents an initial water elevation that rised up until attaining a peak, then , it decreased forming a following second peak. It can be verified in the comparison that there is a similarity in the initial stages of the time series ($0 \text{ s} < t \lesssim 1.25 \text{ s}$) of

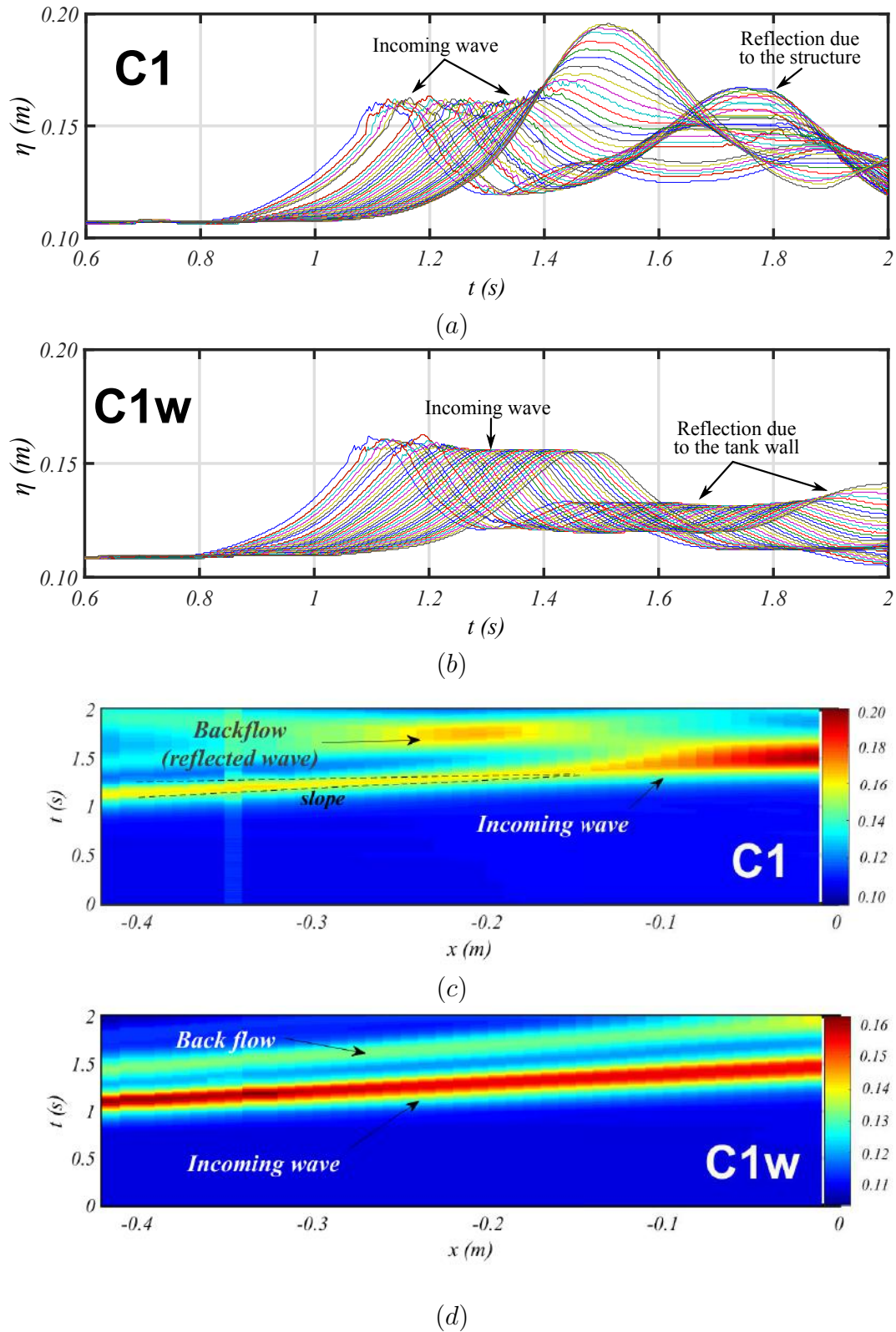


Figure 4.10: Influence of the structure on the incoming wave evolution for Case 1 at several VWPs. (a) η vs t : case with structure. (b) η vs t : case without structure. (c) t vs x : case with structure. (d) t vs x : case without structure.

the cases with and without the structure. However, when the first peak appears, it is presented a difference in the mean maximum values of these time series of

approximately 0.016 m and a shift in time of about 0.036 s in the maximum values. After the first peak, the trend of the signal for the case with structure did not form the second peak observed in the case without structure, then, its trend was not attained.

At $x = -0.2$ m (Fig. 4.11b), there is a better agreement between signals. The maximum values of the first peak of both cases are closer than at $x = -0.1$ m. The spatial and temporal shifts of the maximum values were $\Delta\eta \approx 0.004$ m and $\Delta t \approx 0.012$ s, respectively. This indicates less influence by the structure; however, it can be observed the effect (increase) caused for the second peak at this position, which may be related to the reflected wave by the structure.

For $x = -0.3$ m (Fig. 4.11c), $\Delta\eta \approx 0.002$ m and $\Delta t \approx 0.002$ s were verified for the first peak, which suggests a better agreement between the trend of signals. It is also observed in this case that the elevations for the case with structure attained the cave of the case without structure.

Finally, at $x = -0.4$ m, the closest agreement is observed between both signals. They were observed differences of $\Delta\eta \approx 0.002$ m and $\Delta t \approx 0.002$ s for the first peak values. For the second peaks formed at both signals, $\Delta h_m \approx 0.003$ m and $\Delta t \approx 0.028$ s, were presented. After the second peak the values of both signals were not attained.

For the Case 5 (Fig. 4.12), concerning the case with lower freeboard ($FB \approx 0.006$ m), differences in the water elevations for cases with and without structure were also observed, depending on the VWP distances, as verified for the Case 1. However, for this case, the time series for the case without structure was different from that of Case 1. At the different positions ($x_1 - x_4$), such time series presented a well-defined first peak, in contrast as observed in Case 1, which presented two well defined consecutive peaks. As observed in Case 1, the agreement between the time series for the cases with and without structure was improved as the distance from the structure increased. At $x = -0.1$ m (Fig. 4.12a) and $x = -0.2$ m (Fig. 4.12b), the mean maximum values of the case with structure overestimate the case without structure ones in approximately 10% and 4%, respectively. A $\Delta t \approx 0.044$ s between the maximum values was observed in both cases. Furthermore, at distances $x = -0.3$ m (Fig. 4.12c) and $x = -0.4$ m (Fig. 4.12d), the mean maximum values for both signals were in closer agreement, attaining shifts in time of ~ 0.044 s and ~ 0.026 s, respectively. For the last comparison ($x = -0.4$ m), only the trend of the peak of the signal (from the rising limb to the decreasing limb) was well attained, presenting a notable difference with the second peak.

The presented results demonstrate that there was a considerable influence of the structure on the incoming wave. This influence was more notable as the wave approached the structure.

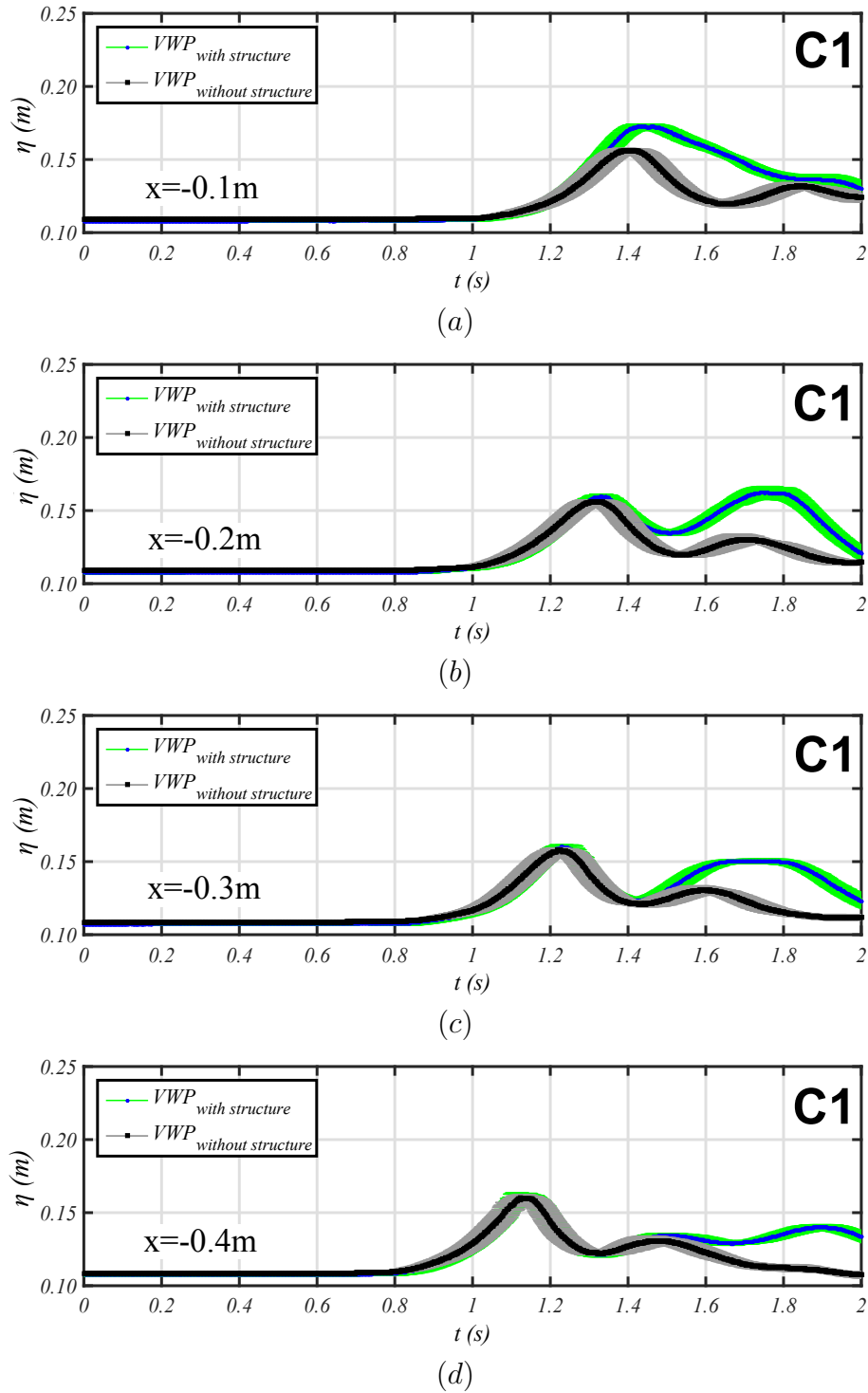


Figure 4.11: Influence of the structure on the incoming wave water elevation time series in experiments with and without the fixed structure for Case 1. The bow edge of the structure is considered as the origin. (a) $x = -0.1$ m. (b) $x = -0.2$ m. (c) $x = -0.3$ m. (d) $x = -0.4$ m.

The increment in the water elevation at regions near the fixed structure may be partially attributed to the bow run-up of the water with the structure. During this run-up interaction, there is a change of momentum in the incoming wave in the

horizontal direction that generates the backflow, as observed by the second peak in the time series data, which may be of significant amplitude if it is compared with the amplitude of the first peak observed.

The behaviour observed in the comparisons was also presented in the other cases of study (Cases 2-4), of course, with different spatial and temporal shifts in maximum values, and different trends for the subsequent peaks. In next subsection, the limits of influence of the structure to estimate the wave kinematics are analyzed.

Incoming wave kinematics

In this section, kinematic parameters of the incoming wave are obtained from experimental data and compared with the analytical theory of STOKER [8]. These parameters are of importance to know the relations between the incoming wave and the shipping of water, as further described in next sections. To begin with the analysis, it is important to know the limit of influence of the structure in the incoming wave. This was accomplished by estimating the maximum elevation values for each case, along the spatial domain for the bore propagation (from $x = -0.4$ m to $x = -0.010$ m), considering the bow edge as the origin, as observed in Fig. 4.13. In the figure, they are shown the mean and standard deviation values obtained experimentally for each study case, and the corresponding theoretical values obtained from STOKER [8].

Figure 4.13a presents the values for the experiment without structure. From this figure, it can be observed that the wave propagates keeping an almost constant elevation. Note that at this part of the tank ($-0.4 \text{ m} < x < 0 \text{ m}$), once the wave has been completely developed, the experimental values overestimated the theoretical ones. For all cases, there was a difference of about 0.020 m between the experimental and theoretical values. It may be related to the shape attained by the well developed bore, as analyzed previously in Section 4.1.1.

Figure 4.13b shows the maximum values for the experiment with structure. Differently from the case without structure, it can be clearly observed the influence of the structure for each case. As described in last section, there is a region where the elevations started increasing from the almost constant wave amplitude, as the wave approached the structure. In the figure, they have been defined five positions ($[A, B, C, D, E], [-0.01, -0.1, -0.2, -0.3, -0.4] \text{ m}$) in order to analyze the influence of the structure. For all cases, it seems that the region defined by points E and D corresponded to a domain in common that contains similar information (i.e., constant wave elevations) as the experiment without structure (see for instance \overline{ED} Fig. 4.13a), despite of differences of some millimetres. In this domain, the difference between the theoretical and experimental values was also about 0.020 m.

On the other hand, for the region defined by the limits D and C it is notable

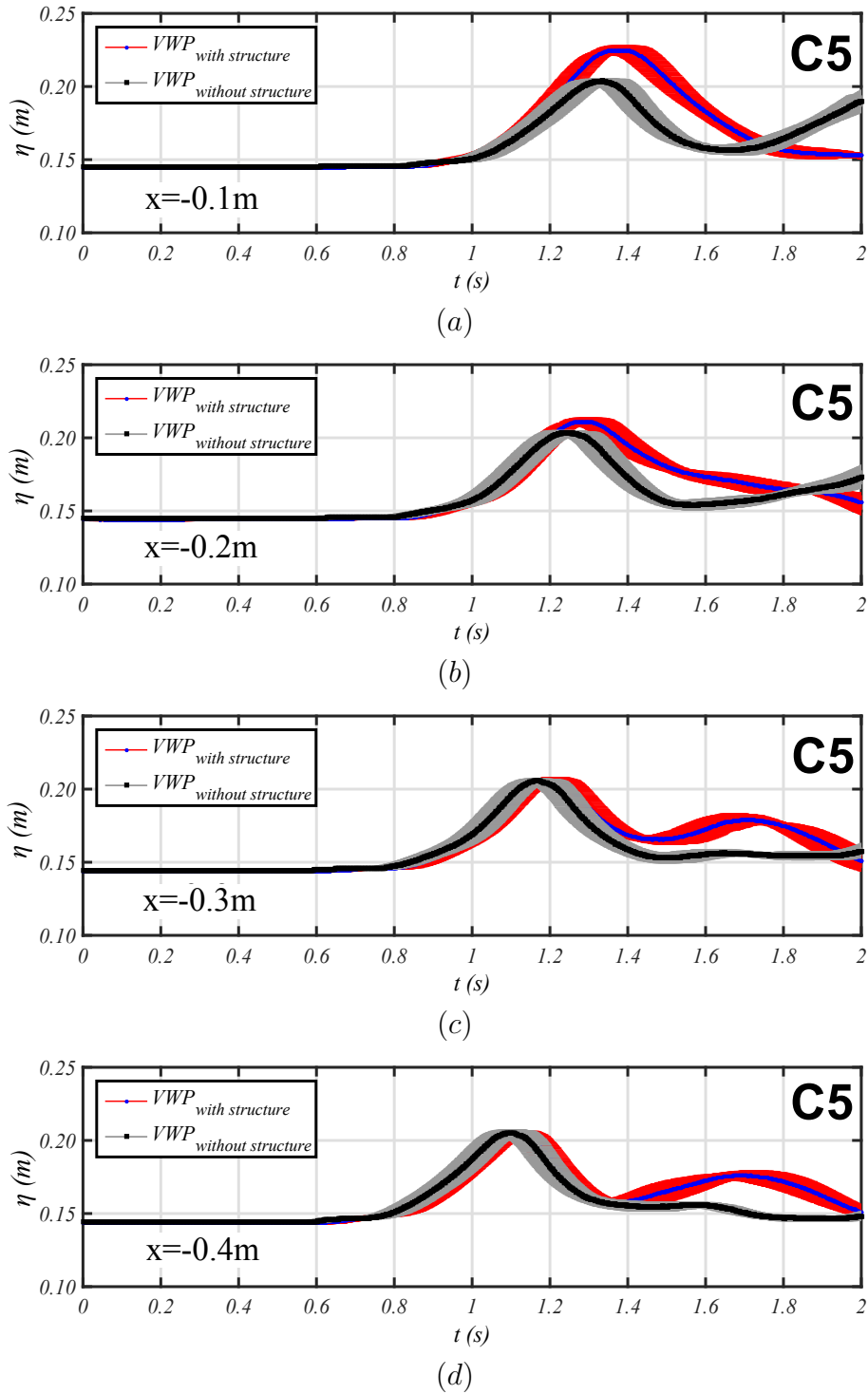


Figure 4.12: Influence of the structure on the incoming wave water elevation time series in experiments with and without the fixed structure for Case 5. The bow edge of the structure is considered as the origin. (a) $x = -0.1$ m. (b) $x = -0.2$ m. (c) $x = -0.3$ m. (d) $x = -0.4$ m.

that elevations start increasing for Cases 3 to 5. Then, for the region defined by C and B , the points of change in maximum elevations may be observed for all cases.

The region defined by E and D was chosen to experimentally calculate the wave

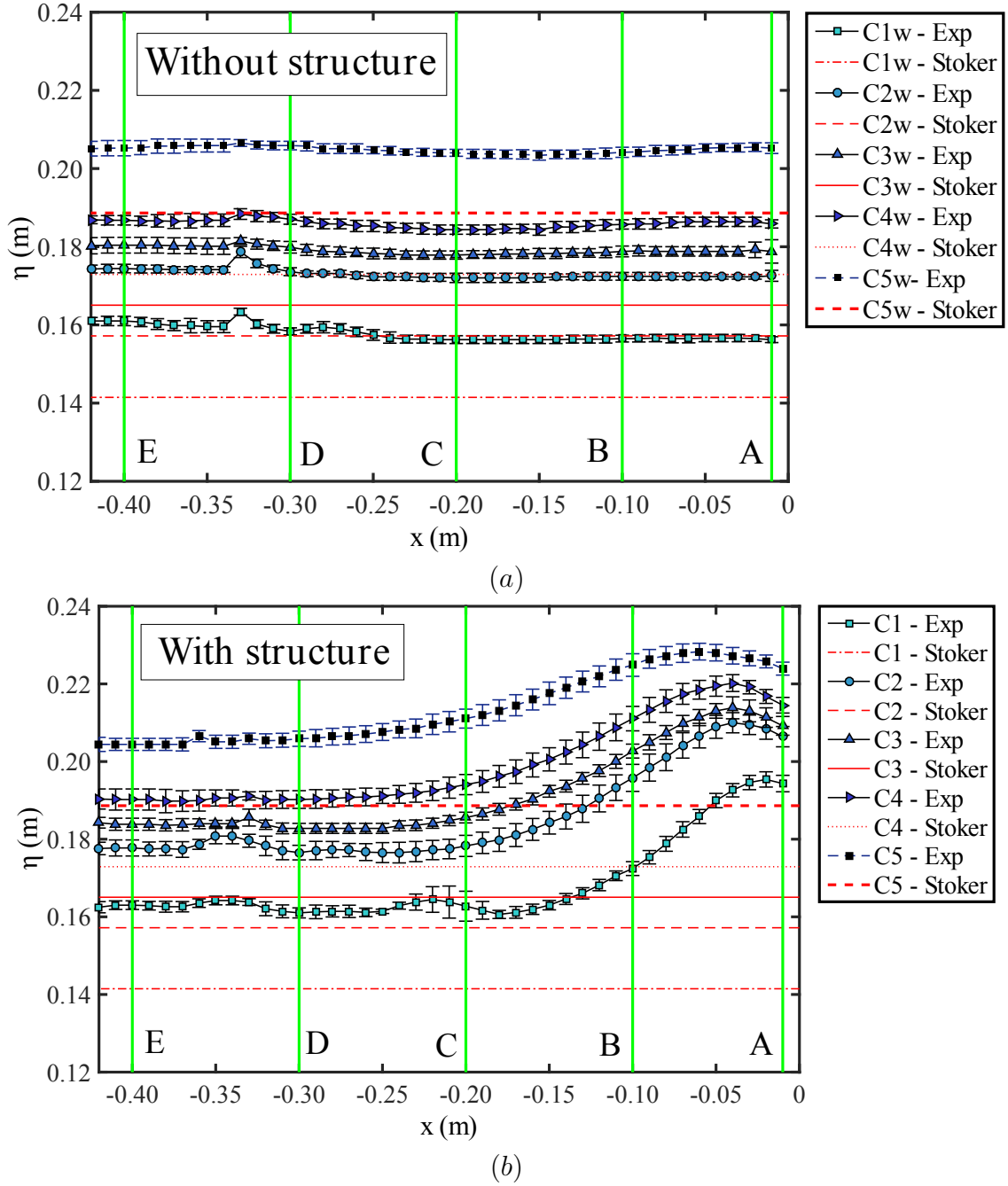


Figure 4.13: Maximum water elevations of the incoming wave (η , mean and standard deviation) at different positions (x) for the five cases considered. (a) Experiment without the fixed structure. (b) Experiment with the structure.

velocity for the case without structure, using the mean maximum values at E and D , and the points in time at which these values occurred.

The mean and standard deviation values of the horizontal wave velocity from points E to D ($\overrightarrow{U_{ED}}$) for the experiment without structure are shown in Fig. 4.14 for all the cases. In the figure, the front velocities given by Stoker theory ($U_{0-Stoker}$) are also shown for comparison. It can be observed a close agreement between the mean experimental velocities and the theoretical ones. All the velocities ranged between

$1 \lesssim U_0 \lesssim 1.5$ m/s. These velocities increased from Case 1 to Case 5, with theoretical velocities from 1.26 m/s to 1.46 m/s, respectively, whereas experimental values of $\overrightarrow{U_{ED}}$ ranged from 1.17 m/s up to 1.33 m/s for these cases.

Table 4.2 summarizes the values obtained. Notice that, for the case without the structure, there are differences of 7% and 9% between the mean experimental values and the theoretical ones for Cases 1 and 5, respectively, which are considered in close agreement.

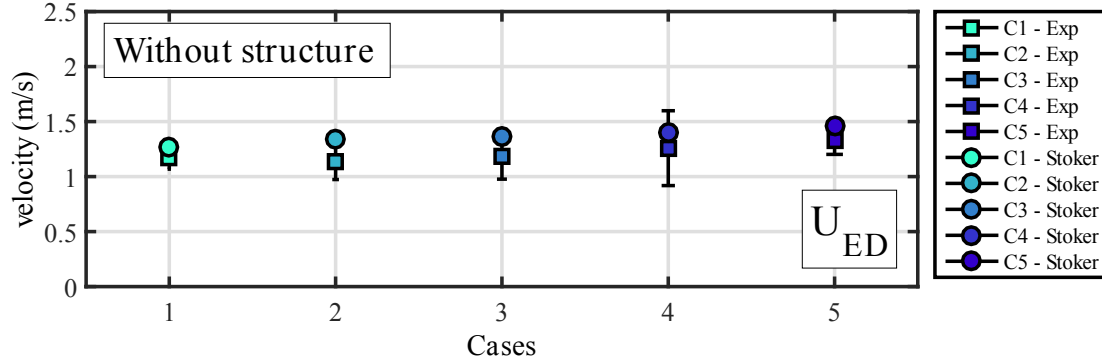


Figure 4.14: Comparison of the incoming wave crest horizontal velocity (U_{ED}) for the experimental setup without structure and the Stoker's approach (U_0).

Once the mean crest velocities of the wave from theory and the experiment without structure are known, it is possible to verify the differences found with the experiment with structure. Figure 4.15 presents these results, which were obtained from the limits A to E shown in Fig. 4.13.

Generally, it can be noted that mean value results in all regions followed the tendency defined by the theoretical values, that is, mean crest horizontal velocities increased from Case 1 to 5.

On the whole, it can be noted that for all cases, most of the results are into the range of velocities from 1 m/s to 1.5 m/s, approximately.

A summary of mean values and respective standard deviations for all the domains defined by points A to D are shown in Table 4.2. Notice that mean values for the region \overline{ED} overestimate even more the theoretical values than the values obtained for the same region in the case without structure. In relation to the Stoker values, mean \overline{ED} values for the case with structure overestimate the theoretical ones in 26% and 14% for Cases 1 and 5, respectively. This suggests that the presence of the structure reduced the crest horizontal velocity in the less influenced region (\overline{ED}). From the mean experimental values, this difference was presented in a reduction of $\approx 20\%$ and $\approx 5\%$ respectively for Cases 1 and 5, in relation to the cases without structure.

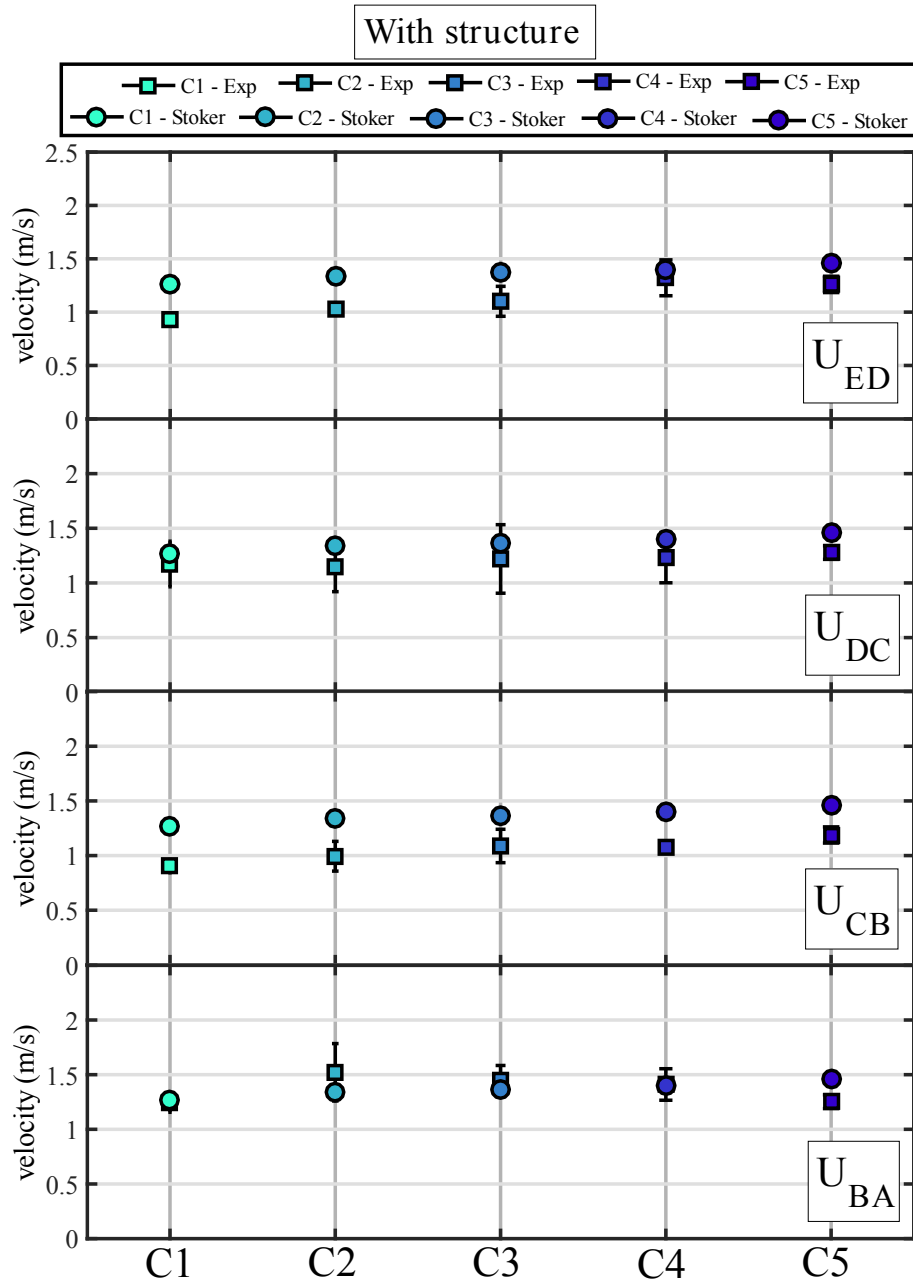


Figure 4.15: Incoming wave crest horizontal velocities for the experimental setup with the internal structure, for regions defined by points A-D. Results obtained with the Stoker's approach for U_0 are shown for comparisons.

4.2 Shipping water

This section presents the experimental results corresponding to the shipping water, which includes the water elevation variation, the kinematics of water on deck and the resultant vertical loading for the five study cases. Relevant information for these parameters was obtained by means of conventional sensors (i.e., wave probes, accelerometers and load cells) and image-based procedures, already described in Section 3. At first, the types of shipping water are identified in a qualitative manner for

Table 4.2: Statistics of incoming wave crest horizontal velocities in different regions for the experiments with and without the structure, and theoretical values from Stoker’s approach.

Case	$U_{0-Stoker}$ (m/s)	WITHOUT ST.		WITH ST.							
		\bar{U}_{EDmean} (m/s)	\bar{U}_{EDsd} (m/s)	\bar{U}_{EDmean} (m/s)	\bar{U}_{EDsd} (m/s)	\bar{U}_{DCmean} (m/s)	\bar{U}_{DCsd} (m/s)	\bar{U}_{CBmean} (m/s)	\bar{U}_{CBsd} (m/s)	\bar{U}_{BAmean} (m/s)	\bar{U}_{BASd} (m/s)
1	1.27	1.18	0.11	0.93	0.04	1.17	0.21	0.90	0.06	1.24	0.08
2	1.33	1.14	0.16	1.03	0.05	1.14	0.22	0.99	0.14	1.52	0.26
3	1.37	1.19	0.21	1.10	0.14	1.22	0.31	1.09	0.15	1.45	0.13
4	1.40	1.26	0.34	1.32	0.17	1.23	0.23	1.07	0.04	1.41	0.14
5	1.46	1.33	0.13	1.26	0.08	1.28	0.06	1.19	0.07	1.25	0.06

all the study cases. Secondly, the evolution of shipping water elevations is treated in a similar way as done in Section 4.1.2, where temporal and spatial distributions were presented for the incoming wave. Next, the shipping water kinematics is examined in order to know typical front velocities for each case and relationships with the kinematics of the incoming wave. Finally, the generated loading on deck and dynamic effects during the experiment are analyzed at the end of the section.

4.2.1 Shipping water events

As defined in previous sections, for the present study five different conditions for the incoming wave interacting with the structure were analyzed. That is, five different freeboards originated the development of five different single waves (bores) using the same ratio of the wet dam-break approach ($h_0/h_1 = 0.6$). Concerning this, five different scenarios of shipping water were obtained due to the combined effects of freeboard and wave steepness for each case.

Main stages of the shipping water events for Cases 1, 3 and 5 (chosen as representative of the other cases) are respectively presented in Figs 4.16, 4.17 and 4.18. These figures show snapshots of flow at different points in time, including the initial (bow run-up) and final (backflow) stages of shipping water. In all the figures, the first image corresponds to the initial condition for each case, from which the freeboard can be observed. Then, snapshots are shown at intervals of 0.06 s, from the instant at which the water level reached the deck level, that is, during the runup stage that occurs at the bow, to the stage where backflow is presented.

For the Case 1 (Fig. 4.16), a very small plunging wave shipped at the bow forming a small cavity. Then, a forward and a backward small water jets were formed as the wave crest approached the deck. When the wave crest was over the bow edge, the cavity started being trapped by the flow while a layer of fluid was observed propagating over the deck. Next, the wavefront of the shipped flow interacted with the vertical wall of the tank, causing run-up on it. After the run-up occurred,

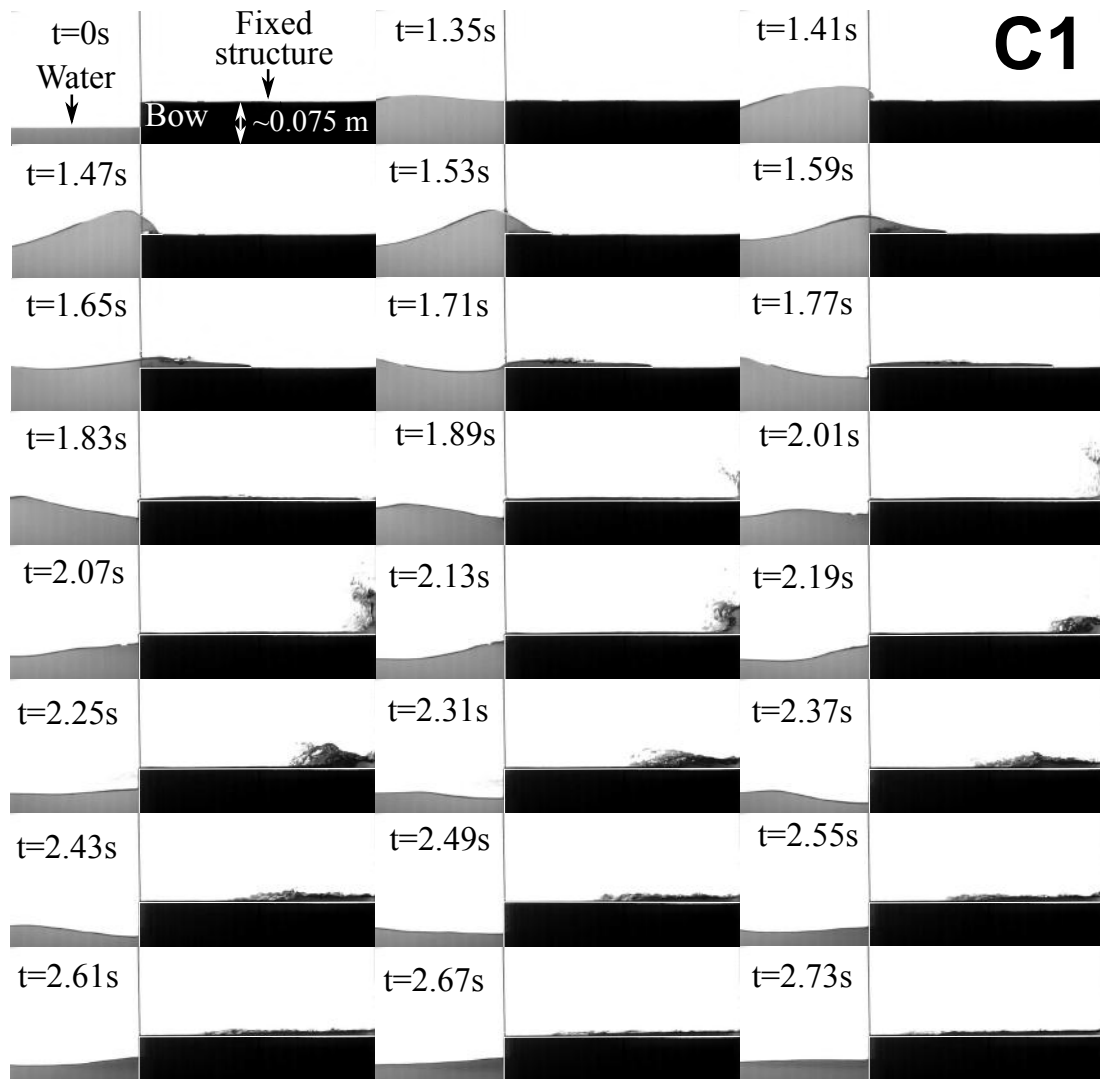


Figure 4.16: Representative snapshots of shipping water for Case 1.

water fell down influenced by gravity action, yielding and a turbulent flow moving backward onto the deck, returning to the reservoir of water.

Similar patterns as the ones found in the Case 1 were observed in the Case 3 (Fig. 4.17); however, they are mainly differentiated by a larger amount of water over the deck, which yielded a thicker layer of water, and a more significant run-up and backflow phenomena. Furthermore, a cavity was also formed at the beginning of the deck, but it was smaller than the one observed in the Case 1.

Finally, the Case 5 (Fig. 4.18) presented the largest volume of water over the deck, maintaining similar patterns in relation to Cases 1 and 3. In Case 5, the run-up and backflow were more significant than in previous cases. However, the cavity formed at the bow edge was not observed.

Results indicate that all the events of shipping water presented similar patterns in their main stages (i.e., flow propagation and run-up trends). However, these are mainly differentiated by the resultant amount of water onto the deck and the

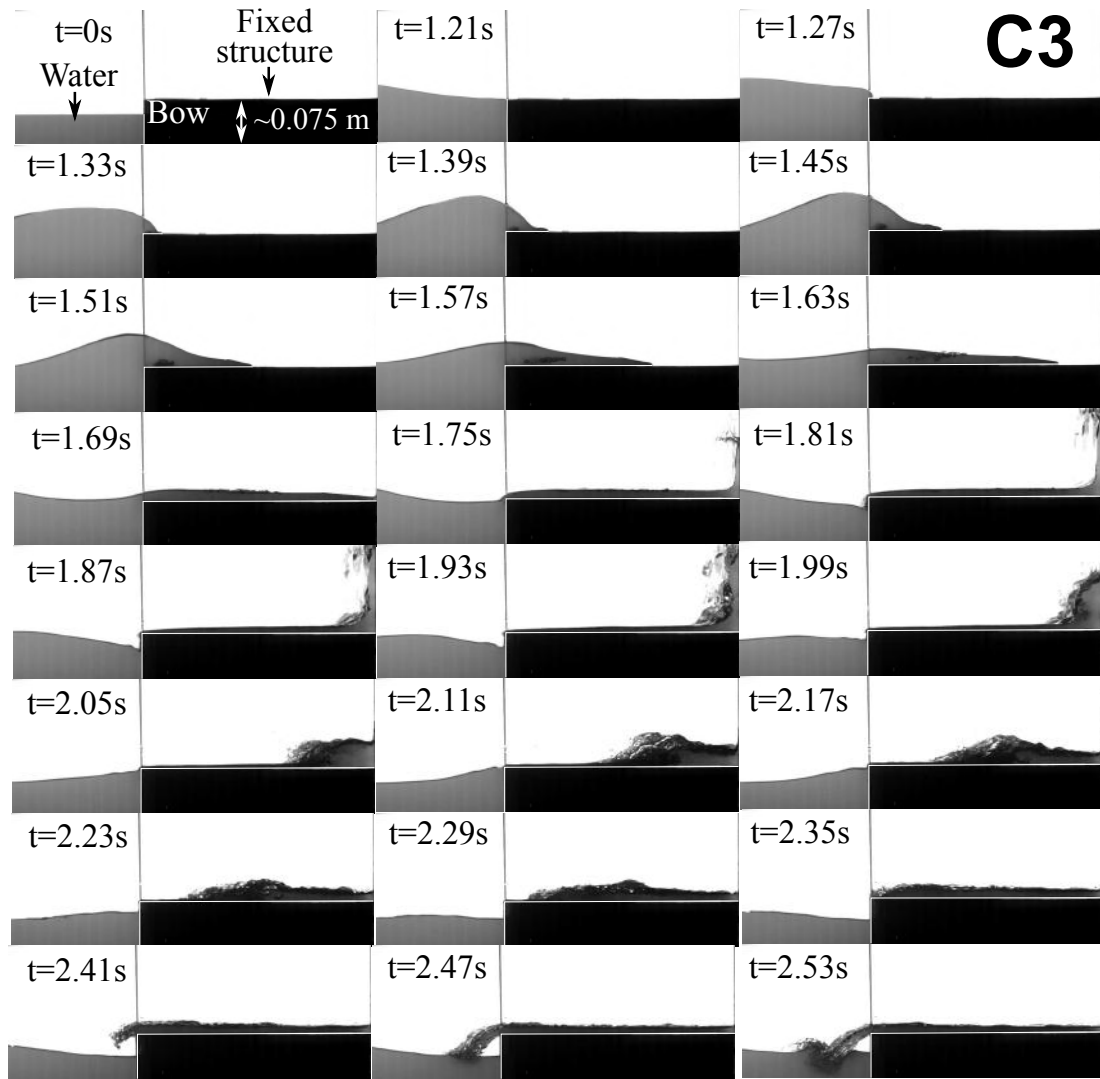


Figure 4.17: Representative snapshots of shipping water for Case 3

formation of a small cavity at the bow edge.

The differences between the initial stages of the shipping water between the cases analyzed can be better verified in the Fig 4.19. The snapshots located at the left side of the figure show the initial stage of water invading the deck for the three cases at different times. Notice that the Case 1 (Fig 4.19a) presented an small cavity formed by the plunging wave. Unlike, for the Case 3 (Fig 4.19c) the cavity also appeared but it was smaller. Then, for the Case 5 (Fig 4.19e) the cavity is not observed. So, it can be noted that the size of the cavity increases as the freeboard also does.

Additionally, the snapshots located at the right side (Figs 4.19b, d and f) represent stages that occurred 0.16 s after the stages shown in the left side. In these images, the differences in the amount of water can be verified for each case. Also, it can be inferred from the position of the wavefront that Case 1 presented a faster horizontal velocity over the deck than the other cases. Thus, it can be defined with the present approach that the wave front velocity increases as the freeboard also

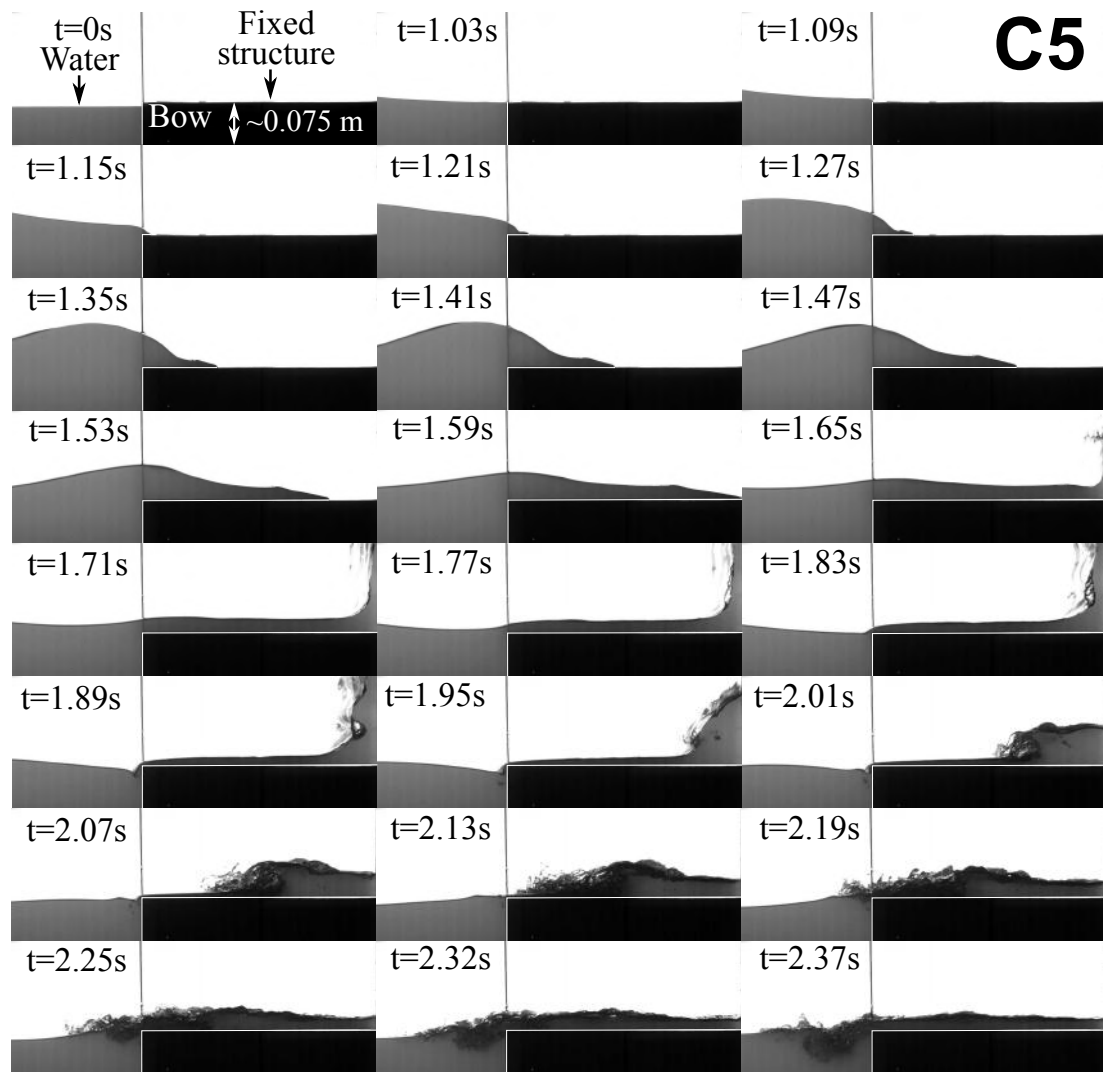


Figure 4.18: Representative snapshots of shipping water for Case 5

does, regardless of an smaller volume of water onto the deck.

Results showed that the wet dam-break approach allowed generating five different cases of shipping water onto the deck, produced by five different waves, which were modified mainly by the freeboard of the structure. They also showed that the wave steepness and freeboard are related to the generation of different sizes of cavities at the bow edge and to the increase of the shipped volume of water onto the deck. These aspects were also identified by HERNÁNDEZ-FONTES *et al.* [4, 5] who observed the freeboard influence with shipping water events generated using the wet dam-break approach in a smaller installation.

Regarding the shipping water events definition made by GRECO *et al.* [3] and HERNÁNDEZ-FONTES *et al.* [4, 5], the shipping water events found in this study may be classified as dam-break (DB) and small-scale plunging-dam-break (PDB) types.

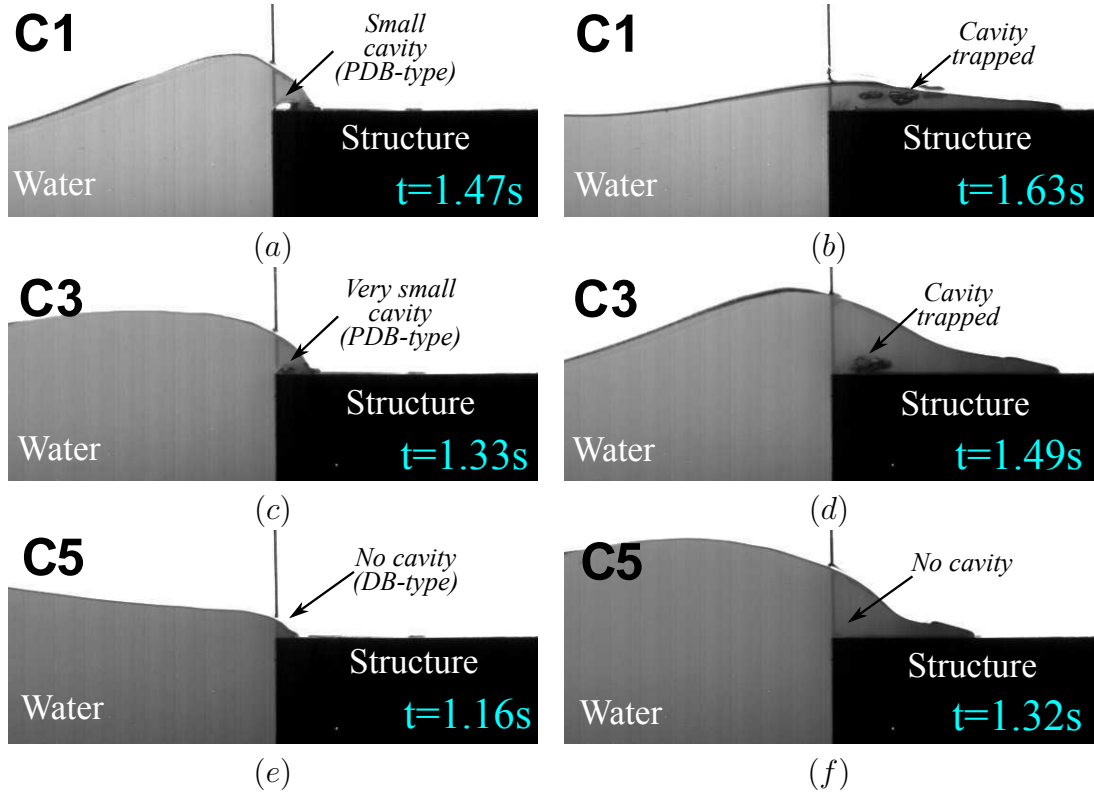


Figure 4.19: Initial stages of shipping water at bow of the structure. (a,b) Case 1. (c,d) Case 3. (e,f) Case 5.

4.2.2 Shipping water evolution

VWPs validation

The validity of the binary-image-based methodology used to capture the water elevations on deck of the structure was verified with time series of conventional wave probe sensors, in a similar way as it was done for the incoming wave. Then, it was applied to measure the water evolutions at different positions over the deck (see Fig. 3.3). Regarding this, Figure 4.20 shows the comparison of the time series of water elevations (η , mean and standard deviation values) obtained with the virtual wave probe (VWP0d) and the respective conventional wave probes (WP1 and WP2), which are located very close to the deck edge ($\approx 2\text{mm}$). Figures 4.20a and b present the comparisons of these series for the Case 3 and 5, respectively. It should be noted that these series represent the freeboard exceedance of the incoming wave.

Small spatial and temporal shifts can be observed in the comparisons, which indicate the good agreement between data considering the range of uncertainty already described for the wave probes calibration and image processing. Analyzing the peak values between WP1 and WP2 (i.e., the conventional probes), we found $\Delta\eta \approx 2\text{ mm}$ and $\Delta t \approx 0.002\text{ s}$ for both cases. Thus, small three-dimensional effects of 3.5% and 3.3% can be inferred for Cases 3 and 5, respectively. Moreover, it is

clear that the VWPs presented a close agreement with the WPs. These attained the peak values in a close way ($\Delta \approx 0.002 - 0.003$ m) and followed the complete trend of the signal along time. These aspects were also observed for the other cases.

From the results obtained in the comparisons of WPs with VWPs, it was verified the potential of the image-based method to measure the evolution of water on deck. Thereby, this was analyzed by two-dimensional reconstruction, using the image based method described before.

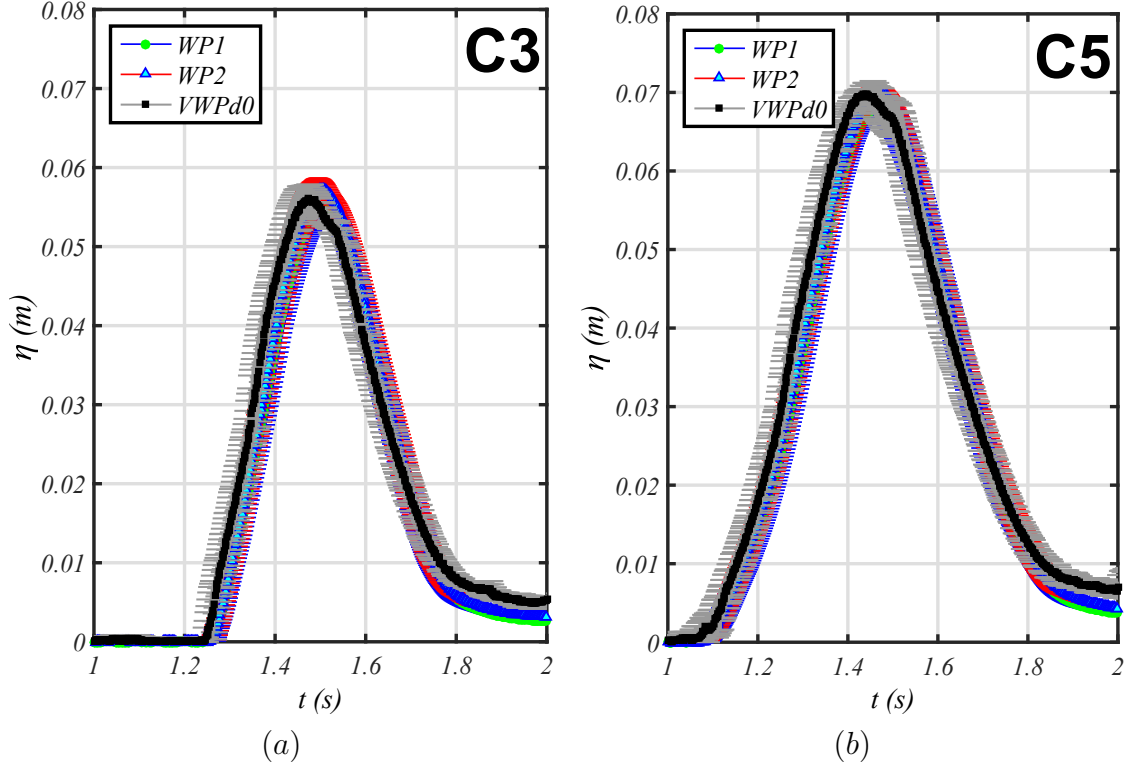


Figure 4.20: Comparison of time series of water elevations (η , mean and standard deviation values) between WP1, WP2 and VWPd0. (a) Case 3. (b) Case 5.

Shipping water elevations

Once the incoming wave interacted with the bow of the structure (horizontal impact and bow run-up stage), an amount of water shipped and propagated onto the deck. This amount of water is affected by characteristics of the incident wave (e.g., wave steepness), freeboard or shape of the structure. Then, as defined in previous sections, in the present study the resultant water-on-deck behaviour is mainly due to the wave steepness and the different freeboards, maintaining the same geometry of the structure.

In order to examine the evolution of water on deck, virtual wave probes located along the deck, separated at a distance of 0.010 m, considering the deck edge as the origin of the coordinates system (see Section 3.3), have been used. This allowed to

reconstruct the spatial and temporal evolution for the five study cases.

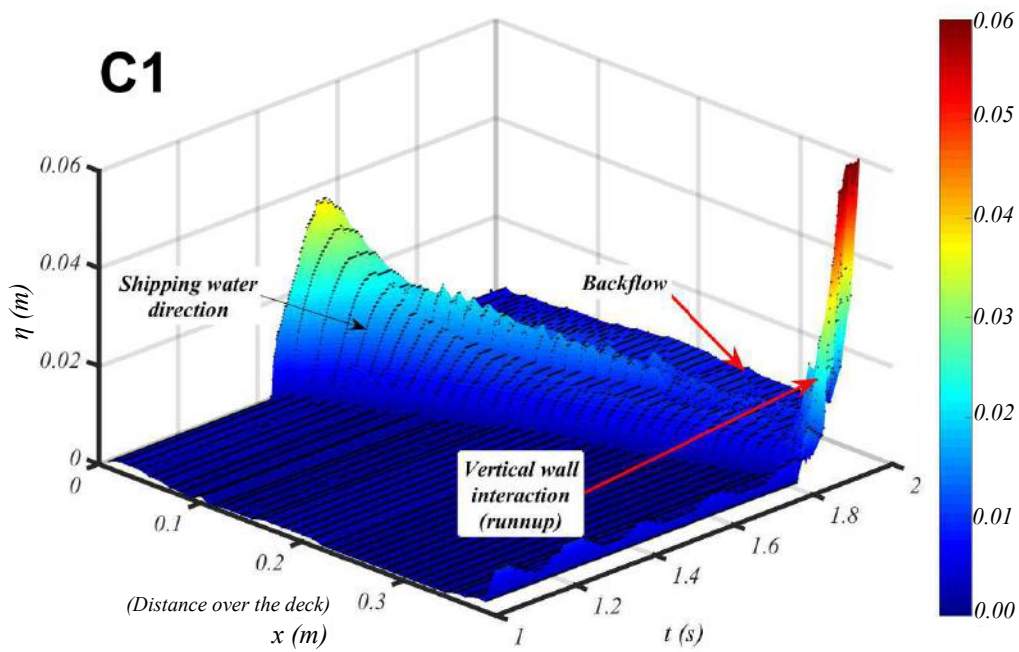
Figures 4.21a and b shows two of the 2D reconstructions, corresponding to the Cases 1 and 4, respectively. In these images, three main stages can be identified: First, the deck was completely dry ($\eta = 0$) until a finite amount of water invaded the deck and propagated to its end ($x = 0.392$ m), where the vertical wall of the tank is placed. Secondly, the water interacted with the vertical wall causing run-up. Finally, the water in the run-up stage fell down by action of gravity and backflow occurred on the deck of the structure. The amount of water differed for each case of study, being larger for the Case 5 (lower freeboard) and smaller for the Case 1 (higher freeboard).

Alternatively, Figure 4.22 presents a different visualization of the shipping water propagation, considering plots of time against distance over the deck. The plots, regarding an scale for the water elevations from 0 to 0.08 m for Cases 1, 2, 4 and 5, are shown in Figs. 4.22a,b,c and d, respectively.

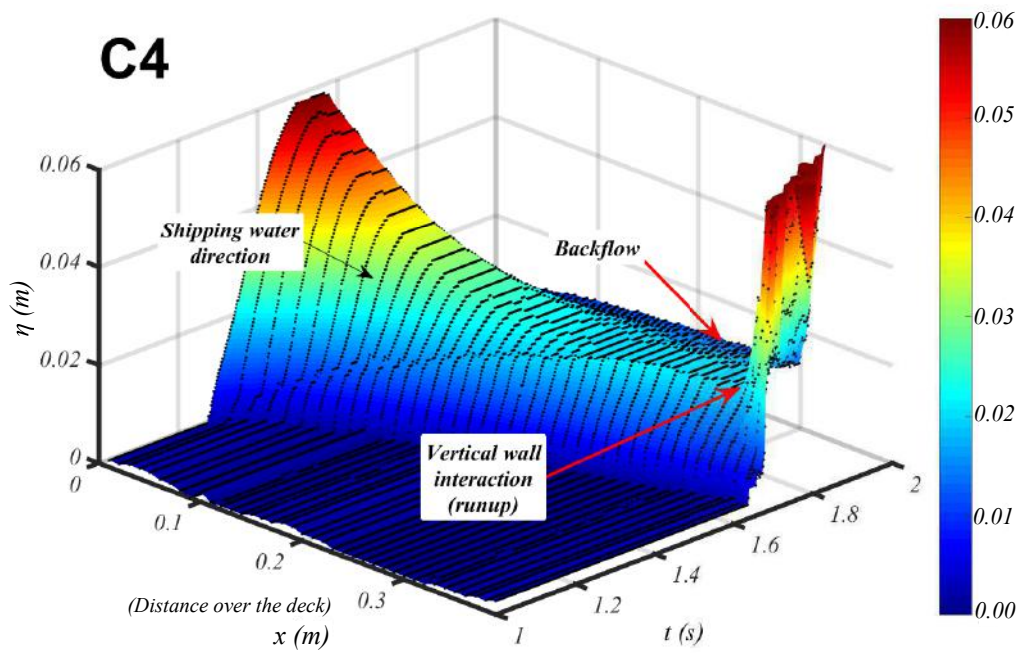
In all figures, it can be observed that the significant water elevations at the beginning of the deck (water entry region), characterized by different colors, correspond to the maximum freeboard exceedance elevations of each case. Concerning the same spatial scale, it can be verified that the freeboard exceedance increased from C1 to C5. The water entry elevations tended to decrease for farther distances in relation to the bow edge ($x > 0$). For $0.35 \leq x \leq 0.40$ m, they are observed the regions where the run-up on the tank wall occurred at different times for each case (see the saturated regions). After such stages, backflow can be observed on the deck; however, it has to be considered that the image-analysis method was not developed to capture broken waves during and after this run-up stage. Despite of such a limitation of the image based method to capture turbulence, the information presented may help to suggest that the backflow on the deck might be significant in the loading on deck, as inferred from the high elevations captured from experiments just after the run-up. The analysis of water evolution and related loading due to backflow is out of the scope of this thesis; however, it is an important topic that should be investigated in further research.

Freeboard exceedance consideration

One of the most important parameters in the analysis of shipping water events is the freeboard exceedance, or the effective water elevations from the incident wave that represent the volume of water that ships onto the deck. These are commonly measured at the beginning of the bow deck of the structure ($x = 0$). However, for prediction purposes, they can also be measured at a distance outside the bow edge of the deck. For example, in ocean basin experiments, a common practice consists in installing a wave probe at some millimetres out the bow edge to measure the relative

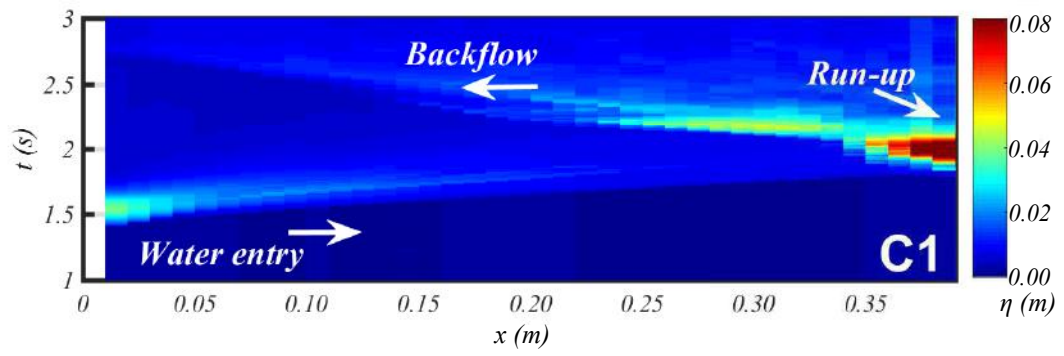


(a)

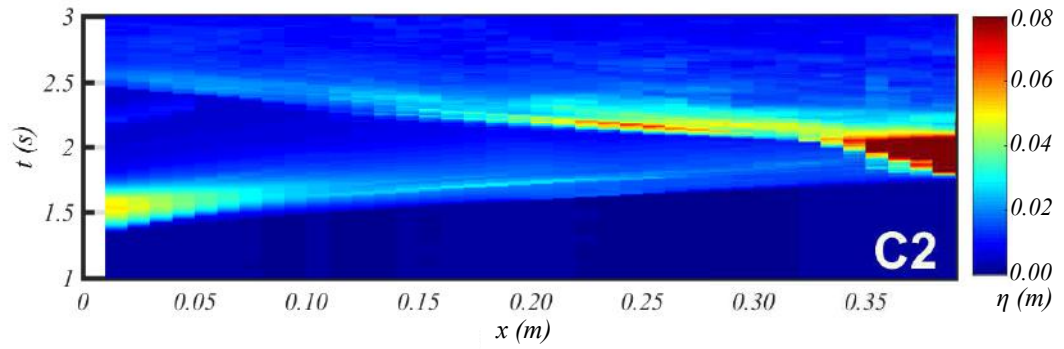


(b)

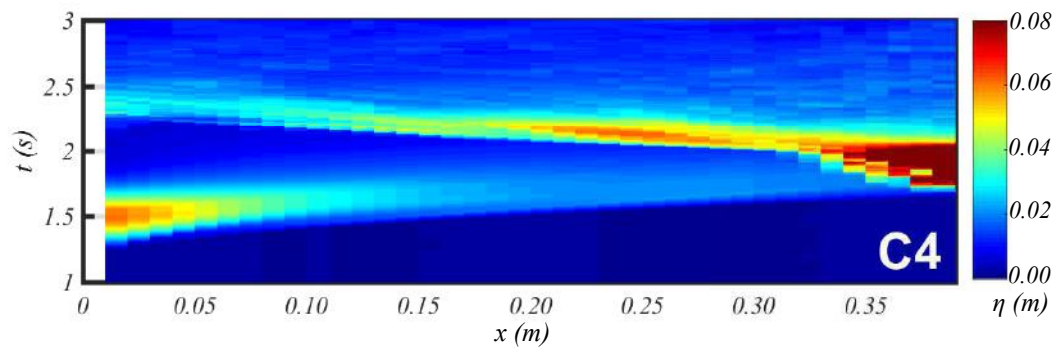
Figure 4.21: 2D reconstruction of the shipping water evolution on deck (η vs x and t). (a) Case 1. (b) Case 4.



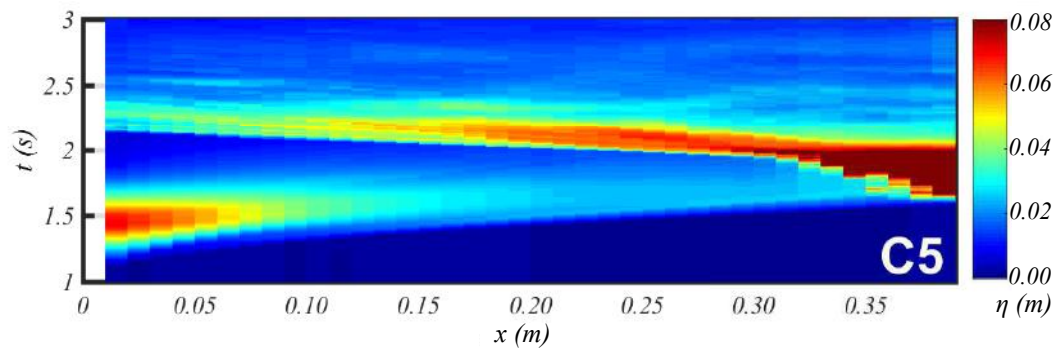
(a)



(b)



(c)



(d)

Figure 4.22: Shipping water evolution (t vs x). (a) Case 1. (b) Case 2. (c) Case 4. (d) Case 5.

bow-wave motions. Thereby, the freeboard exceedance can be estimated from these data.

In this study, the conventional wave probe located at $x = 0.002$ m from the bow edge (see Fig. 3.8, Section 3.3) interfered with the image processing at $x = 0$. Thus, we obtained VWP's time series outside the deck (VWPw0, $x = -0.005$ m) and on the deck (VWPd0, $x = +0.005$ m) because these positions were suitable for the image analysis, to measure freeboard exceedance. Concerning this, we made a comparison between the resultant VWP time series obtained from VWPw0 subtracting the structure height (i.e., $VWPw0 - D$, with D as structure height) and the time series measured on the deck (VWPd0).

The comparisons between the freeboard exceedance, measured at $x = +0.005$ m and $x = -0.005$ m for Cases 1,2,4 and 5, are shown in Figs. 4.23a,b,c and d, respectively. The time series include the mean and standard deviation values estimated from all the repetitions. It is observed that for all cases, the trend of both series is very similar, despite of very small shifts on time between them and some differences in water elevations, mainly at the tail of the curves because of the remained layer of water over the bow. Considering the time at which the water elevations started rising, the shifts in time were about 0.03 s for Cases 1 and 2, and 0.04 s and 0.07 s for Cases 4 and 5, respectively, which are assumed small for the present application.

It is important to mention that the maximum value of these series is known in shipping water studies as the maximum freeboard exceedance (η_0), and it is one of the most common parameters used in the implementation of analytical models to examine the shipping water evolution on decks of structures (e.g., GODA e MIYAMOTO [14], BUCHNER [34]).

For the cases 1 and 2, the maximum freeboard exceedance of the $VWPw0 - D$ time series overestimated that of VWPd0 in approximately 7%, whereas for the cases 3 and 4, the overestimation is approximately 4%. However, it is important to highlight that the maximum values presented a very small shift in time, which ranged from 0.002 s to 0.004 s for all cases, suggesting that maximum values occurred almost at the same time.

Disregarding the small differences observed in the time series of freeboard exceedance measured outside and over the deck, in the present study, the time series $VWPw0 - D$ have been considered as the freeboard exceedance time series. However, to use them, it has to be disregarded the possible loss of water due to backflow during the bow run-up stage.

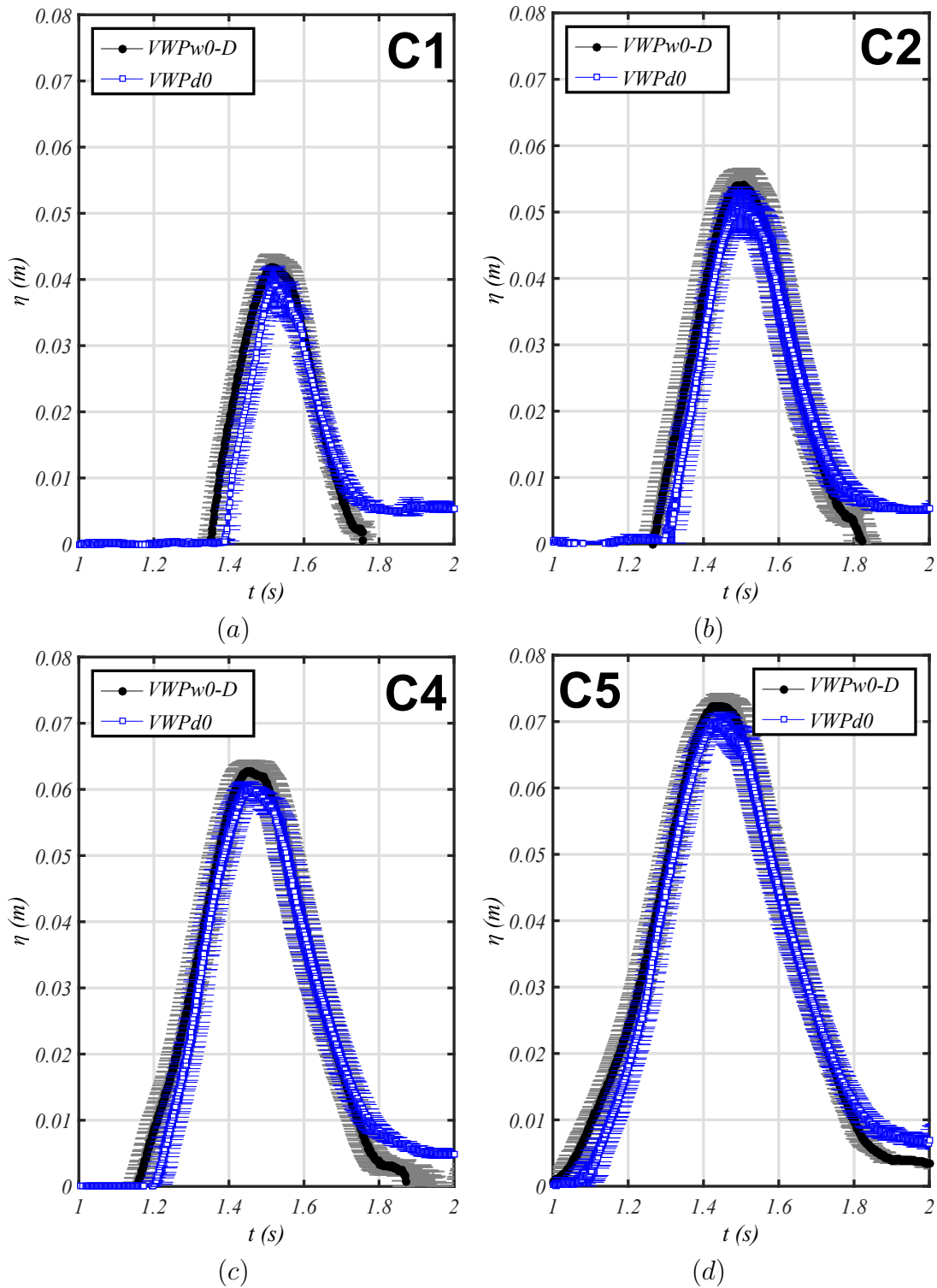


Figure 4.23: Freeboard exceedance time series comparisons by VWPs measured before ($VWPw0 - D$, $x = -0.005$ m) and after ($VWPd0$, $x = 0.005$ m) the bow edge of the deck . (a) Case 1. (b) Case 2. (c) Case 4. (d) Case 5.

Time series of shipping water on deck

Experimental measurements of the time series due to shipping water at several positions on the deck is still a topic that has not been widely explored in literature,

thus, there is a lack of information that allow obtaining details of the evolution of different types of shipping water events. A common practice is to use some conventional wave probes arrangements to extract water elevation information, as for instance GRECO *et al.* [3], GRECO [16]. Conversely, the present results may yield a better understanding of the trends followed by water elevations at several positions over the deck, because it allows obtaining their time series, which is of importance for analytical and numerical model validations nowadays.

As described before, after the bow run-up stage, a finite amount of water invaded the deck in the shipping water events. This water propagated onto the deck decreasing the elevations unless an obstruction remained on its way. In the present two-dimensional study, the amount of water entry can be defined by the freeboard exceedance time series.

For the study cases shown in Figs. 4.23a-d, the corresponding time series of shipping water elevations on the deck are shown in Figs. 4.24a, b, c and d for the cases C1, C2, C3 and C4, respectively. The figures show the time evolution of water elevations (η) for a repetition at several VWPs in the spatial range $0.010 \leq x \leq 0.33$ m, considering the bow edge as the origin ($x = 0$). The VWPs are separated by a distance of 0.010 m from each other, yielding 33 VWPs. The time series are shown regarding the range of applicability of the image-based procedure ($t \sim 2$ s), that is, in the two dimensional flow, before the influence of the tank wall on the flow. For all the cases, the water elevations tend to decrease as x increases. Most of the time series presented an initial rising limb, then, a peak was attained, and finally, a decreasing limb was observed.

For the cases that presented a larger amount of water (see Cases 4 and 5, Figs. 4.24c,d), the effects of the run-up stage at the deck end influenced earlier the signals of the VWPs located closer to the vertical wall, where the image processing method was not fully applicable to measure the effective water elevation because of the turbulent flow. Such an effect increased from the cases with larger to lower freeboards (i.e., from C1 to C5, respectively). Regardless of these effects, it can be verified that the trend followed by elevations in all cases is very similar, differing mainly in the magnitude of the water elevations and the time at which water started to be measured. The resemblance in the trends of the time series may be related to the types of shipping water events under study, which resembled the DB and PDB with small cavity formation.

The water elevations shown in Fig. 4.24 are of importance for the analytical model validation to assess the water elevations on deck, as further described in this work.

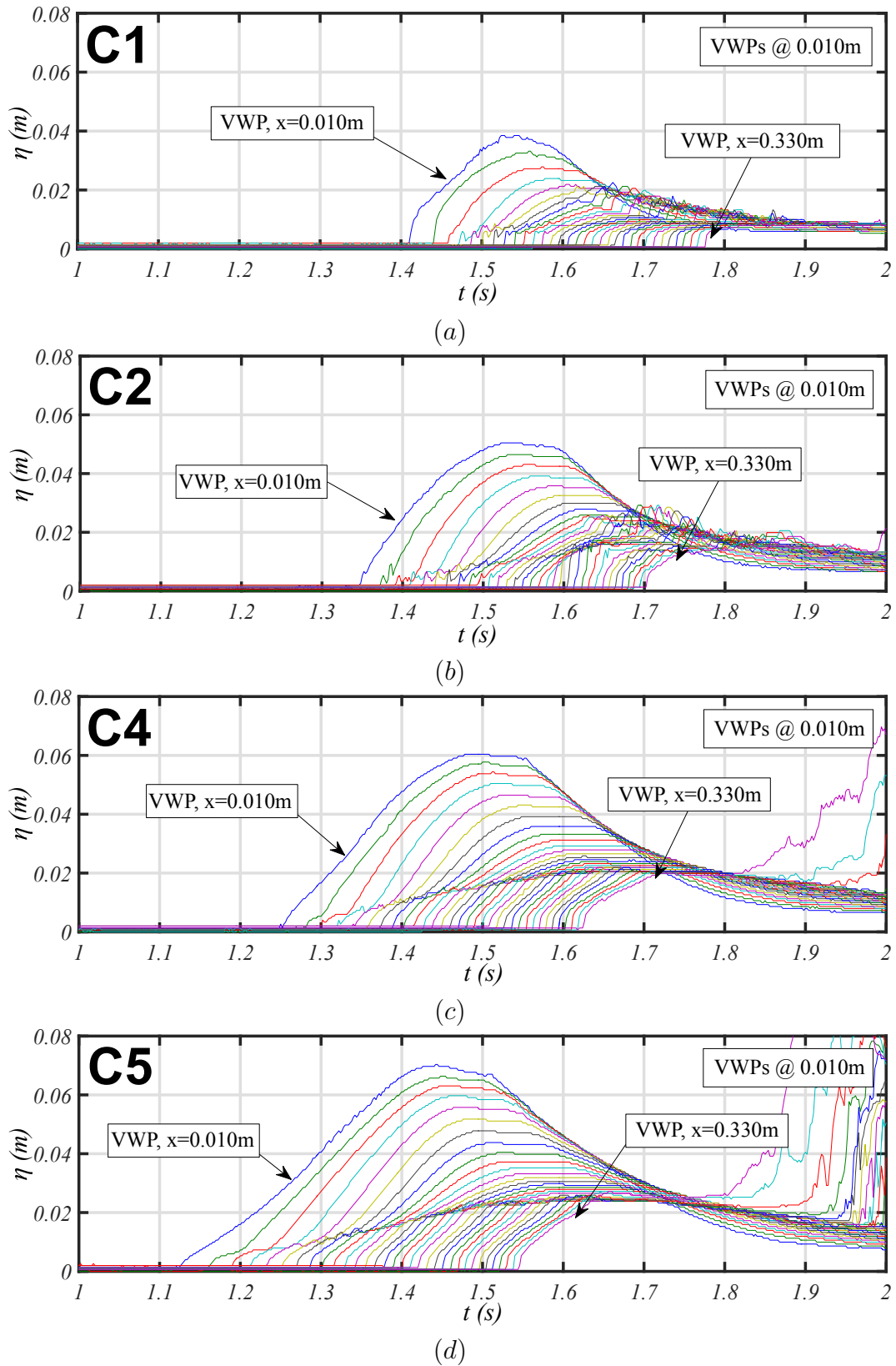


Figure 4.24: Time series of shipping water elevations (η) at different positions onto the deck (33 VWPs, $[0.01 \leq x \leq 0.33$ m, VWPd01 to VWPd33]). (a) Case 1. (b) Case 2. (c) Case 4. (d) Case 5.

4.2.3 Shipping water kinematics

From the available data, information about the shipping water kinematics has been extracted. This information corresponds to the horizontal velocity of the shipping water wavefront (U_{front}), measured from visual inspection of the wavefront edge displacement onto the deck (x_{deck}), as described in Section 3.3.3.

Figure 4.25 presents the mean and standard deviation values of the results obtained from the analysis of the wavefront propagation for some cases considered as representative. Thereby, Figures 4.25a and b show the time series of wavefront displacement over the deck (x_{deck}) against time (t) obtained for the Cases 1 and 3, respectively. The slope of the curves shown can be used to idealize the wave front velocity (U_{front}) for each case. In general, it can be verified that data does not follow a linear relation. Indeed, it can be noted a region where the curves have a smaller slope (I), suggesting a lower wavefront velocity, and a region with a larger slope, suggesting a larger velocity (II). In the former stage the wave front has not been completely developed ($0 \lesssim x \lesssim 0.05$ m, beginning of the water entry), whereas the in the latter, the wave front has been well developed over the deck, after a sudden acceleration.

The behaviour observed in the time series of wavefront displacement can be better understood in the Figs. 4.25c and d, which show the time series of wave front velocity U_{front} for the same cases. It can be observed that, at the beginning of the events (Region I), U_{front} is between 0.2 – 0.4 m/s, approximately. Then, when the wave front is well developed at longer positions over the deck (Region II), it reaches velocities around 1 m/s. On the hole, the trends of data suggest a considerable variable acceleration from region (I) to (II), as inferred from the distributions of mean values.

Rather than from a visual analysis, the mean front velocities estimation for the regions (I) and (II) from Fig. 4.25 has been performed by means of linear regression analysis to the mean values of experimental data (x_{deck} vs t). This was done to obtain the mean U_{front} velocities at different stages of shipping water (i.e., I and II).

Figures 4.26a and c present the linear regression results of the time series of wavefront displacements, regarding the range $0 < x_{deck} < 0.02$ m in the region I for Cases 2 and 4, respectively.

Linear regression fits with coefficients of determination $R^2 \approx 0.99$ were obtained from experimental data. These coefficients are statistical measures of the degree of approximation of data to the fitted regression line. Overall, higher R^2 values indicate a better fitting of the model to the data. In both cases, a mean U_{front} of ≈ 0.3 m/s was verified from the slope of the analytical model for each case. Furthermore, Figs. 4.26b and d shows the linear regressions ($R^2 \approx 0.99$) for the

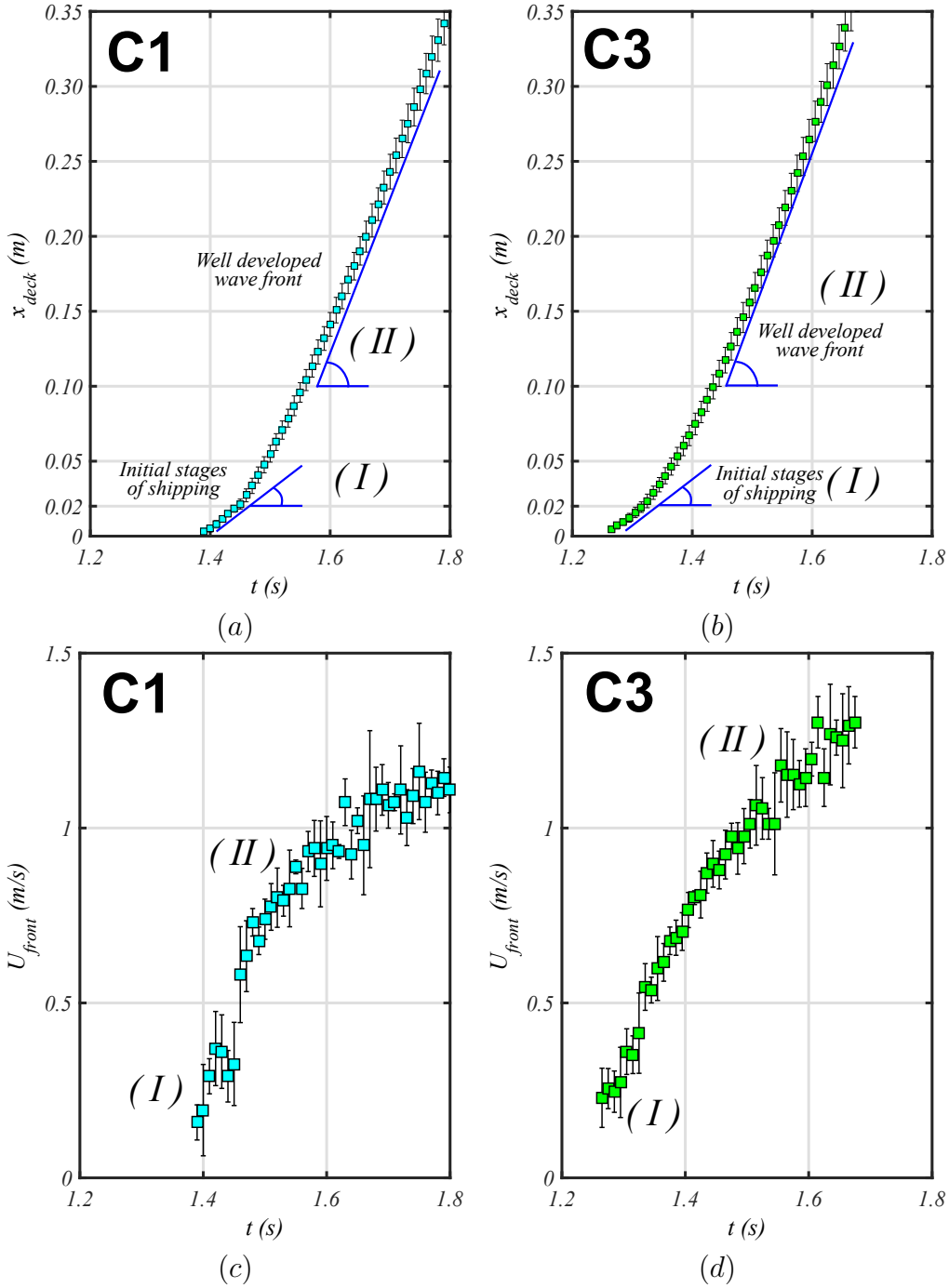


Figure 4.25: Analysis of wavefront propagation onto the deck. (a) Case 1: x_{deck} vs t . (b) Case 3: x_{deck} vs t . (c) Case 1: U_{front} vs t . (d) Case 3: U_{front} vs t .

region II considering $0.1 < x_{deck} < 0.35$ m in both cases. In these regions, the slopes of the models obtained suggest mean $U_{front} \approx 1.1$ m/s.

To verify the changes of the wavefront velocities at different regions over the deck, Table 4.3 summarizes the U_{front} values obtained from linear regression analysis for the five study cases for regions $0 < x < 0.2$ m, $0 < x < 0.5$ m, $0 < x < 0.1$ m and $0.1 < x < 0.4$ m. Notice that in general, even though the velocities are close for all cases, Case 1 presented slightly higher velocities than the other cases.

Moreover, it can be noted that the wavefront velocity is different according to the region considered, that is, it increases as x_{deck} also does. On the whole, it can be verified that the wavefront velocities presented values of 0.3 – 0.4 m/s at the beginning of the deck, and values of 1.0 – 1.1 m/s for the middle and the end of the deck regions.

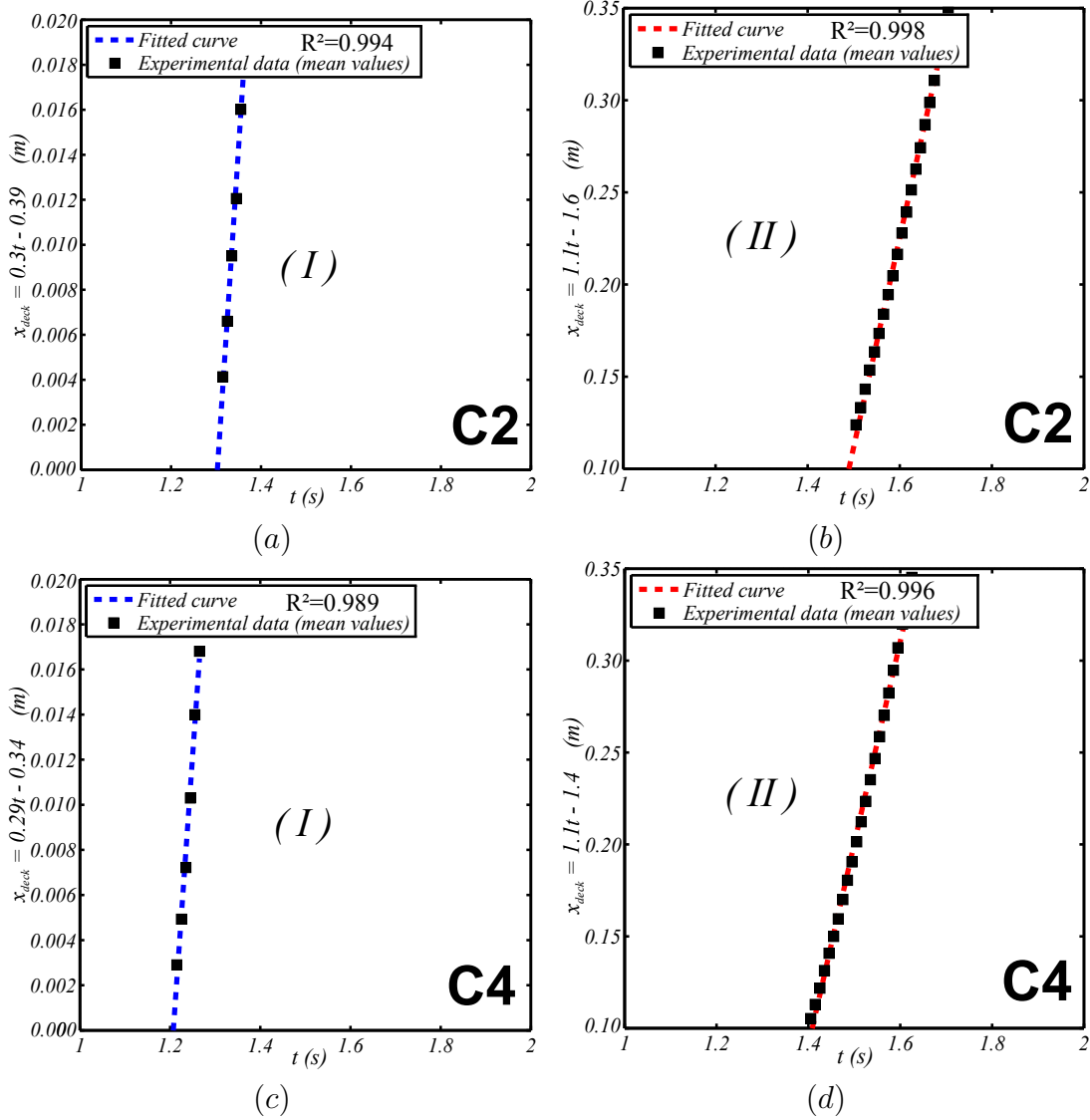


Figure 4.26: Linear regressions performed to mean wavefront edge displacements (x_{deck}) values to estimate the wavefront velocity U_{front} at different regions over the deck. (a) Case 2: x_{deck} vs t for $0 < x < 0.02$ m. (b) Case 2: x_{deck} vs t for $0.1 < x < 0.35$ m. (c) Case 4: x_{deck} vs t for $0 < x < 0.02$ m. (d) Case 4: x_{deck} vs t for $0.1 < x < 0.35$ m.

4.3 Shipping water vertical loading

The shipping water events analyzed caused vertical loading on the structure, which was measured by the force balance embedded to its deck, as already described in

Table 4.3: Mean wavefront velocities (U_{front}) estimated from linear regression analysis at different regions over the deck.

Case	U_{front} ($0 < x < 0.02$ m) (m/s)	U_{front} ($0 < x < 0.05$ m) (m/s)	U_{front} ($0 < x < 0.1$ m) (m/s)	U_{front} ($0.1 < x < 0.4$ m) (m/s)
1	0.31	0.44	0.63	1.1
2	0.30	0.43	0.62	1.1
3	0.30	0.42	0.58	1.1
4	0.29	0.38	0.52	1.1
5	0.31	0.38	0.50	1.0

Section 3.4. Five repetitions were performed and the sum of the signals of the four load cells that form the balance were used to obtain the total vertical loads. Additionally, data from the accelerometers attached to the sensing element of the balance and to the tank wall allowed to identify some responses of the structure during the experiment.

4.3.1 Vertical loading

Individual load cell loading

To start with, the trends of the measurements obtained with the individual load cells that form the balance are analyzed. Figures 4.27a-d show the mean and standard deviation values (considering the five repetitions) of vertical loads measured by load cells LC1-LC4 for the Case 3, respectively. Two seconds were considered to analyze the signals from the trigger activation ($t = 0$) until the loads on deck due to the shipping water occurred, including the maximum load and the decreasing trend of signals.

Figures 4.27a and b show the results for LC1 and LC2, respectively. These load cells are located close to the vertical wall of the structure that is in contact with the water (see Section 3.4.1). It can be observed that signals present a constant amplitude near to zero until $t \approx 0.9$ s, when they start showing negative values. The negative values attained a minimum value at $t = 1.324$ s, then, the signals rose up to zero at $t = 1.446$ s. After this time, force amplitudes increased until attaining peak values, then, they decayed while water developed onto the deck.

Moreover, Figures 4.27c and d show the force time series for LC3 and LC4, which were located farther from the bow than LC1 and LC2. Differently from the trend observed in LC1 and LC2, these load cells measured positive values after $t = 0.9$ s, which increased attaining a peak value at $t \approx 1.65$ s. That is, no negative values were observed. The maximum load standard deviations for the individual load cells did not exceed 0.5N in all cases.

Even though the force magnitudes obtained by the load cells in the different

study cases are different, the trends observed in the signals of Fig. 4.27 are similar for all cases.

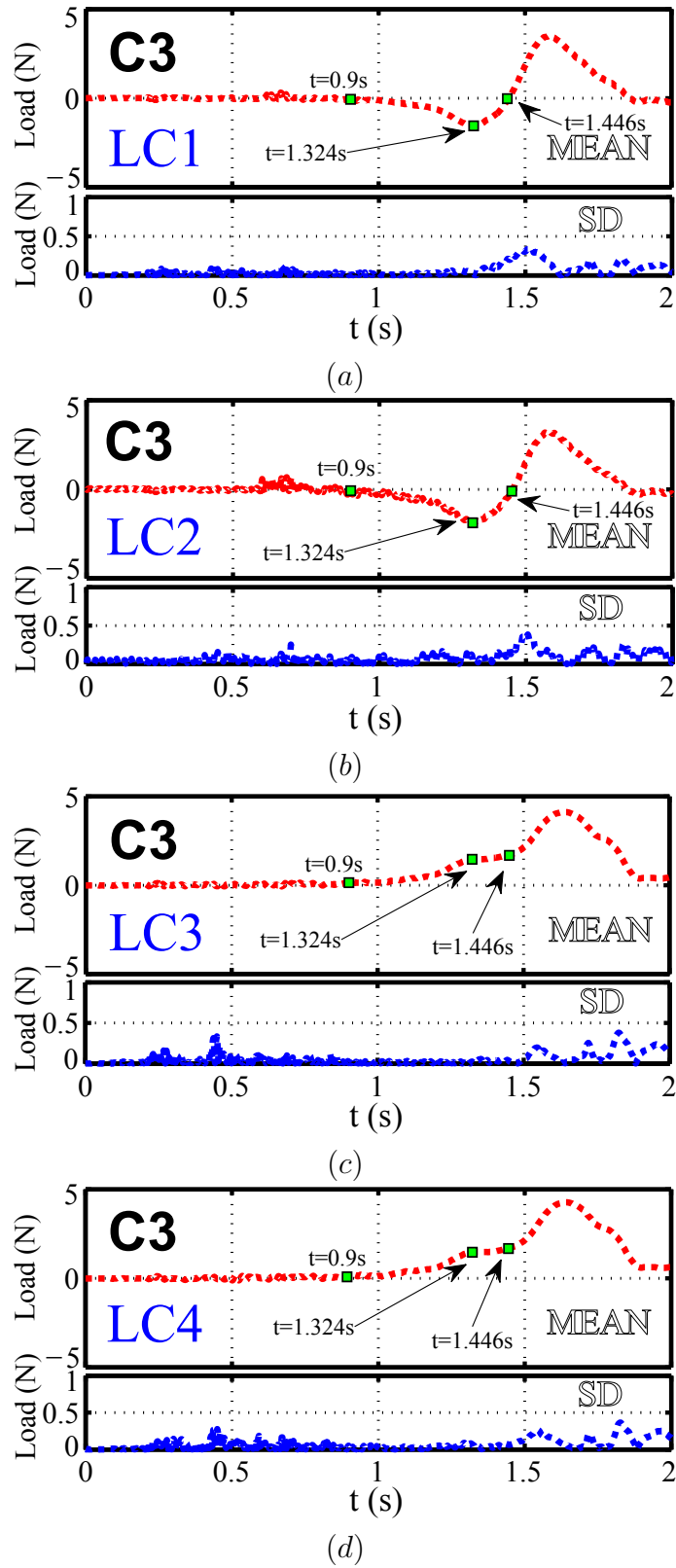


Figure 4.27: Mean and standard deviation values of time series of vertical loads given by the four load cells in the Case 3. (a) Load cell 1 (LC1). (b) Load cell 2 (LC2). (c) Load cell 3 (LC3). (d) Load cell 4 (LC4).

It was identified from video data that the differences observed in Fig. 4.27 for the load cell pairs may be associated to the initial stages of shipping water, which tend to cause a not uniform distribution of loads when the water invaded the beginning of the deck. To exemplify this, Figure 4.28a shows snapshots of the spatial distribution (snapshots) of the points in time highlighted in Fig. 4.27.

It can be verified that at $t = 0.9$ s, the initial water level near the structure started moving due to the incoming wave. Then, note that for $t = 1.324$ s the bow run-up stage already occurred and the water started forming an small forward jet at the instant at which it is over the deck. The sensing element of the balance started being loaded in a not uniform manner through a moment around the y_b axis. Next, from $t = 1.324$ s up to $t = 1.446$ s, the wavefront developed and covered a larger deck region.

It can be suggested that the negative measurements observed in LC1 and LC2 are due to a horizontal wave load effect during the bow run-up on the load cell measurements, as illustrated in Fig. 4.28b. Perhaps, the vertical wall of the balance presented a small horizontal displacement due to a moment caused during the bow run-up stage, influencing the negative loads in LC1 and LC2 ($- \uparrow$). It has to be considered that there is an small separation (~ 0.5 mm) between the vertical wall of the balance and its horizontal sensing plate. When the bow run-up started, the negative loads started to be measured. It is possible that such loads were due to a bow runup moment, which may have pushed the sensing element upwards, causing tension and compression loading in LC1-LC2 and LC3-LC4, respectively. When the shipping water invaded a larger region of the sensing element, the loading became more uniform and all the load cells measured compression loads. Despite of the trends observed in the individual load cells, the resultant vertical load over the balance was obtained as the sum of LC1-LC4, and was measured when the water started to load the balance, as described in next paragraphs.

Total vertical loading repeatability

An analysis of the repeatability of the total vertical loads, calculated as the summation of the individual load cells, is presented. Figure 4.29 shows time series of total vertical loads, obtained for the five repetitions of the Case 3. This case that is the intermediate of the five cases considered was chosen as representative for explanation purposes. In the figure, it can be observed that all the repetitions present a very close agreement in magnitudes and trends followed. Note that for such a case, the sensing element of the balance started to measure the loads after $t \approx 1.35$ s. Then, they raised up to a peak value at $t \approx 1.6$ s, after which they decreased to zero at approximately $t = 1.9$ s.

In order to verify what occurred during the total load measurements, several

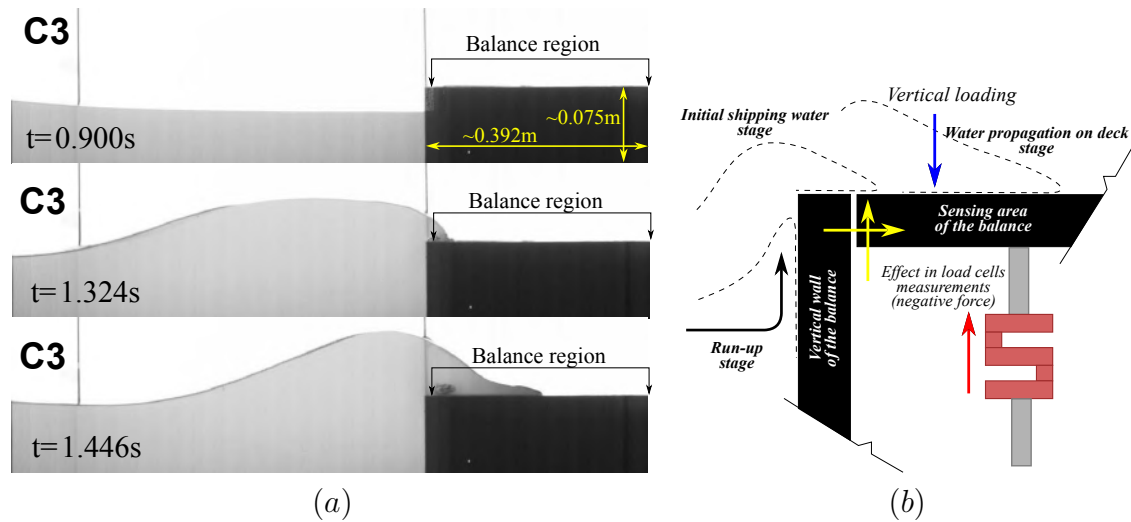


Figure 4.28: Effects of initial stages of shipping water on the individual load cells performance.

points in time were highlighted in Fig. 4.29, corresponding to the snapshots presented in Fig. 4.30. It can be observed in Fig. 4.30 that for $t = 1.364$ s, where it seems

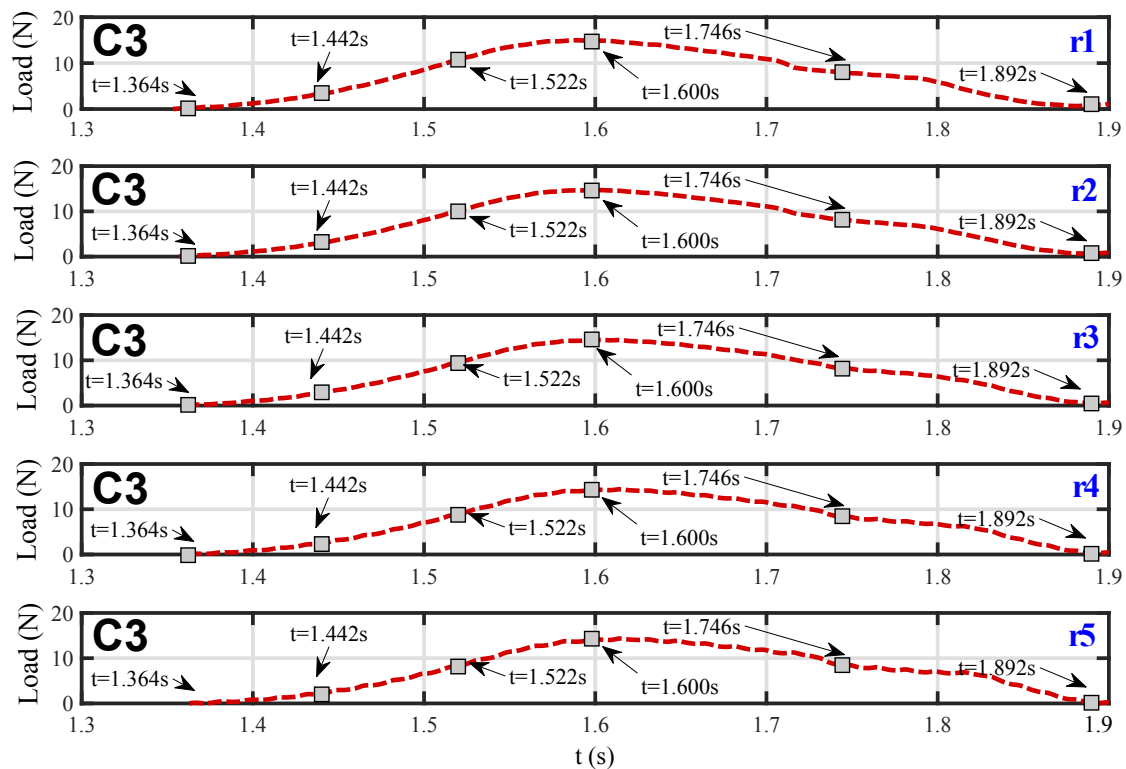


Figure 4.29: Time series of total vertical loads for the five repetitions performed in the Case 3.

that the load started to be measured, the forward jet (wavefront) formed at the early stage of water entry started loading the sensing element of the balance. From Fig. 4.29, this loading increased progressively for $t = 1.442$ s and 1.522 s, until it was attained a peak value at approximately $t = 1.6$ s. In Fig. 4.30, this point in

time (peak value, $t \approx 1.6$ s) indicates the larger amount of water over the sensing element, as shown in the time series. After this stage ($t = 1.746$ s and 1.892 s), the water elevations of the shipping water decreased, which, in turn, reduced the loading, as observed in Fig. 4.29. The loading is reduced because water propagated downstream over the deck, interacting with the tank wall, remaining a thin layer of water over the sensing element. After the run-up occurred, backflow was observed, causing a second loading stage over the balance. The analysis of the second loading stage was not considered in this work, thus, further research may be done for its study.

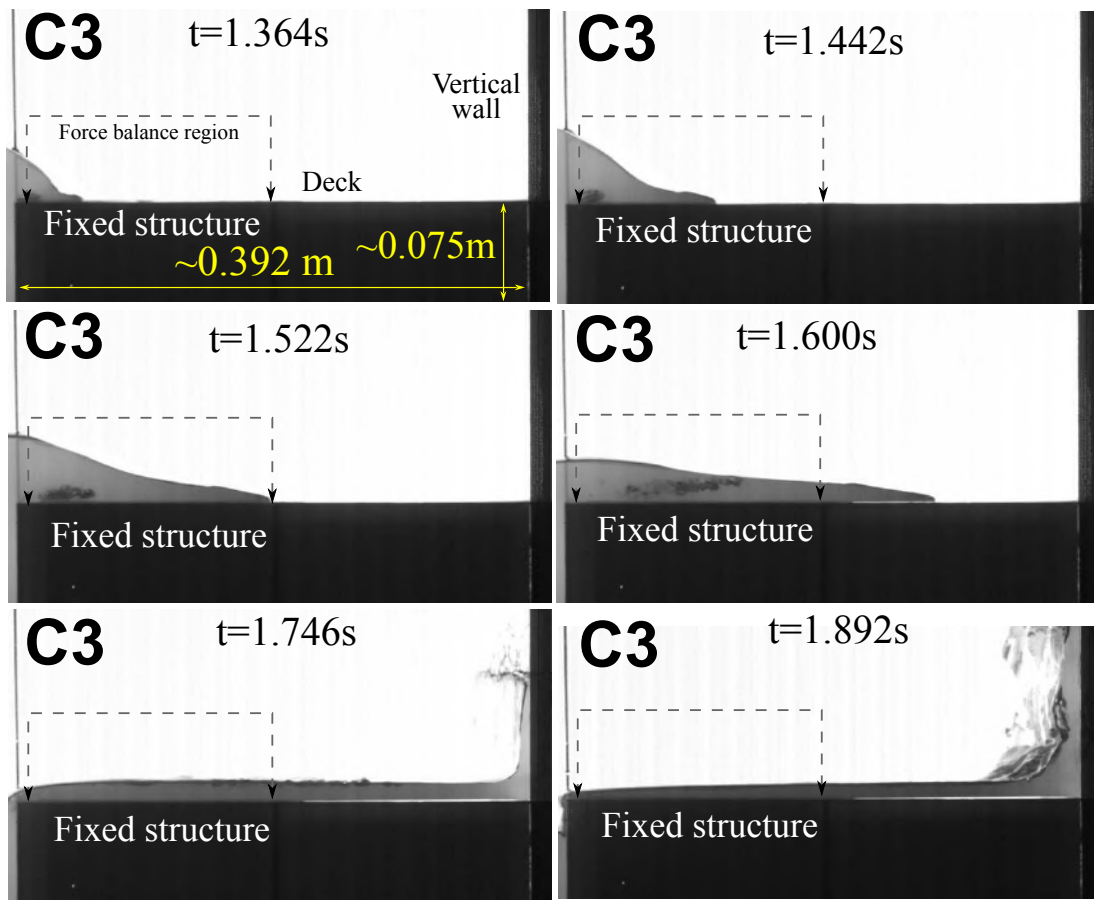


Figure 4.30: Snapshots of representative shipping water propagation stages for vertical loading analysis for the Case 3.

Performance of the balance

The performance of the sensing element of the balance was verified by calculating the point of application of the load time series in the sensing element region, considering its geometrical center as reference to estimate punctual values, as shown in the graphs of Figs. 4.31a and b for Cases 3 (for $1.3 < t < 2$ s) and 5 (for $1.2 < t < 2$ s), respectively. In the graphs, x_b and y_b represent the longitudinal and transversal

coordinates of the sensing element, which has length 0.18 m and width 0.334 m, respectively. Even though there are some points dispersed, mainly around the x_b axis for $x_b > 0$, in both cases almost all the points are grouped very close to the center of the balance. There are loads centered along the y_b -axis, which may indicate the presence of three-dimensional effects during the shipping water on deck. Additionally, the points observed in the first half of the deck length, along the x_b -axis, may be due to a not uniform loading distribution, as suggested by Fig. 4.27, for the initial stages of the events.

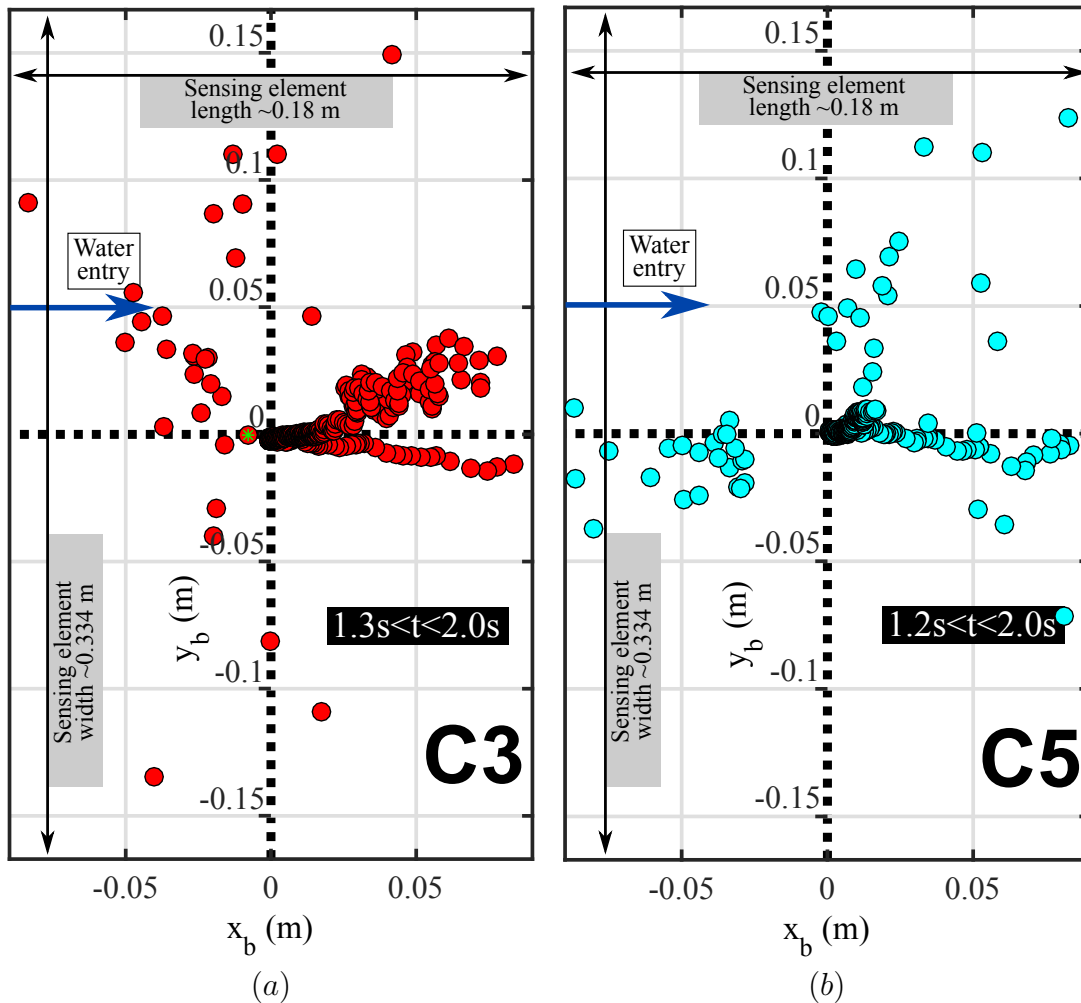


Figure 4.31: Calculated points of application of vertical loads over the sensing element of the balance. (a) Case 3. (b) Case 5.

Total vertical loads

Once the individual load cells loads and the performance of the force balance have been analyzed, it is possible to present the results of time series of total loads, considering the time interval $0 < t < 2$ s.

Figure 4.32 presents the time series of total vertical loads (mean and standard

deviation values) for the Cases 1,2,4 and 5. It can be observed that for all cases, the beginning of the mean load measurements as well as their maxima values occurred at different times. For Cases 1,2 and 3 the maximum standard deviation did not exceed 1 N, whereas for Case 5, it was observed an increase of about 3N as soon as the mean values reached their minimum values ($t \gtrsim 1.95$ s). In this last case, the resultant volume of water on deck was the largest of all cases. Below each graph, it is observed an snapshot indicating the stage corresponding to the maximum loading in each case (point M). The stages shown correspond to the maximum amount of water over the sensing element of the balance. After these stages, the finite volume of water that shipped onto the deck, propagated downstream over it, decreasing the water elevations on the sensing element and, hence, reducing the loading.

Table 4.4: Maximum measured vertical loads for all the study cases.

Case	t_M (s)	F_M (N)	$\%F_M$
C1	1.668	7.3 ± 0.34	4.7
C2	1.626	12.2 ± 0.24	2.0
C3	1.600	14.5 ± 0.28	1.9
C4	1.584	16.9 ± 0.21	1.2
C5	1.566	21.5 ± 0.22	1.0

Note that the maximum loads occurred at shorter times as the amount of water over the deck increased, that is, as freeboard reduced (e.g., Cases 4 and 5). In these cases the time series also started earlier than for the cases with higher freeboards.

In order to compare the vertical loading for all cases, Table 4.4 summarizes relevant data for the five cases of study. These include the mean maximum vertical load with its corresponding standard deviation (F_M), the point in time at which this load occurred (t_M), and the percentage of the standard deviation on the mean value $\%F_M$.

As expected, the largest maximum loading was obtained for Case 5 (21.5 ± 0.22 N), which presented the largest amount of water over the deck, whereas the minimum was for Case 1 (7.3 ± 0.34 N). There is a difference of 14.2 N between the cases with higher (C5) and lower (C1) freeboards. Also, note that these peak values occurred faster for the cases that presented smaller amount of water over the deck, that is, those with the highest freeboards (e.g., C1, C2). Furthermore, it can be verified that these cases presented a larger standard deviation with respect to the mean values ($\%F_M$). That is, it was observed 4.7% and 1% of difference in relation to the mean values for the Cases 5 and 1, respectively. The data presented in this section was employed to validate the application of the proposed analytical approach to estimate the vertical loading over the sensing element, as further presented in Sect. 5.

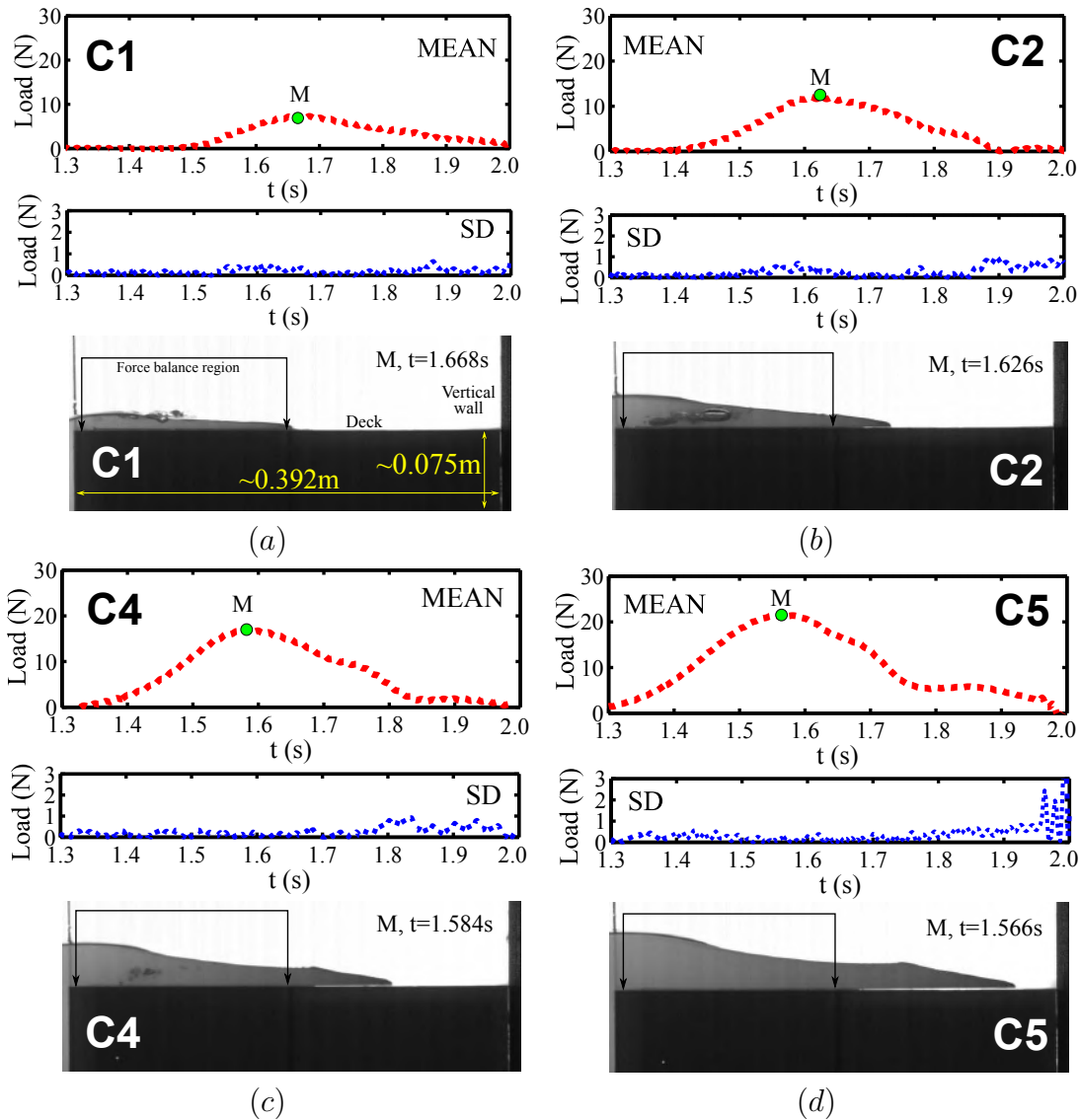


Figure 4.32: Mean and standard deviation values of the total vertical load time series. Images under the graphs represent the stage at which the maximum loading on the balance occurred in each case. (a) Case 1. (b) Case 2. (c) Case 3. (d) Case 4.

4.3.2 Dynamic effects during the experiment

Accelerometer of force balance

As the wet dam-break experiment consists in a sudden release of the gate that divides the upstream and downstream reservoirs of water, the impulsive motion of the gate might have induced vibration in the installation considered for the experiments. In this framework, the accelerometer attached to the force balance was employed to identify dynamic effects (ringing) during the dam-break tests that could have significant influence on the load measurements. The accelerometer has a frequency response from 0 to 200 Hz, so, dynamic responses in such a range were considered.

Figure 4.33 shows time series of accelerations for the five repetitions, which have

been superimposed. These signals were provided by the accelerometer in the three directions (X, Y and Z, Fig. 3.3), from $t = 0$ to $t = 2$ s for Cases 1 and 5, which were selected as representative of all cases. In all signals, it is possible to observe that there is an amplification in the acceleration amplitudes around $t \approx 0.5$ s. This effect is due certainly to the gate release stage, which occurred approximately at that time for all cases. Such an impulsive response is expected since the rapid gate release during dam-break experiments may be subjected to some frictional effects caused by the tank walls and the water at both sides of the gate, then, it might have induced some vibrations in the tank. As can be noted, there is a transient effect during the gate release ($t \approx 0.5$ s) and the subsequent milliseconds, corresponding to the stage of wave generation. However, it can be inferred that the maximum response tended to decrease during the wave propagation and shipping water onto the deck ($t \gtrsim 0.1$ s).

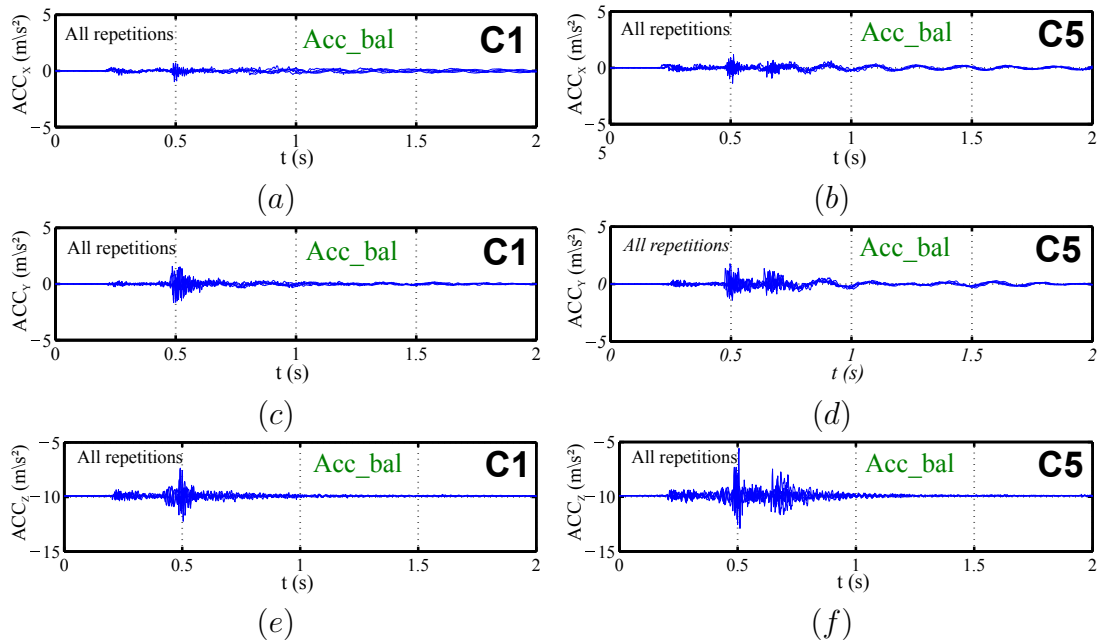


Figure 4.33: Data from the accelerometer attached to the balance (Acc_{bal}). (a) Case 1, acceleration in X. (b) Case 5, acceleration in X. (c) Case 1, acceleration in Y. (d) Case 5, acceleration in Y. (e) Case 1, acceleration in Z. (f) Case 5, acceleration in Z.

Figures 4.33a and b show the acceleration in the x-direction (i.e., longitudinal to the tank) for Cases 1 and 5, respectively. The maximum effect due to the gate release was around $-0.9 \text{ m/s}^2 < ACC_X < 0.9 \text{ m/s}^2$ for Case 1 and $-1.2 \text{ m/s}^2 < ACC_X < 1.2 \text{ m/s}^2$ for Case 5, both at $t \approx 0.5$ s. Then, the amplitudes decreased for longer times. It can be verified that after the transient stage, the signals of Case 5 presented some oscillations of lower frequencies. Probably, the gate release together with the generation of the incoming wave induced an slow motion on the structure, also measured by the balance accelerometer in the X-direction.

Otherwise, Figures 4.33c and d present the accelerations for the Y-direction (i.e., transversal tank direction) for Cases 1 and 5, respectively. In this direction, the effects derived from the gate release originated peak amplitudes in the ranges of $-1.6 \text{ m/s}^2 \lesssim ACC_Y \lesssim 1.6 \text{ m/s}^2$ for Case 1 and $-1.8 \text{ m/s}^2 \lesssim ACC_X \lesssim 1.8 \text{ m/s}^2$ for Case 5. The effects were a little higher than the ones observed in the X-direction. However, a similar slow-frequency oscillation is also observed for longer times in the signals for Case 5. Perhaps, the study cases with larger volumes of water in motion (e.g., Cases 4 and 5), produced such a type of oscillation in the installation, which might be traduced to a small oscillating motion of it.

Finally, Figures 4.33e and f show the accelerations measured in the vertical direction (Z-direction) for Cases 1 and 5, respectively. In this case, peak values in the most amplified stage are in the ranges of $-2.4 \text{ m/s}^2 \lesssim ACC_Y \lesssim 2.4 \text{ m/s}^2$ and $-4.3 \text{ m/s}^2 \lesssim ACC_X \lesssim 4.3 \text{ m/s}^2$ for Case 5, and the decay of higher frequency oscillations is observed for longer times as in the previous cases.

Results suggest that there are some vibrations induced to the structure measured by the force balance accelerometer, attributed mainly to the gate release and wave generation stages, which generated impulsive responses. However, these responses decreased with time, during the incoming wave propagation and the shipping of water. At these stages, slow frequency oscillations are observed in the signals for Case 5, particularly for the X- and Y- directions. For the Z- direction, these oscillations are almost negligible, so, it has been assumed that the load measurements were not influenced by them.

Accelerometer installed on the tank vertical wall

As described above, during the wet dam-break experiment, some vibration was transmitted to the tank. This was also verified by the accelerometer installed to its vertical wall (Fig.3.5), from which the responses in different directions were monitored.

Results obtained for the Cases 1 and 5 for the X, Y and Z directions (i.e., transversal, vertical and longitudinal tank directions) are shown in Figs.4.34, 4.35 and 4.36, respectively, where the time series of the five repetitions shown were superimposed for each case.

Figure 4.34 presents the time series for the acceleration measured in the transversal tank direction (X). The higher amplifications occurred at $t \approx 0.5 \text{ s}$ with maximum values of about $\pm 2.9 \text{ m/s}^2$ and $\pm 4.6 \text{ m/s}^2$ for Cases 1 and 5, respectively, which were originated mainly due to the action of the gate release, as described above for the force balance accelerometer. Then, these higher frequency oscillations reduced their frequency for the time interval at which shipping water on deck occurred ($1 \text{ s} \lesssim t \lesssim 1.5 \text{ s}$).

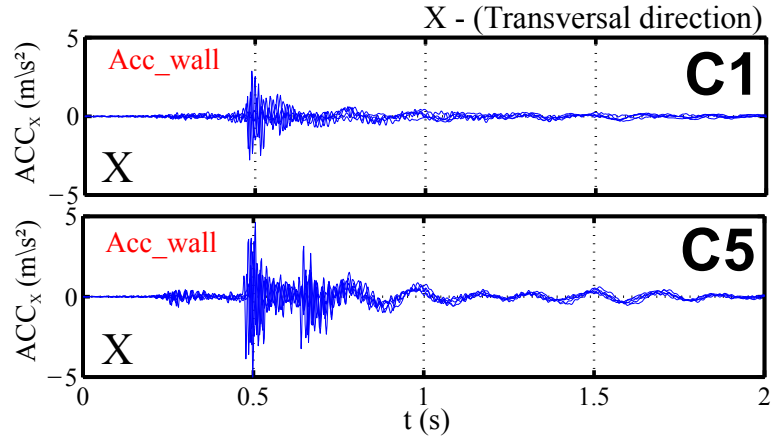


Figure 4.34: Data from accelerometer attached to the tank vertical wall (Acc_{wall}): Cases 1 and 5, transversal direction (X).

Figure 4.35 shows the results for the vertical direction (Y). In this case, the maximum amplifications occurred during and after ≈ 0.3 s from the gate release, before shipping of water on deck. However, in this case the maximum amplifications are lower than the one observed in the transversal direction, that is, approximately ± 1 m/s² and ± 1.6 m/s² for Cases 1 and 5, respectively. The vibration in this direction was less significant than in the X-direction.

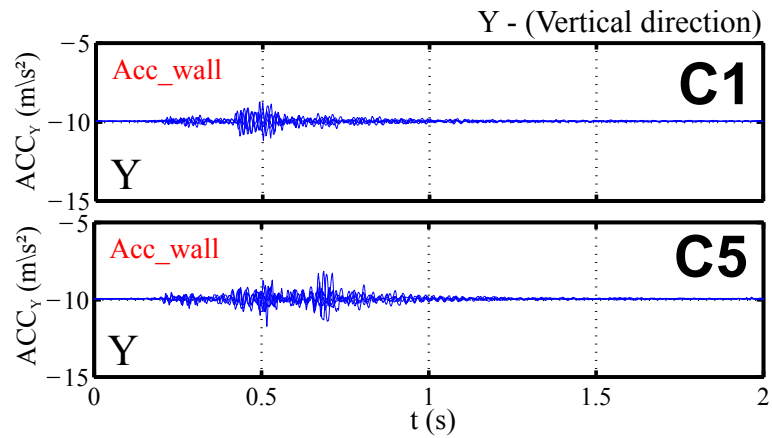


Figure 4.35: Data from accelerometer attached to the tank vertical wall (Acc_{wall}): Cases 1 and 5, vertical direction (Y).

Finally, Figure 4.36 shows the accelerations measured in the tank longitudinal direction (Z). Again, it is clearly observed that the maximum values occurred around $t \approx 0.5$ s, during the gate release. The Case 1 presented maximum values of ± 2.2 m/s² and the Case 5 of ± 5 m/s². This last presented a second maximum oscillation at $t \approx 0.7$ s, which was also reduced its frequency for longer times. This might be attributed to some effects due to the maximum aperture of the gate considering the higher water depths h_1 in the study cases.

Results are coherent with the ones obtained with Acc_{bal} . The gate release stage

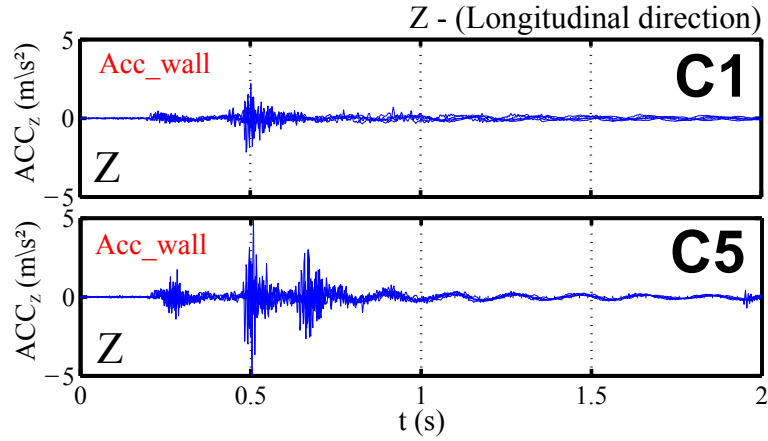


Figure 4.36: Data from accelerometer attached to the tank vertical wall (Acc_{wall}): Case 1 and 5, longitudinal direction (Z).

transmitted impulsive vibrations to the structure, specially at the time $t \approx 0.5$ s, which decayed into slow frequency oscillations after that time, specially for Case 5. This case presented the smallest freeboard and the largest volume of water over the deck. The most significant effects were observed in the transversal (X) and longitudinal directions (Z). It is suggested that at higher initial condition values (i.e., higher h_1 and h_0), or in other words, for larger volumes of water into the tank, the resistance caused by water on the gate release was more significant, being related to the vibrations transmitted to the experimental installation.

Overall, it was verified that for the cases with higher initial condition h_1 (e.g., Case 5), there was a low-frequency oscillation remaining in the transversal and longitudinal directions, which may be associated to a slow motion generated by the larger amount of water moving downstream inside the tank. For the vertical direction, it can be assumed that the vibration transmitted to the tank was minimized during the shipping of water on deck.

Chapter 5

Analytical Results

This chapter presents the analytical results obtained in the present study. In the first part of the chapter, preliminary analysis of the proposed model (i.e., convolution model), including selection of input parameters and calibration, is presented. Next, it was validated with experiments and compared with the classical dam-break approach to estimate the shipping water propagation over the deck. Finally, both, the convolution and dam-break methods were considered for the estimation of vertical loading on deck, comparing the results obtained with experimental data.

5.1 Analytical model preliminaries and calibration

Regarding the implementation of the model, some preliminary steps are shown in this section. First, a procedure followed to define the input function of the model is described. Secondly, an adequate time step has been chosen to implement the convolution in order to avoid underestimation of results and to guarantee computational efficiency. Finally, a parametric analysis considering the input kinematic and frictional parameters has been performed in order to identify their range of applicability for the problem under study. The influence of the resistance coefficient (S_f) and the mean flow velocity (\bar{u}) on the water elevation distributions (i.e., output of the proposed model) has been analyzed at some positions over the x-domain. From this analysis, adequate S_f parameters have been identified considering the Case 1 as reference. With this, the model was calibrated and further implemented to the other cases.

5.1.1 Input function selection

In the present analysis, the input function of the convolution model corresponds to the time series of freeboard exceedance measured at the beginning of the deck. As described in Section 4.2.2, this time series has been evaluated from VWPs located at $x = -0.005$ m and $x = 0.005$ m from the deck edge, for each case. The former VWP time series was obtained outside the deck, subtracting the structure height ($VWPw0 - D$, Section 4.2.2), whereas the latter was acquired over the deck ($VWPD0$). Figure 5.1a shows the comparison of the time series (mean and standard deviation values from repetitions) of water elevations obtained with these VWPs for Case 4, considered as illustrative of the other cases. It is observed that the trend followed for both series is similar and that the peak values of the water elevation distributions have almost the same magnitude and are very close in phase, despite of small differences in amplitudes at the curve tails.

For practical model implementation purposes, the time series obtained outside the deck (mean values) was considered as the input of the present model, as shown in Fig. 5.1b. This might be a practical approach to apply the model in generic applications, because in typical cases, the freeboard exceedance series may be predicted *a priori* based on relative motions between the bow and the incident wave.

Moreover, the maximum value of the freeboard exceedance time series was defined as the maximum freeboard exceedance (η_0). This value is further considered to estimate the diffusion coefficient used in the proposed model (Eq. 2.28) as well as to use the classical dam-break approach of Stoker (Eq. 2.34).

Table 5.1 summarizes the maximum freeboard exceedance (η_0) for each case. It has to be considered that such values were obtained from the mean time series of $VWPw0 - D$ (Fig. 5.1). In addition, the table also shows the points in time at which these time series started, i.e., assumed beginning of the shipping water on deck ($t_{beginning}$), and the time at which the maximum freeboard exceedance occurred (t_{η_0}).

Table 5.1: Main information of maximum freeboard exceedance (η_0) for all cases.

Case	η_0 (m)	$t_{beginning}$ (s)	t_{η_0} (s)
C1	0.042	1.344	1.512
C2	0.054	1.246	1.506
C3	0.058	1.204	1.468
C4	0.063	1.148	1.456
C5	0.072	0.950	1.446

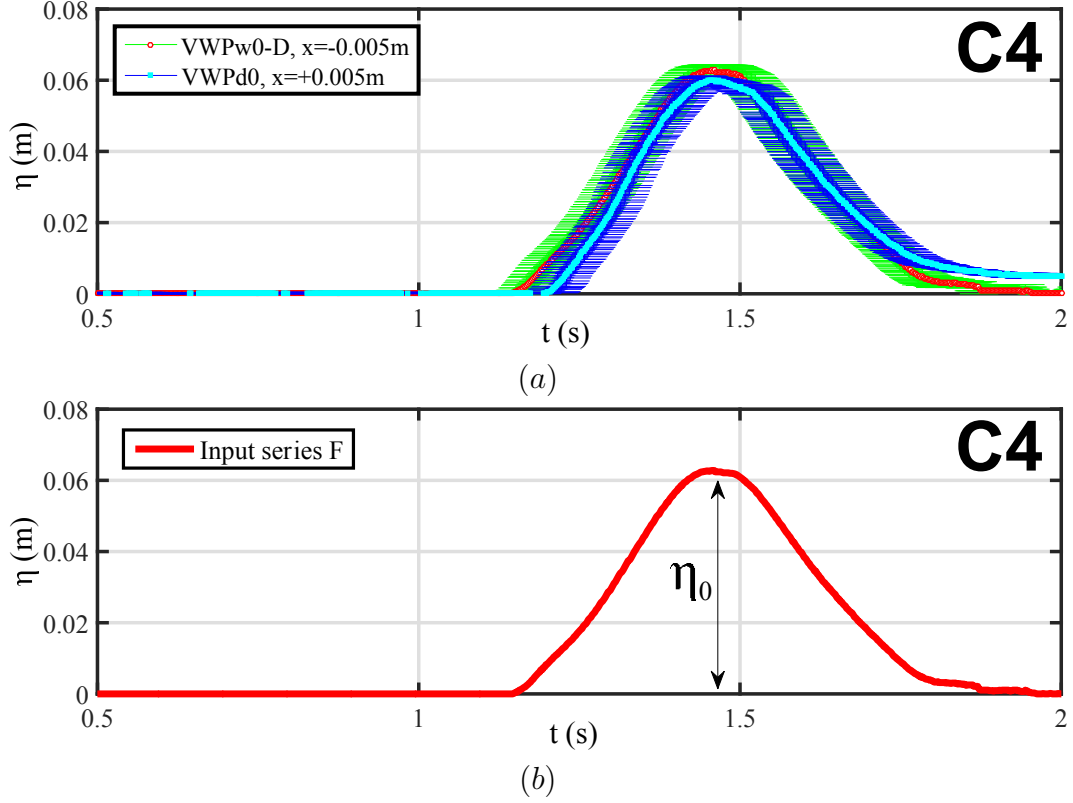


Figure 5.1: Input series selection for Case 4 (a) Mean and standard deviation values of time series measured at $x = -0.005$ m (VWPw0-D) and $x = 0.005$ m (VWPd0). (b) Input series and maximum freeboard exceedance definition (η_0) considered for model implementation.

5.1.2 Kernel function time step analysis

Different time steps were analyzed to verify their effect in assessing the kernel function. This was done because an adequate time step is necessary to attain the rising limb and peak of this function, especially at positions close to the origin ($x \rightarrow 0$), where its shape becomes steeper.

Figure 5.2 shows the kernel functions at different time steps for the Case 1, considering the following input parameters for the kernel: $\bar{u} = 0.3$ m/s (mean U_{front} velocity from $0 < x < 0.02$ m, see Section 4.2.3), $S_f = 0.1$, and η_0 considered as the maximum freeboard exceedance for Case 1. Six time steps ranging from $1E - 5$ s to $1E - 3$ s were considered.

Figure 5.2a presents the kernel function for $x = 0.01$ m. It is observed how the kernel peak is well represented for the shortest time step ($1E - 5$ s). Moreover, the time step $5E - 5$ s also allows capturing the peak value despite a lower resolution to represent the rising limb. For time steps longer than $1E - 3$ s, the kernel peak is not assessed, so, their use may cause loose of information to implement the model at positions near to the origin of the domain (i.e., bow edge).

On the other hand, Figure 5.2b shows the same time step analysis but at a

position farther from the bow edge, $x = 0.03$ m. In the figure, it can be verified that all the time steps analyzed yielded to reproduce the same kernel shape. Even the longer time steps allowed at least a rough representation of the kernel.

In the same way as described above, and only for illustrative purposes, Figures 5.2c and d show the results for positions $x = 0.01$ m and $x = 0.03$ m for Case 5. It can be noted similar effect of the time steps to attain the kernels rising limbs and peaks as for the Case 1. However, in this case the kernel at $x = 0.01$ m presented a higher peak value (that is, a steeper rising limb), which is more difficult to attain with longer time steps. Note that only the time steps $1E - 5$ s and $5E - 5$ s presented good agreement to attain the peak at such a position (Fig. 5.2c). Otherwise, all the time steps allowed an approximated reproduction of the kernel shape for $x = 0.03$ m (Fig. 5.2d).

As it can be noted in the time step analysis results, it is important to define the time step based on the representation of the kernel, considering the nearest working positions to the origin. This would avoid underestimation of results, especially at positions closer to the boundary condition upstream. In the present study, in order to keep computational efficiency and good agreement of the kernel shape, the time step of $5E - 5$ s has been selected for the model implementation.

5.1.3 Sensitivity analysis for model calibration

Once the input function and time step have been defined, it is suggested to do a sensitivity analysis to know the range of applicability of kernel required parameters, allowing calibration of the model for all the test cases. It is necessary to do some preliminary tests according to the case under study, prior implementation of the model, since there are no guidelines available in literature to apply the present advection-diffusion approach to the shipping water problem.

To estimate optimal parameters to reproduce the shipping water evolution in the different cases of application, the influence of the mean shipping flow velocity (\bar{u}) and the resistance coefficient (S_f) present in the B parameter of the model have been investigated through a parametric analysis. To do this, a range of velocities from 0.1 m/s to 1 m/s and S_f values from 0.05 to 0.3 have been considered, from which constant \bar{u} and S_f values were also chosen for the analysis. The former (\bar{u}) was employed as the initial wave front velocity obtained from experiments ($\bar{u} = 0.3$ m/s, Section 4.2.3), as an approximation to the mean shipping flow velocity required. The latter (S_f) was chosen from results obtained by testing the influence of some S_f parameters on the model output. This evaluation to define the constant S_f parameter is described below.

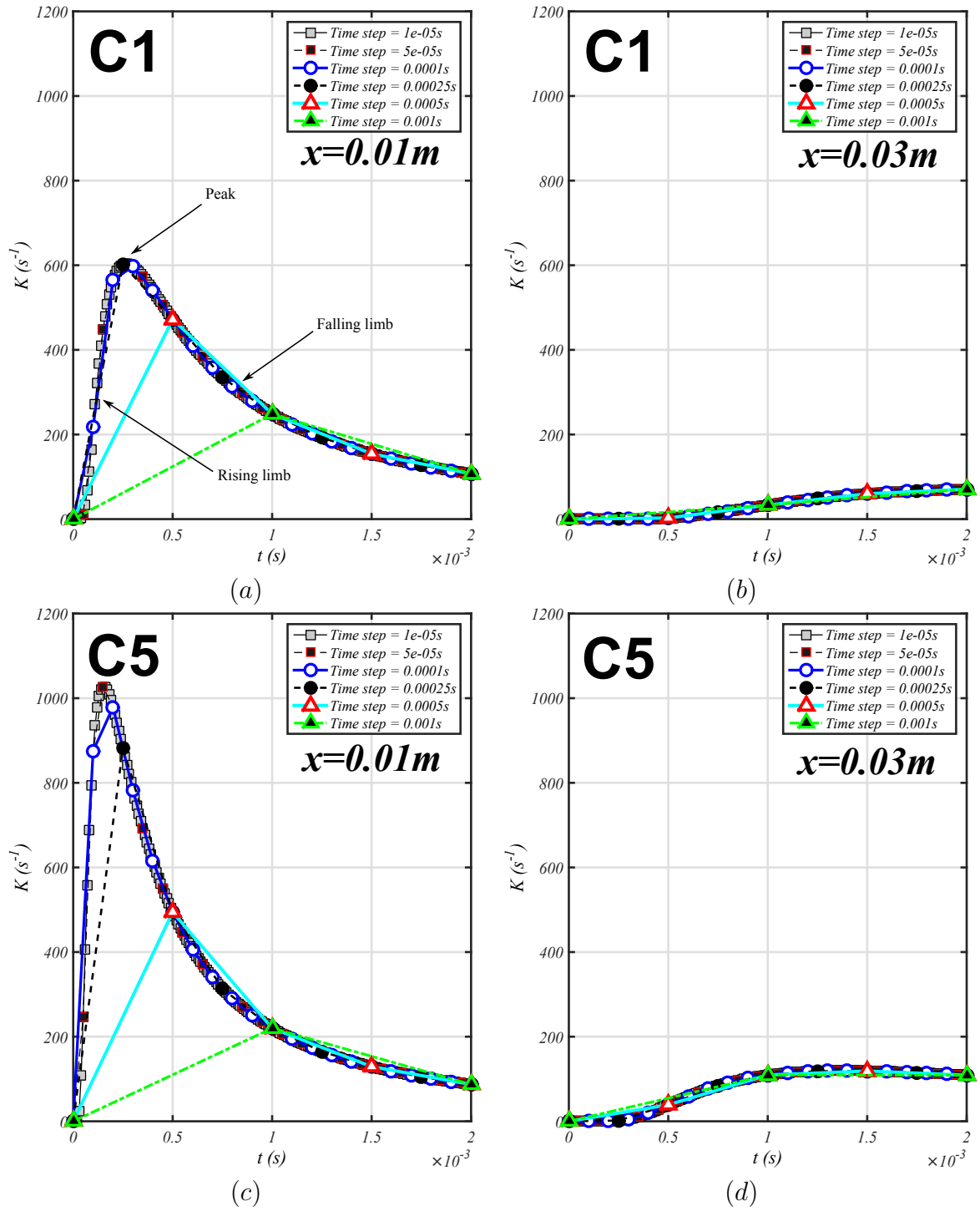


Figure 5.2: Kernel function time step analysis for the Case 1. (a) Kernel function at $x = 0.01$ m. (b) Kernel function at $x = 0.03$ m

Estimation of S_f for the sensitivity analysis

To select the fixed S_f value considered in the sensitivity analysis, a preliminary parametric study was performed. Figure 5.3 show results obtained with the proposed model compared with experimental results (mean and standard deviation values) at a position $x = 0.19m$ for the Case 3, which was considered because it was the

intermediate case. Several velocities ranging from 0.1 m/s to 1 m/s are considered for two different fixed values of S_f ($S_f = 0.1$ and 0.2), as shown in Figs. 5.3a and b, respectively. In both cases, it is observed that results obtained with lower velocities are closer to the elevations given by the experimental results. However, results of Fig. 5.3b ($S_f = 0.2$) are even closer than those observed in Fig. 5.3a ($S_f = 0.1$). In addition, the peak values for results with $S_f = 0.2$ present shorter shifts in time than those for $S_f = 0.1$ in relation to experiments. This suggests that lower values of S_f induce faster flow propagation represented by the obtained results of the proposed model. Note that larger S_f values tended to displace the peaks of the curves to the right, resembling a larger effect of frictional effects. Based on the closer agreement of results obtained with $S_f = 0.2$ with the experimental ones, this value has been considered as the constant value to carry out the sensitivity analysis of \bar{u} and S_f .

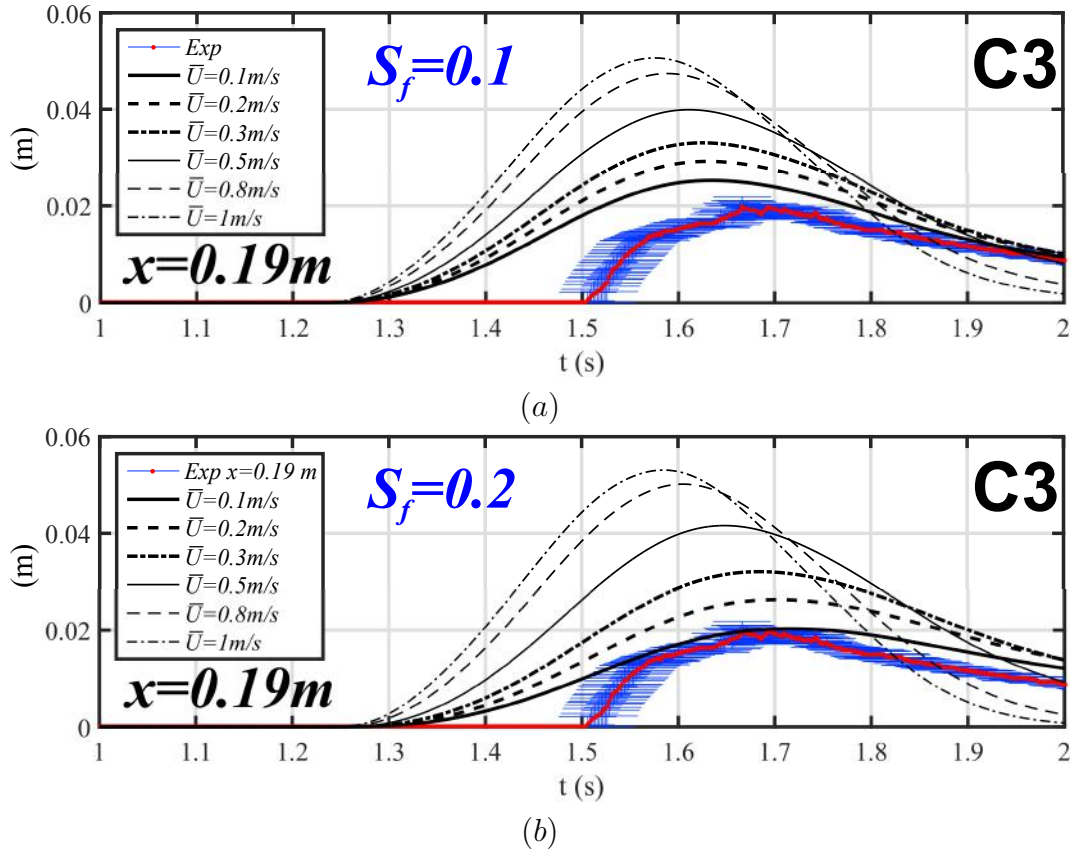


Figure 5.3: Model outputs from the sensitivity analysis to identify the S_f parameter that better attains the maximum elevations of experiments, $x = 0.19$ m, Case 3. (a) $S_f = 0.1$. (b) $S_f = 0.2$.

Sensitivity analysis for model calibration

Once the fixed parameters are estimated ($\bar{u} = 0.3$ m/s and $S_f = 0.2$), the parametric analysis considering variable velocities from 0.1 m/s to 1 m/s and S_f values from 0.05 to 0.3 was performed considering three different positions in the analysis ($x = 0.01$

m, $x = 0.11$ m and $x = 0.19$ m), as presented in Fig. 5.4. It is expected that the present analysis, besides to allow understanding the influence of the \bar{u} and S_f parameters on the model output, it gives information about the order of the roughness Manning coefficients applicable for the present shipping water application, which is information that still is not available in literature.

Figure 5.4 shows the results for the Case 1, which has been considered representative of the other cases. This case, which presented the smallest amount of water on deck was used for model calibration.

Figures 5.4a, c and e show the results for a fixed $S_f = 0.2$ and different velocities for the three positions. In each graph, the advection coefficients of the model (A) corresponding to these velocities are shown to have an idea of their order of magnitude.

It is observed that for $x = 0.01$ m, the obtained results from model agree well with the experimental data from $1.35 \lesssim x \lesssim 1.7$ s, capturing the rising and falling limbs and the peak, even though small differences in elevations are observed at the peaks for the different velocities. These differences are more notable at positions $x = 0.09$ m and $x = 0.19$ m, as shown in Figs. 5.4c and e, respectively, where it can be verified that there is a better agreement for the lower velocities to attain the peak of experiments, and to capture the complete time series in a reasonable manner ($\bar{u} = 1$ to 3 m/s). In Fig. 5.4c, it is observed that model results for $0.1 \leq \bar{u} \leq 0.3$ m/s are which present the best agreement with experiments, being close to the peak value and adjusting well the falling limb. Moreover, at a longer position from the origin ($x = 0.19$, Fig. 5.4e), it can be verified a larger delay in the peaks of model results with respect to experiments.

On the other hand, Figures 5.4b, d and f show the results for a fixed $\bar{u} = 0.3$ m/s and different S_f values. For each S_f value, its corresponding Manning coefficient (n_{Mann}) is calculated (and shown in the legend) according to the formulae described in Section 2.1.2. For $x = 0.01$ m, all the results are very close from each other and agree well with experiments for $1.35 \lesssim t \lesssim 1.7$ s. Then, in Figs. 5.4d and f, spatial shifts in the peak values are observed for each water elevation distribution at $x = 0.09$ m and $x = 0.19$ m, respectively. In both cases, it can be verified that the smaller S_f coefficient gives the model output curve with the highest peak, which presents an evident temporal shift in relation to the one from the experiments. It suggests that water propagates faster with a small effect of frictional effects. Furthermore, it can be observed that as S_f increases, the peaks of model curves displaced to the right, which suggests a slower flow propagation. By observing the Fig. 5.4f ($x = 0.19$ m), it is possible to note that the curves that better approximated the mean maximum value and captured the elevations of the experimental results are those obtained in the range of S_f from $S_f = 0.15$ to 0.30 , which for the present case study would

correspond to n_{Mann} values in the range $0.15 - 0.22m^{1/3}/s$, approximately. From this range is possible to choose a S_f parameter for the model implementation. For purposes of practicability, the intermediate value $S_f = 0.2$ was chosen arbitrarily for the model implementation and validation with all the study cases.

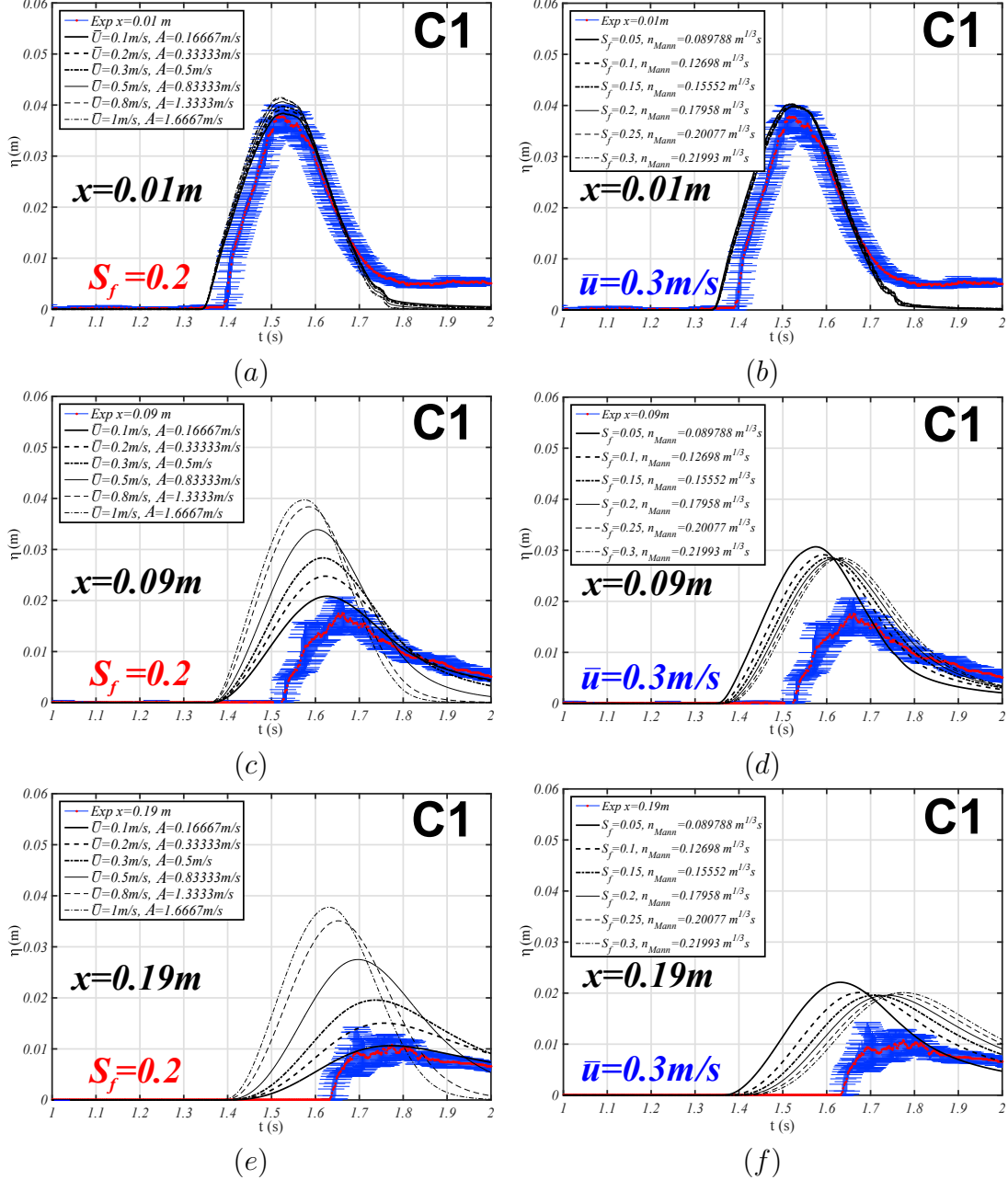


Figure 5.4: Sensitivity analysis of \bar{u} and S_f for Case 1. (a) Constant $S_f = 0.2$, \bar{u} varies, $x = 0.010$ m. (b) Constant $\bar{u} = 0.3$ m/s, S_f varies, $x = 0.010$ m. (c) Constant $S_f = 0.2$, \bar{u} varies, $x = 0.11$ m. (d) Constant $\bar{u} = 0.3$ m/s, S_f varies, $x = 0.11$ m. (e) Constant $S_f = 0.2$, \bar{u} varies, $x = 0.19$ m. (f) Constant $\bar{u} = 0.3$ m/s, S_f varies, $x = 0.19$ m

The same analysis described above for the Case 1 has been performed, only for verification purposes, for Case 5 (Fig 5.5). Figures 5.5a,c and e show the results for

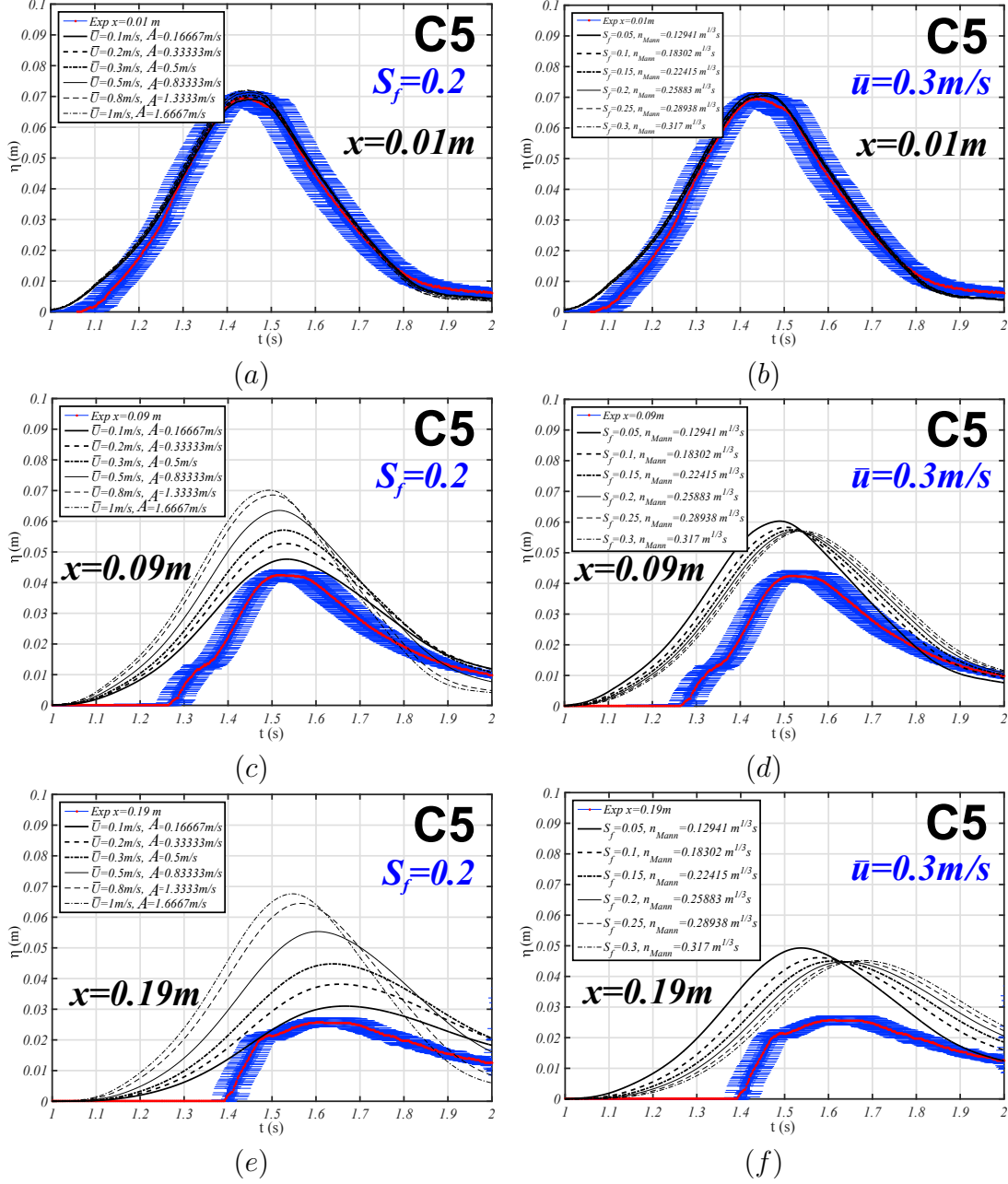


Figure 5.5: Sensitivity analysis of \bar{u} and S_f for Case 5. (a) Constant $S_f = 0.2$, \bar{u} varies, $x = 0.010$ m. (b) Constant $\bar{u} = 0.3$ m/s, S_f varies, $x = 0.010$ m. (c) Constant $S_f = 0.2$, \bar{u} varies, $x = 0.11$ m. (d) Constant $\bar{u} = 0.3$ m/s, S_f varies, $x = 0.11$ m. (e) Constant $S_f = 0.2$, \bar{u} varies, $x = 0.19$ m. (f) Constant $\bar{u} = 0.3$ m/s, S_f varies, $x = 0.19$ m

the different velocities, keeping $S_f = 0.2$ as constant. The trend of the results obtained with the model are quite similar to the ones for Case 1. In Fig 5.5a, all values are close and adjust well the experiments. The differences between the curves are better observed in Figs 5.5c and d. In the former ($x = 0.09$ m), it is clearly observed that the lower velocities ($0.1 \leq \bar{u} \leq 0.3$ m/s) capture well the complete series of experimental data, including the peak. The peaks of the curves obtained presented

shifts between them, and although they are not completely noted in Fig. 5.5c, these are well identified in Fig. 5.5(x = 0.19 m). It seems that, for the present condition of analysis, results in the range of $0.3 < \bar{u} < 0.5$ m/s, approximately, presented a better approximation to the peak of the experiments, in spite of overestimation of the elevations.

On the other hand, Figures 5.5b,d and f present the results for a varying S_f and a fixed $\bar{u} = 0.3$ m/s. All model results agree well with experiments for $x = 0.01$ m (Fig. 5.5b). Then, as observed in the Case 1, for longer positions from the origin, spatial shifts between the curves for the different S_f values are more evident, as observed in Figs. 5.5d and f for $x = 0.09$ m and $x = 0.19$ m, respectively. In both cases, the peaks of the model output curves placed to the left and to the right of the mean maximum value of experiments, suggest faster and lower flow propagation, respectively. Similarly, as found out in Case 1, the results with S_f from 0.15 to 0.3 are the ones from which the peaks in curves presented more temporal agreement with the experimental ones. For these values, the n_{Mann} coefficients ranged from $0.22m^{1/3}s$ to $0.31m^{1/3}s$, respectively.

5.2 Application 1: Shipping water evolution

The proposed model has been implemented with the parameters described in the previous section, that is, $\bar{u} = 0.3$ m/s, $S_f = 0.2$ and time step equal to $1E - 5$ s.

For validation of the model in this application, ten VWPs are considered, which were positioned on the deck from $x = -0.01$ m to $x = 0.19$ m (considering the bow edge as the origin), separated by 0.02 m from each other (see Fig. 3.8 for reference). Mean and standard deviation values are calculated from the repetitions to compare the obtained model results. For each case considered, the input series used in the model corresponds to the freeboard exceedance time series, i.e., F series, of each event.

Figure 5.6 shows the comparisons for the Case 1, which presented a maximum freeboard exceedance (η_0) of 0.042 m. It can be observed that the model agrees well with experiments at the beginning of the deck (e.g., $x = 0.01$ m and $x = 0.03$ m). At this region, obtained results are very close to the range defined by the standard deviations of experiments. However, an small underestimation of amplitudes is observed for the curve tails for $t \gtrsim 1.7$ s. At positions over the deck farther than the origin ($x \gtrsim 0.05$ m), the trend followed at the curve tail starts approximating the experiments in a closer way. At the same time, it is observed that the model overestimates the experiments from the beginning of the curves to the point at which they reach their peaks. Regarding this, it has to be considered that the model was developed under the assumptions of constant propagation velocities and considering

an invariable amount of shipping water as defined by the freeboard exceedance series, then, these might be causes of the differences observed. Despite of this, the model captured the complete trend of the experiments in an approximated way. Moreover, it also approximated the point in time at which the peak values of experiments occurred.

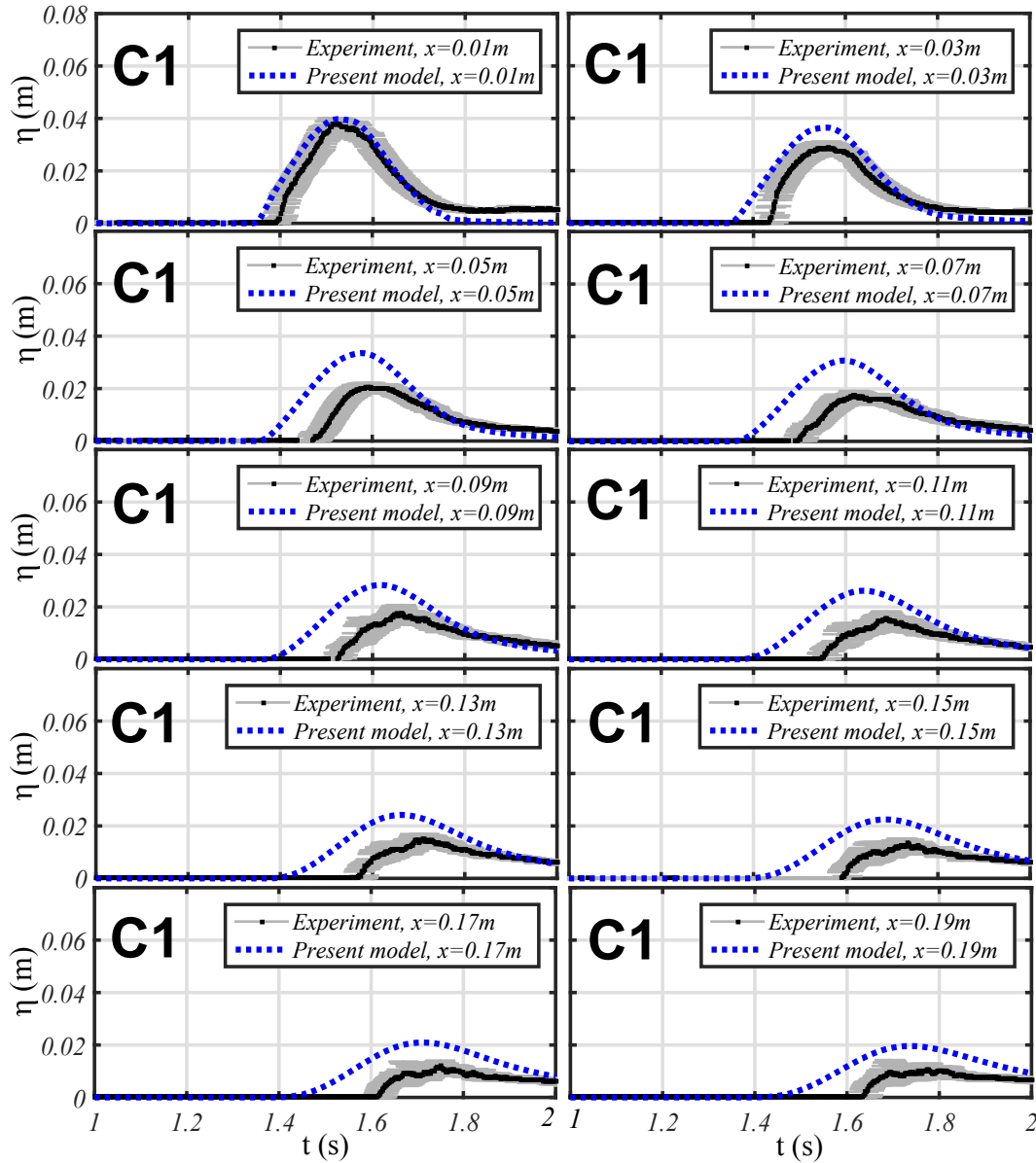


Figure 5.6: Model validation Case 1. Time step = $5E - 5$ s, $S_f = 0.2$, $\bar{u} = 0.3$ m/s.

Figures 5.7 and 5.8 show the results for the Cases 3 and 5, respectively. For these cases, maximum freeboard exceedances of 0.058 m and 0.072 m, respectively, were observed in the input functions, suggesting resultant amounts of water on deck larger than in Case 1. However, it is possible to observe very similar trends of the proposed model to attain the experiments. The overestimation of the curve tail is also observed in these cases at $x = 0.01$ m and $x = 0.03$ m over the deck, were

the water elevations given by the model for $t < 1.7$ s are closer to the experimental ones. Subsequently, as x increases, the model tends to overestimate the experiments including the curves tails. In spite of that, it is interesting to observe how the peak values of model capture the experimental ones.

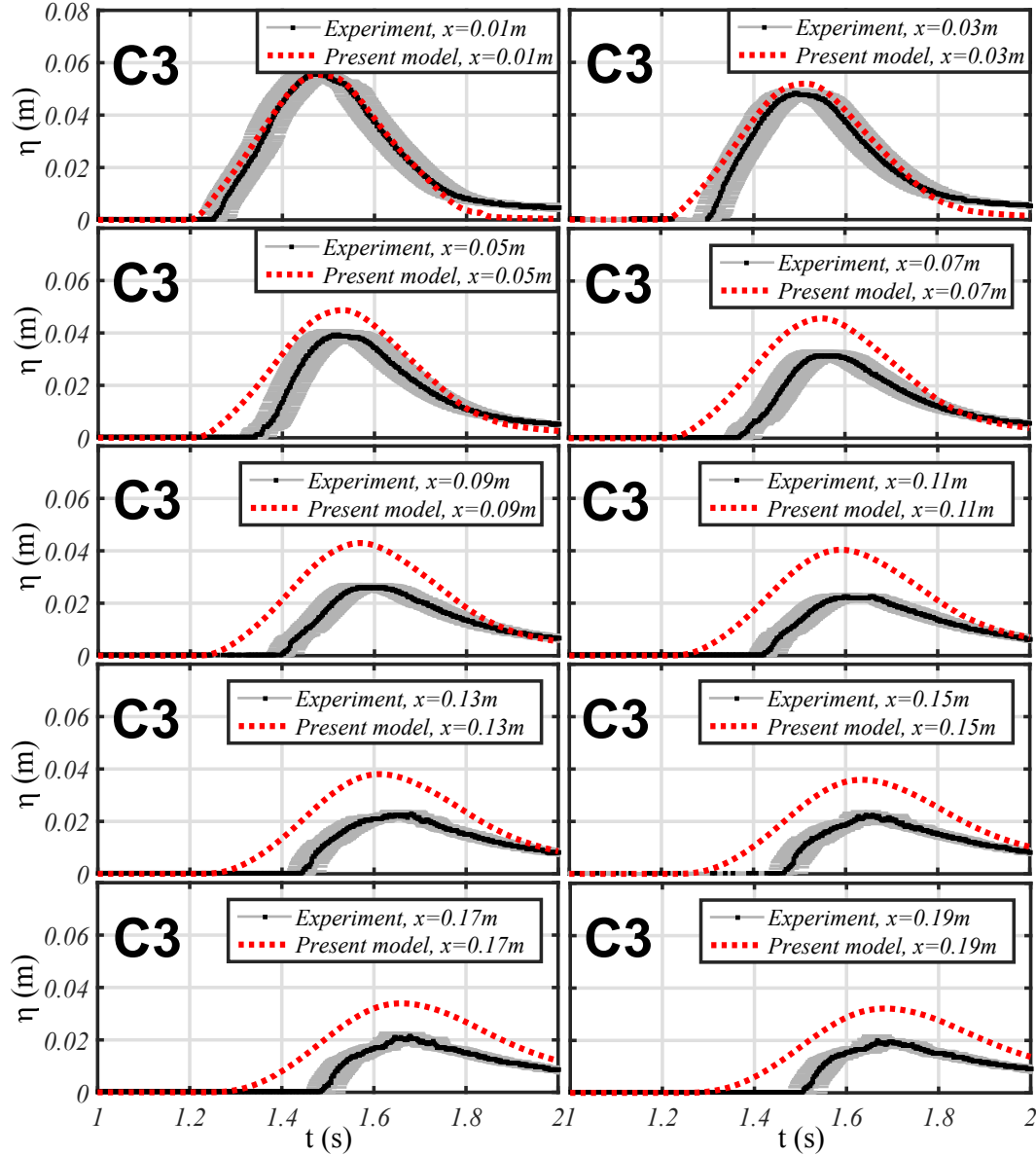


Figure 5.7: Model validation Case 3. Time step = $5E - 5$ s, $S_f = 0.2$, $\bar{u} = 0.3$ m/s.

Overall, results suggest that the proposed model allowed to capture the trend followed by the experiments, despite of two main differences that were derived from the model assumptions. In the first place, the model time series did not started at the same time as the time series of experiments, which may be mainly related to the acceleration effects of the wavefront propagating onto the deck. These effects of acceleration are not considered in the development of the model, which assumes a constant horizontal flow velocity during all the propagation over the deck. In the

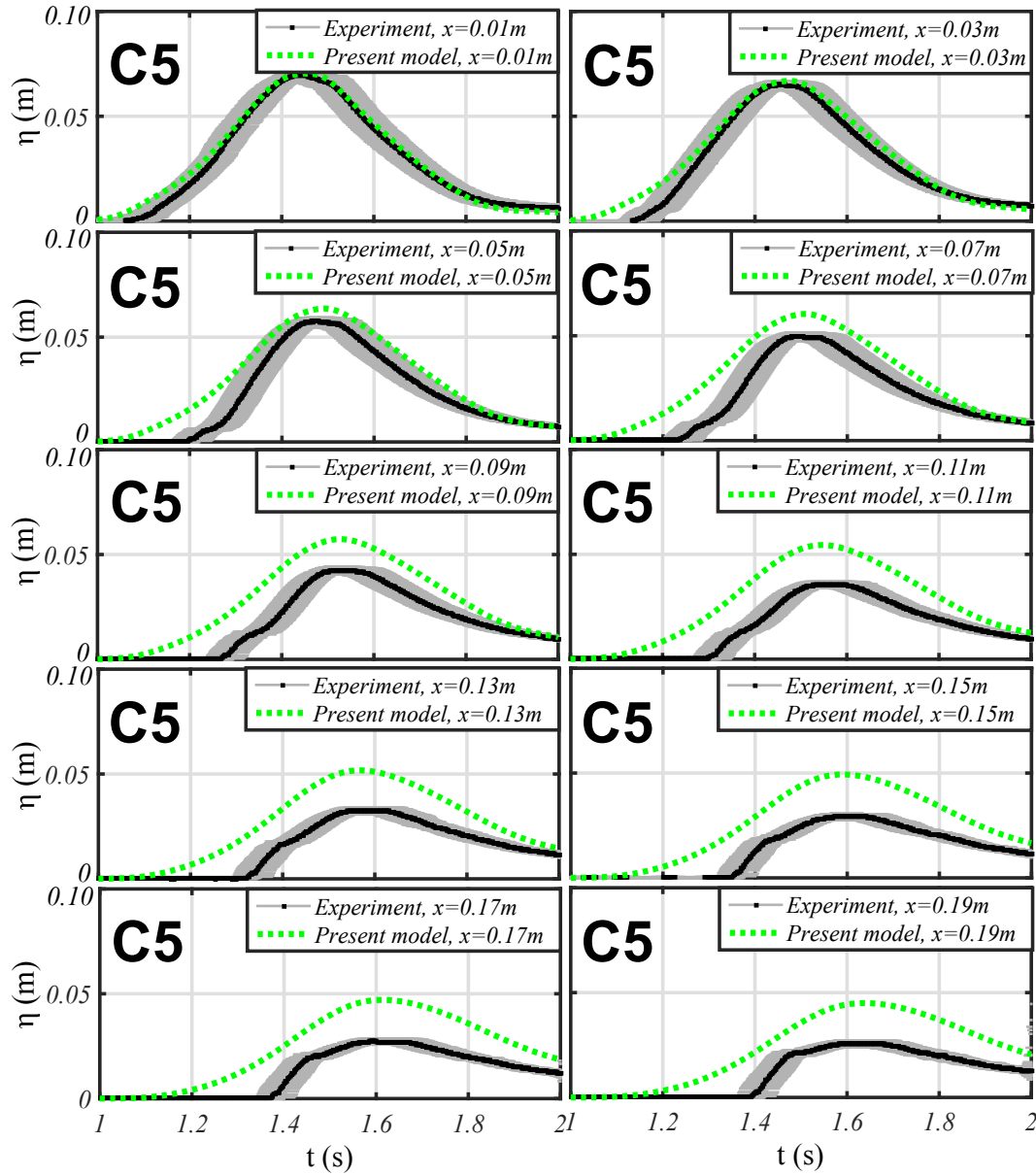


Figure 5.8: Model validation Case 5. Time step = $5E - 5$ s, $S_f = 0.2$, $\bar{u} = 0.3$ m/s.

second place, the model overestimates the amplitudes; however, in an acceptable way if, for instance, a security factor needs to be considered. This may be in part, related to the consideration of an invariant shipping water volume, defined by the freeboard exceedance time series, that is, the input function of the model. Then, it has to be considered that possible changes in the resultant volume on deck due to the wave-bow interaction are disregarded, thus, it might be a reason that explains the overestimation of the experimental amplitudes.

Regardless of the aspects described above, the model captured well the generated trends of the experiments for all cases (i.e., Cases 1 to 5), considering the same kernel parameters and varying only the input data obtained from the input series, say F and η_0 . The model allowed representing the rising limb, peak and falling limb of

experimental data curves. Additionally, it might give approximated information of the points in time at which the maximum values of experimental time series occurred.

5.2.1 Comparison with DB model

The results obtained with the proposed model have been compared with the classical dam-break (DB) approach of Stoker to estimate the shipping water elevations. The DB model of Stoker has been implemented considering the same positions as in the previous section. For all the cases, the respective maximum freeboard exceedance of the input time series F has been considered for its implementation. The model has been started at the time when the shipping water starts invading the deck, which was assumed when the F series began accounting with water elevations $\eta > 0$. For explanation purposes, we present the comparisons for Cases 2 and 4, considered as representative of the other cases, as shown in Figs. 5.9 and 5.10, respectively.

Figure 5.9 shows the comparisons of water elevations (η) at different positions for the Case 2 ($\eta_0 = 0.054$ m). At $x = 0.01$ m, the DB time series maintains an horizontal trend of amplitudes similar to the peak values of the proposed model and experiments for $t > 1.3$ s. At farther positions from the origin, the DB results maintain such an almost constant trend, even though the water elevations of experiments decrease for these positions.

On the other hand, Figure 5.10 presents the comparisons for the Case 4 ($\eta_0 = 0.063$ m). In this case, the shipping water volume was larger than in Case 2; however, the behaviour of the DB results compared with the proposed model and experimental ones is very similar.

In general, it can be verified that, although the DB model almost approached the rising limb of the proposed model curves, it did not give approximated information about peaks time of occurrence, as obtained with the proposed approach. Furthermore, the DB results did not represent the decay tendency observed after the peak values in the proposed model and experiments.

In order to verify how large is the overestimation of the experiments by both, the proposed model and the DB results, a practical approach has been considered as the indicator of overestimation. It consists in considering the areas under the curves of the time series of results (i.e., from $0 \leq t \leq 2$ s) to have a general idea of overestimation between the analytical and experimental approaches.

Figure 5.11 shows the comparisons of the areas under curves for experiments (mean values curves) with the proposed model (Fig. 5.11a), and the DB model (Fig. 5.11b), for the different positions over the deck.

Notice that the proposed model presents a closer agreement with experiments

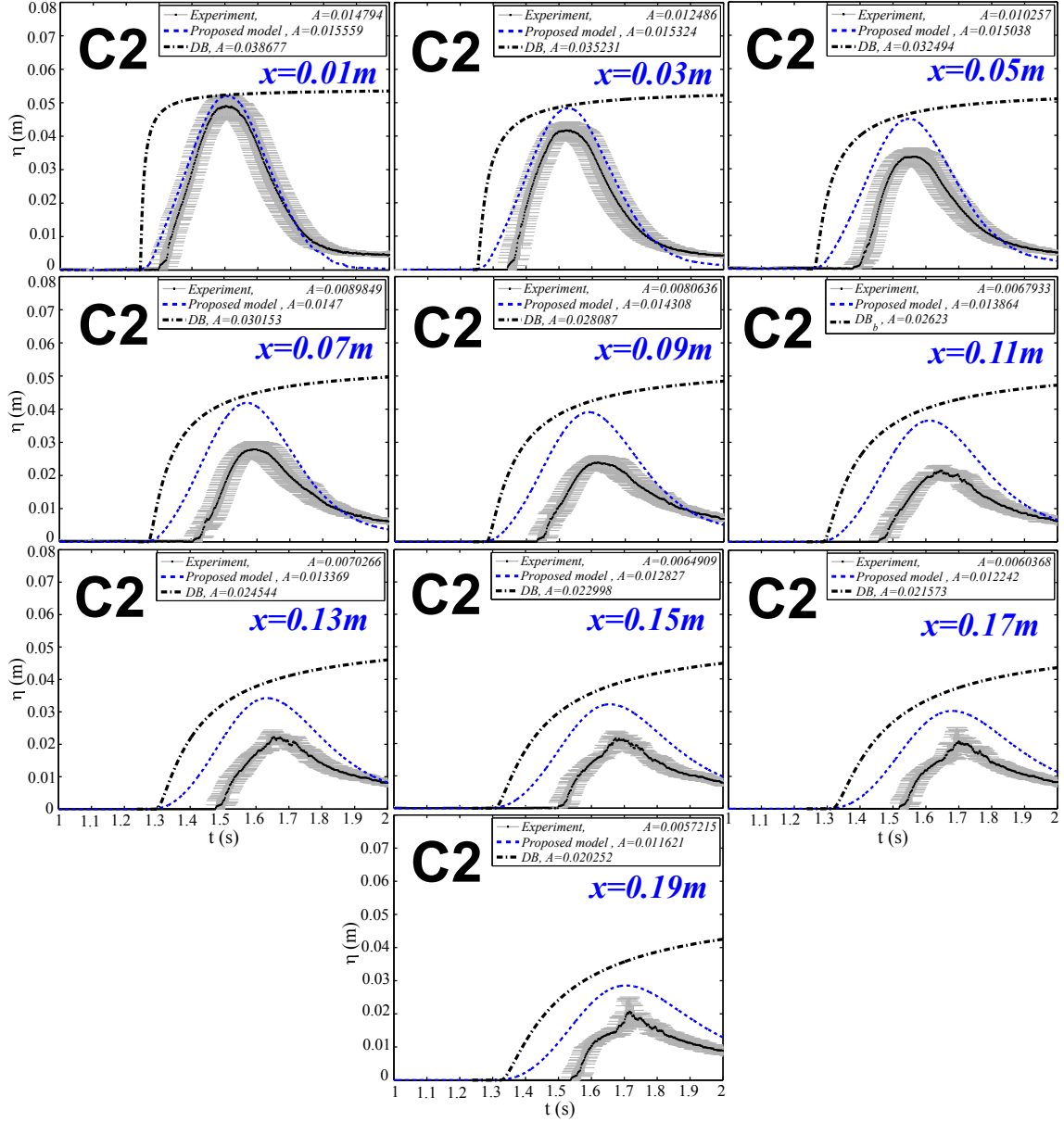


Figure 5.9: Proposed model and experimental results comparison with the DB approach for Case 2. Time step = $5E - 5s$, $S_f = 0.2$, $\bar{u} = 0.3$ m/s, $\eta_0 = 0.054$ m.

than the DB results. For the proposed model, the agreement is closer at positions near the origin, whereas for the DB model, there is an almost constant overestimation for all positions over the deck.

Overall, for both models the differences of areas in relation to experiments are larger for Case 5 and smaller for Case 1. the approximations are better at positions near the origin, and tend to reduce for positions farther from it.

The present approach allowed to verify that results obtained with the proposed model yielded an acceptable overestimation of the resultant water on deck when compared against the DB results.

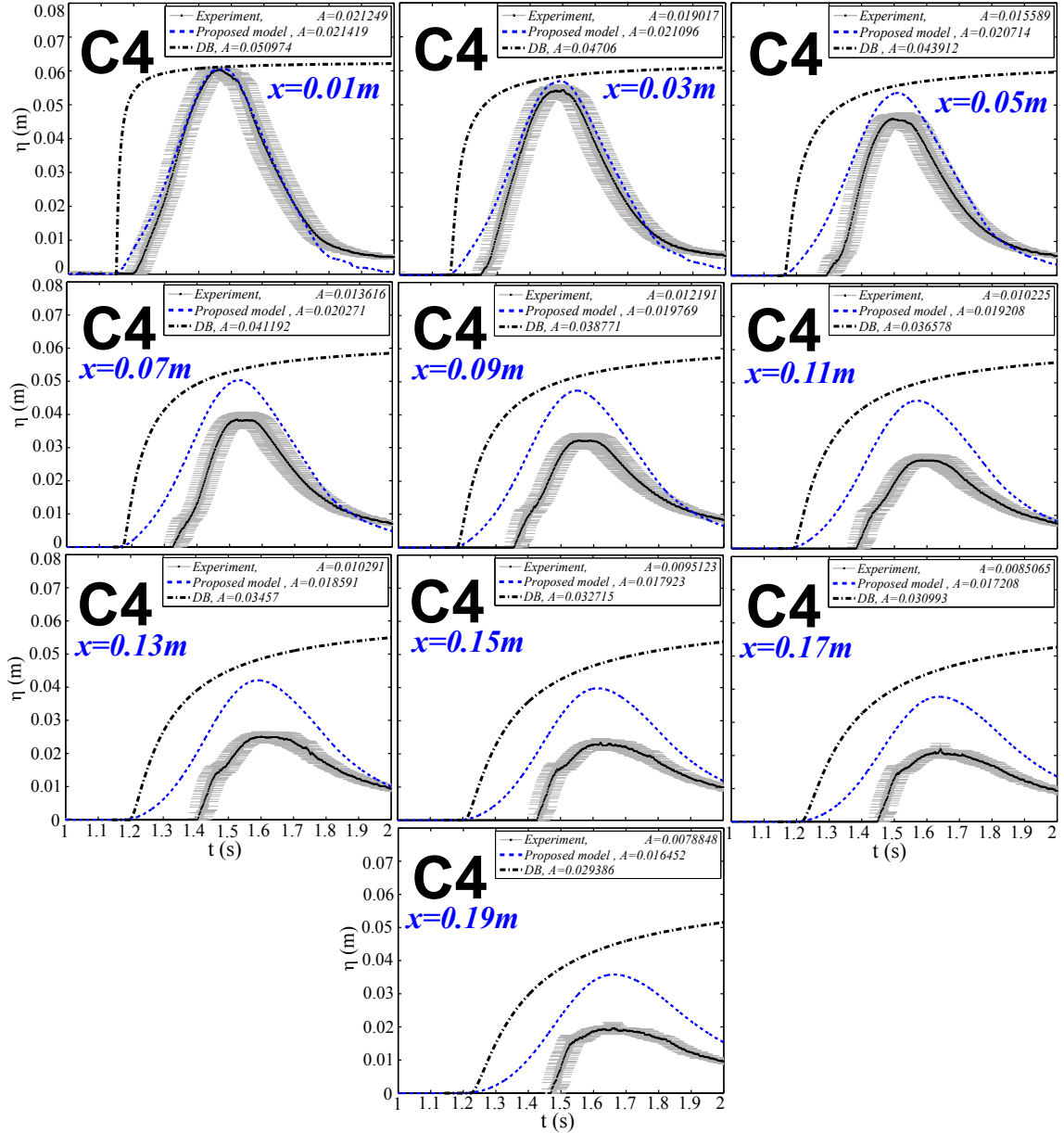


Figure 5.10: Proposed model and experimental results comparison with the DB approach for Case 4. Time step = $5E - 5$ s, $S_f = 0.2$, $\bar{u} = 0.3$ m/s, $\eta_0 = 0.063$ m.

5.3 Application 2: Loading on deck estimation

In this section the model implementation methodology described in previous section was extended to estimate the vertical loading on the force balance region using the approach described in Section 2.3. The structure is fixed, then, static water head is estimated from water elevations obtained with the proposed analytical approach (convolution model) and compared with experimental measurements given by the force balance. Furthermore, the proposed model results are compared with the load results obtained with the dam-break model of Stoker.

As described in Section 2.3, the sensing area of the balance, which was embedded

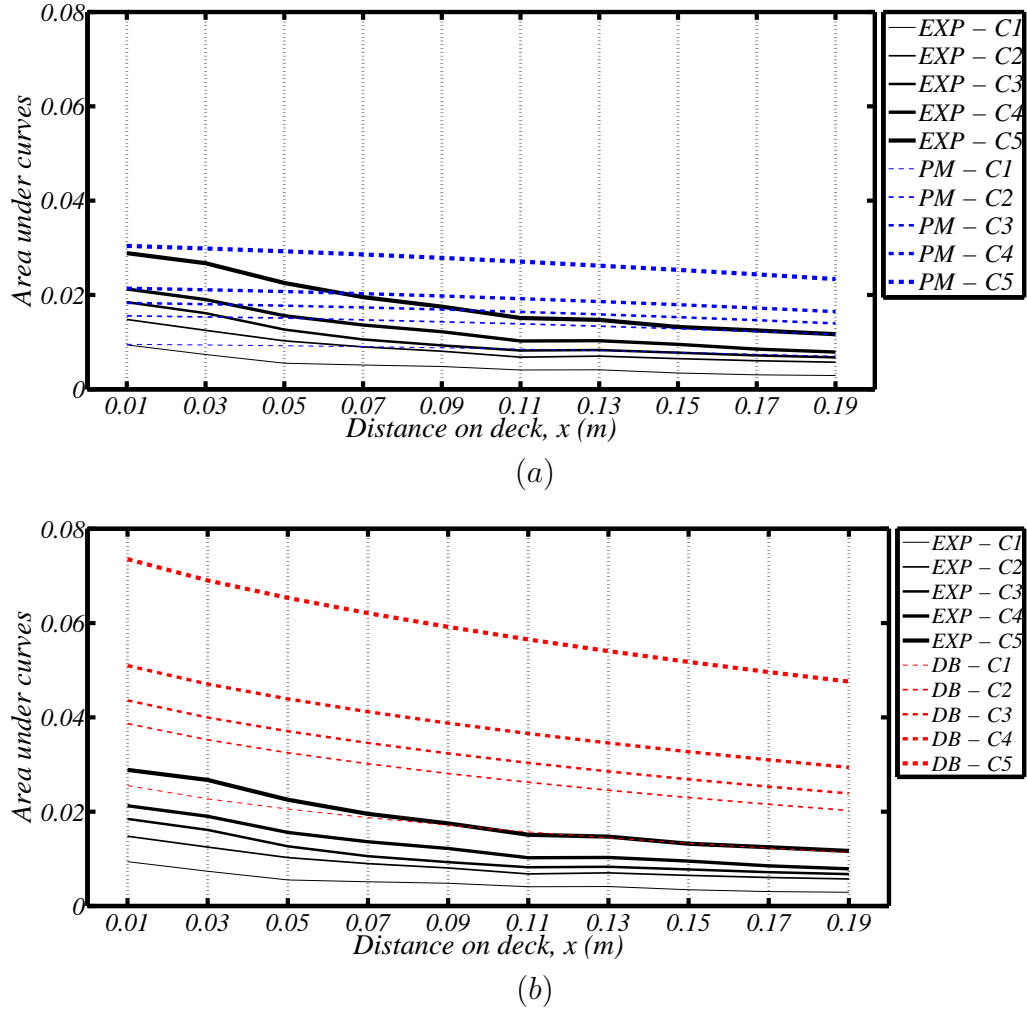


Figure 5.11: Areas under the water elevation time series for $0 < t < 2$ s. (a) Proposed model and experiments. (b) Dam-break approach and experiments.

to the deck of the structure, is discretized in regions defined by virtual wave probes positions, as observed in Fig. 5.12a. In order to cover the sensing area of the balance, 17 VWP's from $x = 0.02$ m (VWP01) to $x = 0.18$ m (VWP17), separated by 0.01 m, were considered for the application. With the water elevations obtained analytically, static pressure was calculated and assumed constant over the deck area adjacent to each wave probe. Then, vertical forces are assumed acting downwards at the regions centres and the total vertical load time series are calculated. Only for illustrative purposes, Figures 5.12b and c show the mean values time series obtained experimentally for the positions at which the model will be implemented in Cases 2 and 4 (17VWP's: VWP01 to VWP17, $0.02 \text{ m} \leq x \leq 0.18 \text{ m}$), to know the typical tendencies followed by the flow in the surface of interest.

The input function to implement the convolution model corresponds to the maximum freeboard exceedance time series obtained from VWPw0 ($x = -0.005$ m, Fig. 5.12a), obtained as described previously in Section 4.2.2. Figures 5.13a-f show

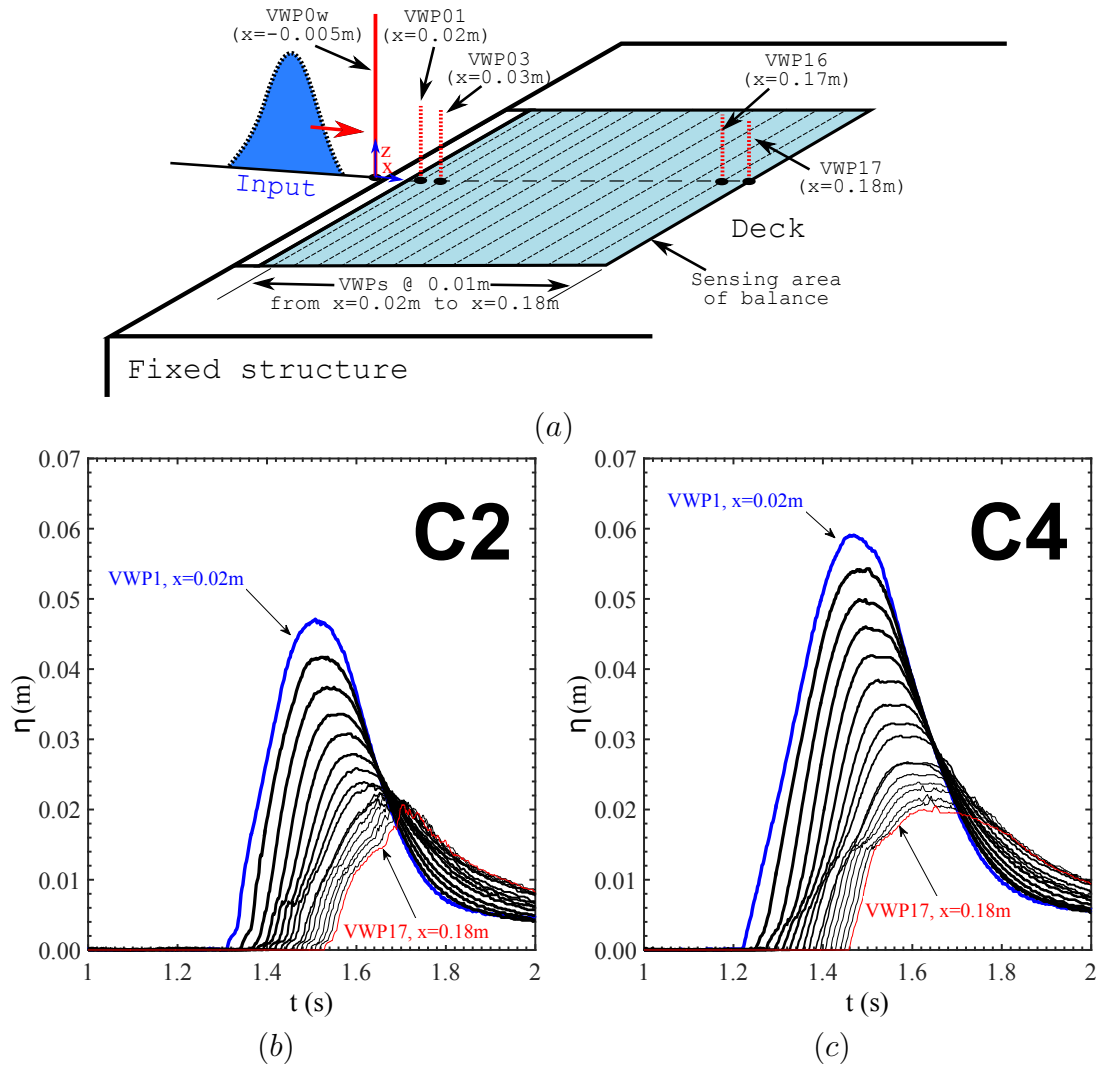


Figure 5.12: Discretization of the sensing area of the balance to estimate time series of water elevations for the vertical loading analysis. (a) Discretization. (b) Mean values of water elevation time series obtained experimentally for Case 2 (illustrative purposes). (c) Mean values of water elevation time series obtained experimentally for Case 4 (illustrative purposes).

the input time series considered for the five study cases. Note that only the mean values are considered for the implementation of the proposed model (PM) and that the start time of those series are considered to implement the DB approach.

Figures 5.14 5.15 and 5.16 present the results of total vertical loading obtained with the analytical models and experiments for the Cases 1,3 and 5, respectively. Each figure shows the comparisons between analytical and experimental results. The results obtained with the present model and those obtained with the dam-break model of Stoker (*DB*) are presented. To implement this last, it was imposed the time at which the series of freeboard exceedance started (see Fig. 5.13 for reference).

In order to analyze the differences in the total loading for each method, comparisons between areas of curves were done. To do this, a parameter α was defined as

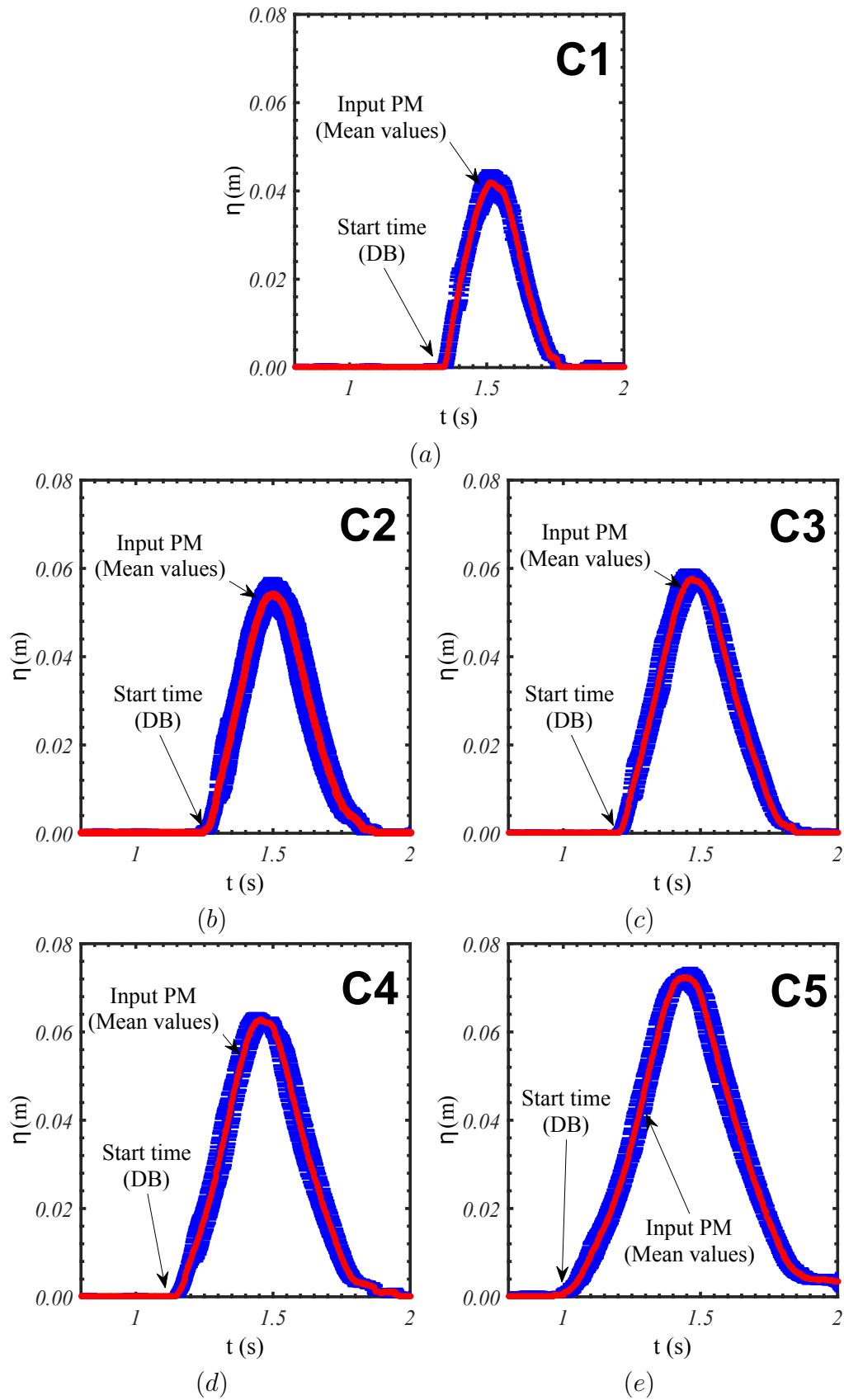


Figure 5.13: Time series of water elevation from experiments used as input series for the vertical loading estimation. (a) Case 1. (b) Case 2. (c) Case 3. (d) Case 4. (e) Case 5.

the ratio of areas under the curves of analytical and experimental results, considering the interval of time $0 \leq t \leq 2$ s. Although the α parameter does not account for specific information such as maximum values or points in time, it may give an idea about the overestimation of the experiments.

Figure 5.14 shows the comparisons for the Case 1. Notice that the proposed model presents a realistic agreement with the experiments. Despite of a shift to attain their starting time, it allows capturing the trend of the complete signal, specially the peak and the falling limb of the curve. As an indicative of overestimation, the α parameter indicates that the area under the curve of the proposed model overestimates that of the mean values of experimental data about 2.4 times. Conversely, the *DB* results overestimated the experimental results in a more significant manner (almost five times the area under the curve of experiments). Moreover, there is also a shift in time to attain the beginning of the experimental series.

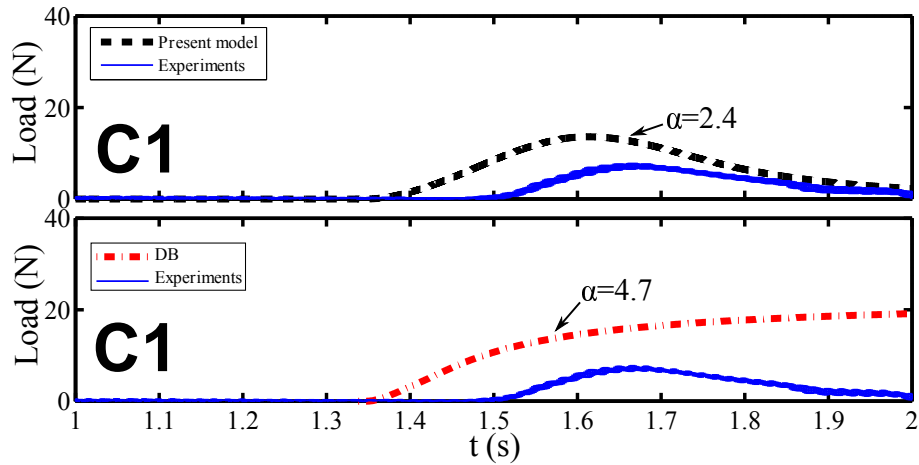


Figure 5.14: Total vertical loading on the force balance for the Case 1: Comparison of experiments and results obtained with the proposed model (above) and the dam-break approach (below).

Figure 5.15 presents the comparisons for the Case 3. The total loading results obtained with the proposed model again captured the complete curve of experimental results, following its trend and almost assessing the time at which maximum load occurred, similarly as it was observed above for the Case 1. The shift in time to attain the initial stage of the experiments is also observed; however, for this case, the overestimation in results is lower than in Case 1, as can be inferred by $\alpha = 2.2$. For the case of the *DB* comparison, it is observed overestimation of experiments similarly as in Case 1. In the present case, the α value decreased about 10% in relation to Case 1.

Finally, Figure 5.16 presents the comparisons for the case that presented the largest amount of water on the deck (Case 5). In this case, the vertical loading started at an earlier time than in previous cases, perhaps due to the small freeboard

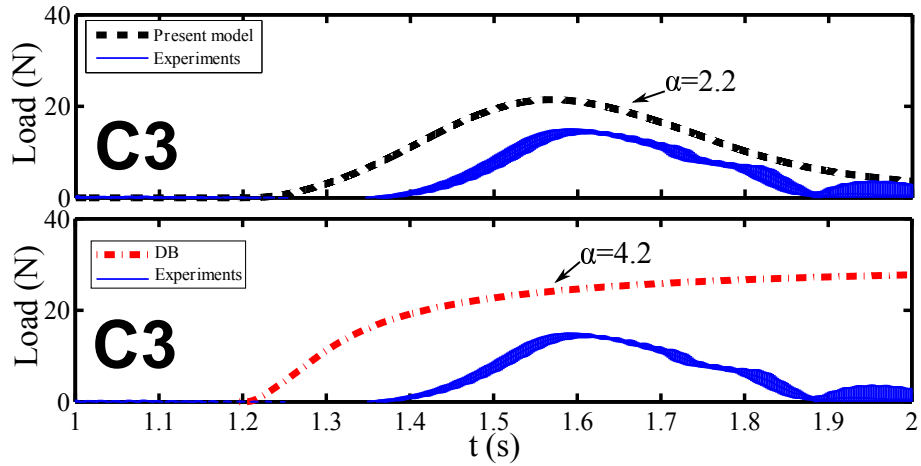


Figure 5.15: Total vertical loading on the force balance for the Case 3: Comparison of experiments and results obtained with the proposed model (above) and the dam-break approach (below).

(~ 0.006 m). Results with the present model still captured the shape and trend followed by experimental data, in spite of an acceptable overestimation in amplitudes, as observed in the other cases. In this case, the α parameter indicates a lower overestimation of areas under results curves than in Cases 1 and 3. This decrease was also observed for the *DB* results. However, for the Case 5, the *DB* results presented overestimation of experiments suggested by $\alpha = 4.5$, lacking of realism to follow their trend.

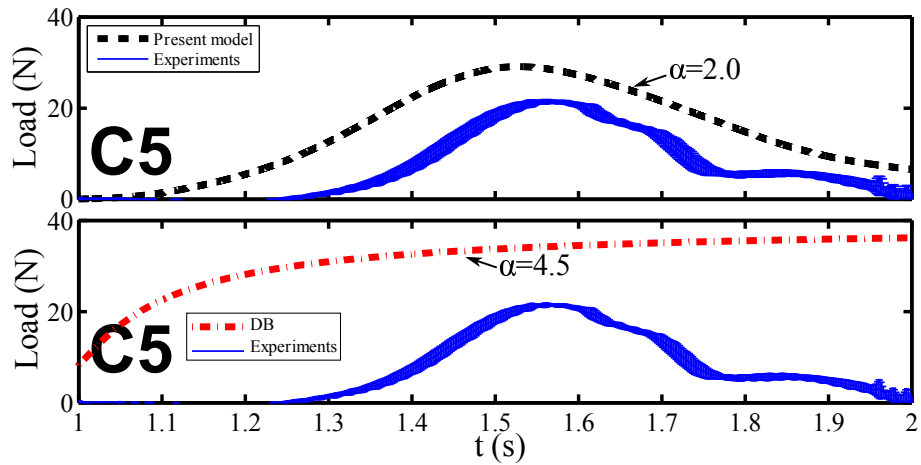


Figure 5.16: Total vertical loading on the force balance for the Case 5: Comparison of experiments and results obtained with the proposed model (above) and the dam-break approach (below).

The areas under the total vertical load curves ($0 \leq t \leq 2$ s), for the five study cases, are summarized in the Fig. 5.17. It can be noted that the areas increase from Case 1 to Case 5 in all the results, where both, the proposed model and the *DB* model overestimated the experimental results. The areas for *DB* are about

four times the area of the experiments, as verified before with the α indicator. Conversely, the proposed model overestimated experiments only about two times. Overall, these results serve as an indicator to estimate of how much the global loading is overestimated for each model, which could be used as an starting point for the design of a security factor in practical applications. However, such general information does not allow defining which model is most adequate because there are other factors of importance that have to be considered such as maximum values and the trends followed by results.

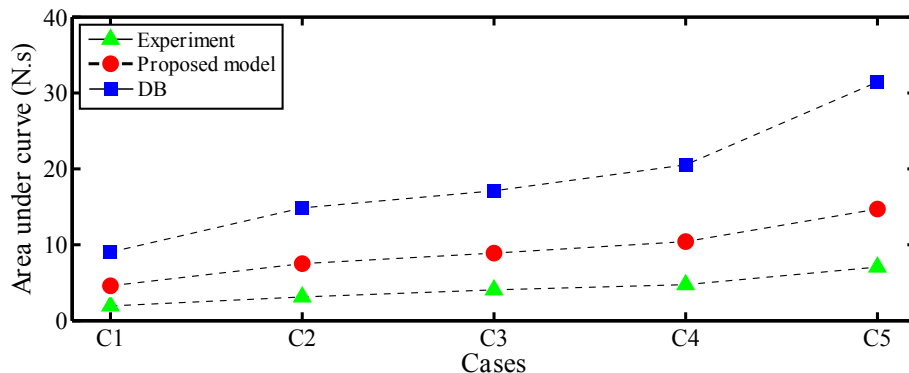


Figure 5.17: Areas under the total vertical loading curves for the experimental and analytical results at each study case.

The observed results clearly demonstrate the strengths and limitations of the analytical models analyzed when compared with experiments. For the case of the dam-break model, there is an ease of implementation. However, besides it overestimates significantly the experiments, it is necessary to know the maximum freeboard exceedance for its implementation. Moreover, the starting time of the simulation has to be imposed according to user's criteria. Results observed clearly demonstrated overestimation of experimental results and a lack of realism to follow their trends, specially to account for important information such as the peak values and the falling limb of time series. In counterpart, results obtained with the proposed model allowed a realistic representation of the signals, giving approximated information about the peak values and covering the complete experimental data. The model presents the limitation to attain the time at which the experiments begin, which is a possible consequence of the constant velocity assumption in its development; however, this is very acceptable since the model does not need to set a point in time to run the simulation, as needed in the *DB* model. In fact, the proposed model considers the complete input function, which in real applications can be measured or predicted before the shipping water on deck.

Chapter 6

Conclusions

The shipping of water on coastal, naval and offshore structures is a problem that requires combination of analytical, numerical and experimental approaches to be studied, aiming to improve design of the structures and to reduce operational problems.

In project or risk assessment stages, practical estimation of shipping water evolution and derived loads are of main interest. Thus, analytical models are valuable tools for their analysis. In this way, development and validation of analytical methodologies are of importance to perform loading estimations. However, validation of methods still requires systematic experiments with high-resolution and repeatable data.

In this thesis, it was proposed an alternative analytical approach to represent the evolution of shipping water and related vertical loads on deck of a fixed structure using convolution. Basically, it regards the direct application of the advection-diffusion equation, widely used in other research areas such as Hydrology, to the shipping water problem. It was validated with systematic experiments of an innovative method to reproduce isolated shipping water events.

Regarding the proposed analytical findings, it is possible to conclude the next points:

- a) The shipping water problem has been modelled concerning the one-dimensional shallow water equations, which were simplified to obtain an advection-diffusion equation applied to the shipping water problem. The approach assumes constant shear stress on the deck using resistance coefficients based on the Manning approach. It allowed considering frictional effects in an approximated way.
- b) A convolution model was considered from a solution of the advection-diffusion equation applied to the shipping water by means of the Green function method, considering a semi-infinite domain with Dirichlet-type boundary conditions,

that is, a boundary condition at the upstream of the domain (i.e., freeboard exceedance time series) and an initial condition in the domain equal to zero (i.e., assuming a dry deck). This solution was represented as a convolution formed by an input and a kernel functions. The latter allowed the use of constant kinematic and diffusion parameters, that is, constant mean shipping flow velocity and a constant resistance coefficient using the Manning approach, respectively.

- b) The model allowed considering the time series of freeboard exceedance as the input of the convolution. This function was convoluted with the kernel function to give water elevations time series at several positions along the deck as outputs.
- c) The model assumes a constant propagation velocity, neglecting acceleration terms. This velocity was considered as the wavefront velocity at the initial stages of shipping water, which corresponds to a horizontal velocity lower than the velocity due to the well developed wavefront over the deck.
- d) A procedure to find adequate input parameters of the proposed model was introduced in order to implement it, verifying the range of applicability of some parameters (i.e., mean shipping flow velocity and resistance coefficient). With adequate parameters, the model was calibrated and applied to the other cases of study.

Furthermore, to validate the proposed model, a systematic experimental investigation of shipping water events was proposed in the present thesis and in related previous papers. It consisted in generation of isolated shipping water events using the wet dam-break method as the wave generation mechanism. It allowed generating five different unbroken waves (bores), which in turn generated five shipping water events. These events, which were of the dam-break and small plunging dam-break types, were used to investigate the applicability of the present analytical approach. It was possible to use high-speed cameras to capture detailed information of the flow propagation, accounting with plenty information to validate the analytical methodology and to identify the main loading stages. Moreover, an experimental procedure was implemented to measure the vertical loading on deck. Regarding the experimental investigation, the next conclusions can be mentioned:

- a) In the shipping water evolution analysis, an image-based methodology that was developed and published in previous research, was employed in this work to obtain two-dimensional reconstruction of the experiments by using virtual wave probes. It allowed obtaining water elevation time series to validate the application of the model for the water evolution.

- b) In the incoming wave evolution analysis, experiments with and without the fixed structure were performed. The generation of the incident waves was investigated in detail and it was verified from image reconstruction the influence of the structure in the features of the incoming wave. As the wave was closer to the structure, more changes in their shape were verified. It was observed that during and after the run-up of the incoming wave on the bow of the structure, there was a reflected wave (backflow) of considerable amplitude. Such a wave may affect the characteristics of the after-coming waves in studies of shipping water events using wave trains, which are typical approaches to study shipping water nowadays. The changed wave patterns may allow events of shipping water different to the expected ones. The single incoming waves generated (i.e., bores) were related to the linear wave theory by making some approximations of their parameters. From the relationships, they were considered waves with steepness of 0.13-0.18 and height of 0.031 m-0.044 m from Cases 1 to 5, respectively. That is, cases with higher freeboard presented steeper waves, whereas cases with lower freeboard longer waves.
- c) For the shipping water evolution analysis with two-dimensional image reconstruction, it was possible to obtain details of water on deck for model validations. The maximum freeboard exceedances were between 0.042 m (Case 1) and 0.072 m (Case 5). All the events presented water propagation onto the deck attaining maximum wavefront velocities in the order of 1-1.1 m/s. Run-up and backflow over the deck of significant amplitudes were also observed for all cases. From observations, it is suggested to perform further studies concerning the backflow loading on deck.
- d) The vertical loading measurements were obtained through a force balance embedded to the deck of the structure. It allowed obtaining time series of total vertical loads on deck, which were employed for the validation of the application of the proposed convolution model to the estimation of vertical loads. The method allowed to know trends of slow-varying shipping water vertical loads for the five cases considered.
- e) The proposed experimental methodology allowed to guarantee the repeatability and reproducibility the data used for model validation.

The proposed analytical approach was implemented to predict shipping water elevations and to estimate the derived vertical loading. Results obtained were compared with the experimental measurements. Also, results of the present work were compared with the classical dam-break model of Stoker, which is a common approach to predict the shipping water evolution. From the comparisons made, the

next conclusions are mentioned:

- a) In the estimation of water elevations at different positions over the deck, the proposed model results presented good agreement with time series given by virtual wave probes (experiments). Main differences were observed to attain the beginning of time series and exact amplitudes in results. The temporal shifts to attain experiments may be related to the assumption of constant propagation velocity to develop the model, neglecting the acceleration effects. Moreover, the overestimation in amplitudes may be related to consider the input series of the model (i.e., freeboard exceedance) outside the deck, then, it is possible that changes in the resultant volume of water on deck due to backflow during the bow run-up stage were disregarded. Despite of these differences, the proposed model captured well the trend followed by experimental data curves, approximating their peaks and decay tendency. On the other hand, the dam-break approach presented overestimation of both proposed model and experimental results, disregarding the expected trend of results along time (i.e., peak values and decay tendencies).
- b) In the estimation of vertical loading by the proposed model, comparisons with experiments demonstrated its improvement over classical approaches (dam-break) for the estimation. Comparisons with measurements of the force balance shown that the proposed model has potential to estimate vertical loading on deck, giving approximate information about the peak values and representing the decay tendency of results.

It is possible to extend the use of the advection-diffusion equation applied to the shipping water problem to several study cases by a preliminary estimation of the advection and diffusion parameters. Regarding the proposed analytical method, more research to evaluate the range of application of the resistance coefficients is suggested. The approach can be extended by investigating solutions obtained with different types of boundary conditions. Concerning the proposed experimental approach, further research may be done to relate it to methods that are typically used (e.g., regular wave trains). It would allow systematic studies to identify local details of shipping water, regarding its interaction with different structure geometries and obstacles over the deck.

Bibliography

- [1] GRECO, M., LUGNI, C., FALTINSEN, O. M. “Can the water on deck influence the parametric roll of a FPSO? A numerical and experimental investigation”, *European Journal of Mechanics-B/Fluids*, v. 47, pp. 188–201, 2014.
- [2] GRECO, M., FALTINSEN, O., LANDRINI, M. “Shipping of water on a two-dimensional structure”, *Journal of Fluid Mechanics*, v. 525, pp. 309–332, 2005.
- [3] GRECO, M., COLICCHIO, G., FALTINSEN, O. M. “Shipping of water on a two-dimensional structure. Part 2”, *Journal of Fluid Mechanics*, v. 581, pp. 371–399, 2007.
- [4] HERNÁNDEZ-FONTES, J. V., VITOLA, M. A., SILVA, M. C., et al. “Use of Wet Dam-Break to Study Green Water Problem”. In: *ASME 2017 36th International Conference on Ocean, Offshore and Arctic Engineering, Trondheim, Norway*. American Society of Mechanical Engineers, 2017.
- [5] HERNÁNDEZ-FONTES, J. V., VITOLA, M. A., SILVA, M. C., et al. “On the generation of isolated green water events using wet dam-break”, *Journal of Offshore Mechanics and Arctic Engineering*, v. 140, 2017.
- [6] BEA, R., XU, T., STEAR, J., et al. “Wave forces on decks of offshore platforms”, *Journal of waterway, port, coastal, and ocean engineering*, v. 125, n. 3, pp. 136–144, 1999.
- [7] BUCHNER, B. *Green Water on Ship-type Offshore Structures*. Tese de Doutorado, Delft University of Thecnology, The Netherlands, 2002.
- [8] STOKER, J. J. *Water Waves: Pure and Applied Mathematics*. Interscience Publishers, 1957.
- [9] NAKAGAWA, H., NAKAMURA, S., ICHIHASHI, K. *Generation and Development of a Hydraulic Bore Due to the Breaking of a Dam*. Relatório Técnico v.19, Part 2, Bulletin of the Disaster Prevention Research Institute, Kyoto University, 1969.

- [10] KLEMP, J. B., ROTUNNO, R., SKAMAROCK, W. C. “On the propagation of internal bores”, *Journal of Fluid Mechanics*, v. 331, pp. 81–106, 1997.
- [11] STANSBY, P. K., CHEGINI, A., BARNES, T. C. D. “The initial stages of dam-break flow”, *Journal of Fluid Mechanics*, v. 370, pp. 203–220, 1998.
- [12] CRESPO, A., GÓMEZ-GESTEIRA, M., DALRYMPLE, R. A. “Modeling dam break behavior over a wet bed by a SPH technique”, *Journal of waterway, port, coastal, and ocean engineering*, v. 134, n. 6, pp. 313–320, 2008.
- [13] MOHAPATRA, P., ESWARAN, V., BHALLAMUDI, S. M. “Two-dimensional analysis of dam-break flow in vertical plane”, *Journal of Hydraulic Engineering*, v. 125, n. 2, pp. 183–192, 1999.
- [14] GODA, K., MIYAMOTO, T. “A Study of Shipping Water Pressure on Deck by Two Dimensional Ship Model Tests”, *Journal of The Society of Naval Architects of Japan*, v. 140, pp. 16–22, 1976.
- [15] BUCHNER, B. “On the impact of green water loading on ship and offshore unit design”. In: Kim, H., Lee, W. (Eds.), *The 6th International Symposium on Practical Design of Ships and Mobile Units (PRADS95)*, v. 1, Seoul, 1995. The Society of Naval Architects of Korea.
- [16] GRECO, M. *A two-Dimensional study of Green Water Loading*. Tese de Doutorado, Norwegian University of Science and Technology, Trondheim, Norway, 2001.
- [17] RYU, Y., CHANG, K.-A., MERCIER, R. “Application of dam-break flow to green water prediction”, *Applied Ocean Research*, v. 29, n. 3, pp. 128–136, 2007.
- [18] OGAWA, Y., MINAMI, M., TANIZAWA, K., et al. “Shipping water load due to deck wetness”. In: *The Twelfth International Offshore and Polar Engineering Conference*. International Society of Offshore and Polar Engineers, 2002.
- [19] HERNÁNDEZ-FONTES, J. V. *Avaliação do carregamento vertical sobre o convés de um navio devido ao embarque de água*. Tese de Mestrado, COPPE, Federal University of Rio de Janeiro, 2014. (in portuguese).
- [20] RAJENDRAN, S., FONSECA, N., SOARES, C. G. “Body nonlinear time domain calculation of vertical ship responses in extreme seas accounting for 2nd order Froude-Krylov pressure”, *Applied Ocean Research*, v. 54, pp. 39–52, 2016.

- [21] HU, Z., XUE, H., TANG, W., et al. “A combined wave-dam-breaking model for rogue wave overtopping”, *Ocean Engineering*, v. 104, pp. 77–88, 2015.
- [22] HAYAMI, S. “On the propagation of flood waves. Disaster Prevention Research Institute, Kyoto University”, *Bulletin*, , n. 1, 1951.
- [23] CHANSON, H. *Hydraulics of open channel flow*. Butterworth-Heinemann, 2004.
- [24] OGAWA, Y., TAGUCHI, H., ISHIDA, S. “Experimental study on shipping water volume and its load on deck”, *Journal of The Society of Naval Architects of Japan*, v. 1997, n. 182, pp. 177–185, 1997.
- [25] OGAWA, Y., MATSUNAMI, R., MINAMI, M., et al. “Green sea loads on general cargo ship”. In: *8th International Conference on the Stability of Ships and Ocean Vehicles STAB 2003, Escuela Tecnica Superior de Ingenieros Navales*, 2003.
- [26] HERNÁNDEZ-FONTES, J., VITOLA, M., ESPERANÇA, P., et al. “An alternative for estimating shipping water height distribution due to green water on a ship without forward speed”, *Marine Systems & Ocean Technology*, v. 10, n. 1, pp. 38–46, 2015.
- [27] BUCHNER, B. “The impact of green water on FPSO design”. In: *Offshore Technology Conference (OTC)*, n. 7698, Houston, Texas, USA, 1995.
- [28] NIELSEN, K. B. *Numerical prediction of green water loads on ships*. Tese de Doutorado, Technical University of Denmark Danmarks Tekniske Universitet, Department of Naval Architecture and Offshore Engineering Institut for Skibs-og Havteknik, 2003.
- [29] OGAWA, Y. “Long-term prediction method for the green water load and volume for an assessment of the load line”, *Journal of Marine Science and Technology*, v. 7, pp. 137–144, 2003.
- [30] GRECO, M., LANDRINI, M., FALTINSEN, O. “Impact flows and loads on ship-deck structures”, *Journal of Fluids and Structures*, v. 19, n. 251-275, 2004.
- [31] GRECO, M., LUGNI, C. “3-D seakeeping analysis with water on deck and slamming. Part 1: Numerical solver”, *Journal of Fluids and Structures*, v. 33, pp. 127–147, 2012.

- [32] GRECO, M., BOUSCASSE, B., LUGNI, C. “3-D seakeeping analysis with water on deck and slamming. Part 2: Experiments and physical investigation”, *Journal of fluids and structures*, v. 33, pp. 148–179, 2012.
- [33] COX, D. T., ORTEGA, J. A. “Laboratory observations of green water overtopping a fixed deck”, *Ocean Engineering*, v. 29, n. 14, pp. 1827–1840, 2002.
- [34] BUCHNER, B. *Green water on ship-type offshore structures*. Tese de Doutorado, Delft University of Technology Delft, 2002.
- [35] SULISZ, W., WILDE, P., WISNIEWSKI, M. “Wave impact on elastically supported horizontal deck”, *Journal of Fluids and Structures*, v. 21, pp. 305–319, 2005.
- [36] RYU, Y., CHANG, K.-A., MERCIER, R. “Runup and green water velocities due to breaking wave impinging and overtopping”, *Experiments in Fluids*, v. 43, n. 4, pp. 555–567, 2007.
- [37] FASHANU-UDOFE, P. T. *Simulation and analysis of wave-structure interactions*. Tese de Doutorado, Newcastle University, Newcastle Upon Tyne, U. K., 2010.
- [38] LEE, H.-H., LIM, H.-J., RHEE, S. H. “Experimental investigation of green water on deck for a *CFD* validation database”, *Ocean Engineering*, v. 42, pp. 47 – 60, 2012.
- [39] SONG, Y. K., CHANG, K.-A., ARIYARATHNE, K., et al. “Surface velocity and impact pressure of green water flow on a fixed model structure in a large wave basin”, *Ocean Engineering*, v. 104, pp. 40–51, 2015.
- [40] SILVA, D. F. C. *Numerical-experimental evaluation of green water on FPSO subjected to quartering and beam Waves*. Tese de Doutorado, COPPE, Federal University of Rio de Janeiro, 2016. (In portuguese).
- [41] SILVA, D. F. C., COUTINHO, A. L. G. A., ESPERANÇA, P. T. T. “Green water loads on FPSOs exposed to beam and quartering seas, part I: Experimental tests”, *Ocean Engineering*, v. 140, pp. 419–433, 2017.
- [42] PHAM, X., VARYANI, K. “Evaluation of green water loads on high-speed containership using CFD”, *Ocean Engineering*, v. 32, n. 5, pp. 571–585, 2005.

- [43] SERINALDI, F., CUOMO, G. “Characterizing impulsive wave-in-deck loads on coastal bridges by probabilistic models of impact maxima and rise times”, *Coastal Engineering*, v. 58, n. 9, pp. 908–926, 2011.
- [44] KIM, S.-Y., KIM, K.-H., KIM, Y. “Comparative study on pressure sensors for sloshing experiment”, *Ocean Engineering*, v. 94, pp. 199–212, 2015.
- [45] SPENCER, D., RYAN, R., STOCKWOOD, B., et al. “Development and Validation of panels to measure slamming forces”. In: *ASME 2014 33rd International Conference on Ocean, Offshore and Arctic Engineering*, 2014.
- [46] VAN NUFFEL, D., VEPA, K., DE BAERE, I., et al. “Study on the parameters influencing the accuracy and reproducibility of dynamic pressure measurements at the surface of a rigid body during water impact”, *Experimental mechanics*, v. 53, n. 2, pp. 131–144, 2013.
- [47] BRADNER, C. *Large-scale laboratory observations of wave forces on a highway bridge superstructure*. Tese de Mestrado, Oregon State University, Corvallis, OR, 2008.
- [48] PARK, H., TOMICZEK, T., COX, D. T., et al. “Experimental modeling of horizontal and vertical wave forces on an elevated coastal structure”, *Coastal Engineering*, v. 128, pp. 58–74, 2017.
- [49] MCPHERSON, R. L. *Hurricane induced wave and surge forces on bridge decks*. Tese de Mestrado, Texas A&M University, College Station, TX, 2008.
- [50] HUERA-HUARTE, F. J., JEON, D., GHARIB, M. “Experimental investigation of water slamming loads on panels”, *Ocean Engineering*, v. 38, n. 11-12, pp. 1347–1355, 2011.
- [51] HERNÁNDEZ, I. D., HERNÁNDEZ-FONTES, J. V., VITOLA, M. A., et al. “Water elevation measurements using binary image analysis for 2D hydrodynamic Experiments”, *Ocean Engineering*, v. 157, pp. 325–338, 2017.
- [52] LIN, P. *Numerical modeling of water waves*. CRC Press, 2008.
- [53] GOTTARDI, G., VENUTELLI, M. “An accurate time integration method for simplified overland flow models”, *Advances in water resources*, v. 31, n. 1, pp. 173–180, 2008.
- [54] XU, Z., TRAVIS, J., BREITUNG, W. *Green’s function method and its application to verification of diffusion models of GASFLOW code*. Forschungszentrum Karlsruhe GmbH, Karlsruhe, 2007.

- [55] STAKGOLD, I. *Green's Functions and Boundary Value Problems*. John Wiley & Sons Inc, New York, 1979.
- [56] ITTC. *Recommended procedures: Uncertainty analysis instrument calibration*. Relatório técnico, International Towing Tank Conference, 2008.
- [57] BALBINOT, A., BRUSAMARELLO, V. J. *Instrumentação E Fundamentos de Medidas. Volume 2* . Grupo Gen-LTC, 2000.
- [58] HAGER, W. H., LAUBER, G. “Hydraulische Experimente zum Talsperrenbruchproblem (Hydraulic experiments to dambreak problem)”, *Schweizer Ingenieur und Architekt*, v. 114, n. 24, pp. 515–524, 1996. (In German).
- [59] LAUBER, G., HAGER, W. H. “Experiments to dambreak wave: Horizontal channel”, *Journal of Hydraulic Research*, v. 36, n. 3, pp. 291–307, 1998.
- [60] ABDUL HADI, M. S., MUSTAPA, M. Z., SAAD, S. “Complete derivation of 2D shallow-water model from the primitive equations governing geophysical flows”. In: *8th International Conference on Marine Technology, Terengganu, Malaysia.*, 2012.

Appendix A

Model development

The model development shown in this appendix has been structured with information available in the literature, considering references such as LIN [52], ABDUL HADI *et al.* [60], XU *et al.* [54], [53], and STAKGOLD [55].

A.1 Assumptions

In the present study, let us consider the shipping water problem as defined in Fig. A.1. Description of the variables can be found in the Sect. 2.1.1 of the thesis. The approximation of irrotational flow with a boundary layer condition at bottom is followed, neglecting the cross-stream variation. Moreover, the fluid is incompressible, there is no density variation, and viscous effects are presented in the form of shear stresses on the boundary layer region due to the no-slip condition on the bottom. It is assumed that the horizontal length-scale is greater than the vertical one ($L_x \gg L_z$), then, the problem was formulated under the shallow water assumptions: disregarding the vertical accelerations and considering an hydrostatic pressure distribution.

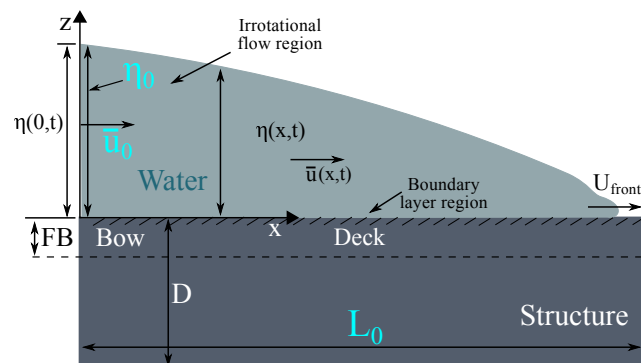


Figure A.1: Region of interest in the present study.

A.2 From Navier-Stokes equations to 2D shallow water equations (z-direction integration)

The Navier Stokes equations can be used to describe the motion of the shipping water represented by the fluid layer shown in Fig [A.1](#). Considering an incompressible, viscous and Newtonian fluid of constant density, the continuity equation can be expressed as:

$$\frac{\partial u}{\partial x} + \frac{\partial v}{\partial y} + \frac{\partial w}{\partial z} = 0 \quad (\text{A.1})$$

and the x -, y -, z - direction momentum equations can be written as follows:

$$\frac{\partial u}{\partial t} + u \frac{\partial u}{\partial x} + v \frac{\partial u}{\partial y} + w \frac{\partial u}{\partial z} = -\frac{1}{\rho} \frac{\partial p}{\partial x} + g_x + \frac{1}{\rho} \left[\frac{\partial \tau_{xx}}{\partial x} + \frac{\partial \tau_{xy}}{\partial y} + \frac{\partial \tau_{xz}}{\partial z} \right] \quad (\text{A.2})$$

$$\frac{\partial v}{\partial t} + u \frac{\partial v}{\partial x} + v \frac{\partial v}{\partial y} + w \frac{\partial v}{\partial z} = -\frac{1}{\rho} \frac{\partial p}{\partial y} + g_y + \frac{1}{\rho} \left[\frac{\partial \tau_{xy}}{\partial x} + \frac{\partial \tau_{yy}}{\partial y} + \frac{\partial \tau_{zy}}{\partial z} \right] \quad (\text{A.3})$$

$$\frac{\partial w}{\partial t} + u \frac{\partial w}{\partial x} + v \frac{\partial w}{\partial y} + w \frac{\partial w}{\partial z} = -\frac{1}{\rho} \frac{\partial p}{\partial z} + g_z + \frac{1}{\rho} \left[\frac{\partial \tau_{xz}}{\partial x} + \frac{\partial \tau_{yz}}{\partial y} + \frac{\partial \tau_{zz}}{\partial z} \right] \quad (\text{A.4})$$

where u, v and w are the x, y and z components of velocity, respectively; ρ is water density; p is pressure; g is gravity; and the terms τ_{ij} indicate the i - shear stress component in the j - direction.

When the assumption of $L_x \gg L_z$ is considered, the z-direction integration of the Navier Stokes equations yields the shallow water ones. These allow the description of a thin layer of fluid in hydrostatic balance, bounded by a free surface and a bottom topography.

Let us consider a layer of fluid bounded by a bottom topography and a free surface following the Euler system as shown in Fig [A.2](#). The shallow water equations can be obtained from integrating Eqs. [\(A.2\)](#) to [\(A.4\)](#) along the z -coordinate.

A.2.1 Depth-averaged integration of the continuity equation

The continuity equation [\(A.1\)](#) can be integrated from the bottom ($z = -h$) to the free surface ($z = \eta$) as follows

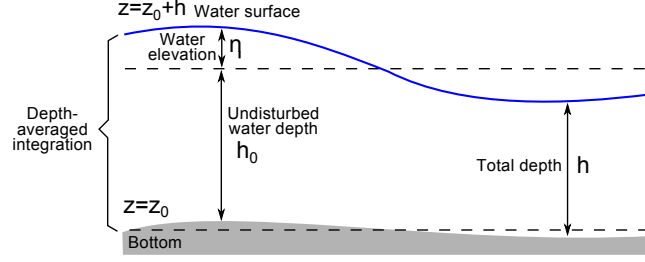


Figure A.2: Euler system defining the layer of fluid bounded by bottom and free surface.

$$\int_{-h}^{\eta} \left(\frac{\partial u}{\partial x} + \frac{\partial v}{\partial y} + \frac{\partial w}{\partial z} \right) dz = \int_{-h}^{\eta} \frac{\partial u}{\partial x} dz + \int_{-h}^{\eta} \frac{\partial v}{\partial y} dz + \int_{-h}^{\eta} \frac{\partial w}{\partial z} dz = 0 \quad (\text{A.5})$$

which can also be expressed as

$$\int_{-h}^{\eta} \frac{\partial u}{\partial x} dz + \int_{-h}^{\eta} \frac{\partial v}{\partial y} dz + w(x, y, \eta) - w(x, y, -h) = 0 \quad (\text{A.6})$$

To go further in the development of the integration, let us introduce the Leibnitz rule briefly, which is used to express the integral of a derivative as a derivative of an integral. It is applicable to the terms described above. The next procedure exemplifies the use of the Leibnitz rule:

$$\frac{\partial}{\partial x} \int_{a(x)}^{b(x)} F(x, y) dy = \int_{a(x)}^{b(x)} \frac{\partial}{\partial x} F(x, y) dy + F(x, b(x)) \frac{\partial b(x)}{\partial x} - F(x, a(x)) \frac{\partial a(x)}{\partial x} \quad (\text{A.7})$$

or

$$\int_{a(x)}^{b(x)} \frac{\partial}{\partial x} F(x, y) dy = \frac{\partial}{\partial x} \int_{a(x)}^{b(x)} F(x, y) dy - F(x, b(x)) \frac{\partial b(x)}{\partial x} + F(x, a(x)) \frac{\partial a(x)}{\partial x} \quad (\text{A.8})$$

Applying the Leibnitz rule to express the equation [\(A.6\)](#) we obtain the following expression:

$$\begin{aligned} & \frac{\partial}{\partial x} \int_{-h}^{\eta} u dz - u(x, y, \eta) \frac{\partial \eta}{\partial x} - u(x, y, -h) \frac{\partial h}{\partial x} + \\ & + \frac{\partial}{\partial y} \int_{-h}^{\eta} v dz - v(x, y, \eta) \frac{\partial \eta}{\partial y} - v(x, y, -h) \frac{\partial h}{\partial y} + \\ & + w(x, y, \eta) - w(x, y, -h) = 0 \end{aligned} \quad (\text{A.9})$$

Next subsections present the boundary conditions of the flow layer, which are defined at the free surface and bottom.

Kinematic boundary conditions at the free surface

We can define the surface motion as:

$$z_{surf} = \eta \quad (\text{A.10})$$

where $\eta = f(x, y, t)$. The vertical velocity of the free surface is expressed as:

$$w(x, y, \eta) = \frac{D\eta}{Dt} \quad (\text{A.11})$$

or

$$w(x, y, \eta) = \frac{\partial \eta}{\partial t} + \frac{\partial x}{\partial t} \frac{\partial \eta}{\partial x} + \frac{\partial y}{\partial t} \frac{\partial \eta}{\partial y} \quad (\text{A.12})$$

$$w(x, y, \eta) = \frac{\partial \eta}{\partial t} + u(x, y, \eta) \frac{\partial \eta}{\partial x} + v(x, y, \eta) \frac{\partial \eta}{\partial y} \quad (\text{A.13})$$

Kinematic boundary conditions at bottom

The bottom bed is considered impermeable, which means the absence of mass flux perpendicular to it:

$$\vec{u} \cdot \vec{n}_{bot} = 0 \quad (\text{A.14})$$

where n_{bot} is the normal vector to the bed. Defining the bottom reference as

$$z_{bot} = -h \quad (\text{A.15})$$

with $h = f(x, y, t)$. The vertical velocity at the bottom is expressed by the next material derivative:

$$w(x, y, -h) = \frac{D(-h)}{Dt} \quad (\text{A.16})$$

$$w(x, y, -h) = \frac{\partial(-h)}{\partial t} + \frac{\partial x}{\partial t} \frac{\partial(-h)}{\partial x} + \frac{\partial y}{\partial t} \frac{\partial(-h)}{\partial y} \quad (\text{A.17})$$

$$w(x, y, -h) = -\frac{\partial h}{\partial t} - u(x, y, -h) \frac{\partial h}{\partial x} - v(x, y, -h) \frac{\partial h}{\partial y} \quad (\text{A.18})$$

Boundary conditions substitution

The next step consists in substituting both the free surface and bottom boundary conditions (Equations (A.13) and (A.18), respectively) as well as the depth-averaged flow velocities (Equations and) into the continuity equation ((A.9)).

To simplify the equation (A.9), the free surface boundary condition should be substituted as

$$\frac{\partial \eta}{\partial t} = w(x, y, \eta) - u(x, y, \eta) \frac{\partial \eta}{\partial x} - v(x, y, \eta) \frac{\partial \eta}{\partial y} \quad (\text{A.19})$$

and the bottom boundary condition as

$$\frac{\partial h}{\partial t} = -w(x, y, -h) - u(x, y, -h) \frac{\partial h}{\partial x} - v(x, y, -h) \frac{\partial h}{\partial y} \quad (\text{A.20})$$

Then, it is introduced the use of the depth-averaged flow velocities in the x - and y - directions (\bar{u} and \bar{v} , respectively) as follows:

$$\bar{u} = \frac{1}{H} \int_{-h}^{\eta} u dz \quad (\text{A.21})$$

$$\bar{v} = \frac{1}{H} \int_{-h}^{\eta} v dz \quad (\text{A.22})$$

where H is the total water depth ($H = \eta + h$). Replacing equations (A.19)-(A.22) into (A.9) yields

$$\frac{\partial \bar{u} H}{\partial x} + \frac{\partial \eta}{\partial t} + \frac{\partial h}{\partial t} + \frac{\partial \bar{v} H}{\partial y} = 0 \quad (\text{A.23})$$

or

$$\frac{\partial (\eta + h)}{\partial t} + \frac{\partial \bar{u} H}{\partial x} + \frac{\partial \bar{v} H}{\partial y} = 0 \quad (\text{A.24})$$

$$\frac{\partial H}{\partial t} + \frac{\partial \bar{u} H}{\partial x} + \frac{\partial \bar{v} H}{\partial y} = 0 \quad (\text{A.25})$$

A.2.2 Depth-averaged integration of the momentum equation

To show the development to integrate the momentum equation in the vertical direction, a similar procedure as done with the continuity equation is followed. The conservative form of the momentum equation in the x - ((A.2)) and y - ((A.3)) directions are expressed as in the equations (A.26) and (A.27), respectively (LIN [52]):

$$\frac{\partial u}{\partial t} + \frac{\partial u^2}{\partial x} + \frac{\partial (uv)}{\partial y} + \frac{\partial (uw)}{\partial z} = -\frac{1}{\rho} \frac{\partial P}{\partial x} + \frac{1}{\rho} \left[\frac{\partial \tau_{xx}}{\partial x} + \frac{\partial \tau_{xy}}{\partial y} + \frac{\partial \tau_{xz}}{\partial z} \right] \quad (\text{A.26})$$

$$\frac{\partial v}{\partial t} + \frac{\partial(uv)}{\partial x} + \frac{\partial v^2}{\partial y} + \frac{\partial(vw)}{\partial z} = -\frac{1}{\rho} \frac{\partial P}{\partial y} + \frac{1}{\rho} \left[\frac{\partial \tau_{xy}}{\partial x} + \frac{\partial \tau_{yy}}{\partial y} + \frac{\partial \tau_{zy}}{\partial z} \right] \quad (\text{A.27})$$

Due to the shallow water condition, the horizontal length-scale exceed the vertical length-scale. Thus, several terms in the z-direction momentum equation ((A.4)) can be neglected. Then, hydrostatic balance can be assumed, considering the pressure as

$$P = P_a + \rho g(z + \eta) \quad (\text{A.28})$$

where P_a is the atmospheric pressure. Then, the pressure term in equation (A.26) is expressed as LIN [52]:

$$-\frac{1}{\rho} \frac{\partial P}{\partial x} = -\frac{1}{\rho} \frac{\partial P_a}{\partial x} - g \frac{\partial \eta}{\partial x} - \frac{g\eta}{\rho} \frac{\partial \rho}{\partial x} \quad (\text{A.29})$$

In a similar way as done with the continuity equation ((A.1)), the x - and y -direction momentum equations are vertically integrated from the bottom to the free surface by applying the Leibnitz relationship and substituting the hydrostatic balance expression as well as the free surface and bottom boundary conditions. The corresponding procedure is shown below, showing the integration of the momentum equation terms separately .

Kinematic boundary conditions

The kinematic boundary conditions at the free surface and the bottom are the same described by equations (A.13) and (A.18), respectively.

Dynamic boundary conditions

The dynamic boundary conditions are due to the shear stress on the free surface and bottom. These are respectively represented by (A.30) and (A.31) as follows (ABDUL HADI *et al.* [60]):

$$\tau(x, \eta) = \tau_{sur} = -\tau_{xx, \eta} \frac{\partial \eta}{\partial x} - \tau_{xy, \eta} \frac{\partial \eta}{\partial y} + \tau_{xz, \eta} \quad (\text{A.30})$$

$$\tau(x, -h) = \tau_{bot} = \tau_{xx, -h} \frac{\partial h}{\partial x} + \tau_{xy, -h} \frac{\partial h}{\partial y} - \tau_{xz, -h} \quad (\text{A.31})$$

where τ_{xi} are the x -direction stress components acting in a plane normal to the i -direction.

Integration of the derivative and advection terms

To show the development of the integration along the z-direction of the momentum equations, let us consider the equation (A.26). First, let us integrate the left hand terms of such a equation:

$$\int_{-h}^{\eta} \left[\frac{\partial u}{\partial t} + \frac{\partial u^2}{\partial x} + \frac{\partial(uv)}{\partial y} + \frac{\partial(uw)}{\partial z} \right] dz = \int_{-h}^{\eta} \frac{\partial u}{\partial t} dz + \int_{-h}^{\eta} \frac{\partial u^2}{\partial x} dz + \int_{-h}^{\eta} \frac{\partial(uv)}{\partial y} dz + \int_{-h}^{\eta} \frac{\partial(uw)}{\partial z} dz \quad (\text{A.32})$$

Applying Leibnitz rule ((A.8)), as done with the continuity equation, it is possible to expand the right-hand terms of equation (A.32) as follows:

$$\begin{aligned} & \int_{-h}^{\eta} \left[\frac{\partial u}{\partial t} + \frac{\partial u^2}{\partial x} + \frac{\partial(uv)}{\partial y} + \frac{\partial(uw)}{\partial z} \right] dz = \\ & \frac{\partial}{\partial t} \int_{-h}^{\eta} u dz - u(x, y, \eta) \frac{\partial \eta}{\partial t} - u(x, y, -h) \frac{\partial h}{\partial t} + \dots \\ & \dots + \frac{\partial}{\partial x} \int_{-h}^{\eta} u^2 dz - u^2(x, y, \eta) \frac{\partial \eta}{\partial x} - u^2(x, y, -h) \frac{\partial h}{\partial x} + \dots \\ & \dots + \frac{\partial}{\partial y} \int_{-h}^{\eta} (uv) dz - (uv)(x, y, \eta) \frac{\partial \eta}{\partial y} - (uv)(x, y, -h) \frac{\partial h}{\partial y} + \dots \\ & \dots + (uw)(x, y, \eta) - (uw)(x, y, -h) \end{aligned} \quad (\text{A.33})$$

As $w = 0$ at the free surface and bottom boundaries (i.e., material derivative equals zero), the kinematic boundary conditions ((A.13) and (A.18)) can be expressed as

$$w(x, y, \eta) - \frac{\partial \eta}{\partial t} - u(x, y, \eta) \frac{\partial \eta}{\partial x} - v(x, y, \eta) \frac{\partial \eta}{\partial y} = 0 \quad (\text{A.34})$$

$$-w(x, y, -h) - \frac{\partial h}{\partial t} - u(x, y, -h) \frac{\partial h}{\partial x} - v(x, y, -h) \frac{\partial h}{\partial y} = 0 \quad (\text{A.35})$$

Rearranging terms, (A.33) can be written as

$$\begin{aligned} & \int_{-h}^{\eta} \left[\frac{\partial u}{\partial t} + \frac{\partial u^2}{\partial x} + \frac{\partial(uv)}{\partial y} + \frac{\partial(uw)}{\partial z} \right] dz = \\ & \frac{\partial}{\partial t} \int_{-h}^{\eta} u dz + \frac{\partial}{\partial x} \int_{-h}^{\eta} u^2 dz + \frac{\partial}{\partial y} \int_{-h}^{\eta} (uv) dz + \dots \\ & \dots + u(x, y, \eta) \left[w(x, y, \eta) - u(x, y, \eta) \frac{\partial \eta}{\partial x} - v(x, y, \eta) \frac{\partial \eta}{\partial y} - \frac{\partial \eta}{\partial t} \right] + \dots \\ & \dots + u(x, y, -h) \left[-w(x, y, -h) - u(x, y, -h) \frac{\partial h}{\partial x} - v(x, y, -h) \frac{\partial h}{\partial y} - \frac{\partial h}{\partial t} \right] \end{aligned} \quad (\text{A.36})$$

Substituting (A.35) and (A.36) into (A.36), it is possible to neglect the last two terms of (A.36). It yields

$$\int_{-h}^{\eta} \left[\frac{\partial u}{\partial t} + \frac{\partial u^2}{\partial x} + \frac{\partial(uv)}{\partial y} + \frac{\partial(uw)}{\partial z} \right] dz = \frac{\partial}{\partial t} \int_{-h}^{\eta} u dz + \frac{\partial}{\partial x} \int_{-h}^{\eta} u^2 dz + \frac{\partial}{\partial y} \int_{-h}^{\eta} (uv) dz \quad (\text{A.37})$$

Considering the depth-averaged flow velocities introduced before ((A.21), (A.21)), the first term of the right-hand side of (A.37) is simplified:

$$\int_{-h}^{\eta} \left[\frac{\partial u}{\partial t} + \frac{\partial u^2}{\partial x} + \frac{\partial(uv)}{\partial y} + \frac{\partial(uw)}{\partial z} \right] dz = \frac{\partial(\bar{u}H)}{\partial t} + \frac{\partial}{\partial x} \int_{-h}^{\eta} u^2 dz + \frac{\partial}{\partial y} \int_{-h}^{\eta} (uv) dz \quad (\text{A.38})$$

To simplify the last two terms of above equation, we have to decompose the momentum vertical field into mean (depth-integrated) and fluctuating values. The velocity can be represented as an analogy to the Reynolds-average assumptions as (ABDUL HADI *et al.* [60]):

$$u(z) = \bar{u} + \tilde{u} \quad (\text{A.39})$$

where \bar{u} is the mean velocity and \tilde{u} is the fluctuating velocity. The next integration rule can be considered to simplify the product of two velocities (ABDUL HADI *et al.* [60]):

$$\int_{-h}^{\eta} (\bar{u} + \tilde{u})(\bar{u} + \tilde{u}) dz = \int_{-h}^{\eta} \bar{u}^2 dz + \int_{-h}^{\eta} (\tilde{u}\tilde{u}) dz \quad (\text{A.40})$$

Applying these assumptions to to expand the last terms of (A.38) we have:

$$\int_{-h}^{\eta} \left[\frac{\partial u}{\partial t} + \frac{\partial u^2}{\partial x} + \frac{\partial(uv)}{\partial y} + \frac{\partial(uw)}{\partial z} \right] dz = \frac{\partial(\bar{u}H)}{\partial t} + \frac{\partial(\bar{u}^2 H)}{\partial x} + \frac{\partial(\bar{u}\bar{v}H)}{\partial y} + \frac{\partial}{\partial x} \int_{-h}^{\eta} (\tilde{u}\tilde{u}) dz + \frac{\partial}{\partial y} \int_{-h}^{\eta} (\tilde{u}\tilde{v}) dz \quad (\text{A.41})$$

Integration of the pressure terms

Let us consider the pressure term of the momentum equation as defined in (A.29). The integration in the z-direction is expressed as follows:

$$\int_{-h}^{\eta} -\frac{1}{\rho} \frac{\partial P}{\partial x} = -\frac{1}{\rho} \int_{-h}^{\eta} \frac{\partial P_a}{\partial x} dz - \int_{-h}^{\eta} g \frac{\partial \eta}{\partial x} dz - \int_{-h}^{\eta} \frac{g\eta}{\rho} \frac{\partial \rho}{\partial x} dz \quad (\text{A.42})$$

Integrating each of the right-hand terms of (A.42), disregarding the P_a variation across the vertical direction, we have:

$$-\frac{1}{\rho} \int_{-h}^{\eta} \frac{\partial P_a}{\partial x} dz = -\frac{1}{\rho} \frac{\partial P_a}{\partial x} \int_{-h}^{\eta} dz = -\frac{1}{\rho} \frac{\partial P_a}{\partial x} (\eta + h) \quad (\text{A.43})$$

Considering $H = \eta + h$:

$$-\frac{1}{\rho} \int_{-h}^{\eta} \frac{\partial P_a}{\partial x} dz = -\frac{H}{\rho} \frac{\partial P_a}{\partial x} \quad (\text{A.44})$$

For the second term of (A.42):

$$-\int_{-h}^{\eta} g \frac{\partial \eta}{\partial x} dz = -g \frac{\partial \eta}{\partial x} \int_{-h}^{\eta} dz = -g \frac{\partial \eta}{\partial x} (\eta + h) = -gH \frac{\partial \eta}{\partial x} \quad (\text{A.45})$$

and for the third term of (A.42):

$$-\int_{-h}^{\eta} \frac{g\eta}{\rho} \frac{\partial \rho}{\partial x} dz = -\frac{g\eta}{\rho} \frac{\partial \rho}{\partial x} \int_{-h}^{\eta} dz = -\frac{g\eta}{\rho} \frac{\partial \rho}{\partial x} (\eta + h) = -\frac{g\eta H}{\rho} \frac{\partial \rho}{\partial x} \quad (\text{A.46})$$

Finally, the depth-integrated pressure term is expressed as

$$\int_{-h}^{\eta} -\frac{1}{\rho} \frac{\partial P}{\partial x} = -\frac{H}{\rho} \frac{\partial P_a}{\partial x} - gH \frac{\partial \eta}{\partial x} - \frac{g\eta H}{\rho} \frac{\partial \rho}{\partial x} \quad (\text{A.47})$$

Integration of the shear stress terms

The integration of the shear stress terms of (A.26) is performed as follows:

$$\int_{-h}^{\eta} \frac{1}{\rho} \left(\frac{\partial \tau_{xx}}{\partial x} + \frac{\partial \tau_{xy}}{\partial y} + \frac{\partial \tau_{xz}}{\partial z} \right) dz = \frac{1}{\rho} \int_{-h}^{\eta} \frac{\partial \tau_{xx}}{\partial x} dz + \frac{1}{\rho} \int_{-h}^{\eta} \frac{\partial \tau_{xy}}{\partial y} dz + \frac{1}{\rho} \int_{-h}^{\eta} \frac{\partial \tau_{xz}}{\partial z} dz \quad (\text{A.48})$$

Applying the Leibnitz rule to each term of (A.48) the next expressions are obtained:

$$\begin{aligned} & \int_{-h}^{\eta} \frac{1}{\rho} \left(\frac{\partial \tau_{xx}}{\partial x} + \frac{\partial \tau_{xy}}{\partial y} + \frac{\partial \tau_{xz}}{\partial z} \right) dz = \\ & \frac{1}{\rho} \left[\frac{\partial}{\partial x} \int_{-h}^{\eta} \tau_{xx} dz - \tau_{xx}(x, \eta) \frac{\partial \eta}{\partial x} - \tau_{xx}(x, -h) \frac{\partial h}{\partial x} \right] + \dots \\ & \dots + \frac{1}{\rho} \left[\frac{\partial}{\partial y} \int_{-h}^{\eta} \tau_{xy} dz - \tau_{xy}(x, \eta) \frac{\partial \eta}{\partial y} - \tau_{xy}(x, -h) \frac{\partial h}{\partial y} \right] + \dots \\ & \dots + \frac{1}{\rho} [\tau_{xz}(\eta) - \tau_{xz}(-h)] \end{aligned} \quad (\text{A.49})$$

Depth-averaged momentum equation

Considering equations (A.41), (A.47) and (A.49), the x-direction depth-averaged momentum equation can be expressed as

$$\begin{aligned}
& \frac{\partial(\bar{u}H)}{\partial t} + \frac{\partial(\bar{u}^2H)}{\partial x} + \frac{\partial(\bar{u}\bar{v}H)}{\partial y} + \frac{\partial}{\partial x} \int_{-h}^{\eta} (\tilde{u}\tilde{u})dz + \frac{\partial}{\partial y} \int_{-h}^{\eta} (\tilde{u}\tilde{v})dz = \\
& -\frac{H}{\rho} \frac{\partial P_a}{\partial x} - gH \frac{\partial \eta}{\partial x} - \frac{g\eta H}{\rho} \frac{\partial \rho}{\partial x} + \frac{1}{\rho} \left[\frac{\partial}{\partial x} \int_{-h}^{\eta} \tau_{xx} dz - \tau_{xx}(x, \eta) \frac{\partial \eta}{\partial x} - \tau_{xx}(x, -h) \frac{\partial h}{\partial x} \right] + \dots \\
& \dots + \frac{1}{\rho} \left[\frac{\partial}{\partial y} \int_{-h}^{\eta} \tau_{xy} dz - \tau_{xy}(x, \eta) \frac{\partial \eta}{\partial y} - \tau_{xy}(x, -h) \frac{\partial h}{\partial y} \right] + \frac{1}{\rho} [\tau_{xz}(\eta) - \tau_{xz}(-h)]
\end{aligned} \tag{A.50}$$

By grouping terms in the equation (A.50), it can be rewritten as

$$\begin{aligned}
& \frac{\partial(\bar{u}H)}{\partial t} + \frac{\partial(\bar{u}^2H)}{\partial x} + \frac{\partial(\bar{u}\bar{v}H)}{\partial y} + \frac{\partial}{\partial x} \int_{-h}^{\eta} (\tilde{u}\tilde{u})dz + \frac{\partial}{\partial y} \int_{-h}^{\eta} (\tilde{u}\tilde{v})dz = \\
& -\frac{H}{\rho} \frac{\partial P_a}{\partial x} - gH \frac{\partial \eta}{\partial x} - \frac{g\eta H}{\rho} \frac{\partial \rho}{\partial x} + \frac{1}{\rho} \frac{\partial}{\partial x} \int_{-h}^{\eta} \tau_{xx} dz + \frac{1}{\rho} \frac{\partial}{\partial y} \int_{-h}^{\eta} \tau_{xy} dz + \dots \\
& \dots + \frac{1}{\rho} \left[-\tau_{xx}(x, \eta) \frac{\partial \eta}{\partial x} - \tau_{xy}(x, \eta) \frac{\partial \eta}{\partial y} + \tau_{xz}(\eta) \right] + \dots \\
& \dots - \frac{1}{\rho} \left[\tau_{xx}(x, -h) \frac{\partial h}{\partial x} + \tau_{xy}(x, -h) \frac{\partial h}{\partial y} - \tau_{xz}(-h) \right]
\end{aligned} \tag{A.51}$$

Substituting the dynamic boundary conditions (A.30) and (A.31) into (A.51) we obtain the 2D shallow water momentum equation in the x-direction:

$$\begin{aligned}
& \frac{\partial(\bar{u}H)}{\partial t} + \frac{\partial(\bar{u}^2H)}{\partial x} + \frac{\partial(\bar{u}\bar{v}H)}{\partial y} + \frac{\partial}{\partial x} \int_{-h}^{\eta} (\tilde{u}\tilde{u})dz + \frac{\partial}{\partial y} \int_{-h}^{\eta} (\tilde{u}\tilde{v})dz = \\
& -\frac{H}{\rho} \frac{\partial P_a}{\partial x} - gH \frac{\partial \eta}{\partial x} - \frac{g\eta H}{\rho} \frac{\partial \rho}{\partial x} + \frac{1}{\rho} \frac{\partial}{\partial x} \int_{-h}^{\eta} \tau_{xx} dz + \frac{1}{\rho} \frac{\partial}{\partial y} \int_{-h}^{\eta} \tau_{xy} dz + \frac{1}{\rho} \tau_{sur} - \frac{1}{\rho} \tau_{bot}
\end{aligned} \tag{A.52}$$

where τ_{sur} and τ_{bot} are assumed to be due to $\tau_{xz, \eta}$ (stress due to wind) and $\tau_{xz, -h}$ (stress due to bottom friction), respectively (see (A.30) and (A.31)).

Simplified form of the 2D shallow water momentum equation in x-direction assuming independence of τ_{xx} and τ_{xy} from z

Several shallow water applications are carried out depending how the flow and viscous terms of (A.50) or (A.52) are assumed (LIN [52]). In this case, let us consider

uniform velocity and uniform stresses in the vertical direction. With these assumptions, it is possible to neglect the terms due to the velocity fluctuations. Moreover, let us assume that the terms $\partial\tau_{xx}/\partial x$ and $\partial\tau_{xy}/\partial y$ are constant in the z -direction due to independence of τ_{xx} and τ_{xy} from z . It allows to integrate the fourth and fifth right-hand side terms of (A.52) in the vertical direction. Thus, (A.52) can be simplified to

$$\begin{aligned} & \frac{\partial(\bar{u}H)}{\partial t} + \frac{\partial(\bar{u}^2H)}{\partial x} + \frac{\partial(\bar{u}\bar{v}H)}{\partial y} = \\ & -\frac{H}{\rho} \frac{\partial P_a}{\partial x} - gH \frac{\partial \eta}{\partial x} - \frac{g\eta H}{\rho} \frac{\partial \rho}{\partial x} + \frac{H}{\rho} \frac{\partial \tau_{xx}}{\partial x} + \frac{H}{\rho} \frac{\partial \tau_{xy}}{\partial y} + \frac{1}{\rho} \tau_{xz,\eta} - \frac{1}{\rho} \tau_{xz,-h} \end{aligned} \quad (\text{A.53})$$

By a similar procedure, the y -direction simplified shallow water momentum equation can be obtained as follows

$$\begin{aligned} & \frac{\partial(\bar{v}H)}{\partial t} + \frac{\partial(\bar{u}\bar{v}H)}{\partial x} + \frac{\partial(\bar{v}^2H)}{\partial y} = \\ & -\frac{H}{\rho} \frac{\partial P_a}{\partial y} - gH \frac{\partial \eta}{\partial y} - \frac{g\eta H}{\rho} \frac{\partial \rho}{\partial y} + \frac{H}{\rho} \frac{\partial \tau_{yx}}{\partial x} + \frac{H}{\rho} \frac{\partial \tau_{yy}}{\partial y} + \frac{1}{\rho} \tau_{yz,\eta} - \frac{1}{\rho} \tau_{yz,-h} \end{aligned} \quad (\text{A.54})$$

A.3 From 2D to 1D shallow water equations (y -direction integration)

The 2D shallow water system of equations, neglecting the dependence of τ_{xx} and τ_{xy} from z , can be defined by the continuity equation (A.25) and the x - and y -direction momentum equations (A.53) and (A.54), respectively.

To obtain the 1D shallow water system of equations, the 2D (z -integrated Navier Stokes equations) shallow water system of equations will be integrated along the y -direction (from $-B/2$ to $B/2$) of a layer of width B , as shown in Fig A.3. The flow follows the x -direction, and at the sides, shear stresses are not considered. The main stresses are due to the wind and bottom, which are opposed to the flow direction.

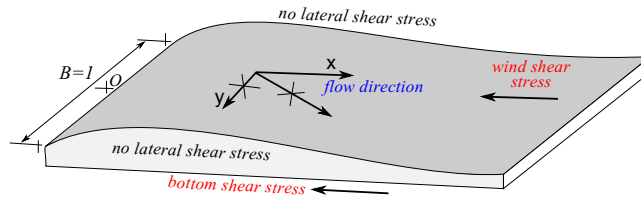


Figure A.3: Fluid layer for the y -direction integration of the shallow water equations.

A.3.1 1D shallow water equations: Integration of the continuity equation

Following a procedure similar as for the 2D shallow water equations, the procedure to obtain the 1D shallow water system of equations is described. Let us start with the y -direction integration of the continuity equation (A.25):

$$\int_{-B/2}^{B/2} \frac{\partial H}{\partial t} dy + \int_{-B/2}^{B/2} \frac{\partial(\bar{u}H)}{\partial x} dy + \int_{-B/2}^{B/2} \frac{\partial(\bar{v}H)}{\partial y} dy = 0 \quad (\text{A.55})$$

Applying Leibnitz and integration rules to the terms of (A.55), we have

First term:

$$\int_{-B/2}^{B/2} \frac{\partial H}{\partial t} dy = \frac{\partial}{\partial t} \int_{-B/2}^{B/2} H dy - H(x, B/2) \frac{\partial(B/2)}{\partial t} + H(x, -B/2) \frac{\partial(-B/2)}{\partial t} \quad (\text{A.56})$$

Second term:

$$\int_{-B/2}^{B/2} \frac{\partial(\bar{u}H)}{\partial x} dy = \frac{\partial}{\partial x} \int_{-B/2}^{B/2} (\bar{u}H) dy - \bar{u}H(x, B/2) \frac{\partial(B/2)}{\partial x} + \bar{u}H(x, -B/2) \frac{\partial(-B/2)}{\partial x} \quad (\text{A.57})$$

Third term:

$$\int_{-B/2}^{B/2} \frac{\partial(\bar{v}H)}{\partial y} dy = \bar{v}H(x, B/2) - \bar{v}H(x, -B/2) \quad (\text{A.58})$$

Kinematic boundary conditions at the sides of domain

To express the kinematic boundary conditions at the $B/2$ and $-B/2$ lateral boundaries, let us consider impermeable walls at the sides, that is, no mass flux perpendicular to them:

$$\bar{v} \cdot n_{wall} = 0 \quad (\text{A.59})$$

where n_{wall} is the vector normal to the wall and \bar{v} is the mean velocity in the y -direction, as defined before. At the boundary $-B/2$ we have:

$$\bar{v}(x, -B/2) = \frac{D(-B/2)}{Dt} \quad (\text{A.60})$$

$$\bar{v}(x, -B/2) = \frac{\partial(-B/2)}{\partial t} + \frac{\partial x}{\partial t} \frac{\partial(-B/2)}{\partial x} = \frac{\partial(-B/2)}{\partial t} + \bar{u} \frac{\partial(-B/2)}{\partial x} \quad (\text{A.61})$$

$$\frac{\partial(-B/2)}{\partial t} + \bar{u} \frac{\partial(-B/2)}{\partial x} - \bar{v}(x, -B/2) = 0 \quad (\text{A.62})$$

In a similar way, for the boundary $B/2$ we have

$$\bar{v}(x, B/2) = \frac{D(B/2)}{Dt} \quad (\text{A.63})$$

$$\bar{v}(x, B/2) = \frac{\partial(B/2)}{\partial t} + \frac{\partial x}{\partial t} \frac{\partial(B/2)}{\partial x} = \frac{\partial(B/2)}{\partial t} + \bar{u} \frac{\partial(B/2)}{\partial x} \quad (\text{A.64})$$

$$\frac{\partial(B/2)}{\partial t} + \bar{u} \frac{\partial(B/2)}{\partial x} - \bar{v}(x, B/2) = 0 \quad (\text{A.65})$$

Simplifying the extended terms of the continuity equation

Equations (A.56) to (A.58) can be grouped as follows:

$$\begin{aligned} & \frac{\partial}{\partial t} \int_{-B/2}^{B/2} H dy - H(x, B/2) \frac{\partial(B/2)}{\partial t} + H(x, -B/2) \frac{\partial(-B/2)}{\partial t} + \frac{\partial}{\partial x} \int_{-B/2}^{B/2} (\bar{u}H) dy - \\ & \bar{u}H(x, B/2) \frac{\partial(B/2)}{\partial x} + \bar{u}H(x, -B/2) \frac{\partial(-B/2)}{\partial x} + \bar{v}H(x, B/2) - \bar{v}H(x, -B/2) = 0 \end{aligned} \quad (\text{A.66})$$

or

$$\begin{aligned} & \frac{\partial}{\partial t} \int_{-B/2}^{B/2} H dy + \frac{\partial}{\partial x} \int_{-B/2}^{B/2} (\bar{u}H) dy + \dots \\ & \dots + H(x, -B/2) \left[\frac{\partial(-B/2)}{\partial t} + \bar{u} \frac{\partial(-B/2)}{\partial x} - \bar{v}(x, -B/2) \right] - \dots \\ & \dots - H(x, B/2) \left[\frac{\partial(B/2)}{\partial t} + \bar{u} \frac{\partial(B/2)}{\partial x} - \bar{v}(x, B/2) \right] = 0 \end{aligned} \quad (\text{A.67})$$

Replacing (A.61) and (A.65) into (A.67), and applying the rule of integration to the first two terms, considering H and \bar{u} independent of y , we have:

$$\frac{\partial H}{\partial t} [y]_{(-B/2)}^{(B/2)} + \frac{\partial(\bar{u}H)}{\partial x} [y]_{(-B/2)}^{(B/2)} = \frac{\partial H}{\partial t} (B/2 + B/2) + \frac{\partial(\bar{u}H)}{\partial x} (B/2 + B/2) = 0 \quad (\text{A.68})$$

which yields

$$\frac{\partial(BH)}{\partial t} + \frac{\partial(\bar{u}BH)}{\partial x} = 0 \quad (\text{A.69})$$

Considering B equal to the unity, the 1D shallow water continuity equation can be expressed as

$$\frac{\partial H}{\partial t} + \frac{\partial(\bar{u}H)}{\partial x} = 0 \quad (\text{A.70})$$

A.3.2 1D shallow water equations: Integration of the momentum equation

The x-direction momentum 2D shallow water equation (A.53), neglecting the dependence of τ_{xx} and τ_{xy} from z , the atmospheric pressure variation ($\partial P_a/\partial x$) and the density variation ($\partial\rho/\partial x$), can be rewritten as

$$\begin{aligned} & \frac{\partial(\bar{u}H)}{\partial t} + \frac{\partial(\bar{u}^2H)}{\partial x} + \frac{\partial(\bar{u}\bar{v}H)}{\partial y} = \\ & -gH\frac{\partial\eta}{\partial x} + \frac{H}{\rho}\frac{\partial\tau_{xx}}{\partial x} + \frac{H}{\rho}\frac{\partial\tau_{xy}}{\partial y} + \frac{1}{\rho}\tau_{xz,\eta} - \frac{1}{\rho}\tau_{xz,-h} \end{aligned} \quad (\text{A.71})$$

Let us integrate (A.71) in the y -directions by steps, starting with its left-hand inertial terms, following with the body force terms and finishing with the viscous terms.

Integration in the y-direction of local acceleration and advection terms

The left side terms of (A.71) are integrated as follows:

$$\begin{aligned} & \int_{-B/2}^{B/2} \left[\frac{\partial(\bar{u}H)}{\partial t} + \frac{\partial(\bar{u}^2H)}{\partial x} + \frac{\partial(\bar{u}\bar{v}H)}{\partial y} \right] dy = \\ & \int_{-B/2}^{B/2} \frac{\partial(\bar{u}H)}{\partial t} dy + \int_{-B/2}^{B/2} \frac{\partial(\bar{u}^2H)}{\partial x} dy + \int_{-B/2}^{B/2} \frac{\partial(\bar{u}\bar{v}H)}{\partial y} dy \end{aligned} \quad (\text{A.72})$$

Applying Leibnitz and integration rules to the above terms we obtain:

First term:

$$\begin{aligned} & \int_{-B/2}^{B/2} \frac{\partial(\bar{u}H)}{\partial t} dy = \\ & \frac{\partial}{\partial t} \int_{-B/2}^{B/2} \bar{u}H(t, y) dy - \bar{u}H(t, B/2) \frac{\partial(B/2)}{\partial t} + \bar{u}H(t, -B/2) \frac{\partial(-B/2)}{\partial t} \end{aligned} \quad (\text{A.73})$$

Second term:

$$\begin{aligned} & \int_{-B/2}^{B/2} \frac{\partial(\bar{u}^2H)}{\partial x} dy = \\ & \frac{\partial}{\partial x} \int_{-B/2}^{B/2} \bar{u}^2H(x, y) dy - \bar{u}^2H(x, B/2) \frac{\partial(B/2)}{\partial x} + \bar{u}^2H(x, -B/2) \frac{\partial(-B/2)}{\partial x} \end{aligned} \quad (\text{A.74})$$

Third term:

$$\int_{-B/2}^{B/2} \frac{\partial(\bar{w}H)}{\partial y} dy = \bar{w}H(x, B/2) - \bar{w}H(x, -B/2) \quad (\text{A.75})$$

Kinematic boundary conditions at the sides of the domain

Let us consider again the kinematic boundary condition at $-B/2$, (A.62):

$$\frac{\partial(-B/2)}{\partial t} + \bar{u} \frac{\partial(-B/2)}{\partial x} - \bar{v}(x, -B/2) = 0 \quad (\text{A.76})$$

then, at $B/2$:

$$\frac{\partial(B/2)}{\partial t} + \bar{u} \frac{\partial(B/2)}{\partial x} - \bar{v}(x, B/2) = 0 \quad (\text{A.77})$$

Replacing the terms of (A.72) by the ones of (A.73), (A.74) and (A.75), and grouping them, we have:

$$\begin{aligned} & \int_{-B/2}^{B/2} \left[\frac{\partial(\bar{u}H)}{\partial t} + \frac{\partial(\bar{u}^2H)}{\partial x} + \frac{\partial(\bar{w}H)}{\partial y} \right] dy = \\ & \frac{\partial}{\partial t} \int_{-B/2}^{B/2} \bar{u}H(t, y) dy + \frac{\partial}{\partial x} \int_{-B/2}^{B/2} \bar{u}^2H(x, y) dy + \dots \\ & \dots + \bar{u}H(x, -B/2) \left[\frac{\partial(-B/2)}{\partial t} + \bar{u} \frac{\partial(-B/2)}{\partial x} - \bar{v}(x, -B/2) \right] + \dots \\ & \dots + \bar{u}H(x, B/2) \left[-\frac{\partial(B/2)}{\partial t} - \bar{u} \frac{\partial(B/2)}{\partial x} + \bar{v}(x, B/2) \right] \end{aligned} \quad (\text{A.78})$$

Substituting the kinematic boundary condition it is possible to neglect the last terms of (A.78). \bar{u} is constant in the y -direction and H is independent of y . Then, we can integrate the remaining terms as follows:

$$\frac{\partial(\bar{u}H)}{\partial t} [y]_{-B/2}^{B/2} + \frac{\partial(\bar{u}^2H)}{\partial x} [y]_{-B/2}^{B/2} = \frac{\partial(\bar{u}HB)}{\partial t} + \frac{\partial(\bar{u}^2HB)}{\partial x} \quad (\text{A.79})$$

Integration of the body force term in the y-direction

Considering that the variation of η along x is independent of y , the integration of the corresponding term is expressed as:

$$\int_{-B/2}^{B/2} -gH \frac{\partial \eta}{\partial x} dy = -gBH \frac{\partial \eta}{\partial x} \quad (\text{A.80})$$

Considering that $H = h + \eta$:

$$-gBH \frac{\partial \eta}{\partial x} = -gBH \frac{\partial H}{\partial x} + gBH \frac{\partial h}{\partial x} \quad (\text{A.81})$$

Integration of the viscous term in the y-direction

The viscous terms of (A.53) are integrated in the y-direction as follows:

$$\int_{-B/2}^{B/2} \left[\frac{H}{\rho} \frac{\partial \tau_{xx}}{\partial x} + \frac{H}{\rho} \frac{\partial \tau_{xy}}{\partial y} + \frac{1}{\rho} (\tau_{xz,\eta} - \tau_{xz,-h}) \right] dy = \int_{-B/2}^{B/2} \frac{H}{\rho} \frac{\partial \tau_{xx}}{\partial x} dy + \int_{-B/2}^{B/2} \frac{H}{\rho} \frac{\partial \tau_{xy}}{\partial y} dy + \int_{-B/2}^{B/2} \frac{1}{\rho} \tau_{xz,\eta} dy + \int_{-B/2}^{B/2} -\frac{1}{\rho} \tau_{xz,-h} dy \quad (\text{A.82})$$

Applying Leibnitz rule to the first term:

$$\int_{-B/2}^{B/2} \frac{H}{\rho} \frac{\partial \tau_{xx}}{\partial x} dy = \frac{\partial}{\partial x} \int_{-B/2}^{B/2} \frac{H}{\rho} \tau_{xx}(x, y) dy - \frac{H}{\rho} \tau_{xx}(x, B/2) \frac{\partial(B/2)}{\partial x} + \dots \dots + \frac{H}{\rho} \tau_{xx}(x, -B/2) \frac{\partial(-B/2)}{\partial x} \quad (\text{A.83})$$

Integrating the second term:

$$\int_{-B/2}^{B/2} \frac{H}{\rho} \frac{\partial \tau_{xy}}{\partial y} dy = \frac{H}{\rho} \tau_{xy}(x, B/2) - \frac{H}{\rho} \tau_{xy}(x, -B/2) = \frac{HB}{\rho} \tau_{xy}(x) \quad (\text{A.84})$$

Integrating the third term:

$$\int_{-B/2}^{B/2} \frac{1}{\rho} \tau_{xz,\eta} dy = \frac{1}{\rho} \tau_{xz,\eta}(B/2) - \frac{1}{\rho} \tau_{xz,\eta}(-B/2) = \frac{B}{\rho} \tau_{xz,\eta} \quad (\text{A.85})$$

Integrating the fourth term:

$$\int_{-B/2}^{B/2} \frac{1}{\rho} \tau_{xz,-h} dy = \frac{1}{\rho} \tau_{xz,-h}(B/2) - \frac{1}{\rho} \tau_{xz,-h}(-B/2) = \frac{B}{\rho} \tau_{xz,-h} \quad (\text{A.86})$$

Grouping the terms from (A.83) to (A.86)

$$\begin{aligned}
& \int_{-B/2}^{B/2} \left[\frac{H}{\rho} \frac{\partial \tau_{xx}}{\partial x} + \frac{H}{\rho} \frac{\partial \tau_{xy}}{\partial y} + \frac{1}{\rho} (\tau_{xz,\eta} - \tau_{xz,-h}) \right] dy = \\
& \frac{\partial}{\partial x} \int_{-B/2}^{B/2} \frac{H}{\rho} \tau_{xx}(x, y) dy - \frac{H}{\rho} \tau_{xx}(x, B/2) \frac{\partial(B/2)}{\partial x} + \dots \\
& \dots + \frac{H}{\rho} \tau_{xx}(x, -B/2) \frac{\partial(-B/2)}{\partial x} + \frac{BH}{\rho} \tau_{xy}(x) + \frac{B}{\rho} \tau_{xz,\eta} + \frac{B}{\rho} \tau_{xz,-h}
\end{aligned} \tag{A.87}$$

Assuming B as constant along x , we can neglect the right-side second and third terms of (A.87). It yields:

$$\begin{aligned}
& \int_{-B/2}^{B/2} \left[\frac{H}{\rho} \frac{\partial \tau_{xx}}{\partial x} + \frac{H}{\rho} \frac{\partial \tau_{xy}}{\partial y} + \frac{1}{\rho} (\tau_{xz,\eta} - \tau_{xz,-h}) \right] dy = \\
& \frac{BH}{\rho} \frac{\partial \tau_{xx}}{\partial x} + \frac{BH}{\rho} \tau_{xy}(x) + \frac{B}{\rho} \tau_{xz,\eta} + \frac{B}{\rho} \tau_{xz,-h}
\end{aligned} \tag{A.88}$$

Neglecting shear stresses in the y-plane:

$$\int_{-B/2}^{B/2} \left[\frac{H}{\rho} \frac{\partial \tau_{xx}}{\partial x} + \frac{H}{\rho} \frac{\partial \tau_{xy}}{\partial y} + \frac{1}{\rho} (\tau_{xz,\eta} - \tau_{xz,-h}) \right] dy = \frac{BH}{\rho} \frac{\partial \tau_{xx}}{\partial x} + \frac{B}{\rho} \tau_{xz,\eta} + \frac{B}{\rho} \tau_{xz,-h} \tag{A.89}$$

Grouping all terms of the x-momentum equation

From the development shown above, the one-dimensional (x -direction) shallow water momentum equation, considering $B = 1$, is expressed as:

$$\begin{aligned}
\frac{\partial(\bar{u}H)}{\partial t} + \frac{\partial(\bar{u}^2 H)}{\partial x} &= -gH \frac{\partial H}{\partial x} + gH \frac{\partial h}{\partial x} + \frac{H}{\rho} \frac{\partial \tau_{xx}}{\partial x} \\
&+ \frac{1}{\rho} \tau_{xz,\eta} - \frac{1}{\rho} \tau_{xz,-h}
\end{aligned} \tag{A.90}$$

Neglecting the τ_{xx} normal stress due to the assumption of no viscous effects, which are presented only in the shear stress components in the boundaries, we have:

$$\frac{\partial(\bar{u}H)}{\partial t} + \frac{\partial(\bar{u}^2 H)}{\partial x} = -gH \frac{\partial H}{\partial x} + gH \frac{\partial h}{\partial x} + \frac{1}{\rho} \tau_{xz,\eta} - \frac{1}{\rho} \tau_{xz,-h} \tag{A.91}$$

It is considered an horizontal bottom and the mean level located at the bottom surface. Then equality $H = \eta + h$, with $h = 0$ becomes $H = \eta$. From this,

$dh/dx = 0$, and the above equation can be expressed as:

$$\frac{\partial(\bar{u}\eta)}{\partial t} + \frac{\partial(\bar{u}^2\eta)}{\partial x} = -g\eta\frac{\partial\eta}{\partial x} + \frac{1}{\rho}\tau_{xz,\eta} - \frac{1}{\rho}\tau_{xz,-h} \quad (\text{A.92})$$

Assuming the shear stress caused by the air is smaller than the one caused by the bottom boundary ($\tau_{xz,-h} \gg \tau_{xz,\eta}$), last equation can be rewritten as:

$$\frac{\partial(\bar{u}\eta)}{\partial t} + \frac{\partial(\bar{u}^2\eta)}{\partial x} = -g\eta\frac{\partial\eta}{\partial x} - \frac{1}{\rho}\tau_{xz,-h} \quad (\text{A.93})$$

The 1D (x-direction) system of shallow water equations is summarized as follows:

Continuity equation

$$\frac{\partial\eta}{\partial t} + \frac{\partial(\bar{u}\eta)}{\partial x} = 0 \quad (\text{A.94})$$

or in its non-conservative form:

$$\frac{\partial\eta}{\partial t} + \eta\frac{\partial\bar{u}}{\partial x} + \bar{u}\frac{\partial\eta}{\partial x} = 0 \quad (\text{A.95})$$

Momentum equation

$$\frac{\partial(\bar{u}\eta)}{\partial t} + \frac{\partial(\bar{u}^2\eta)}{\partial x} = -g\eta\frac{\partial\eta}{\partial x} - \frac{1}{\rho}\tau_{xz,-h} \quad (\text{A.96})$$

A.4 Dimensional analysis to simplify terms

The momentum equation of the 1D shallow water system (A.96) is nonlinear. This restricts the development of analytical approximate solutions for the considered problem. Identification of convenient terms can be made by normalizing the governing equations to verify the order of the terms involved to perform simplifications. To do this, any convenient variables of the problem can be defined as characteristic or reference parameters. For this study, let us define the reference parameters as follows: η_0 corresponds to the maximum water elevation of the event at upstream ($x = 0$). \bar{u}_0 is the horizontal flow velocity at upstream ($x = 0$) at η_0 occurrence, and L_0 is the structure length. With these reference parameter the next dimensionless parameters are defined to characterize the water-on-deck events:

$$\eta^* = \frac{\eta}{\eta_0} \quad (\text{A.97})$$

$$\bar{u}^* = \frac{\bar{u}}{\bar{u}_0} \quad (\text{A.98})$$

$$\bar{x}^* = \frac{\bar{x}}{L_0} \quad (\text{A.99})$$

$$t^* = \frac{\bar{u}_0 t}{L_0} \quad (\text{A.100})$$

Replacing the above terms, the continuity equation (A.94) can be rewritten as:

$$\frac{\bar{u}_0 \eta_0}{L_0} \left(\frac{\partial \eta^*}{\partial t^*} + \frac{\partial \eta^* \bar{u}^*}{\partial x^*} \right) = 0 \quad (\text{A.101})$$

which yields:

$$\left(\frac{\partial \eta^*}{\partial t^*} + \frac{\partial \eta^* \bar{u}^*}{\partial x^*} \right) = 0 \quad (\text{A.102})$$

Following a similar procedure, the momentum equation (A.94) can be expressed as:

$$\frac{\bar{u}_0^2 \eta_0}{L_0} \frac{\partial (\bar{u}^* \eta^*)}{\partial t^*} + \frac{\bar{u}_0^2 \eta_0}{L_0} \frac{\partial (\bar{u}^{2*} \eta^*)}{\partial x^*} = -\frac{g \eta_0^2}{L_0} \frac{\partial \eta^*}{\partial x^*} \eta^* - \frac{\tau_{xz,-h}}{\rho} \quad (\text{A.103})$$

multiplying by $\frac{L_0}{g \eta_0^2}$ we have:

$$F_n^2 \left(\frac{\partial (\bar{u}^* \eta^*)}{\partial t^*} + \frac{\partial (\bar{u}^{2*} \eta^*)}{\partial x^*} \right) = -\frac{\partial \eta^*}{\partial x^*} \eta^* - \frac{L_0}{g \eta_0^2} \frac{\tau_{xz,-h}}{\rho} \quad (\text{A.104})$$

where F_n represents the Froude number, which in the present work is defined as:

$$F_n = \frac{\bar{u}_0}{\sqrt{g \eta_0}} \quad (\text{A.105})$$

Let us neglect the inertial terms (left-side) by assuming subcritical flow ($F_n < 1$). Analyzing the order of the terms we observe that for such assumption, the momentum equation can be simplified as follows:

$$\frac{\partial \eta}{\partial x} = -\frac{\tau_{xz,-h}}{g \rho \eta} \quad (\text{A.106})$$

A.5 The constant shear stress assumption

The τ_{xz} component of the shear stress sensor noted in the equation of momentum (A.106) can be considered in vectorial form, accounting for the shear stress on the bottom at different x and t . However, for practical application, it is assumed that the roughness of the surface is constant. The shear stresses can be accounted for as resistance coefficients, which can be defined as [52]:

$$S_f = \frac{\tau_b}{\rho g \eta} \quad (\text{A.107})$$

where τ_b is the constant shear stress (i.e., constant τ_{xz} for the present approach). Simplified scalar assumptions to relate constant bottom shear stresses (τ_b) to constant resistance coefficients (S_f) are preferred in many cases in terms of practical implementation. Use of Chezy or Manning empirical formulations are alternatives. The Chezy or Manning approaches can be considered through the next expression [53]:

$$S_f = \left(\frac{\bar{u}}{k\eta^m} \right)^2 \quad (\text{A.108})$$

where, for the Manning friction approach: $k = 1/n_m$, with n_m as the Manning roughness coefficient (dimension $L^{1/3}T$) and $m = 2/3$. Furthermore, for the Chezy approach: $k = C_c$, with C_c as the Chezy friction coefficient (dimension $L^{1/2}T$) and $m = 1/2$.

A.6 The advection-diffusion model

Let us consider the 1D shallow water continuity equation (A.94) in its non-conservative form:

$$\frac{\partial \eta}{\partial t} + \eta \frac{\partial \bar{u}}{\partial x} + \bar{u} \frac{\partial \eta}{\partial x} = 0 \quad (\text{A.109})$$

Defining the bottom resistance coefficient as $S_f = \frac{\tau_b}{g\rho\eta}$ ([52], page 223), the momentum equation (A.106) is rewritten as:

$$\frac{\partial \eta}{\partial x} = -\frac{\tau_b}{g\rho\eta} = -S_f \quad (\text{A.110})$$

A single partial differential equation with η as the dependent variable, allowing analytical solutions, will be obtained by following the next steps:

1. To replace (A.108) into (A.110);
2. To derive the resulting equation with respect to x ;
3. To replace the obtained $\partial \bar{u} / \partial x$ expression into the continuity equation (A.109);
4. To simplify the resulting equation until obtaining an advection-diffusion equation.

Thus, substituting (A.108) into (A.110) gives:

$$\frac{\partial \eta}{\partial x} = -S_f = -\left(\frac{\bar{u}}{k\eta^m} \right)^2 = -\frac{\bar{u}^2}{(k\eta^m)^2} = -\frac{\bar{u}^2}{k^2\eta^{2m}} \quad (\text{A.111})$$

Deriving with respect to x :

$$\frac{\partial^2 \eta}{\partial x^2} = -\frac{(k\eta^m)^2(2\bar{u})\frac{\partial \bar{u}}{\partial x} - \bar{u}^2 k^2(2m)(\eta^{2m-1})\frac{\partial \eta}{\partial x}}{k^4 \eta^{4m}} \quad (\text{A.112})$$

$$\frac{\partial^2 \eta}{\partial x^2} = -\frac{2\bar{u}\frac{\partial \bar{u}}{\partial x}}{k^2 \eta^{2m}} + \frac{2m\bar{u}^2 \frac{\partial \eta}{\partial x}}{k^2 \eta^{2m} \eta} \quad (\text{A.113})$$

$$\frac{\partial^2 \eta}{\partial x^2} - \frac{2m\bar{u}^2}{k^2 \eta^{2m} \eta} \frac{\partial \eta}{\partial x} = -\frac{2\bar{u}}{k^2 \eta^{2m}} \frac{\partial \bar{u}}{\partial x} \quad (\text{A.114})$$

$$-\frac{k^2 \eta^{2m}}{2\bar{u}} \frac{\partial^2 \eta}{\partial x^2} - \left(-\frac{k^2 \eta^{2m}}{2\bar{u}} \right) \frac{2m\bar{u}^2}{k^2 \eta^{2m} \eta} \frac{\partial \eta}{\partial x} = \frac{\partial \bar{u}}{\partial x} \quad (\text{A.115})$$

$$\frac{\partial \bar{u}}{\partial x} = -\frac{k^2 \eta^{2m}}{2\bar{u}} \frac{\partial^2 \eta}{\partial x^2} + \frac{\bar{u}m}{\eta} \frac{\partial \eta}{\partial x} \quad (\text{A.116})$$

Substituting $\partial \bar{u}/\partial x$ in the continuity equation (A.109):

$$\frac{\partial \eta}{\partial t} + \bar{u} \frac{\partial \eta}{\partial x} + \eta \left(-\frac{k^2 \eta^{2m}}{2\bar{u}} \frac{\partial^2 \eta}{\partial x^2} + \frac{\bar{u}m}{n} \frac{\partial \eta}{\partial x} \right) = 0 \quad (\text{A.117})$$

$$\frac{\partial \eta}{\partial t} + \bar{u} \frac{\partial \eta}{\partial x} - \frac{k^2 \eta^{2m}}{2\bar{u}} \frac{\partial^2 \eta}{\partial x^2} + \bar{u}m \frac{\partial \eta}{\partial x} = 0 \quad (\text{A.118})$$

$$\frac{\partial \eta}{\partial t} + \bar{u}(m+1) \frac{\partial \eta}{\partial x} = \frac{k^2 \eta^{2m} \eta}{2\bar{u}} \frac{\partial^2 \eta}{\partial x^2} \quad (\text{A.119})$$

which after some algebra yields,

$$\frac{\partial \eta}{\partial t} + \bar{u}(m+1) \frac{\partial \eta}{\partial x} = \frac{\bar{u}\eta}{2S_f} \frac{\partial^2 \eta}{\partial x^2} \quad (\text{A.120})$$

Finally, it has been obtained an advection-diffusion equation with η as the dependent variable. From this equation, the advection and diffusion coefficients are defined by (A.121) and (A.122), respectively:

$$A = \bar{u}(m+1) \quad (\text{A.121})$$

$$B = \frac{\bar{u}\eta}{2S_f} \quad (\text{A.122})$$

where m is considered as $m = 2/3$ or $m = 1/2$ for the Manning or Chezy approaches to consider the resistance coefficients, respectively. Both coefficients have to be considered constant to allow analytical solutions of (A.120) for different initial and boundary conditions. Among the possible mathematical methods that can be

used to obtain the solutions, it is possible to mention the Laplace transform and the Green function methods. The latter was considered in the present work for a boundary-value problem of the Dirichlet-type in semi-infinite domain. Details of the procedure to obtain the solution of such a problem can be found in [54].

Appendix B

Complementary experimental setup illustrations

In this appendix some figures of the experimental setup are presented as complementary information for illustration purposes.



Figure B.1: General view of the complete experimental setup, considering the experiment with the rectangular fixed structure inside the tank.

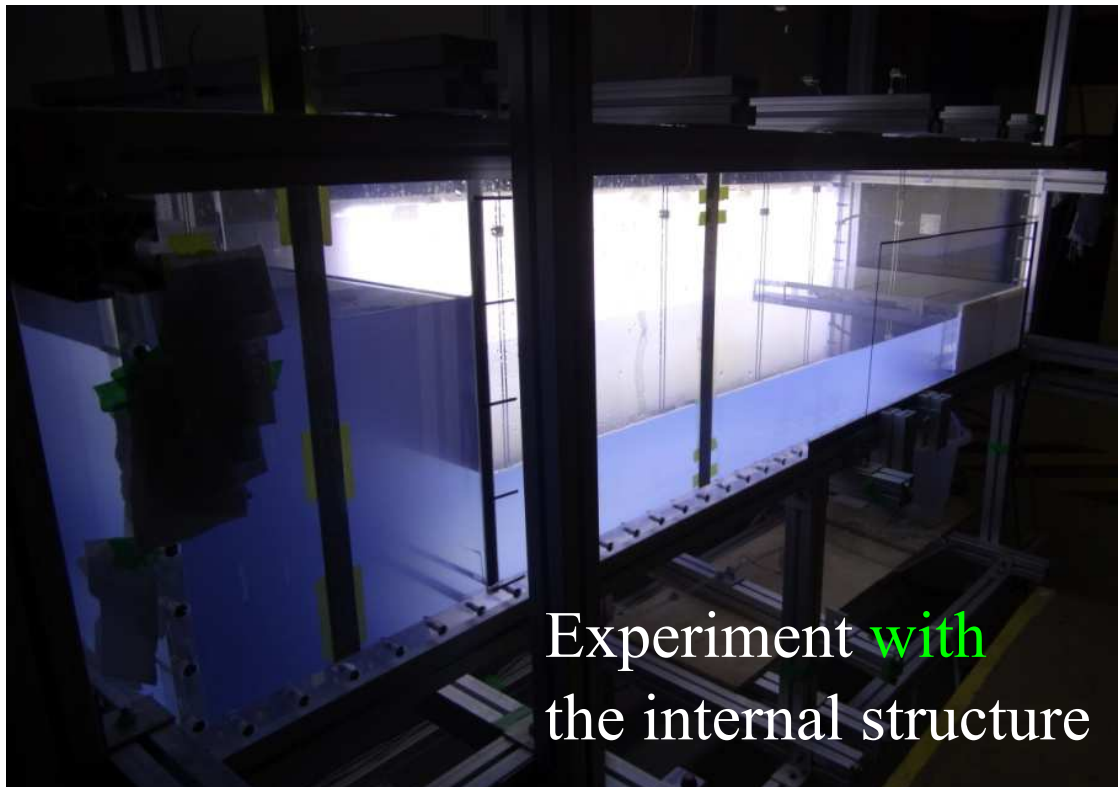
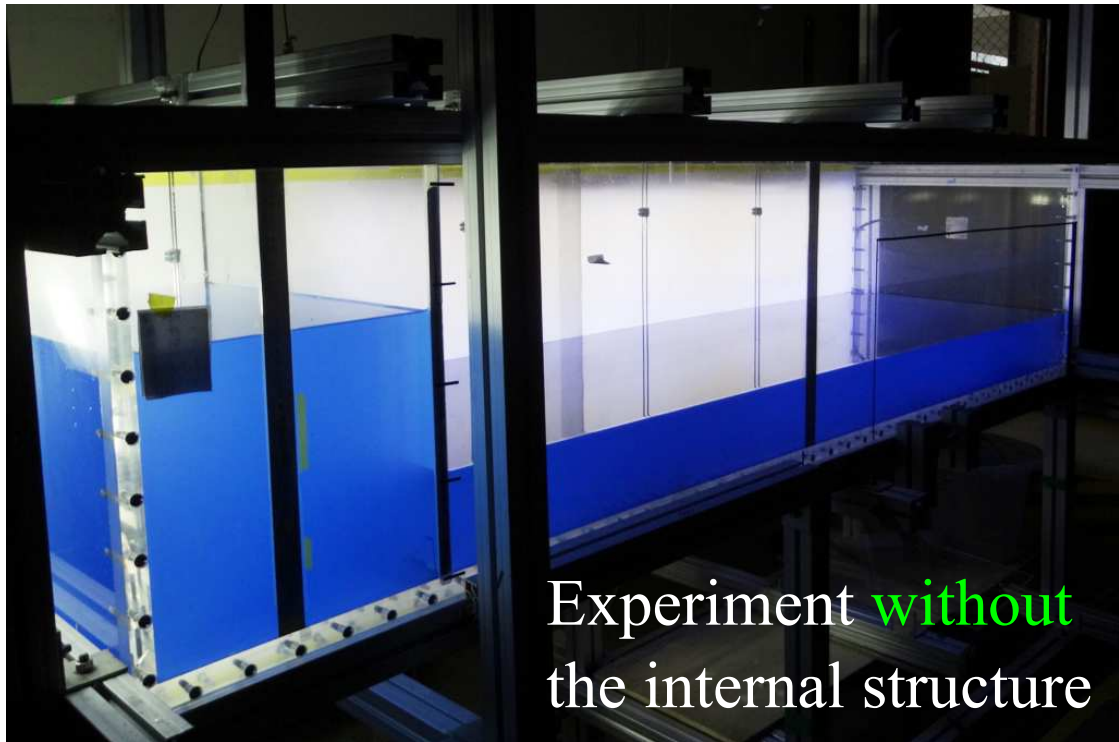


Figure B.2: Typical views of initial conditions for the experiments without (above) and with (below) the internal fixed structure.

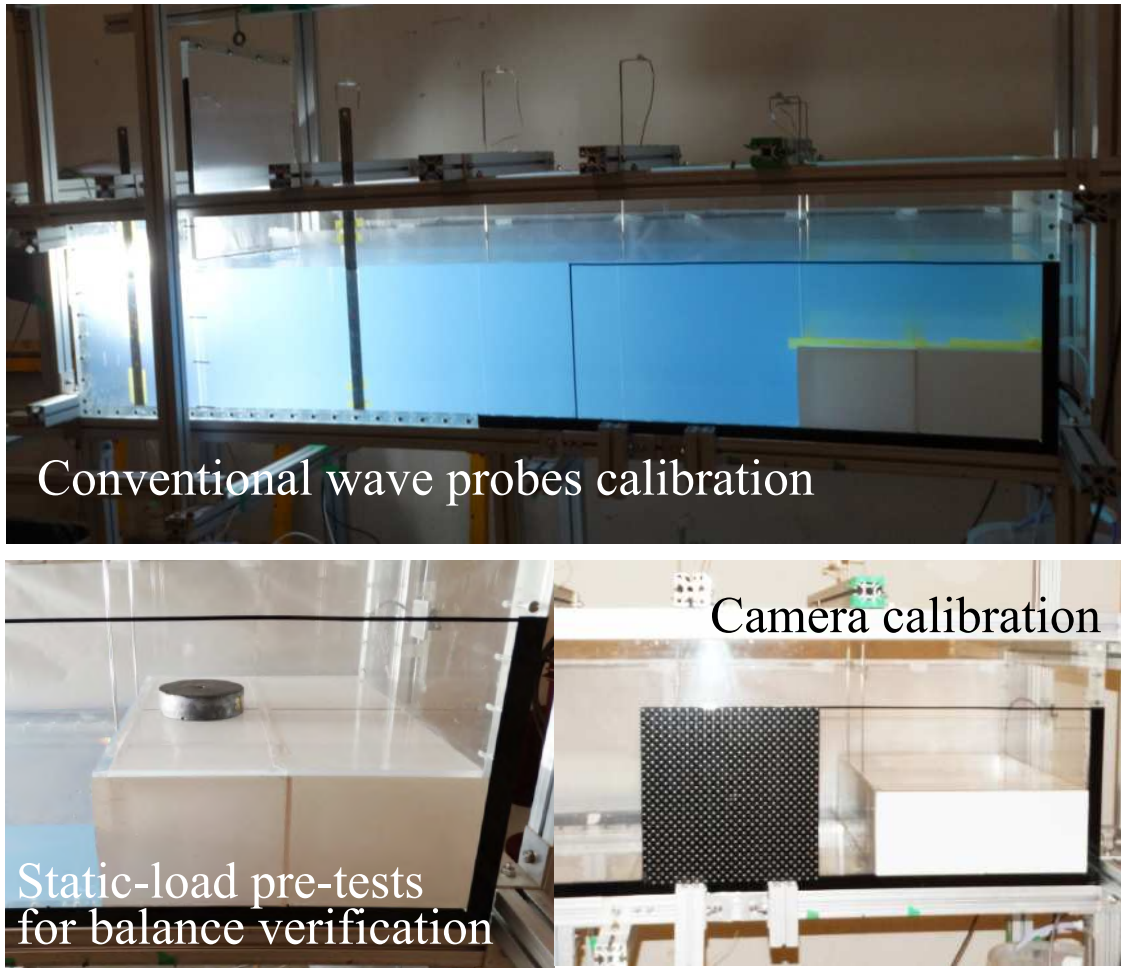


Figure B.3: Some important stages during sensors preliminary tests: conventional wave probes calibration (above), static-load pre-tests of the balance before each test (below-left) and camera calibration following the image-based methodology described in the Experimental Methods section (below-right).

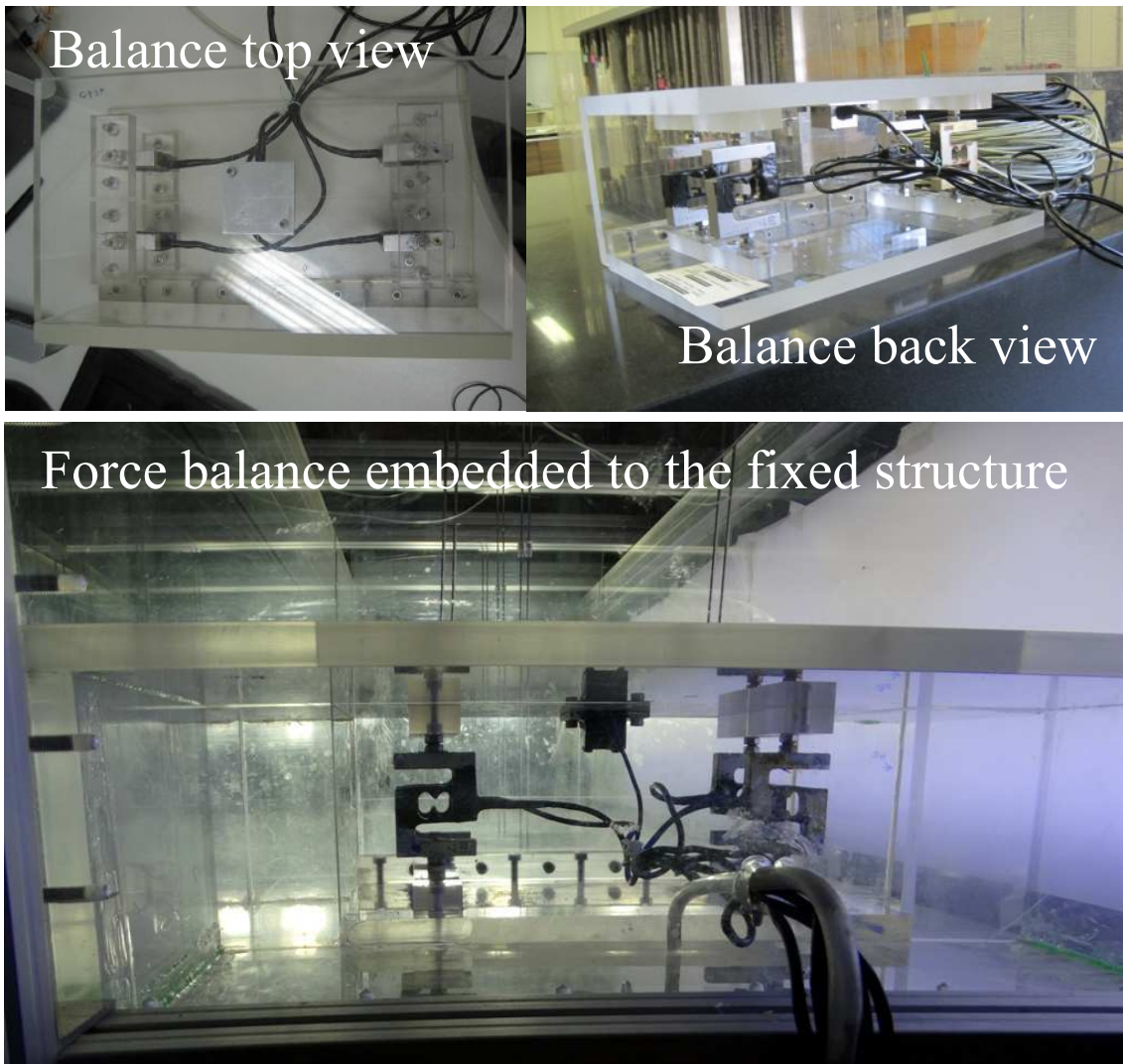


Figure B.4: Force balance top view (above left) and back view (above right). Detailed view of the force balance embedded to the internal fixed structure (below).

Appendix C

A tentative for wave characterization

This appendix presents a tentative to characterize the steepness of the resulting wet dam-break wave in order to relate it with regular waves (i.e., linear wave theory). It has to be mentioned that the physics of both waves is completely different, and that the present procedure is described merely for illustrative purposes.

The sketch of Figure [C.1](#) shows parameters considered to estimate the bore steepness, following the approach of NAKAGAWA *et al.* [\[9\]](#). To do this, spatial distributions of water elevations (η vs x) are used to estimate the bore steepness as $(\eta_2 - \eta_1)/L$, considering the parameters illustrated in the figure.

The spatial distributions (η vs x) have been obtained from virtual wave probe measurements in the experiment without the internal fixed structure using the CAM2, which was set to visualize the region of the tank near the gate (see Chapter [3](#) for details). This region was chosen regarding the better visualization of the well developed bore with minimum effects of the downstream tank wall on it.

Figure [C.2](#) shows the spatial distributions of the bore for all cases, from which mean values were considered to estimate the parameters indicated in Fig. [C.1](#) at the points indicated by the arrows. From the available information, a common time stage ($t = 0.85\text{s}$) was selected for all cases in order to capture as much as possible the formation of the after-coming second peak in the wave trend, for the spatial range $0 < x < 0.6\text{m}$, where the gate was considered as reference.

The approximated bore parameters measured for each case are summarized in Table [C.1](#). Also, the resultant regular wave relations are presented in the right side of the table. These last were obtained considering the regular wave steepness as H_w/L_w (where H_w and L_w are wave height and length, respectively) and assuming that $L_w = L$ and $H_w = \eta_0 - \eta_1$ (Fig. [C.1](#)). Then, it can be assumed that the cases considered in this study may resemble regular waves for the model scale in the ranges $0.17 \leq L_w \leq 0.34$ m and $0.031 \leq H_w \leq 0.044$ m for Cases 1w and 5w,

respectively. In other words, it can be generalized that in cases that present the higher freeboards (e.g., C1w, C2w) steeper waves are generated by the wet dam-break approach, whereas in cases with smaller freeboard (e.g., C4w, C5w), longer waves are generated, as verified from the wave periods shown in the table.

It is important to note that although the wet dam-break ratio is the same for all cases, changes in the freeboard maintaining the same ratio for the five cases yielded five different waves, which for further analyses they may be assumed to be in the range of wave steepness from 0.01 to 0.02, approximately.

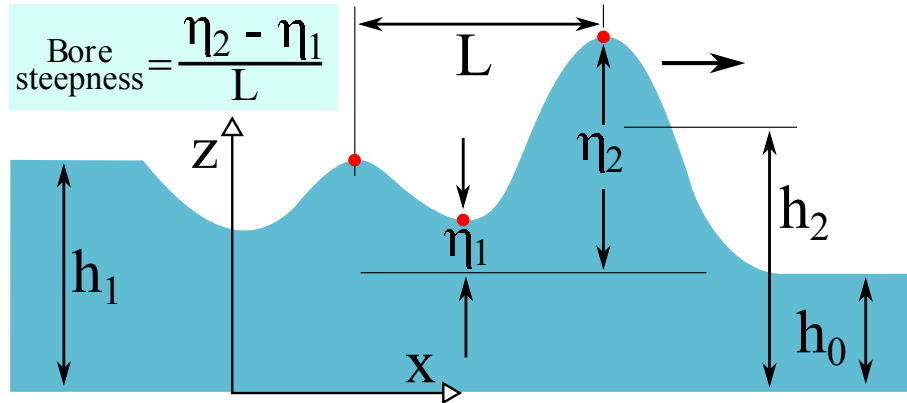


Figure C.1: Incoming wave (bore) steepness characterization.

Table C.1: Values of the incoming wave (bore) characterization of steepness and their relationship with regular waves.

<i>Case</i>	Bore		⇔	Regular wave					
	<i>L</i> (m)	<i>Steepness</i>	⇔	<i>H_w</i> (m)	<i>Amplitude</i> (m)	<i>L_w</i> (m)	<i>Steepness</i>	<i>Frequency</i> (rad/s)	<i>Period</i> (s)
C1w	0.17	≈ 0.18	⇔	0.031	0.015	0.17	0.18	19.04	0.33
C2w	0.21	≈ 0.18	⇔	0.037	0.018	0.21	0.18	17.13	0.37
C3w	0.23	≈ 0.16	⇔	0.037	0.018	0.23	0.16	16.37	0.38
C4w	0.26	≈ 0.15	⇔	0.039	0.019	0.26	0.15	15.40	0.41
C5w	0.34	≈ 0.13	⇔	0.044	0.022	0.34	0.13	13.46	0.47

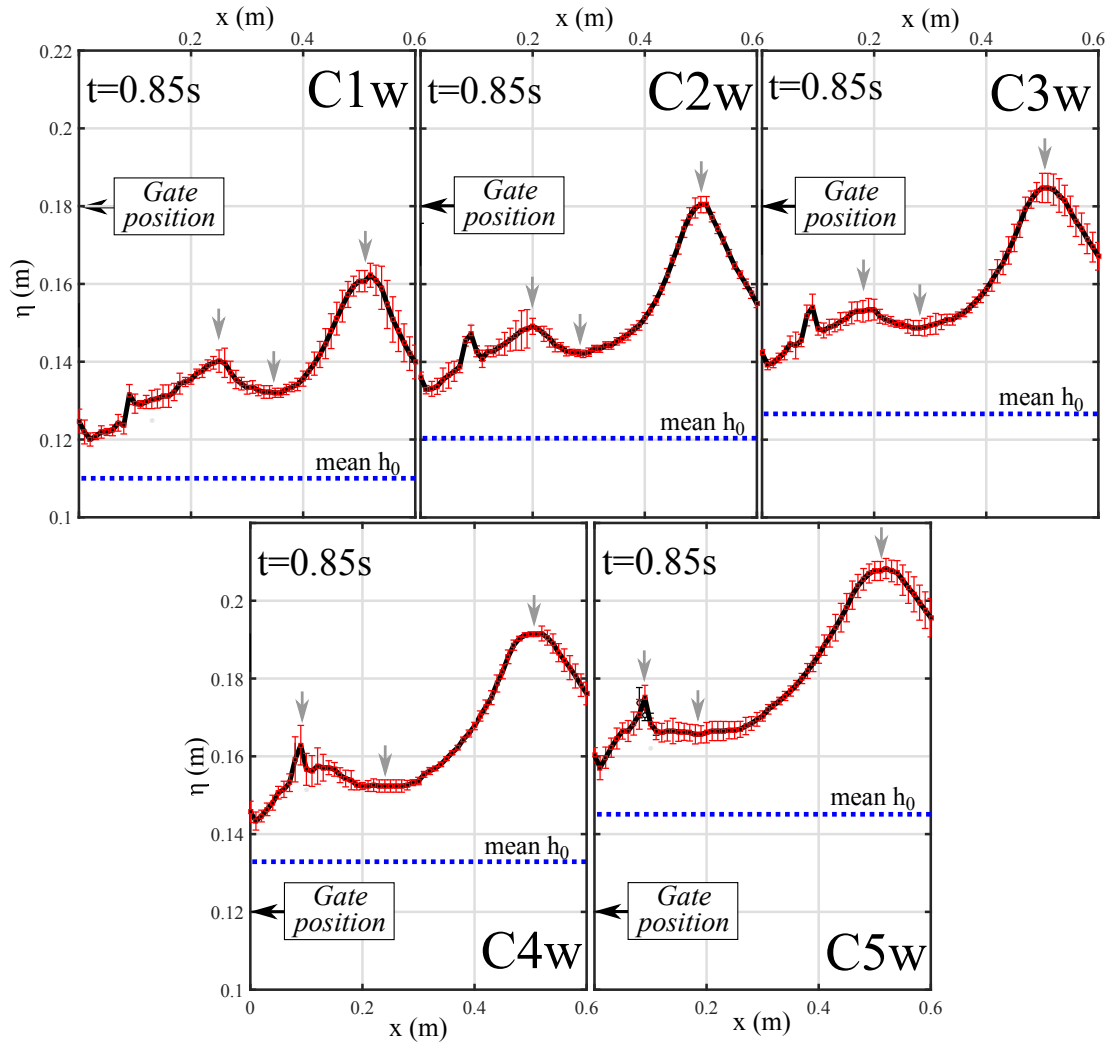


Figure C.2: Spatial distributions of water elevations considered for $t = 0.85$ s to characterize the steepness of the resulting bores for the experiment without structure. (a) C1w. (b) C2w. (c) C3w. (d) C4w. (e) C5w.

Appendix D

Examples of shipping water events obtained with $h_0/h_1 = 0.6, 0.5, 0.4$

During the experimental investigation, it was verified that the wet dam-break approach allowed reproducing several types of isolated shipping water events. If the structure is the same, then, the resulting events will depend on the characteristics of the incoming wave. With the dam-break installation used in the present investigation, it was verified that, for instance, for ratios higher than 0.6, the incident waves were unbroken, whereas for ratios lower than 0.6 the incident waves presented their front partially broken. The present work was focused in the ratio 0.6; however, as object of illustration, some events obtained with unbroken waves are presented in this appendix.

Figures [D.1](#), [D.2](#) and [D.3](#) show time series of some events generated with the same freeboard ($FB = 0.042$ m, $h_0 = 0.108$ m) and wet dam-break ratios $h_0/h_1 = 0.6, 0.5$ and 0.4 , respectively.

The former event (Fig [D.1](#)) was generated by an unbroken wave, and it corresponds to the type of event investigated in the present thesis.

On the other hand, Figures [D.2](#) and [D.3](#) show events generated with broken waves, that is, with their front partially broken.

It can be verified from all cases that the resultant patterns of shipping water depend of a combination of the structure and wave parameters. Thereby, the experimental approach proposed in the present thesis enables the possibility to investigate details of different types of shipping water in a systematic and practical way.

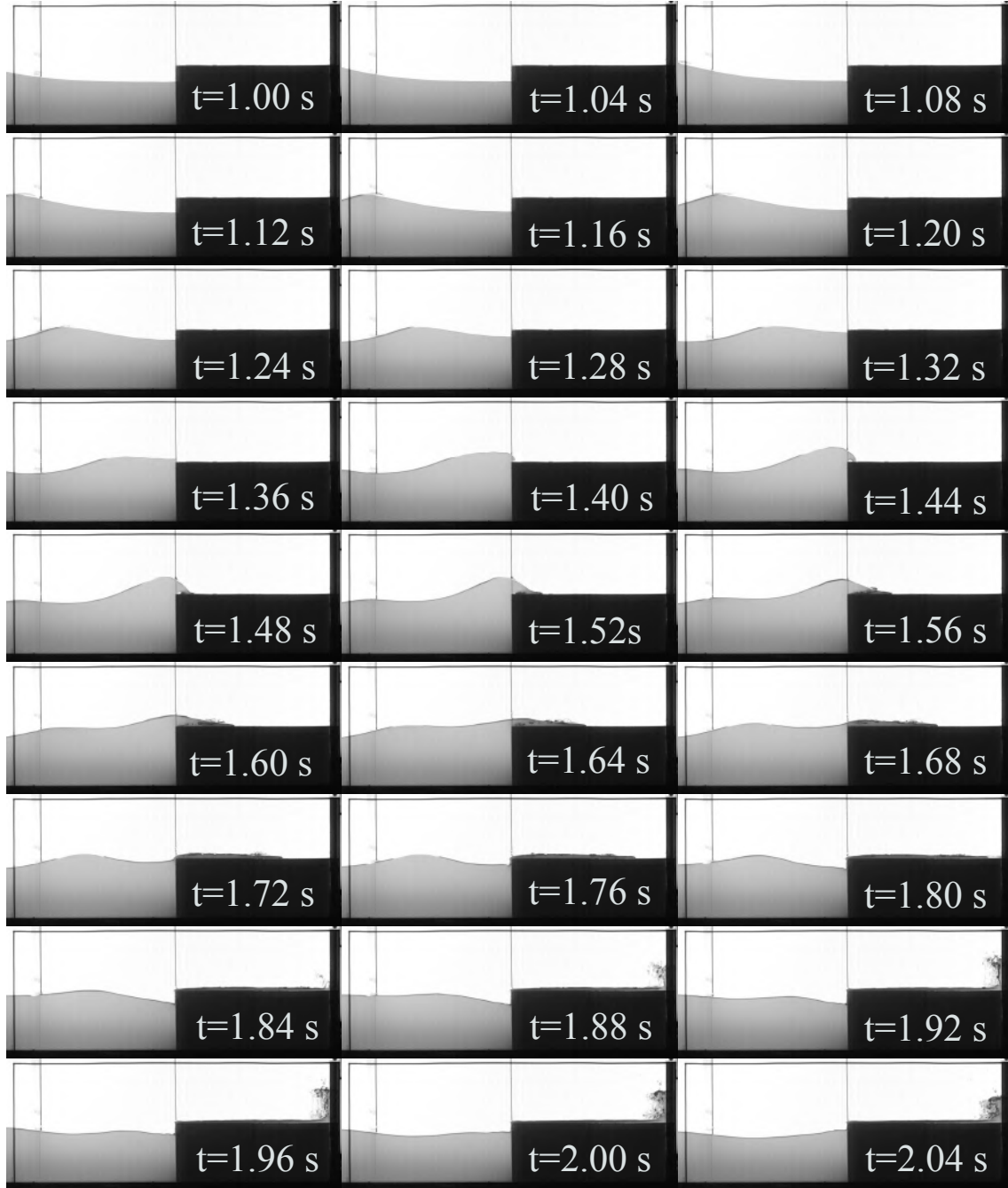


Figure D.1: Snapshots of a shipping water event generated with $h_0/h_1 = 0.6$, $h_0 = 0.108$ m and $FB = 0.042$ m (unbroken wave).

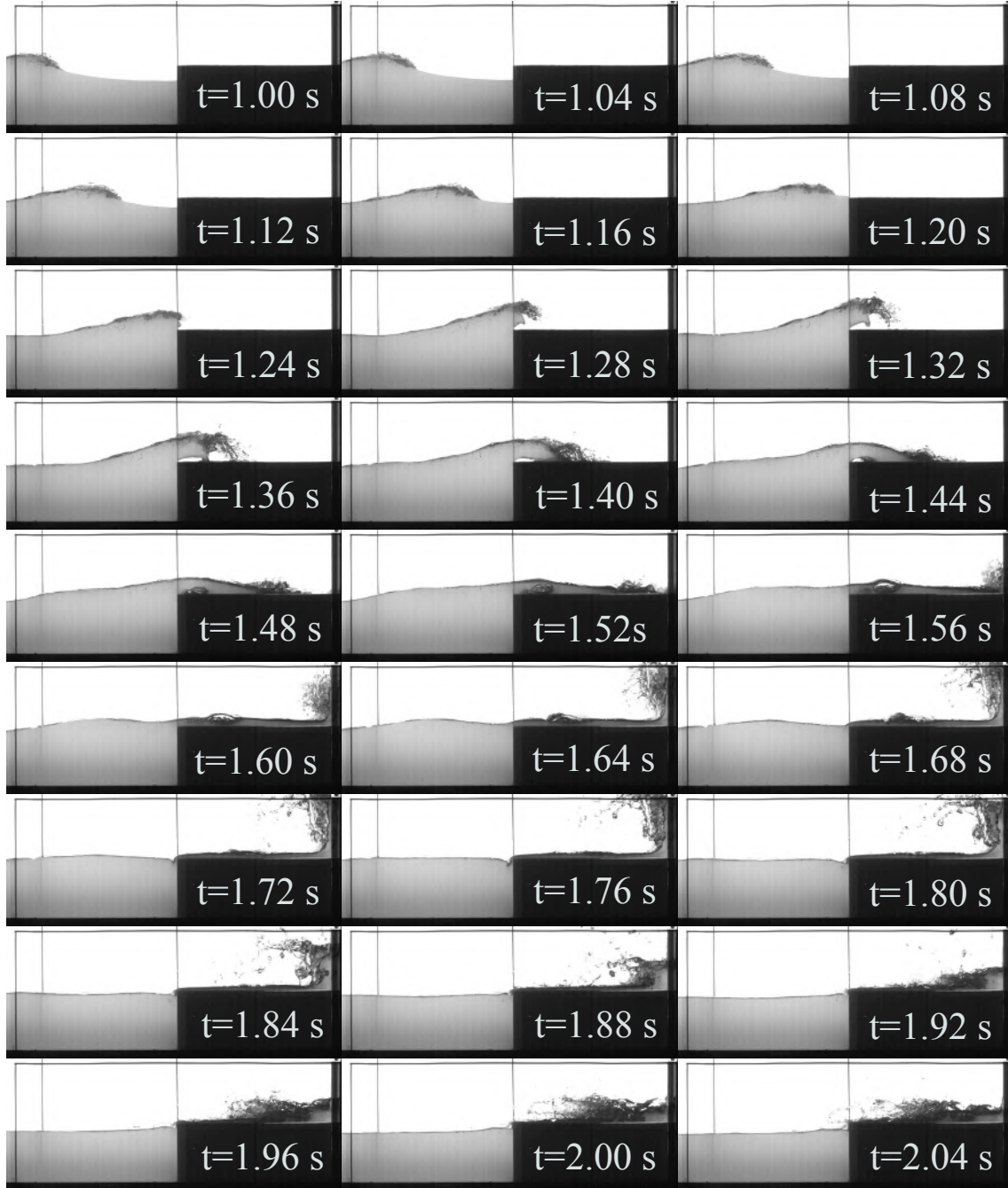


Figure D.2: Snapshots of a shipping water event generated with $h_0/h_1 = 0.5$, $h_0 = 0.108$ m and $FB = 0.042$ m (unbroken wave).

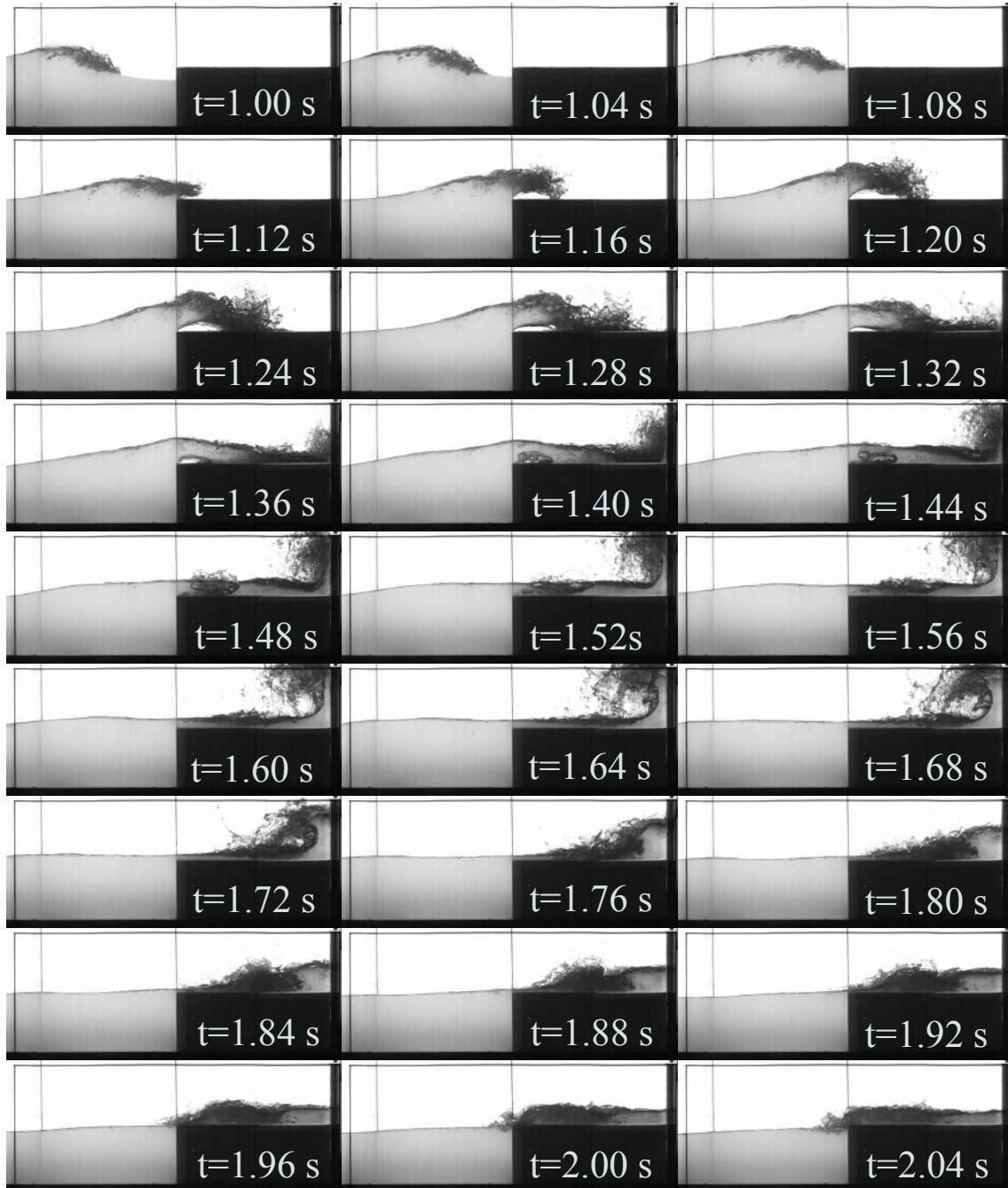


Figure D.3: Snapshots of a shipping water event generated with $h_0/h_1 = 0.4$, $h_0 = 0.108$ m and $FB = 0.042$ m (unbroken wave).

Appendix E

Related publications

Accepted publications in journals

1. Hernández-Fontes J.V., Vitola M.A., Esperança P.T.T., Sphaier S.H. An alternative for estimating shipping water height distribution due to green water on a ship without forward speed, *Marine Systems and Ocean Technology*, 10 (1), 38-46, 2015.
2. Hernández I.D., Hernández-Fontes J.V., Vitola M.A., Silva M.C., Esperança P.T.T., Water elevation measurements using binary image analysis for 2D hydrodynamic experiments, *Ocean Engineering*, Volume 157, pages 325-338, 2018.
3. Hernández-Fontes, J. V., Vitola, M. A., Silva, M. C., Esperança, P. T. T., Sphaier, S. H. On the generation of isolated green water events using wet dam-break. *Journal of Offshore Mechanics and Arctic Engineering*, 2018.

Accepted publications in congresses

1. Hernández-Fontes J.V., Vitola M.A., Esperança P.T.T., Sphaier S.H., An alternative to estimate the shipping water height distribution due to green water on a ship without forward speed, 25 Congresso Nacional de Transporte Aquavirio, Construção Naval e Offshore, SOBENA - Sociedade Brasileira de Engenharia Naval, Rio de Janeiro, Brazil, 2014.
2. Hernández-Fontes, J. V., Vitola, M. A., Silva, M. C., Esperança, P. T. T., Sphaier, S. H. Use of wet dam-break to study green water problem. In: OMAE 2017, 36th International Conference on Ocean, Offshore and Arctic Engineering, Trondheim, Norway. American Society of Mechanical Engineers.

Journal article No. 1

Marine Systems & Ocean Technology (2015), Volume 10, Issue 1, pages 3846.

DOI 10.1007/s40868-015-0003-6

An alternative for estimating shipping water height distribution due to green water on a ship without forward speed

Hernández-Fontes J.V. ✉, Vitola M.A., Esperança P.T.T., Sphaier S.H.

Abstract

The aim of this paper was to present a practical approach for estimating the distribution of water height on the deck of a ship due to a green water event. This distribution can be used to estimate vertical loading on ship and platform decks in the early design phase. The present approach is an extension of the methodology proposed by Ogawa et al. in *J Soc Naval Archit Jpn* 182:177185 (1997) for estimating that distribution on a ship with advance speed. In this study, the methodology was adapted for application to a ship without forward speed. The analytical formulation is presented, followed by a parametric study to evaluate the influence of the main input parameters in the results. The results are compared with experimental data from Buchner in *Offshore Technology Conference (OTC)*, vol 7698, Houston, Texas, (1995a) and numerical results from Nielsen in *numerical prediction of green water loads on ships*, Technical University of Denmark, Lyngby (2003). It is observed that the parameters with the greatest influence on the resultant water height distribution are the initial water height at the stem of the ship and the breadth of the incoming volume of water. A smaller influence is observed for the other input parameters. The results indicate potential for the adapted model to estimate shipping water height distributions due to green water events, at least in early design stages.

Water elevation measurements using binary image analysis for 2D hydrodynamic experiments

Hernández I.D., Hernández-Fontes J.V. ✉, Vitola M.A., Silva M.C.,
Esperança P.T.T.

Abstract

This paper presents an alternative and open-source methodology based on binary image analysis to measure water elevations in two-dimensional hydrodynamic experiments. The proposed methodology considers the three main stages of an artificial vision system: image digitalization, processing and analysis. In the image processing stage, binary images were obtained by intensity modulation and pseudo-color-based segmentation. The image analysis stage employs simplified morphological operations to measure water elevations at specified regions of interest in the binary images. The image processing and analysis stages were developed in scripts for the ImageJ open-source software. The applicability of the proposed methodology was verified by comparing measurements of water elevations obtained using the proposed approach and conventional wave probes during experiments of shipping water on a fixed structure. The experiments included cases where single-valued and double-valued water surfaces were observed. For all the test cases, the water elevation time series obtained using the proposed approach were in good agreement with the experiments before three-dimensional effects on flow were significant. For the case in which a double-valued water surface was observed, it was confirmed that the proposed procedure possesses the capability to measure the effective water height at specified regions of interest.

On the generation of isolated green water events using wet dam-break

Hernández-Fontes J.V. ✉, Vitola M.A., Silva M.C., Esperança P.T.T., Sphaier S.H.

Abstract

Green water occurs when an incoming wave exceeds the freeboard and propagates onto the deck of naval/offshore structures, such as FPSOs and platforms. This water can affect the integrity of facilities and equipment that are installed on the deck, compromise the safety of the crew and affect the dynamic stability of the structure. Traditionally, wave trains have been used to study the green water problem, which is a good approach to analyzing consecutive green water events. However, to carry out systematic studies that allow local details to be identified for different types of green water, an alternative method is to study isolated events generated by a single incoming wave. The purpose of this paper was to experimentally investigate the generation of different types of isolated green water events using the wet dam-break approach as an alternative to generating the incoming wave. Tests were carried out in a rectangular tank with a fixed internal structure. Different freeboard conditions were tested for two aspect ratios of the wet dam-break ($h_0/h_1 = 0.40$ and 0.6). Conventional wave probes were used to measure the water levels in the tank, and a high-speed camera was set to capture details of the generated green water events. The results demonstrated the ability of this approach to represent different types of green water, similar to those obtained with unbroken regular waves in barge-shaped fixed structures, including dam-break, plunging-dam-break and hammer-fist.